Quasi-analytic modal expansion methods for optical modelling of cylindrical nanostructures in GaN LEDs

O'Kane, Simon

Award date:
2015

Awarding institution:
University of Bath

Quasi-analytic modal expansion methods for optical modelling of cylindrical nanostructures in GaN LEDs

submitted by

Simon O'Kane

for the degree of Doctor of Philosophy of the

University of Bath

Department of Electronic and Electrical Engineering

December 2015

Summary

Gallium nitride (GaN)-based light-emitting diodes (LEDs) with cylindrical nanostructures have been the subject of significant research interest in the past decade, due to the potential of such structures to increase light extraction efficiency and deliver highly directional light emission. Nanorod LEDs, where the light emission is within the nanocylinder, have the additional potential to increase internal quantum efficiency and emit in colours previously thought impractical with GaN-based LEDs.

Optical modelling of nanostructured LEDs is usually carried out using finite-difference time-domain methods, which are computationally intensive and do not always provide sufficient insight into the physics underlying the simulation results.

This thesis proposes an intuitive, quasi-analytic method based on modal expansion. It is found that it is possible to calculate the far field diffraction patterns of all guided modes supported by a single nanorod, with full consideration of Fabry-Pérot effects, in minutes using a standard office desktop computer.

Focus is placed on the case of a nanorod of radius 140 nm, for which angular photoluminescence measurements were available to provide a means of validating the model. Consideration of the guided modes alone provides a compelling explanation for gross features in the measured data where none previously existed.

It is shown that, using a standard equation from a textbook, it is possible to calculate how much each of the guided and radiation modes of a single nanorod is excited by a Hertzian dipole of known position and orientation with respect to the nanorod geometry. When interference between these modes is considered, it is possible to calculate the total far field angular emission pattern due to that dipole. Comparing these patterns with photoluminescence measurements allows one to infer the locations and orientations of dipole current sources; the results are found to be consistent with those of cathodoluminescence studies.

Acknowledgements

I owe an immense amount to everyone in the Solid State Lighting research group at Bath. First of all, I'd like to thank my original supervisor Dr. Federica Causa for seeing fit to give me the incredible opportunity to do this course. Then there's my eventual primary supervisor Dr. Duncan Allsopp. Thanks for all your support and your incredibly wide knowledge of the area, but mostly for putting up with me and my... uniqueness for so long. Dr. Allsopp also played a direct role in the empirical fitting process in chapter 10. There's my informal mentor Dr. J. Sarma, whose knowledge of the theoretical literature and being fantastic company have been invaluable. Thanks also to my second supervisor Dr. Paul Snow, who has always been there on the few occasions I needed him.

Then there's the rest of the group. In terms of direct contribution to the substance of the work I must especially acknowledge Dr. Yiding Zhuang for fabricating nanorod structures I could test my theories on and Chris Lewins and Sophia Fox for actually doing the measurements using Lewins' amazing system. Szymon Lis' FDTD simulations were great for giving me something to test my theory against while I was still perfecting it, not to mention our joint international conference paper at the 10th International Conference on Nitride Semiconductors in Washington, D.C. But everyone in the group has helped my both scientifically and emotionally: Kate Cavanagh, Dr. Pierre-Marie Coulon, Dr. Margaret Hopkins, Ionut Gîrgel, Dr. Quanzhong Jiang, Paulo Ki, Dr. Emmanuel Le Boulbar, Dr. Philip Shields, Dr. Siva Sivaraya, Professor Wang Wang and Dr. Qian Yi.

Then there's the wider scientific community from which I've drawn my inspiration. Special thanks to Professors Allan Snyder and John Love, without whose work on the continuum modes of cylindrical structures this work would have been very different and probably not for the better. Thanks to Dr. Matthew Henderson for allowing me to access his raw data so that I was able to replicate his results. Thanks to Professor Fred Schubert and the publishers Cambridge University Press for putting the images from his textbook *Light-Emitting Diodes* online for anyone to use with permission. Thanks to Dr. Jochen Bruckbauer and his supervisor Dr. Rob Martin for their cathodoluminescence studies on Dr. Zhuang's nanorods, which have given a lot of insight into how emission in nanorods works, not to mention a co-authored paper.

There is of course the wider University community I must acknowledge. Complet-

ing two degrees at the University of Bath has changed my life; I've learned so much more about the world than just physics as well as becoming a more sociable and confident person compared to when I went in. If I was going to acknowledge everyone that would be a thesis in itself, but the following people deserve a special shout-out as they've been constantly here for me throughout my second degree and in many cases much of my first: Anna Dickson, Dr. Emily Parkes, Charlie Slack, Tim Stoneman, Dr. Anthony Masters, Richard Guthrie, Professor Alison Walker, David Howells, Dr. Siân Jenkins, Rhiannon Norfolk, Lawrence Hone, Annie Marks, Sue Mahmoud, Dr. Maddy Stow and Dr. Caroline Davies. The rest of you know who you are.

I must also of course mention my family as well as the few friends from up North who have actually stayed in touch with me; again you know who you are.

I would finally like to acknowledge financial support from the European Union (FP7 Contract No.: 228999, SMASH) and the EPSRC, UK via Grant No. EP/I012591/1 Lighting the Future.

Contents

List of symbols

Physical constants

Symbol	Definition	Value (SI units)
c_0	Speed of light in vacuum	2.998×10^8 ms^{-1}
h	Planck's constant	6.626×10^{-34} Js
k_B	Boltzmann constant	1.381×10^{-23} JK^{-1}
q	Electronic charge	$+1.602 \times 10^{-19}$ C
Z_0	Vacuum impedance	376.7 Ω
ϵ_0	Vacuum permittivity	8.854×10^{-12} Fm^{-1}
μ_0	Vacuum permeability	1.257×10^{-6} Hm^{-1}

Bessel and Hankel functions

Symbol	Definition
$H_N^{(1)}(x)$	Hankel function of the first kind of order N
$H_N^{(2)}(x)$	Hankel function of the second kind of order N
$J_N(x)$	Bessel function of the first kind of order N
$K_N(x)$	Modified Bessel function of the second kind of order N
$Y_N(x)$	Bessel function of the second kind of order N

Vector quantities

Symbol	Definition
$\vec{A}$	Area vector (vector potential is not used in this work)
$\vec{B}$	Magnetic flux density
$\vec{D}$	Electric flux density
$\vec{E}$	Electric field
$\hat{E}_j$	Electric field of guided (discrete) mode j of a nanorod
$\hat{e}$	Electric field of radiation modes of a homogeneous medium
$\tilde{e}$	Electric field of radiation modes based on Hankel functions
$\hat{e}_R$	Electric field of radiation modes of a nanorod
$\vec{H}$	Magnetic field
$\hat{H}_j$	Magnetic field of guided (discrete) mode j of a nanorod
$\hat{h}$	Magnetic field of radiation modes of a homogeneous medium
$\tilde{h}$	Magnetic field of radiation modes based on Hankel functions
$\hat{h}_R$	Magnetic field of radiation modes of a nanorod
$\vec{J}$	Electric current density
$\vec{j}$	Vector amplitude of a Hertzian dipole (see section 6.5)
$\vec{K}$	Magnetic surface current
$\vec{k}$	Wavevector
$\hat{k}$	Unit wavevector
$\vec{r}$	Position vector
$\vec{S}$	Time-averaged Poynting vector
$\hat{x}$, $\hat{y}$ and $\hat{z}$	Cartesian (rectangular) unit vectors
$\hat{\rho}$, $\hat{\phi}$ and $\hat{z}$	Cylindrical polar unit vectors

Scalar quantities (Uppercase italic)

A_j and B_j	Normalization constants of guided mode j
C_j	Expansion coefficient of guided mode j
C_{norm}	Normalization constant of Gaussian distribution
E_N	Electric field amplitude, where N is a non-negative integer
E_{ph}	Photon energy
E_x, E_y and E_z	Shorthand for $\vec{E} \cdot \hat{x}$, $\vec{E} \cdot \hat{y}$ and $\vec{E} \cdot \hat{z}$ respectively
E_ρ, E_ϕ and E_z	Shorthand for $\vec{E} \cdot \hat{\rho}$, $\vec{E} \cdot \hat{\phi}$ and $\vec{E} \cdot \hat{z}$ respectively
F	See section 5.5
G	Gaussian distribution
H_x, H_y and H_z	Shorthand for $\vec{H} \cdot \hat{x}$, $\vec{H} \cdot \hat{y}$ and $\vec{H} \cdot \hat{z}$ respectively
H_ρ, H_ϕ and H_z	Shorthand for $\vec{H} \cdot \hat{\rho}$, $\vec{H} \cdot \hat{\phi}$ and $\vec{H} \cdot \hat{z}$ respectively
I	Intensity (power per unit area)
I_{LED}	Current through the LED
M	See section 8.4
N	Non-negative integer governing azimuthal variation
P	Power
R	Power reflectance or nanorod radius, depending on context
T	Power transmittance
V	$k_0 R\sqrt{n_{core}^2 - n_{clad}^2}$ (dV denotes a volume differential)
V_{app}	Applied voltage
V_{bi}	Built-in voltage
W	Full width at half maximum of Gaussian distribution
X and Y	See section 8.4

Scalar quantities (lowercase italic)

Symbol	Definition
$\tilde{a}$	Complex overlap of radiation modes (see section 9.5)
a and b	Core normalization constants of radiation modes
c	Expansion cofficient of radiation mode
c_j and d_j	Expansion coefficients for decomposition of guided modes
c_f and d_f	Cladding constants for free space component of radiation modes
c_s and d_s	Cladding constants for scattered component of radiation modes
$d_\pm$	Distances of cavity boundaries from Hertzian dipole source
d	Cavity width; $d = d_+ + d_-$
f	Can be either $\sin(N\phi)$ or $\cos(N\phi)$
g	Derivative of f above with respect to $N\phi$
j	Index corresponding to a guided mode
k_0	Free space wavenumber
n	Refractive index
p	Power in a single radiation mode (i.e. prior to integrating)
r	Fresnel reflection coefficient or radial distance, depending on context
t	Fresnel transmission coefficient or time, depending on context
v_p	Phase velocity
w	Index corresponding to a quantum well
x, y and z	Cartesian (rectangular) coordinates

Scalar quantities (Greek)

Symbol	Definition
ρ, ϕ and z	Cylindrical polar coordinates
α	Exponential decay constant
β	Propagation constant (z component of wavevector)
γ	Imaginary ρ component of wavevector
Δ	$n_{clad}^2 n_{core}^{-2}$
ϵ	Electric permittivity
ζ	Impedance distortion (see section 9.4)
η	Efficiency (see section 1.4)
θ	Angle with respect to z axis
κ and σ	Real ρ component of wavevector
λ_0	Free space wavelength
μ	Magnetic permeability
ν	Photon frequency
Ξ_{0N}	$\frac{1}{\sqrt{2}}$ if $N = 0$; 1 otherwise (see section 6.6)
ρ_q	Electric charge density
σ_q	Surface charge density
τ	Transmission coefficient from inside a cavity (see section 5.5)
υ and χ	See section 5.5
Φ	Angle between dipole current and ρ axis (see section 6.5)
ψ_e and ψ_h	z components of $\hat{e}_R$ and $\hat{h}_R$ respectively
$\Omega_\pm$	Far-field angular emission pattern from a nanorod (see chapter 10)
ω	Angular frequency of radiation

Angles are given in radians, except where the degree symbol is used. For example, $\theta = \frac{\pi}{2} = 90^\circ$ denotes a right angle.

Scalar quantities for chapter 2 only

Chapter 2 contains some quantities that are not used elsewhere in the thesis (except for (8.25) and (8.26), which are derived from that chapter) that have the same standard notation (see for example Schubert 2006 and Kasap 2013) as quantities used in later chapters. This provides an opportunity to use separate notation for chapter 2. It was felt this was clearer than departing from standard notation for these quantities.

*n in (2.10) corresponds to refractive index, as in the rest of the thesis, as opposed to

Symbol	Definition
A	Einstein spontaneous emission coefficient
B	Einstein stimulated emission/absorption coefficient
E_1 and E_2	Electron energy levels for two-level system
E_C and E_V	Conduction and valance band edges
E_g	Band gap energy
E_T	Trap level energy
E_{ph}	Photon energy
N_1 and N_2	Number density of electrons in states 1 and 2
n	Electron density in semiconductor*
p	Hole density in semiconductor
δn	Electron-hole density in excess of equilibrium
R	Recombination rate
T	Temperature
η_{IQE}	Internal quantum efficiency
ν	Photon frequency
$\rho(\nu)$	Photon energy density
τ_{nr}	Non-radiative lifetime

electron density. This is clearly stated in the text.

Chapter 1

Introduction

Light emitting diodes (LEDs), a review of which is given by Schubert (2006), are semiconductor p-n junctions that emit light through radiative electron-hole recombination (see chapter 2), functioning as both a diode and a light source. LEDs have been used as indicator lights in electronic equipment and for polymer optical fiber applications for decades. Although LEDs are already used for a wide range of lighting and display applications, known collectively as solid state lighting, there exist a number of challenges that prevent solid state lighting from achieving its full potential. LEDs still struggle to compete with fluorescent tubes and liquid crystal displays (LCD) in many applications, while altogether new applications such as smart LED lighting, visible light communication and integration into electronic devices are limited by these various barriers.

Most LEDs used in lighting applications are based on gallium nitride (GaN) and indium gallium nitride (InGaN); a review of GaN-based LEDs is provided by Mottier (2008). Being direct band gap semiconductors with high band gap energies and adequate carrier mobilities, GaN and InGaN are the ideal materials for blue and green LEDs, which are required as part of white light sources and multi-coloured displays. InGaN typically has a bandgap energy in the blue or green depending on alloy composition, while GaN is transparent to visible radiation, so both are required to make a useful LED device. However, GaN-based LEDs that emit at yellow or higher wavelengths are unavailable outside the laboratory, causing the 'green gap' problem. In addition, the high refractive index of GaN means that most of the light emitted is trapped inside the LED chip. This can be remedied via surface roughening, at the cost of losing control over the directionality of the emitted light without secondary optics such as lenses, which somewhat compromise the compact nature of LEDs. Cylindrical nanostructures, particularly nanorod emitters, have been proposed as a potential solution to many of these

problems, providing a motive to investigate their optical properties in detail. Reviews of nanostructured LEDs are provided by Wiesmann *et al.* (2009) and Li and Waag (2012), while Bavencove *et al.* (2011) is also very readable. The goal of this thesis is to advance understanding of the optical proprties of nanorod LEDs, with particular emphasis on the directionality in the resulting light emission. The detailed objectives are presented later.

This thesis begins with a review of historical and current LED technologies (this chapter), a review of how LEDs work (chapters 2 and 3) and a brief summary of the mathematical theory of classical optics (chapter 4). Building on this knowledge base, a theoretical approach to optical modelling of planar GaN-based LED devices is presented in chapter 5 and complemented with numerical simulations. Following a thorough introduction to the theory of electromagnetic modes of optical systems in chapter 6, a review of state of the art nanorod LED technology is presented in chapter 7. The main results of the thesis are contained in chapters 8, 9 and 10 where it is explained how the modal simulation methods of chapter 6 can be used to undertake optical modelling of nanorod LEDs, with numerical results from these simulations also presented. Possibilities for future work are presented in chapter 11, followed by a summary of the main conclusions and a list of references.

Note that organic light-emitting diodes (OLEDs) are beyond the scope of this work as their principles of operatation are very different to those of inorganic LEDs. Chapter 8 of Mottier (2009) contains a brief review.

It should also be noted this thesis does not have a "literature review" chapter. Reviews of the literature are instead dispersed throughout the thesis in the relevant chapters. For example, in this chapter the interested reader is directed to a range of literature on LED history and applications, while light extraction technologies are reviewed in section 1.5.

1.1 A brief history of LEDs

Chapter 1 of Schubert (2006) provides a review of the history of LEDs, which is summarized here. The first LED was discovered accidentally by Round (1907) when he observed that crystals of silicon carbide (SiC) glowed when a current was passed through them, despite the crystals being far too cool for incandescence to occur. SiC is an indirect bandgap semiconductor and therefore has no practical use for LEDs. The

first practical visible spectrum LED was invented by Holonyak and Bevacqua (1962); it emitted in the red and was made from gallium arsenide phosphide (GaAsP), an alloy of gallium arsenide (GaAs) and gallium phosphide (GaP). The fundamental band gap of GaAs is equal to the energy of an infrared photon, while the band gap of GaP is equal to the energy of a green photon (although it is an indirect bandgap semiconductor). It is therefore possible to adjust the colour of the photons emitted through electron-hole recombination by varying the amount of arsenic and phosphorus in the alloy; the more phosphorus is present, the higher the energy of the emitted photons. Through variation of the alloy composition in this way, LEDs were soon developed in a range of colours from red to green (Logan *et al.* 1968, Herzog *et al.* 1969, Groves *et al.* 1971, Logan *et al.* 1971, Craford *et al.* 1972; for a review see Duke and Holonyak 1973). LEDs in the blue, violet and ultraviolet, however, remained elusive until the development by Akasaki *et al.* (1992) and Nakamura *et al.* (1993a, 1993b, 1994) of LEDs based on gallium nitride (GaN) and its alloys aluminium gallium nitride (AlGaN) and indium gallium nitride (InGaN). GaN has a band gap in the near-ultraviolet while the band gap of InN lies in the infrared; as the indium content is increased, the emission shifts from the near-UV through the violet and blue into the green. However, InGaN with a high indium content is thermodynamically unstable and has a high lattice mismatch with GaN, leading to intense strains that make growth of InGaN with more than 25% InN mole fraction extremely difficult, meaning that GaN-based LEDs emitting yellow or longer-wavelength light are unavailable outside the laboratory. AlN has a band gap in the deep ultraviolet, so AlGaN is used to make LEDs emitting in the deep ultraviolet (3.5 eV and beyond). Currently, InGaN is the standard material for LEDs emitting in the blue, green and violet, while aluminium gallium indium phosphide (AlGaInP) is used to make LEDs emitting in the red, orange and yellow; AlGaInP cannot emit in the green as it becomes an indirect bandgap semiconductor if the band gap exceeds around 2.25 eV. The efficiency of both of these main LED types falls dramatically in the green spectral range; this phenomenon is called the 'green gap' and is one of the main obstacles to implementation of solid state lighting.

1.2 White light sources based on LEDs

LEDs are inherently near-monochromatic devices, as all photons they generate have an energy close to the band gap of the material being used. For most lighting applications, however, white light is required. White light can be obtained either by mixing the light from several LEDs of different colours, or by using phosphors; various ways of doing this are shown in Figures 1-1 and 1-2.

Figure 1-1 shows how two or more LEDs emitting different colours can be combined

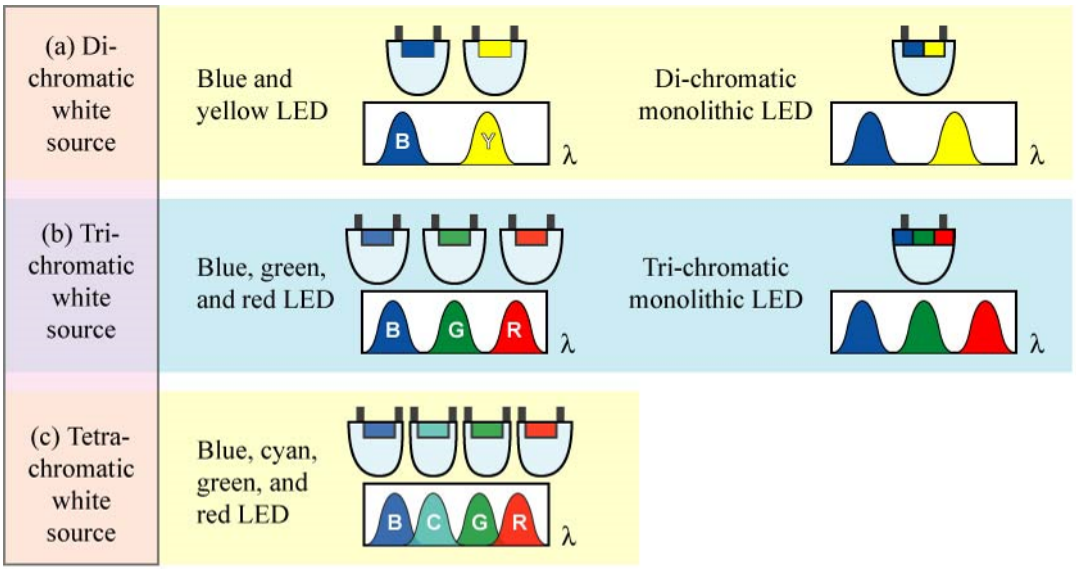

Figure 1-1: Generation of white light by combining LEDs of different colours. © E. Fred Schubert (2006), published by Cambridge University Press, reproduced with permission.

to create white light. This method achieves good colour rendering, which is explained in detail in chapter 19 of Schubert (2006) but can roughly be defined as the range of colours present in the light. The lack of phosphors extends the lifetime of the lighting system, as the phosphor can be the first part of the system to degrade, especially at higher temperatures (Meneghini *et al.* 2010). The single-chip, multiple-unit approach (Figure 1-1, left) involves using a different LED unit to produce each colour. With this approach, the exact colour of white (the 'white point') can be controlled by altering the electrical power supplied to the various LEDs, according to taste or even the time of day (Schubert and Kim 2005). The monolithic or multiple-chip approach (Figure 1-1, right) uses a single LED with multiple chips, which is useful for applications such as torches and displays where compactness is required. However, the reliance on a green LED reduces the efficiency of these methods.

Figure 1-2 (a) depicts a blue LED covered with a cerium-doped yttrium aluminium garnet (Ce:YAG) phosphor, which absorbs some of the blue light and re-emits yellow light; the yellow and blue light mix to form a blueish white known as 'cold white'. As yellow photons have less energy than blue photons, the wavelength conversion process consumes energy. This system is highly efficient, compact and cheap to manufacture,

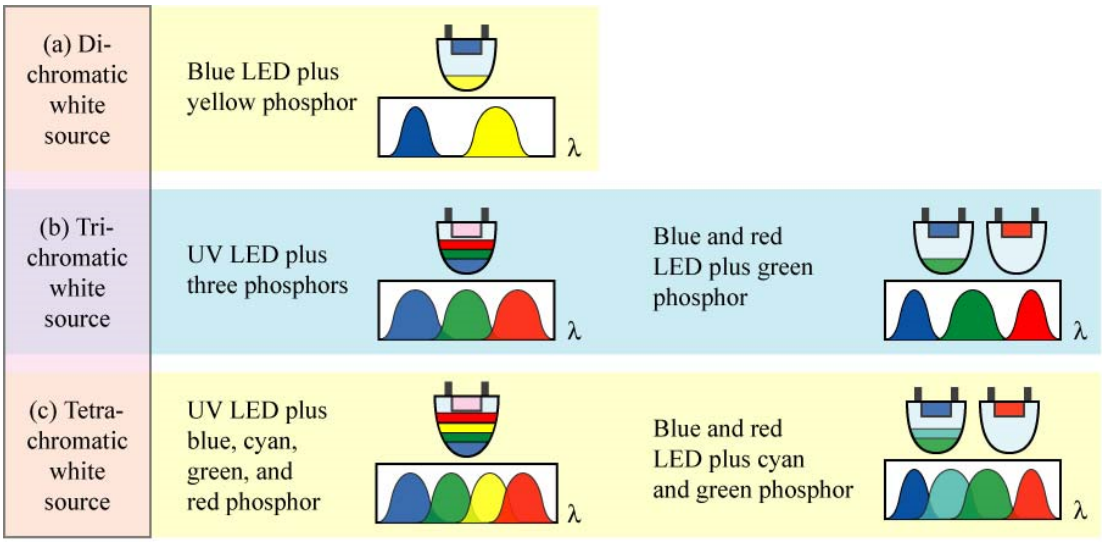

Figure 1-2: Generation of white light using LEDs and phosphors. © E. Fred Schubert (2006), published by Cambridge University Press, reproduced with permission.

making it the 'workhorse' of the solid state lighting industry. However, the colour rendering is poor and the light unappealing to humans, as it does not resemble anything in nature. Although these problems can be remedied by the addition of a red phosphor, there are currently no phosphors that absorb in the blue, emit in the red and have efficiencies comparable to Ce:YAG, so the addition of a red phosphor to create 'warm white' reduces the efficiency considerably.

Figure 1-2 (b) depicts an LED emitting in the deep ultraviolet striking red, blue and green phosphors, which absorb the ultraviolet light and re-emit visible light. This method also offers good colour rendering and is easy to implement as efficient phosphors that absorb and re-emit at the required wavelengths are already widely used in fluorescent lamps. However, the energy difference between the phosphor absorption and emission is greater than that in Figure 1-2 (a), making these LEDs less efficient than 'cold white' LEDs. The use of ultraviolet light also rules out this solution for illuminating anything that might be damaged by such radiation, such as art, historical artifacts or sensitive equipment.

1.3 Advantages of solid state lighting

The advantages and potential advantages of solid state lighting over existing lighting technologies are manifold.

LED chips fabricated in laboratories show the highest efficiency of any light source (Cree 2011). The efficiency of commercial LED lamps is already comparable to that of compact fluorescent lamps, but is currently lower than that of linear fluorescent tubes (Osram 2011). Efficient light sources provide economic benefits and facilitate in addressing sustainability concerns surrounding the use of fossil fuels.

The average lifetime of LED lamps is far greater than those of linear fluorescent tubes and greater still than those of compact fluorescent lamps (US Department of Energy 2006). In addition, LED lamps are much less fragile than fluorescent tubes.

LED chips are far brighter than most other light sources (except for stimulated emission devices such as lasers) in terms of emitted power per surface area (the typical LED chip size is around 1 mm^2), allowing for the creation of very high intensity light sources.

The emission spectra of LEDs are much narrower than those of most light sources (again excluding stimulated emission devices), so the colour is very pure and can be modified in accordance with the needs of the application by altering the alloy composition of the active region. This makes LEDs suitable for communication (Bockstaele *et al.* 1999), health (Crawford *et al.* 2011), scientific and horticultural (Morrow 2008) applications in addition to general space lighting.

By using reflecting contacts, distributed Bragg reflectors (DBRs), cavity resonances, photonic crystals, photonic quasi-crystals and other such technologies, it is often possible to design the LED chip so as to emit a desired spatial/angular power distribution without the need for secondary optics. This is discussed in more detail in section 1.5.

LEDs and other light sources based on semiconductors are much smaller than other light sources, allowing incorporation into displays and many other devices such as torches, ornaments, medical instruments and electronic equipment. LEDs without secondary optics are even more compact.

Another advantage of LEDs over 'traditional' light sources is their ability to switch on and off rapidly without consuming much energy. This is appealing to users when they want bright light immediately without a 'warm up' period, while also increasing the energy saving potential of turning lights off when not in use.

Like other electronic devices, LEDs use direct current (DC) electrical power as opposed to the alternating current (AC) used by traditional electrical lamps. Under the short distance, low voltage conditions present in domestic and business micro-grids, the transmission of DC power is much more efficient than that of AC, further enhancing the energy saving potential of LEDs. It is also possible to take LEDs and other DC devices 'off grid' and power them using photovoltaic installations, avoiding the conversion losses incurred by rectifying AC mains power into DC (Shenai and Shah 2011).

The compactness, rapid response and low voltage requirement (due to use of DC power) of LEDs facilitate integration into electronic equipment, i.e. LEDs can provide light and convey digital information simultaneously. This property of LEDs is already used for dual lighting/display applications such as road signs, bus destination displays, billboards and televisions, but many other applications have yet to be commercially realized. Visible light communication, where LED lamps modulate at frequencies too fast for the human eye to detect in order to transmit information to and from other electronic devices such as computers and smartphones, has already been demonstrated in the laboratory (Zeng *et al.* 2009). There is also the potential to integrate LEDs with sensors, so as the alter the colour of light based on the time of day, or to switch lights on and off based the number of people present and their location. Further speculation on such 'smart lighting' applications is given by Schubert and Kim (2005).

1.4 LED efficiency definitions

There are several different efficiency quantities associated with LEDs. Each has a different definition and relates to different properties of the LED. LEDs Magazine (2004) provides an incomplete list of such quantities, which is reviewed here; other efficiency definitions involving photometric quantities are discussed in chapter 16 of Schubert (2006).

An LED chip consists of electrical contacts and a light-emitting active region, connected by transparent semiconducting confinement regions. Not all current is necesarily injected into the active region; for example, electrical conduction may occur at surfaces where the band structure is disrupted. The injection efficiency η_{inj} is the fraction of electron-hole pairs injected into the entire device (i.e. the fraction of electrons passed through the device) that reaches and remains in the active region.

Once an electron-hole pair reaches the active region, it can undergo either radiative or

non-radiative recombination (see section 2.3). The internal quantum efficiency η_{IQE} is defined as the fraction of recombination events that are radiative.

The extraction efficiency η_{ext} is the fraction of photons emitted by radiative recombination that are extracted from the LED into the surrounding environment, net of the emitted photons that are absorbed inside the LED system or trapped by total internal reflection.

The external quantum efficiency η_{EQE} is defined as the number of photons extracted from the device divided by the number of electrons passing into the device via its contacts. The EQE is equivalent to the product of the injection efficiency, IQE and extraction efficiency:

$$\eta_{EQE} = \eta_{inj}\eta_{IQE}\eta_{ext}. \tag{1.1}$$

The power conversion efficiency, denoted as η_{pow} or simply η, is equal to the total optical power extracted from the device divided by the electrical input power; it is also called the wall plug efficiency (η_{wp}) and is given by the equation

$$\eta_{pow} = \frac{1}{V_{app}I_{LED}} \oint_A \vec{S} \cdot \mathrm{d}\vec{A} = \frac{h\nu}{q|V_{app} - V_{bi}|}\eta_{EQE} = \eta_{feed}\eta_{EQE}, \tag{1.2}$$

where $\vec{S}$ is the Poynting vector, A is a closed surface surrounding the LED, V_{app} is the voltage applied across the diode, I_{LED} is the current through the LED, h is Planck's constant, ν is the energy of the emitted photons, q is the electronic charge, V_{bi} is the built-in voltage and η_{feed} is the feeding efficiency, which is given by

$$\eta_{feed} = \frac{h\nu}{q|V_{app} - V_{bi}|}. \tag{1.3}$$

In practice, the feeding efficiency is limited mainly by parasitic series resistances but also by the difference in band gap between the active and confinement regions; the larger this difference, the lower the feeding efficiency. This means that for InGaN/GaN LEDs, the feeding efficiency will always be lower for green LEDs than blue ones; this efficiency loss is unavoidable and exacerbates the 'green gap' problem further.

1.5 The challenge of light extraction

The main objective of this work is to identify ways of maximizing the extraction efficiency of GaN-based LEDs and tailoring their angular emission patterns to suit their applications. As semiconductor material quality improves, extraction efficiency be-

comes the main limiting factor on the external quantum efficiency. The main limiting factor on the extraction efficiency is total internal reflection, which confines light within the LED semiconductor chip as shown in Figure 1-3. The refractive index of GaN at blue and green wavelengths varies between 2.4 and 2.5 (Takeuchi *et al.* 2010), whereas the refractive index of most incapsulants is much lower, ranging between 1.4 and 1.6 (Zhou *et al.* 2008, Lin *et al.* 2010). This results in around 72% (see section 5.3) of the light being emitted outside of the light escape cone (see section 4.5) and being confined inside the chip, where it is mostly absorbed by the active region, metal contacts and defects within the GaN, particularly at the highly defective GaN nucleation/template layer (Schad *et al* 2004, Mottier 2009 chapter 2). Even for light emitted into the escape cone, lossy metal reflectors and the nuclation layer can hinder light extraction further. There exist several technologies designed to increase extraction efficiency, an incomplete summary of which is provided below.

The encapsulation of LED chips inside a transparent and durable substance such as

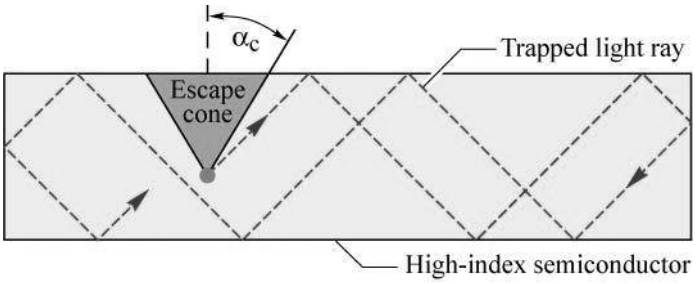

Figure 1-3: Total internal reflection inside a high-index semiconductor. © E. Fred Schubert (2006), published by Cambridge University Press, reproduced with permission.

epoxy resin not only protects the chip but also increases the size of the light escape cone and by extension the extraction efficiency, as explained in section 3.7. Note that the 72% figure quoted above accounts for the presence of an epoxy encapsulant, but this can be improved by using an encapsulant of higher refractive index.

Half of all light emitted by an LED is directed 'downward' towards the chip header, as opposed to 'upward' into the environment, necessitating the use of reflectors; Schubert (2006, chapter 10) provides a detailed overview of the subject. Metallic reflectors are omnidirectional but lossy, while dielectric distributed Bragg reflectors (DBRs) are efficient but highly directional. Efficient omnidirectional reflectors (ODRs) can be constructed either from a combination of metal and dielectric layers or with just dielectrics

(Fink *et al.* 1998).

Any given LED chip with smooth surfaces will exhibit Fabry-Pérot resonances, resulting in emission from the active region being enhanced for some angles and suppressed for others. It is possible to design the Fabry-Pérot cavity so that emission into the light escape cone is enhanced at the expense of emission outside of it, improving the extraction efficiency. Chapter 5 explains how this is done. This technique is also useful for manipulating the LED's angular emission pattern. Delbeke *et al.* (2002) provide a review.

The metallic electrical contacts can hinder light extraction by absorbing part of the incident light while reflecting the rest of it back into the chip. This can be avoided by using flip-chip packaging (see section 3.5), where the contacts do not hinder light extraction but actually enhance it by functioning as reflectors. For LEDs grown on sapphire, the light can be emitted through the substrate or the substrate can be removed; silicon substrates on the other hand must be removed in order for flip-chip packaging to work owing to the absorption of visible light by silicon.

Sapphire substrates can be removed by laser lift-off, where a laser is shone through the sapphire to destroy the GaN nucleation layer via an ablation effect, detaching the substrate in the process; silicon substrates can be removed by a combination of grinding and chemical etching. Either way, light extraction is improved by the removal of the absorbing nucleation layer and roughening of the surface, the exposure of which paves the way for additional roughening (see below).

Surface roughening using the techniques outlined above acts to scatter light out of guided modes and into radiation modes (see Figure 1-4). A combination of encapsulation, flip-chip packaging, substrate removal and surface roughening has been shown to yield extraction efficiencies approaching 80% (Shchekin *et al.* 2006, cited in Mottier 2009).

An alternative to roughening the GaN surface is to etch nanopyramid structures into the suface of the sapphire substrate using a dry chemical etch; this has been shown to enhance light extraction in a similar way to surface roughening (Yamada *et al.* 2002). Simulations of patterned substrate LEDs with epoxy encapsulants predict light extraction efficiencies similar to those achieved experimentally by substrate removal and surface roughening (Lee *et al* 2007). Substrate patterning in this manner has yet to be

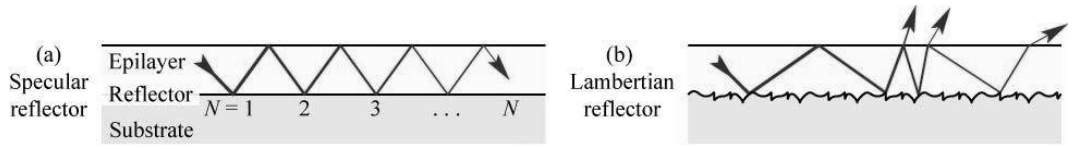

Figure 1-4: Scattering of light from guided modes by a roughened surface. © E. Fred Schubert (2006), published by Cambridge University Press, reproduced with permission.

demonstrated for LEDs with silicon substrates, mostly because the absorbing nature of silicon means any benefit to light extraction would be minimal.

Another alternative to surface roughening is the use of photonic crystals, an approach reviewed by Wiesmann *et al* (2009). 'Shallow etched' photonic crystals, depicted in figure 1-5 (b), scatter light out of guided modes more efficiently than surface roughening by utilising Bragg scattering mechanisms. Extraction efficiencies of over 70% have been obtained for unencapsulated LEDs using such structures (Wierer *et al.* 2009), providing a higher extraction efficiency than unencapsulated LEDs with roughened surfaces. Only one group has published data on encapsulated (Cho *et al.* 2005, 2008) photonic crystal LEDs and their results are less encouraging; this could be due to the group's use of indium tin oxide (ITO) transparent electrodes, which have a weak refractive index contrast with epoxy encapsulants. 'Deep-etched' photonic crystals, depicted in figure 1-5 (d), can achieve near-unity extraction efficiencies by inhibiting spontaneous emission into guided modes via a photonic bandgap, although this inhibition reduces the internal quantum efficiency. Both 'shallow-etched' and 'deep-etched' photonic crystals can be 'buried' by growing a planar semiconductor layer on top; this is useful for forming good electrical contacts and further increasing the range of structures available (Lewins *et al.* 2013).

LED chips with dimensions on the order of micrometres (micro-LEDs) can improve light extraction by introducing additional light escape cones on the sides of the chips as well as on top (Jiang and Lin 2013). Nano-LEDs, which have dimensions on the order of nanometres or lower, provide providing the potential to exploit the resonant cavity effect in three dimensions (Purcell 1946) and can also be arranged in a photonic crystal structure to further enhance light extraction and give designers control over the directionality of light emission. A more detailed discussion of the advantages and disadvantages of nano-LEDs is given in chapter 7.

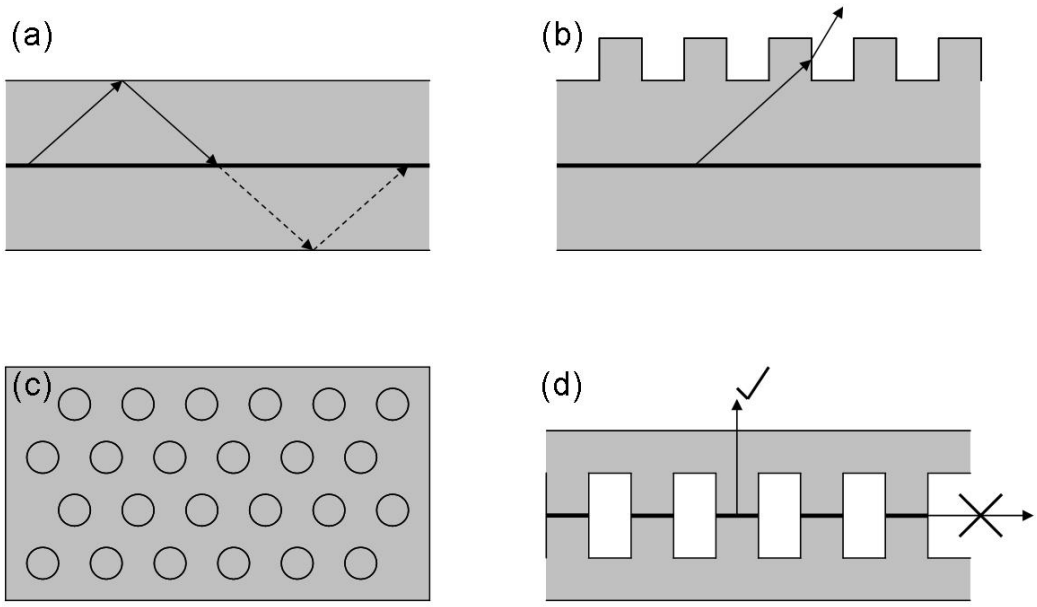

Figure 1-5: (a) Depiction of total internal reflection in a planar LED chip. (b) Use of 'shallow-etched' photonic crystals to scatter light out of guided modes. (c) View of a shallow-etched hexagonal photonic crystal structure from above, where the circles represent nano-columns or nano-holes of GaN. (d) Use of a 'deep-etched' photonic crystal to prevent emission into guided modes using a photonic band gap.

1.6 Summary

In this chapter a brief outline of the thesis is presented, followed by a discussion of the history and applications of LEDs and solid state lighting, as well as the challenges still faced by the technology. This chapter serves to provide a background for the rest of the thesis and explain how the physics discussed in later chapters is relevant to solid state lighting applications. Sections 1.1 and 1.2 discuss how to obtain white light from LEDs while also introducing the 'green gap' problem. Section 1.3 discusses the myriad of present and future applications of solid state lighting and establishes the motivations for using it. Section 1.4 defines the various efficiencies of LEDs, while section 1.5 focuses on the challenge of light extraction, reviewing both mature and novel solutions. Light extraction, along with the directionality of the light output, are the primary focuses of this thesis. With this background in mind, the basic physics of LEDs is discussed in the next chapter.

Chapter 2

Radiative Processes

2.1 Introduction

Crucial to understanding LED physics is an understanding of radiative processes, a topic for which Kasap (2013) provides a very readable introduction. In this chapter, the three main radiative processes, i.e. interactions between photons and other particles (usually electrons) are introduced, followed by a discussion of spontaneous emission, non-radiative recombination and absorption in the direct band gap semiconductors from which LEDs are made.

It is known from quantum theory that the energy of an electron in an atom must take one of a number of discrete values. This chapter considers two such energies, E_1 and E_2, where $E_2 > E_1$. This two-level system can interact with photons of energy $E_2 - E_1$ in three different ways: absorption, stimulated emission and spontaneous emission. The frequency ν of such a photon is given in terms of E_1, E_2 and Planck's constant h by the equation

$$h\nu = E_2 - E_1. \tag{2.1}$$

Equation (2.1) and the subsequent analysis in this section applies to an isolated atom, making it applicable to gases. In solid-state systems, disorder introduces a broadening δE_{ph} to the transition. This is discussed further in section 2.3.

Absorption occurs when a photon with energy $E_2 - E_1$ is incident upon the system when the electron has the lower energy E_1. The photon is absorbed by the electron and its energy is used to raise the electron's energy to E_2. Stimulated emission occurs when a photon is incident upon the system when the electron has the higher energy E_2, inducing the electron to emit a second identical photon by lowering its energy to E_1.

The two photons are coherent (see section 4.9), and have the same phase, polarization and direction. Another emission process can occur without the need for the prescence of an incident photon. The electron lowers its energy from E_2 to E_1 and emits a photon of energy $E_2 - E_1$. This process is called spontaneous emission.

Real atoms consist of many more than two energy levels, but those levels are still

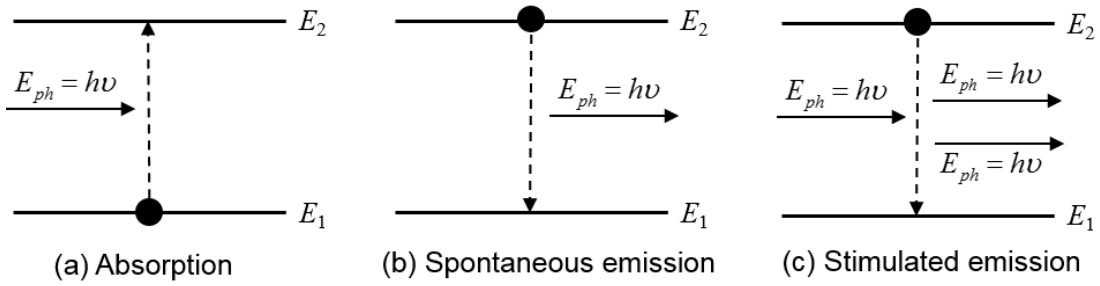

Figure 2-1: The three ways photons can interact with a two-level atom (adapted from Kasap 2013).

discrete. Therefore atoms can absorb only photons whose energy corresponds to the difference between two of those levels. Shining white light through a sufficiently dense ensemble of gas atoms therefore results in certain wavelengths being absorbed and the rest transmitted, giving rise to absorption line spectra that can be used to identify gases. Conversely, if energy is supplied to a dense gas, exciting some of the electrons to higher energies, the electrons will undergo spontaneous emission and fall to lower energies. The resulting emission contains a discrete set of wavelengths called an emission line spectrum. Street lamps and fluorescent tubes work by bombarding gas atoms with free electrons, causing atomic electrons to be excited so as to produce the emission lines. Lasers operate by using stimulated emission to amplify light: if a large number of electrons are excited to a higher energy level E_2, one of them will undergo spontaneous emission, emitting a photon of energy $E_2 - E_1$. This photon causes another electron with energy E_2 to undergo stimulated emission, so there are now two photons of energy $E_2 - E_1$; the original emission is therefore amplified and the process repeats itself in a chain reaction. Net amplification of light requires the majority of electrons to be in the E_2 state, otherwise the emitted photons will be absorbed by electrons in the E_1 state. This requirement is called population inversion and can be achieved by supplying either electrical or optical energy to the system.

2.2 Emission/absorption rates and Einstein coefficients

The rate per unit volume $R_{1\to2}$ at which absorption events occur is proportional to both the number of electrons per unit volume N_1 in state 1 and the photon energy density ρ at the frequency ν given by (2.1):

$$R_{1\to2} = B_{1\to2} N_1 \rho(\nu), \tag{2.2}$$

where $B_{1\to2}$ is a constant of proportionality known as the Einstein B absorption coefficient. The emission rate per unit volume $R_{2\to1}$ must take into account both spontaneous and stimulated emission. The former depends only upon the number of electrons per unit volume N_2 in state 2 while the latter depends upon both N_2 and $\rho(\nu)$:

$$R_{2\to1} = N_2(B_{2\to1}\rho(\nu) + A), \tag{2.3}$$

where A is the Einstein A spontaneous emission coefficient and $B_{2\to1}$ is the Einstein B stimulated emission coefficient.
The relationships between the three Einstein coefficients can be found by considering the conditions at thermal equilibrium, at which the absorption and emission rates must be equal:

$$\begin{aligned} R_{1\to2} &= R_{2\to1}, \\ B_{1\to2} N_1 \rho(\nu) &= N_2(B_{2\to1}\rho(\nu) + A). \end{aligned} \tag{2.4}$$

In addition, at thermal equilibrium Boltzmann statistics demand that

$$\frac{N_2}{N_1} = \exp\left(-\frac{E_2 - E_1}{k_B T}\right), \tag{2.5}$$

where k_B is the Boltzmann constant and T is the absolute temperature. The final condition imposed by thermal equilibrium is that $\rho(\nu)$ is given by Planck's black body radiation law:

$$\rho(\nu) = \frac{8\pi h\nu^3}{c_0^3\left[\exp\left(\frac{h\nu}{k_B T}\right) - 1\right]}, \tag{2.6}$$

where h is Planck's constant and c_0 is the speed of light in a vacuum. Substituting (2.1) into (2.6) then substituting (2.6) and (2.5) into (2.4) and re-arranging yields

$$B_{1\to2} = \left(B_{2\to1} + A\frac{c_0^3\left[\exp\left(\frac{E_2-E_1}{k_B T}\right) - 1\right]}{8\pi h\nu^3}\right)\exp\left(-\frac{E_2 - E_1}{k_B T}\right) \tag{2.7}$$

or

$$B_{1\to 2} - B_{2\to 1}\exp\left(-\frac{E_2 - E_1}{k_B T}\right) = A\frac{c_0^3\left[1 - \exp\left(-\frac{E_2-E_1}{k_B T}\right)\right]}{8\pi h\nu^3}. \tag{2.8}$$

Equation (2.8) can only be satisfied if

$$B_{1\to 2} = B_{2\to 1} = B = \frac{c_0^3}{8\pi h\nu^3}A. \tag{2.9}$$

Equation (2.9) gives the relationship between the three Einstein coefficients. Firstly, it shows that the two B coefficients are in fact one and the same. Secondly, it relates this single B coefficient to the A spontaneous emission coefficient via universal constants and the frquency ν, which is proportional to the difference $E_2 - E_1$ between the two energy levels. Note that this result applies to atoms in a vacuum; for atoms in a transparent homogeneous medium, simply replace c_0 in the above equations with $\frac{c_0}{n}$, where n is the refractive index of the medium (Yariv 1982):

$$B = \frac{c_0^3}{8\pi h\nu^3 n^3}A. \tag{2.10}$$

The presence of n in (2.10) is evidence of an important principle: that the optical properties of the medium in which spontaneous emission occurs affects the strength of such emission, through the photon energy density $\rho(\nu)$. While (2.10) is sufficient to describe emission within transparent homogeneous media, the situation becomes more complex when the emitting atom is close to one or more interfaces between media. The use of such effects to improve LED functionality is the primary focus of this thesis.

2.3 Spontaneous emission in semiconductors

Schubert (2006, chapter 2) gives an introduction to radiative and non-radiative recombination in semiconductors, along with suggestions for further reading. Near the Fermi level, the energy structure of a semiconductor consists of the valence and conduction bands with respective edges E_V and E_C, in an analogy with the two-level atomic system discussed above and its two energy levels E_1 and E_2. It is therefore expected that the three radiative processes that occur in atomic systems also occur in semiconductors. It turns out this is indeed the case; semiconductors are strongly absorbing for photons of energy exceeding the band gap energy $E_g = E_C - E_V$, while being essentially transparent for energies sufficiently far below the band gap. Semiconductors are also the basis for three different types of light source: superluminescent diodes (SLDs) and laser diodes utilise stimulated emission while light emitting diodes (LEDs), the subject

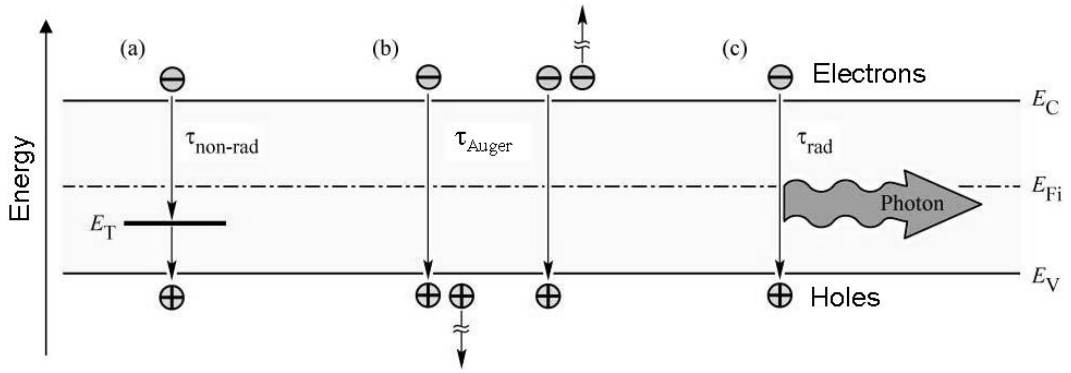

Figure 2-2: The non-radiative deep level (a) and Auger (b) recombination processes, shown alongside band-to-band radiative recombination (c). ©E. Fred Schubert (2006), published by Cambridge University Press, reproduced with permission.

of this research, utilise spontaneous emission. In a direct bandgap semiconductor, it can be assumed that all simple band-to-band electron-hole recombination events are radiative i.e. the difference in energy $E_{ph} \approx E_C - E_V = E_g$ is released in the form of a photon of energy $E_{ph} = h\nu \approx E_g$ as opposed to being released as heat. The equation for the radiative recombination rate per unit volume R_{rad} takes a similar form to the spontaneous emission term in (2.3), except there are now two particles, an electron and a hole, involved in the emission process:

$$R_{rad} = \frac{1}{\tau_{rad}} = Anp, \tag{2.11}$$

where τ_{rad} is the radiative recombination lifetime, n and p are the respective electron and hole number densities and here A is the bimolecular recombination coeficient, analogous with the Einstein A spontaneous emission coefficient. It is through this process that spontaneous emission occurs in semiconductors. However there are, broadly speaking, two non-radiative recombination processes that can occur even in a direct bandgap semiconductor: in both cases, no photon is emitted and the energy is lost as heat. At defects and surfaces, electron energy levels that lie in the forbidden band gap become allowed. At these defects, the simple band-to-band radiative recombination process is replaced by a two-stage process (Shockley and Read 1952, cited in Schubert 2006) where the electron moves to this 'trap level' E_T before recombination takes place. In most cases, transitions to and from the trap level are indirect and therefore non-radiative. The non-radiative recombination rate per unit volume R_{nr} is given by

summing the rates corresponding to each type of trap E_T:

$$R_{nr} = \delta n \sum_{E_T} \frac{1}{\tau_{nr}(E_T)} = \delta p \sum_{E_T} \frac{1}{\tau_{nr}(E_T)}, \tag{2.12}$$

where $\delta n = \delta p$ is the number density of electron-hole pairs that have been generated or injected in excess of their equilibrium values and $\tau_{nr}(E_T)$ is the non-radiative recombination lifetime for trap level E_T. More complex processes involving multiple trap levels can also occur (Breitenstein *et al.* 2010).

However, there is another mechanism for non-radiative recombination in addition to those due to trap levels. As n and/or p increases, so does the probability that the energy released is transferred to another electron or hole rather than by emitting a photon. This is known as the *Auger process*; the rate per unit volume R_{Auger} at which it occurs is given by

$$R_{Auger} = \frac{1}{\tau_{Auger}} = C_n n^2 p + C_p p^2 n, \tag{2.13}$$

where C_n (C_p) is the Auger coefficient for such an event involving two electrons (holes) and a hole (electron). The cubic carrier concentration dependence makes Auger recombination negligible unless the concentration is unusually high (corresponding to high injection currents). The total recombination rate per unit volume R is found by summing (2.11), (2.12) and (2.13):

$$R = R_{nr} + R_{rad} + R_{Auger} = \delta n \sum_{E_T} \frac{1}{\tau_{nr}(E_T)} + Anp + C_n n^2 p + C_p p^2 n. \tag{2.14}$$

The internal quantum efficiency η_{IQE} of an LED is defined as the fraction of total recombination events that are radiative, which is given by dividing (2.11) by (2.14):

$$\eta_{IQE} = \frac{R_{rad}}{R} = \frac{Anp}{\delta n \sum \frac{1}{\tau_{nr}} + Anp + C_n n^2 p + C_p p^2 n}. \tag{2.15}$$

Inspection of (2.15) reveals that the internal quantum efficiency is maximised by keeping defects and surfaces to a minimum, which corresponds to large values of τ_{nr}, while keeping injection currents below the level at which the unavoidable Auger process becomes significant.

2.4 Basic LED operation and quantum wells

The basic principle of an LED is to convert electrical energy into light through radiative recombination. Simultaneously, holes are injected from a p-type region and electrons from an n-type region into an 'active' volume, usually the p-n junction itself, where they recombine to emit light via spontaneous emission. As a p-n junction is involved, the device also functions as a diode, hence the name light emitting diode and corresponding acronym LED. However, this simple design is highly inefficient, as most of the emitted photons will be re-absorbed within the semiconductor. Practical LEDs therefore use quantum wells to act as the p-n junction. A quantum well consists of an extremely narrow (on the order of nanometres) undoped or lightly doped region with a band gap significantly lower than that of the surrounding confinement layers, one of which is p-type and the other n-type. The difference in band gap acts to confine electrons and holes in the same place, so that they recombine much more quickly than they would otherwise; in addition, the confinement layers are essentially transparent to the emitted light. The confinement and emission processes are depicted in figure 2-3.

Most LEDs use multiple quantum wells, which are placed close together in an un-

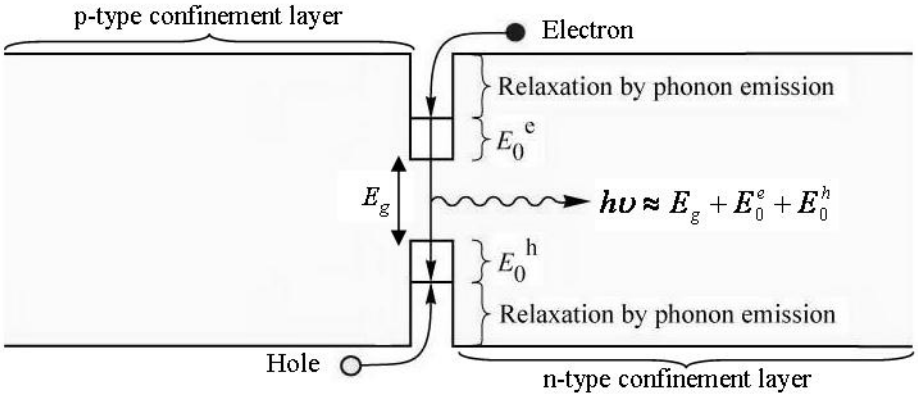

Figure 2-3: Carrier confinement and recombination in a quantum well. © E. Fred Schubert (2006), published by Cambridge University Press, adapted with permission.

doped or lightly doped active region. The quantum wells are separated by regions of higher band gap that are also only a few nanometres thick; these are often called barrier layers. Both confinement and barrier layers are essentially transparent to the emitted light. This transparency, combined with the narrow thickness of the absorbing quantum wells, means very little light is absorbed (Miyajima *et al.* 2011).

2.5 Summary

In this chapter, the reader is taken from an abstract discussion of radiative processes in a two-level system to a justification of the the modern multiple quantum well based LED in terms of these same processes. The role of defects in lowering the internal quantum efficiency is also introduced, as is the dependence of the spontaneous emission rate A on the photon energy density $\rho(\nu)$, which is also known as the optical density of states. Equation (2.15) shows how η_{IQE} is effected by $\rho(\nu)$ via A. A qualitative discussion of how the multiple quantum well is incorporated into a packaged GaN LED device is given in the next chapter.

Chapter 3

LED structure and packaging

3.1 Introduction

The entire field of optoelectronics depends on the ability to bridge the quantum physics discussed in chapter 2 and the macroscopic physics of the finished device; this interface occurs inside the LED chip. This chapter contains a brief qualitative discussion of the structure of LED chips and how they fit into the full packaged LED device; for a more detailed review see chapters 4 and 5 of Mottier (2008). The material in this chapter is not critical to understanding the wider thesis, although concepts introduced here are referred to in later chapters.

3.2 Chip structure of gallium nitride (GaN)-based LEDs

Today, most LEDs used for general lighting applications are based on the III-V semiconductor gallium nitride (GaN), which is traditionally grown as thin films on sapphire substrates. As sapphire is electrically insulating, both the p-type and n-type contacts must lie on the same side of the wafer, as depicted in figure 3-1 (a), with access to the n-type GaN being enabled by mesa-etching. In recent years, however, GaN has been grown on silicon substrates in growing quantities at a much lower cost; for a review see Zhu *et al.* (2013). Unlike sapphire, silicon is semiconducting, so the two contacts can be placed on opposite sides of the wafer as shown in figure 3-1 (b), in addition to the configuration shown in figure 3-1 (a). GaN is ideally suited to LEDs because it is essentially transparent to visible radiation; the actual light emission takes place in quantum wells made of indium gallium nitride (InGaN), which has a lower band gap. LEDs emitting in the yellow, red and orange are made of AlGaInP as opposed to GaN; AlGaInP is grown on GaAs substrates, which are much like silicon substrates in that

they are semiconducting but also absorbing.

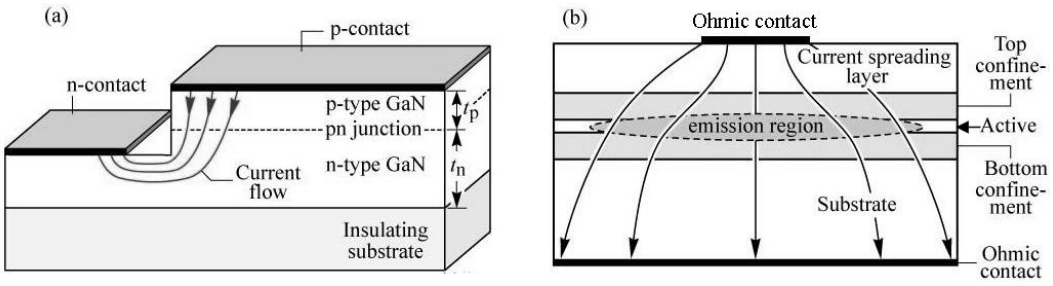

Figure 3-1: LED chip with a (a) lateral and (b) vertical structure. ©E. Fred Schubert (2006), published by Cambridge University Press, reproduced with permission.

3.3 Packaging the LED chip

The LED chip itself is not sufficient to form a useful product. In order to form a practical device, the chip must be connected to an electrical power source, any required electronics and a heat sink into which any heat generated by non-radiative recombination and Joule heating can be dissipated. This is generally done by connecting the LED chip to a chip header using surface mount technology (SMT). In addition, the chip is fragile and must be shielded from its external environment by encapsulation in a transparent material such as acryllic, silicone or epoxy. Section 3.2 descrbed two different types of LED chip, lateral and vertical, which must be packaged in different ways. The two possible substrate types, sapphire and siilicon, have very different properties that affect the choice of packaging process; sapphire is electrically and thermally insulating and optically transparent, while silicon is electrically and thermally semiconducting and opaque to visible radiation.

3.4 Conventional chip LEDs

Conventional chip LEDs, in which the substrate faces the chip header and the contacts face away from it, are the simplest and cheapest lateral LEDs to make. The contacts are connected to the external circuit by wire bonding. There are, however, two main disadvantages to this process. Firstly, the metal contacts will inevitably prevent some of the light from escaping from the chip, reducing the extraction efficiency. The use of transparent contacts such as indium tin oxide (ITO) (Cho *et al.* 2005, 2008) and aluminium zinc oxide (AZO) (Kong *et al.* 2011) can alleviate this problem, although this is at present a highly expensive solution. The second problem concerns heat

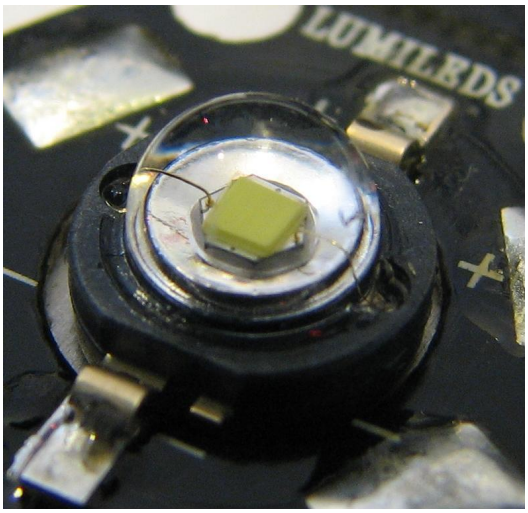

Figure 3-2: A commercial flip-chip InGaN/GaN LED package. (Philips Lumileds 2006 and Wysocki 2007)

dissipation. The sapphire substrate is thermally insulating, making it difficult to remove heat generated by non-radiative recombination from the chip, causing heat to build up and damage the chip. Silicon has a higher thermal conductivity than sapphire making this less of a problem, although a metal would be preferable. A reflector of some variety is necessary in order to redirect light emitted towards the chip header. For the case of transparent sapphire substrates, a metal mirror placed on the far side of the sapphire is sufficient. For the case of silicon substrates, an in-situ DBR (distributed Bragg reflector) or something similar must be fabricated between the active region and substrate, or the substrate must be removed.

3.5 Flip-chip LEDs

The use of flip-chip LEDs is a simple and effective solution to the problems associated with conventional chip LEDs. In flip-chip LEDs the contacts face the chip header while the substrate faces away or is removed altogether. The contacts must be connected to the circuit by solder-bump bonding; although this is more expensive than wire bonding, the resulting increase in efficiency usually ensures the cost-effectiveness of flip-chip packaging. The metal contacts, facing the chip header and the heat sink, no longer impede the propagation of light; in addition they act as reflectors while providing a path of high thermal conductivity between the chip and heat sink. For LEDs grown on sapphire substrates, the light can pass through the substrate unimpeded, although the highly-defective GaN nucleation layer between the substrate and the rest of the chip

absorbs some of the light (Schad *et al.* 2004, Mottier 2009 chapter 2); the most efficient GaN-on-sapphire LEDs employ a technique called laser lift-off where the nucleation layer is destroyed by shining a high-intensity laser through the substrate, detaching the sapphire in the process. Laser lift-off also roughens what remains of the GaN chip, scattering some of the light that would otherwise be confined to the chip by total internal reflection. Flip-chip packaging cannot be implemented for the case of silicon substrates without removing the absorbing silicon. As laser lift-off is not suitable for silicon substrates, chemical etching is required.

3.6 Packaging of vertical LEDs

Vertical LEDs have the n and p-type contacts on opposite sides of the wafer. Without substrate removal, this packaging process is unsuitable for insulating sapphire substrates, so it can be used for silicon only. Although in-situ DBRs can still be fabricated to reflect light away from the absorbing substrate, they usually consist of GaN alternating with another semiconductor of higher bandgap, such as AlGaN (Calle *et al.* 2002) or AlInN (Dorsaz *et al.* 2005, Cosendey *et al.* 2011). Materials with higher bandgap than GaN act as a barrier to electrons or holes attempting to pass through them, resulting in a decrease in the injection efficiency, while materials of lower bandgap tend to be absorbing in the visible (the bandgap of GaN is 3.45 eV, in the near-ultraviolet). This results in a trade-off; either forego the use of a DBR and accept a very low extraction efficiency, or use the DBR and accept a reduced injection efficiency. The only way around this is to remove the substrate, so that the contact on the chip header side can also function as a reflector and heat sink; with substrate removal, the vertical structure can also be implemented for chips grown on sapphire. The main advantage of vertical packaging is that it requires neither mesa-etching or solder-bump bonding; the main disadvantage is that the contact on the side opposite the chip header will always hinder light extraction to some extent. Substrate-free vertical packages generally have the most efficient heat dissipation.

3.7 Encapsulation

The material used for encapsulation must be soft or liquid while hot and become rigid and durable upon cooling, as well as being transparent. Examples of such materials include various plastics such as acryllic in addition to many varieties of silicone and epoxy. In addition to protecting the fragile semiconductor chip and its connections to the external circuit, the encapsulant also enhances light extraction compared to what

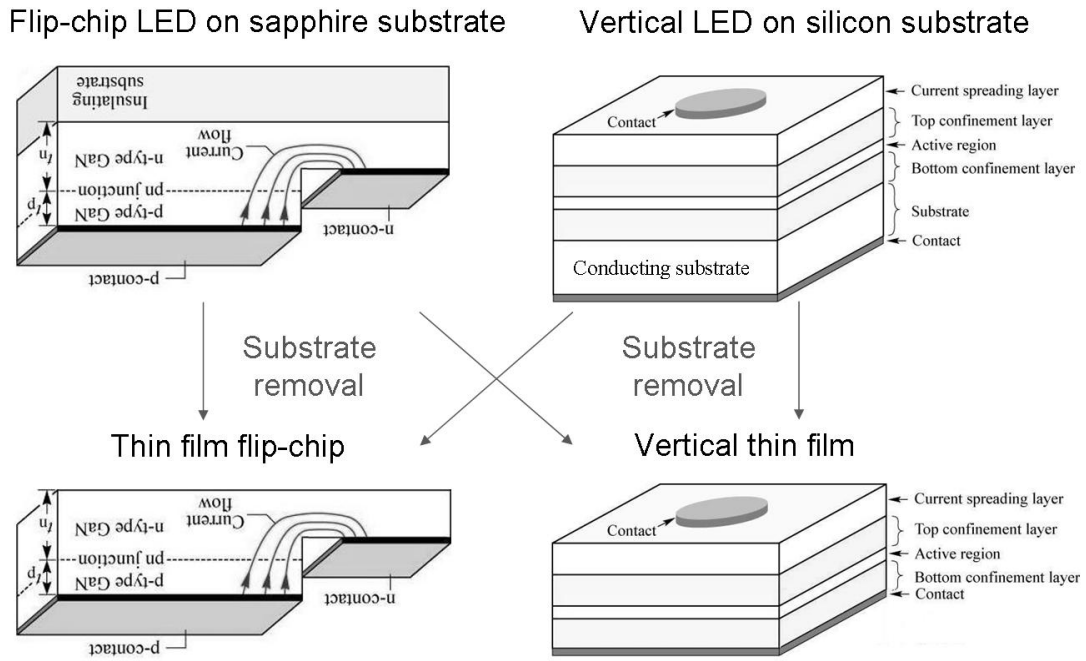

Figure 3-3: A graphical summary of the various types of LED chip structure, showing the flexibility added by substrate removal. © E. Fred Schubert (2006), published by Cambridge University Press, adapted with permission.

it would be if the chip was in direct contact with air. If the encapsulant takes the shape of a hemisphere with the chip at its centre and is sufficiently large compared to the chip, light emitted from the chip in any direction is incident upon the encapsulant/air interface at near-normal incidence and therefore undergoes little reflection. As the refractive index of most encapsulants is around 1.5 as opposed to unity for air, the critical angle of total internal reflection at the chip/encapsulant interface and by extension the extraction efficiency are therefore significantly increased by the use of encapsulants in this manner. For applications requiring high directionality, the encapsulant is often shaped into a lens in order to collimate the light into a near-surface normal direction.

3.8 Summary

This chapter provides a brief summary of the various options for packaging LEDs; this is not critical to understanding the thesis but provides useful background information. In particular, the ability of hemispherical encapsulants to increase the extraction efficiency is important and is revisited in later chapters.

Chapter 4

Maxwell's equations

4.1 Introduction

Classical electromagnetism is governed in its entirety by Maxwell's equations, from which any and all equations and identities concerning electromagnetism are derived. This chapter introduces Maxwell's equations and key equations that can be derived from them, including the interface conditions, the wave equations, Snell's law and the Fresnel equations, as well as important concepts such as plane waves, waveguiding, the far field and coherence. The derivations of these equations are not given here, although the interested reader is referred to Jackson (1999) and Sadiku (2007) for a broad overview, while other useful textbooks for specific concepts are listed in the relevant sections.

Maxwell's equations can be found in any textbook on electromagnetism, such as Sadiku (2007, pp. 400-401) and are usually given in coordinate-free vector differential form:

$$\vec{\nabla} \cdot \vec{D} = \rho_q \tag{4.1}$$

$$\vec{\nabla} \cdot \vec{B} = 0 \tag{4.2}$$

$$\vec{\nabla} \times \vec{E} = -\frac{\partial \vec{B}}{\partial t} \tag{4.3}$$

$$\vec{\nabla} \times \vec{H} = \vec{J} + \frac{\partial \vec{D}}{\partial t} \tag{4.4}$$

$$\vec{D} = \epsilon \vec{E} \tag{4.5}$$

$$\vec{B} = \mu \vec{H}, \tag{4.6}$$

where $\vec{E}$ and $\vec{H}$ are the respective electric and magnetic fields, $\vec{D}$ and $\vec{B}$ are the respective electric and magnetic flux densities, ρ_q is the electric charge density per unit

volume, $\vec{J}$ is the electric current density per unit area and t is time. The permittivity ϵ and permeability μ are generally 3x3 matrices that depend on the respective electric or magnetic field strength. However, for many cases, including this work, the materials involved can be treated as linear (ϵ and μ are independent of field strength), isotropic (ϵ and μ are scalars) and homogeneous ($\vec{\nabla}\epsilon = \vec{\nabla}\mu = 0$, except at boundaries). These conditions are assumed throughout this work.

4.2 Interface conditions

The optical systems considered in this work consist of linear, isotropic and homogeneous materials separated by abrupt interfaces such as the one considered in figure 4-1 between a medium with permittivity ϵ_+ and permeability μ_+ and a medium with permittivity ϵ_- and permeability μ_-. $\vec{E}_\pm$ and $\vec{H}_\pm$ are the respective electric and magnetic fields

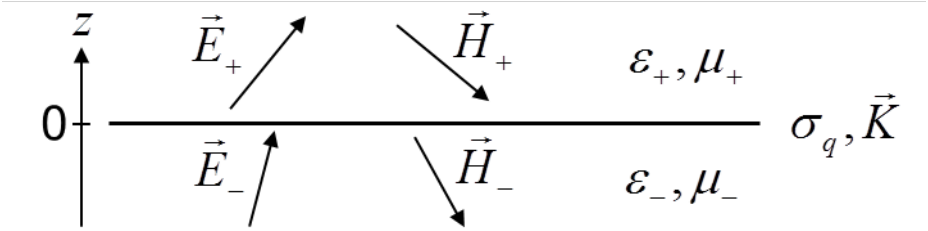

Figure 4-1: A interface between two media with different permittivities ϵ and permeabilities μ.

immediately either side of the interface:

$$\vec{E}_\pm = \lim_{z\to 0^\pm}(\vec{E}) \quad \text{and} \quad \vec{H}_\pm = \lim_{z\to 0^\pm}(\vec{H}), \tag{4.7}$$

while σ_q and $\vec{K}$ are the surface charge density and surface current density on the interface respectively. It can be shown (Sadiku 2007 pp. 190-192, 344-346, 401) that the interface conditions on Maxwell's equations are

$$(\vec{D}_- - \vec{D}_+) \cdot \hat{z} = \sigma_q \tag{4.8}$$

$$(\vec{B}_- - \vec{B}_+) \cdot \hat{z} = 0 \tag{4.9}$$

$$(\vec{E}_- - \vec{E}_+) \times \hat{z} = 0 \tag{4.10}$$

$$(\vec{H}_- - \vec{H}_+) \times \hat{z} = \vec{K}, \tag{4.11}$$

where $\hat{z}$ is the unit vector in the positive z direction. In almost all practical cases, with the notable exception of the perfect conductor boundary condition that is not

considered in this work, there are no surface charges or currents, therefore

$$(\vec{D}_- - \vec{D}_+) \cdot \hat{z} = 0 \tag{4.12}$$

$$(\vec{H}_- - \vec{H}_+) \times \hat{z} = 0. \tag{4.13}$$

Equations (4.10) and (4.13) imply that the components of the electromagnetic fields $\vec{E}$ and $\vec{H}$ tangential to an interface are continuous across the interface, while (4.9) and (4.12) imply that the components of the flux densities $\vec{D}$ and $\vec{B}$ normal to an interface are continuous across the interface.

4.3 The wave equations and refractive index

Assuming the absence of any charges or currents ($\rho_q = \vec{J} = 0$), the six Maxwell equations can be combined to form the electromagnetic wave equations:

$$\nabla^2 \vec{E} = \mu\epsilon \frac{\partial^2 \vec{E}}{\partial t^2} = \frac{1}{v_p^2} \frac{\partial^2 \vec{E}}{\partial t^2} \tag{4.14}$$

$$\nabla^2 \vec{H} = \mu\epsilon \frac{\partial^2 \vec{H}}{\partial t^2} = \frac{1}{v_p^2} \frac{\partial^2 \vec{H}}{\partial t^2}, \tag{4.15}$$

where the phase velocity v_p of the electromagnetic waves is given by

$$v_p = \frac{1}{\sqrt{\mu\epsilon}}. \tag{4.16}$$

The phase velocity c_0 of light in a vaccuum is given by substituting the vacuum permeability $\mu = \mu_0 = 4\pi \times 10^{-7}$ Hm^{-1} and vacuum permittivity $\epsilon_0 = 8.854 \times 10^{-12}$ Fm^{-1} into (4.16), which yields

$$c_0 = \frac{1}{\sqrt{\mu_0\epsilon_0}} = 2.998 \times 10^8 \mathrm{ms}^{-1}. \tag{4.17}$$

The phase velocity v_p of light in a homogeneous, isotropic material can now be expressed as a multiple of c_0:

$$v_p = \frac{1}{\sqrt{\mu\epsilon}} = c_0 \sqrt{\frac{\mu_0\epsilon_0}{\mu\epsilon}} = \frac{c_0}{n}, \tag{4.18}$$

where the refractive index n is given by

$$n = \sqrt{\frac{\mu\epsilon}{\mu_0\epsilon_0}} = \sqrt{\mu_r\epsilon_r} \tag{4.19}$$

and the relative permeability μ_r and relative permittivity ϵ_r are defined as

$$\mu_r = \frac{\mu}{\mu_0}, \quad \text{and} \quad \epsilon_r = \frac{\epsilon}{\epsilon_0}. \tag{4.20}$$

Substituting (4.18) into (4.14) and (4.15) gives

$$\nabla^2 \vec{E} = \frac{n^2}{c_0^2} \frac{\partial^2 \vec{E}}{\partial t^2} \tag{4.21}$$

$$\nabla^2 \vec{H} = \frac{n^2}{c_0^2} \frac{\partial^2 \vec{H}}{\partial t^2}. \tag{4.22}$$

The solutions to the wave equations are assumed to have a harmonic time dependence:

$$\vec{E} \sim \mathrm{e}^{-\mathrm{i}\omega t} \quad \vec{H} \sim \mathrm{e}^{-\mathrm{i}\omega t}, \tag{4.23}$$

where $\mathrm{i} = +\sqrt{-1}$ and the angular frequency of the electromagnetic waves under investigation ω is related to the free space wavenumber k_0 and free space wavelength λ_0 by

$$\omega = k_0 c_0 = \frac{2\pi}{\lambda_0} c_0. \tag{4.24}$$

The permittivity ϵ, the permeability μ and therefore the refractive index n all generally vary with ω.

4.4 Electromagnetic plane waves

In an unbounded homogeneous medium, where n is the same for all space, the standard solution to the wave equations (4.21) and (4.22) is a plane wave:

$$\vec{E} = \vec{E}_0 \mathrm{e}^{\mathrm{i}(\vec{k}\cdot\vec{r}-\omega t)} \quad \vec{H} = \vec{H}_0 \mathrm{e}^{\mathrm{i}(\vec{k}\cdot\vec{r}-\omega t)}, \tag{4.25}$$

where $\vec{E}_0$ and $\vec{H}_0$ are vector amplitudes, $\vec{r}$ is the position vector and $\vec{k}$ is the wavevector whose magnitude is the wavenumber $|\vec{k}|$:

$$|\vec{k}| = \frac{\omega}{v_p} = n\frac{\omega}{c_0} = k_0 n. \tag{4.26}$$

Note that an equally valid formulation of (4.25) uses $\mathrm{e}^{\mathrm{i}(\omega t - \vec{k}\cdot\vec{r})}$. However, the convention in (4.25) is used throughout this thesis. Different sources, or even different chapters of the same textbook (e.g. Sadiku 2007), use different conventions, so great care must be taken to ensure any and all equations are derived using the correct convention.

Without loss of generality, it can be assumed that $\vec{E}_0$ has only an x component ($\vec{E}_0 \times \hat{x} = 0$) in the Cartesian rectangular coordinate system. By substituting (4.25) into (4.3) and (4.4) under this condition, it can be established that $\vec{E}_0$ and $\vec{H}_0$ are orthogonal, therefore $\vec{H}_0$ can be assumed to have only a y component. Substituting (4.25) into (4.3) and (4.4) under both of these conditions yields

$$k_z E_{0x} = \omega \mu H_{0y} \tag{4.27}$$

$$k_z H_{0y} = \omega \epsilon E_{0x}, \tag{4.28}$$

where E_{0x} and H_{0y} the respective electric and magnetic field amplitudes and k_z is the z component of the wavevector. Dividing (4.27) by (4.28) and rearranging gives

$$\frac{E_0 x}{H_0 y} = Z = \sqrt{\frac{\mu}{\epsilon}}, \tag{4.29}$$

where Z is the impedance of a medium of permittivity ϵ and permeability μ to the propagation of an electromagnetic wave. The impedence Z_0 of free space is given by

$$Z_0 = \sqrt{\frac{\mu_0}{\epsilon_0}}. \tag{4.30}$$

Substituting (4.29) back into (4.28) shows that

$$k_z = \omega \epsilon Z = \omega \sqrt{\mu \epsilon} = n \frac{\omega}{c_0} = k_0 n = |\vec{k}|, \tag{4.31}$$

i.e. $\vec{k}$ has only a z component. More generally, $\vec{E}_0$, $\vec{H}_0$ and $\vec{k}$ are all orthogonal for a plane wave. The time-averaged power flow per unit area carried by an electromagnetic wave with harmonic time dependence (4.23) is given by the time-averaged Poynting vector $\vec{S}$ (Sadiku 2007 pp. 454-457):

$$\vec{S} = \tfrac{1}{2} \mathrm{Re}(\vec{E} \times \vec{H}^*), \tag{4.32}$$

where $\vec{H}^*$ is the complex conjugate of the magnetic field. The power flow P through an area A is found by integrating the Poynting vector over A:

$$P = \int \int_A \vec{S} \cdot \, \mathrm{d}\vec{A}. \tag{4.33}$$

Substituting (4.25) and (4.29) into (4.32) yields the Poynting vector of a plane wave:

$$\vec{S} = \frac{|\vec{E}_0|^2}{2Z}\hat{z}, \tag{4.34}$$

where $\hat{z}$ is the unit vector in the z direction. The permittivity ϵ and permeability μ are generally complex numbers, in order to account for optical absorption and electrical conductivity; the refractive index n and impedance Z are therefore also generally complex. All of the equations in this chapter remain valid for complex ϵ and μ except for (4.34), which becomes

$$\vec{S} = \frac{|\vec{E}_0|^2}{2\mathrm{Re}(Z)}\mathrm{e}^{-2k_0\mathrm{Im}(n)z}\hat{z}. \tag{4.35}$$

Inspection of (4.35) reveals that $\mathrm{Im}(n) > 0$ corresponds to absorption, $\mathrm{Im}(n) < 0$ corresponds to gain (for example in lasers) and $\mathrm{Im}(n) = 0$ for transparent media. Although the equations of electromagnetism are valid for absorbing media, some concepts such as transmittance, total internal reflection and waveguiding are much more difficult to define in such cases. Therefore ϵ, μ, n and Z are assumed to be real throughout this work.

4.5 Reflection and refraction at an interface

Consider a single planar interface between two semi-infinite homogeneous media as depicted in Figure 4-2; the space where $z < 0$ is occupied by a medium of refractive index n_1 while the space where $z > 0$ is occupied by a medium of index n_2. This time, $\vec{k}$ has both a z component β and a transverse component κ in the place of the interface:

$$\vec{E}_i = \vec{E}_{0i}\mathrm{e}^{\mathrm{i}(\kappa_i x + \beta_i z - \omega t)}, \tag{4.36}$$

$$\vec{E}_r = \vec{E}_{0r}\mathrm{e}^{\mathrm{i}(\kappa_r x - \beta_r z - \omega t)}, \tag{4.37}$$

$$\vec{E}_t = \vec{E}_{0t}\mathrm{e}^{\mathrm{i}(\kappa_t x + \beta_t z - \omega t)}. \tag{4.38}$$

Conservation of the wavevector requires that

$$\kappa_i = \sqrt{k_0^2 n_1^2 - \beta_i^2}, \quad \kappa_r = \sqrt{k_0^2 n_1^2 - \beta_r^2}, \quad \text{and} \quad \kappa_t = \sqrt{k_0^2 n_2^2 - \beta_t^2}. \tag{4.39}$$

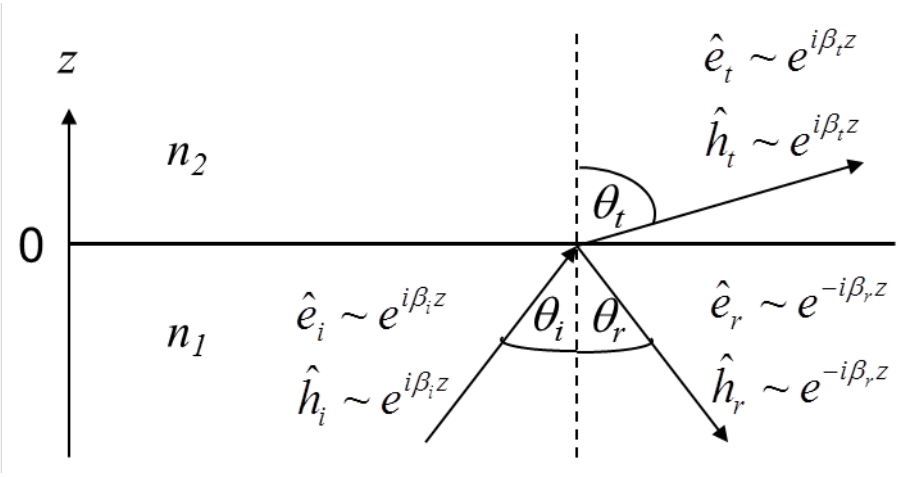

Figure 4-2: Reflection and refraction of a plane wave at a planar interface. The phase of the backward-propagating reflected wave r varies as $\mathrm{e}^{-\mathrm{i}\beta_r z}$ while those of the forward-propagating incident wave i and transmitted wave t vary as $\mathrm{e}^{+\mathrm{i}\beta_i z}$ and $\mathrm{e}^{+\mathrm{i}\beta_t z}$ respectively.

The κ and β are related to the angle θ between $\vec{k}$ and the surface normal vector $\hat{z}$ as follows:

$$\beta_i = k_0 n_1 \cos\theta_i, \quad \beta_r = k_0 n_1 \cos\theta_r, \quad \beta_t = k_0 n_2 \cos\theta_t, \tag{4.40}$$

$$\kappa_i = k_0 n_1 \sin\theta_i, \quad \kappa_r = k_0 n_1 \sin\theta_r \quad \text{and} \quad \kappa_t = k_0 n_2 \sin\theta_t. \tag{4.41}$$

The interface conditions (4.10) and (4.13) can only be satisfied at all points on the plane if

$$\kappa_i = \kappa_r = \kappa_t, \tag{4.42}$$

from which can be derived the law of reflection

$$\theta_i = \theta_r \tag{4.43}$$

and Snell's law of refraction

$$n_1 \sin\theta_1 = n_2 \sin\theta_2. \tag{4.44}$$

Without loss of generality, electromagnetic plane waves can be divided into two sets. Waves with transverse electric (TE) polarization have no z component in their electric field ($\vec{E} \cdot \hat{z} = 0$) while waves with transverse magnetic (TM) polarization have no z component in their magnetic field ($\vec{H} \cdot \hat{z} = 0$). By considering the interface conditions (4.10) and (4.13) at the interface, the relative amplitudes of the incident, reflected and transmitted waves are given by the Fresnel equations, which are different for TE and

TM waves. For TE waves

$$r = \frac{|\vec{E}_{0r}|}{|\vec{E}_{0i}|} = \frac{\mu_2\beta_i - \mu_1\beta_t}{\mu_2\beta_i + \mu_1\beta_t} \tag{4.45}$$

$$t = \frac{|\vec{E}_{0t}|}{|\vec{E}_{0i}|} = \frac{2\mu_2\beta_i}{\mu_2\beta_i + \mu_1\beta_t}, \tag{4.46}$$

where r and t are the Fresnel reflection and transmission coefficients respectively. For TM waves

$$r = \frac{|\vec{E}_{0r}|}{|\vec{E}_{0i}|} = \frac{\epsilon_1\beta_t - \epsilon_2\beta_i}{\epsilon_1\beta_t + \epsilon_2\beta_i} \tag{4.47}$$

$$t = \frac{|\vec{E}_{0t}|}{|\vec{E}_{0i}|} = \frac{2\epsilon_2\beta_i}{\epsilon_1\beta_t + \epsilon_2\beta_i}. \tag{4.48}$$

Integrating the Poynting vectors over the interface gives the power P in the incident, reflected and transmitted waves:

$$P_i = \frac{|\vec{E}_{0i}|^2}{2Z_1}\cos\theta_i \tag{4.49}$$

$$P_r = |r|^2\frac{|\vec{E}_{0i}|^2}{2Z_1}\cos\theta_i \tag{4.50}$$

$$P_t = |t|^2\frac{|\vec{E}_{0i}|^2}{2Z_2}\mathrm{Re}(\cos\theta_t). \tag{4.51}$$

The reflectance R and transmittance T are given by

$$R = \frac{P_r}{P_i} = |r|^2 \tag{4.52}$$

$$T = \frac{P_t}{P_i} = \frac{\mu_1 n_2 \mathrm{Re}(\beta_t)}{\mu_2 n_1 \beta_i}|t|^2. \tag{4.53}$$

The presence of $\mathrm{Re}(\cos\theta_t)$ in (4.51) and (4.53) accounts for total internal reflection, which occurs for large θ_i where $n_1 > n_2$, as is the case for high-index semiconductor media ($n \approx 2.45$ for GaN) surrounded by low-index encapsulants ($n \approx 1.5$) or air ($n = 1$). If $n_1 > n_2$, there exists a critical angle $\theta_i = \theta_c$ at which $\theta_t = \frac{\pi}{2}$, given by Snell's law:

$$\theta_c = \arcsin\left(\frac{n_2}{n_1}\right). \tag{4.54}$$

For $\theta_i \geq \theta_c$, $R = 1$ and $T = 0$ for both TE and TM waves, i.e. 100% of the optical power is reflected. If total internal reflection occurs at two parallel surfaces, the ray is confined between them; this is the basis of waveguiding in dielectric structures.

4.6 Plane wave expansion and far field

As plane waves are a complete orthonormal set of functions, any electromagnetic fields can be expressed in terms of a superposition of plane waves:

$$\vec{E}(\vec{r},t) = \int_0^{\infty}\int_{-\infty}^{+\infty}\int_{-\infty}^{+\infty} c(\kappa,\sigma,\omega)\vec{E}_0(\kappa,\sigma,\omega)\mathrm{e}^{\mathrm{i}(\kappa x+\sigma y+\beta z-\omega t)}\,\mathrm{d}\kappa\,\mathrm{d}\sigma\,\mathrm{d}\omega \tag{4.55}$$

$$\vec{H}(\vec{r},t) = \int_0^{\infty}\int_{-\infty}^{+\infty}\int_{-\infty}^{+\infty} c(\kappa,\sigma,\omega)\vec{H}_0(\kappa,\sigma,\omega)\mathrm{e}^{\mathrm{i}(\kappa x+\sigma y+\beta z-\omega t)}\,\mathrm{d}\kappa\,\mathrm{d}\sigma\,\mathrm{d}\omega, \tag{4.56}$$

assuming there are no boundaries other than those perpendicular to the z axis (otherwise the integrals over κ and σ would have to extend over the entire complex plane) and

$$\kappa^2+\sigma^2+\beta^2 = k_0^2n^2 = \left(\frac{\omega n}{c_0}\right)^2. \tag{4.57}$$

Equations (4.55) and (4.56) can be transformed into spherical polar (r,θ,ϕ) coordinates:

$$\vec{E}(\vec{r},t) = \int_0^{\infty}\int_{-\infty}^{+\infty}\int_{-\infty}^{+\infty} c(\kappa,\sigma,\omega)\vec{E}_0(\kappa,\sigma,\omega)\mathrm{e}^{\mathrm{i}r(\kappa\sin\theta\cos\phi+\sigma\sin\theta\sin\phi+\beta\cos\theta-\omega t)}\,\mathrm{d}\kappa\,\mathrm{d}\sigma\,\mathrm{d}\omega \tag{4.58}$$

$$\vec{H}(\vec{r},t) = \int_0^{\infty}\int_{-\infty}^{+\infty}\int_{-\infty}^{+\infty} c(\kappa,\sigma,\omega)\vec{H}_0(\kappa,\sigma,\omega)\mathrm{e}^{\mathrm{i}r(\kappa\sin\theta\cos\phi+\sigma\sin\theta\sin\phi+\beta\cos\theta-\omega t)}\,\mathrm{d}\kappa\,\mathrm{d}\sigma\,\mathrm{d}\omega. \tag{4.59}$$

The case of $r\to\infty$ is called the far field and is of great importance when studying LEDs, as the Poynting vector $\vec{S}$ in the far field gives the intensity seen by the end user of an LED device. It can be shown (Clarke and Brown 1980) that as $r\to\infty$, $c(\kappa,\sigma,\omega)$ is zero except when

$$\kappa = k_0n\sin\theta\cos\phi \quad\text{and}\quad \sigma = k_0n\sin\theta\sin\phi, \tag{4.60}$$

assuming any and all sources are located at finite r. In other words, only plane waves with $\vec{k}$ parallel to the position vector $\vec{r}$ from a finite region where there are sources contribute to the electromagnetic fields at $\vec{r}$.

4.7 Waveguiding

Adams (1981) provides a readable introduction to waveguides and waveguiding. Waveguides confine electromagnetic waves in either one or two dimensions and are widely used to transmit electromagnetic signals over long distances. For microwaves, a pair of metal

mirrors (one-dimensional confinement) or a metal tube (two-dimensional confinement) can be used to make an efficient waveguide. However, for visible light absorption by the metal(s) is too great to make a useful waveguide, so total internal reflection must be used instead.

Figure 4-3 shows the simplest possible one-dimensional dielectric waveguide: a core of refractive index n_{core} with a finite thickness in one dimension (denoted here as z), surrounded by an infinite cladding of a lower refractive index n_{clad}. The choice of notation for the x and z axes is the reverse of that used in most of the literature on one-dimensional waveguides. This has been done to ensure continuity with the rest of the thesis, so that the axis perpendicular to a planar interface (i.e. the surface of the GaN film) is always labelled z.

The symmetric slab waveguide supports two different types of electromagnetic waves,

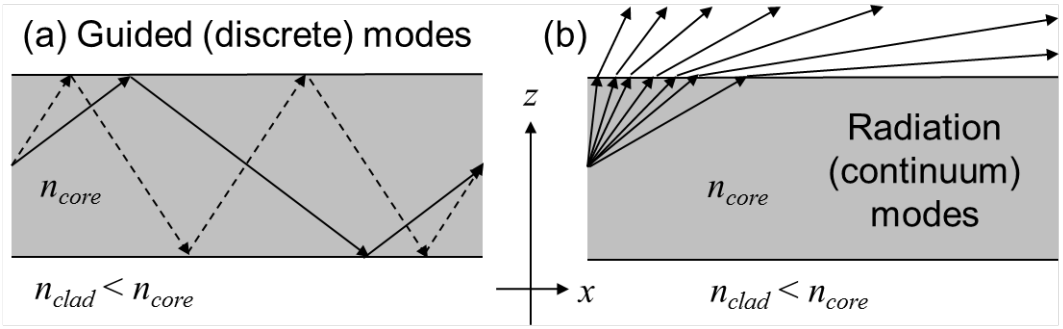

Figure 4-3: A symmetric slab dielectric waveguide. (a) Guided modes are discrete and the power is confined within the waveguide. Two guided modes are depicted here. (b) Radiation modes form a continuous spectrum and power can leave (or enter) the waveguide from outside.

also known as modes. Guided modes are subject to total internal reflection at both of the core-cladding interfaces. This has the effect of confining the power inside the slab; the z component of the time-averaged Poynting vector normal is zero, i.e. no power can enter or leave. As there is no loss of power as the mode propagates along the slab, the phase shift in the z direction must be a multiple of 2π as the wave is reflected from each surface once and returns to its original z position. This condition means that only certain values of $\vec{k} \cdot \hat{x}$ within the range $k_0 n_{clad} < \vec{k} \cdot \hat{x} < k_0 n_{core}$ are allowed, i.e. the spectrum of guided modes is discrete (Adams 1991 pp. 22, 30-31). Figure 4-3 (a) depicts the ray paths of two guided modes.

The other set of modes is that of radiation modes, for which $\vec{S} \cdot \hat{z} \neq 0$, i.e. power can and does enter and leave. This means that there is no restriction on the round-trip phase shift, meaning that any $\vec{k} \cdot \hat{x}$ within the range $0 < \vec{k} \cdot \hat{x} < k_0 n_{clad}$ is allowed. Radiation modes are very similar to plane waves; each mode in the continuum corresponds to a different propagation angle in the cladding, as depicted in Figure 4-3 (b).

More complex waveguide structures can be formed by having a different cladding on each side of the slab, or even adding additional layers. LED chips form waveguides consisting of a GaN core and the substrate and encapsulant as the two claddings; indeed, most of the power is emitted into guided modes as previously discussed. The most common two-dimensional dielectric waveguide is the cylindrical dielectric rod. These are ubiquitious in the form of optical fibres but also have many other applications, including in nanostructured LEDs. The waveguiding properties of the cylindrical dielectric rod are discussed in detail in chapter 8; this analysis is extended to finite-length cylindrical nanostructures in chapters 9 and 10.

4.8 Simplification for non-magnetic materials

All materials investigated in this work are non-magnetic ($\mu = \mu_0$), which simplifies many of the equations in this chapter. For example, (4.19) becomes

$$n = \sqrt{\epsilon_r}, \tag{4.61}$$

equation (4.29) becomes

$$Z = \sqrt{\frac{\mu_0}{\epsilon}} = \frac{Z_0}{n} \tag{4.62}$$

and (4.34) becomes

$$\vec{S} = \frac{n|\vec{E}_0|^2}{2Z_0}\hat{z}. \tag{4.63}$$

In particular, the Fresnel equations for TE waves can now be written in terms only of β:

$$r = \frac{\beta_i - \beta_t}{\beta_i + \beta_t} \tag{4.64}$$

$$t = \frac{2\beta_i}{\beta_i + \beta_t}, \tag{4.65}$$

while those for TM modes cannot:

$$r = \frac{n_1^2\beta_t - n_2^2\beta_i}{n_1^2\beta_t + n_2^2\beta_i} \tag{4.66}$$

$$t = \frac{2n_2^2\beta_i}{n_1^2\beta_t + n_2^2\beta_i}. \tag{4.67}$$

The assumption that $\mu_1 = \mu_2$ removes the symmetry between the Fresnel equations that apply to TE and TM waves, leading to the idea of the Brewster angle. Snell's law implies that

$$\beta_t = \sqrt{k_0^2 n_2^2 - \kappa_t^2} = \sqrt{k_0^2 n_2^2 - \kappa_i^2}. \tag{4.68}$$

By substituting (4.68) into (4.66), it can be shown that $r = 0$ for TM waves when

$$\frac{\kappa_i}{\beta_i} = \frac{n_2}{n_1}, \tag{4.69}$$

which occurs when θ_i is equal to the Brewster angle

$$\theta_i = \theta_B = \tan^{-1}\left(\frac{n_2}{n_1}\right). \tag{4.70}$$

All non-magnetic dielectric-dielectric interfaces for which n_1 and n_2 are both real have a Brewster angle. Conversely, there is no equivalent for TE waves unless one or more of the media involved are magnetic; the reflectance of TE waves invariably increases with angle and is smallest when $\theta_i = 0$. The reflectance is always greater for TE waves than for TM waves incident upon the same interface at the same angle, except for the special cases of $\theta_i = 0$ and $\theta_i \geq \theta_c$ where they are equal.
Equations (4.49)-(4.51) become

$$P_i = \frac{|\vec{E}_{0i}|^2}{2Z_0}\beta_i \tag{4.71}$$

$$P_r = |r|^2\frac{|\vec{E}_{0i}|^2}{2Z_0}\beta_i \tag{4.72}$$

$$P_t = |t|^2\frac{|\vec{E}_{0i}|^2}{2Z_0}\mathrm{Re}(\beta_t). \tag{4.73}$$

and finally

$$R = \frac{P_r}{P_i} = |r|^2 \tag{4.74}$$

$$T = \frac{P_t}{P_i} = \frac{n_2\mathrm{Re}(\beta_t)}{n_1\beta_i}|t|^2. \tag{4.75}$$

The reflection and transmission coefficients r and t of a set of multiple parallel interfaces between non-magnetic materials can be found via a transfer matrix method, as outlined by Hecht (2004 pp. 426-428). The law of reflection, Snell's Law and equations (4.71)-(4.75) can be adapted for this more general case by substituting n_1 and n_2 for the first and last materials of the optical stack, denoted by Hecht as n_0 and n_f. The change in phase as the plane waves travel between interfaces causes r and t to become complex. The transfer matrix method remains valid if one of more materials in the stack have complex n, provided that n_0 and n_f remain real; if they are not, the transmittance T is not defined (Yeh 1988 pp. 65).

4.9 Superposition of fields and coherence

An important consequence of the linear nature of Maxwell's equations is the principle of superposition, which states that the electromagnetic fields due to two or more charges/currents are the sum of the fields due to each individual charge/current:

$$\vec{E}(\vec{r},t) = \sum_p \vec{E}_p(\vec{J}_p) + \sum_q \vec{E}_q(\rho_q) \quad \text{and} \quad \vec{H}(\vec{r},t) = \sum_p \vec{H}_p(\vec{J}_p) + \sum_q \vec{H}_q(\rho_q), \quad (4.76)$$

where the ρ_q are volume densities of charge and the $\vec{J}_q$ are areal current densities. The principle of superposition applies to electromagnetic waves, which are generally emitted by some kind of current source, giving rise to the concept of coherence. Two or more electomagnetic waves are coherent if they are emitted at the same time with the same phase; this occurs either in the case of stimulated emission or for two or more waves emitted in the same spontaneous emission event. The electric field due to two coherent plane waves with different amplitudes $\vec{E}_N$ but identical $\vec{k}$ and ω is the sum of those due to the individual waves:

$$\vec{E}(\vec{r},t) = \sum_N [\vec{E}_N \mathrm{e}^{\mathrm{i}(\vec{k}\cdot\vec{r}-\omega t)}] = \mathrm{e}^{\mathrm{i}(\vec{k}\cdot\vec{r}-\omega t)} \sum_N \vec{E}_N. \quad (4.77)$$

As the magnetic fields sum in the same manner, the total Poynting vector is given by

$$\vec{S} = \frac{n}{2Z_0} \left| \sum_N \vec{E}_N \right|^2 \hat{k}, \quad (4.78)$$

where $\hat{k}$ is the unit wavevector. If the waves are incoherent, however, as is the case for waves emitted in different spontaneous emission events, they are emitted with different,

unknown phases, represented by detunings δ_N:

$$\vec{E}(\vec{r},t) = \sum \left[\vec{E}_N \mathrm{e}^{\mathrm{i}(\vec{k}\cdot\vec{r}-\omega t+\delta_N)}\right] = \mathrm{e}^{\mathrm{i}(\vec{k}\cdot\vec{r}-\omega t)} \sum_N \vec{E}_N \mathrm{e}^{\mathrm{i}\delta_N}. \tag{4.79}$$

The Poynting vector is therefore given by

$$\vec{S} = \frac{n}{2Z_0} \left| \sum_N \vec{E}_N \mathrm{e}^{\mathrm{i}\delta_N} \right|^2 \hat{k}. \tag{4.80}$$

All values of the unknown δ_N are equally likely, so the most likely value of $\vec{S}$ is given by taking the average of (4.80):

$$\vec{S} = \frac{n}{2Z_0} \frac{1}{2\pi} \int_0^{2\pi} \left| \sum_N \vec{E}_N \mathrm{e}^{\mathrm{i}\delta_N} \right|^2 \mathrm{d}\delta_N \hat{k} = \frac{n}{2Z_0} \sum_N |\vec{E}_N|^2 \hat{k}. \tag{4.81}$$

Equation (4.81) becomes a more accurate approximation as the number of incoherent waves involved increases. The difference between equations (4.78) and (4.81) is subtle but critically important. For coherent waves, the relative phases of the waves are taken into account when calculating the Poynting vector; for incoherent waves, they are not. The influence of phase information on the intensity of light is called interference and lies at the heart of how resonant cavities work. It is important to note that, as discussed in section 4.6, only waves for which the wavevector and position vector are parallel contribute to the far field. Therefore, when calculating $\vec{S}$ in the far field, (4.76)-(4.81) apply only when adding plane waves for which $\vec{k} \parallel \vec{r}$.

4.10 Summary

This chapter aims to provide a readable introduction to the mathematics of electromagnetic optics. Many of the concepts introduced here, such as plane waves, the Fresnel equations, far field and coherence, are required for the next chapter, which discusses the mathematics of resonant cavity LEDs. Chapter 6, which discusses modal methods for solving the wave equations (4.21) and (4.22), builds directly on various concepts introduced in this chapter, including the interface conditions and conservation of wavevector. It is worth noting that although the systems simulated in this thesis are non-magnetic, the general case of materials with variable permeability μ can be an invaluable mathematical tool even for non-magnetic systems, as discussed in chapter 9.

Chapter 5

Resonant Cavities

5.1 Introduction

As established in section 4.5, light incident on any smooth planar surfaces obeys the law of reflection. An important consequence of this for LEDs is that all LEDs with smooth surfaces form one-dimensional resonant cavities, regardless of whether or not this is done intentionally. However, the use of surface roughening (or naturally rough surfaces such as unpolished sapphire) destroys the resonant cavity effect by scattering the light at the rough surface, as depicted in Figure 1-4.

Where surface roughening is not used, it is possible to design the cavity in order to optimize the directionality and/or extraction efficiency of the LED device. To this end, this chapter deals with emission from inside one-dimensional resonant cavities, which have a finite length along the optical axis (denoted in this chapter as the z axis) of the cavity and are infinite in the other two dimensions.

5.2 Definitions and notation

Although the literature contains many perspectives on resonant cavities (see for example Deppe *et al.* 1994, Bjork *et al.* 1995 and Delbeke *et al.* 2002), Benisty *et al.*'s (1998) treatment is probably the most rigorous. In general, a one-dimensional resonant cavity consists of any two parallel surfaces with Fresnel reflection coefficients $r_{\pm}$ and transmission coefficients $t_{\pm}$, separated by a distance $d = d_- + d_+$ filled with a medium of refractive index n_{int} and surrounded by a medium of refractive index n_{ext}. The two surfaces can consist of anything from an interface between two dielectrics to metals and advanced reflector structures such as distributed Bragg reflectors and omnidirectional

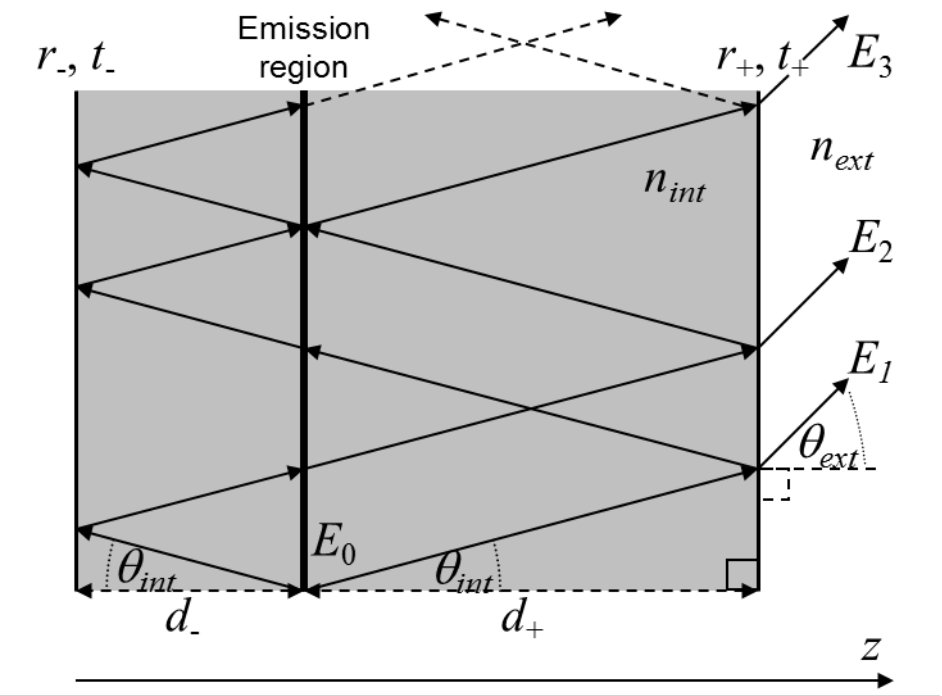

Figure 5-1: A single quantum well active region emitting inside a resonant cavity.

reflectors (Schubert 2006, chapter 10). Figure 5-1 depicts a situation where a single quantum well, positioned a distance d_- from reflector - and d_+ from reflector +, emits a plane wave with electric field amplitude E_0 in both directions at an angle θ_{int} to the optical axis. The width of the quantum well is assumed to be negligible compared to $d_\pm$. The Fresnel coefficients are in general dependent on the emission angle θ_{ext}, the free space wavenumber k_0 and the polarization of the emitted radiation, which can be either TE or TM. The E_N (where $N = 1, 2, 3...$) in Figure 5-1 are the complex electric field amplitudes emitted out of reflector + after undergoing $N - 1$ reflections. Light emitted at an angle θ_{int} to the optical axis exits the cavity at a different angle θ_{ext}, given by Snell's law:

$$n_{int} \sin \theta_{int} = n_{ext} \sin \theta_{ext}. \tag{5.1}$$

Assuming that $n_{int} > n_{ext}$, there exists a critical angle θ_c of total internal reflection:

$$\theta_c = \arcsin\left(\frac{n_{ext}}{n_{int}}\right). \tag{5.2}$$

The critical angle θ_c defines what is called the light escape cone; light emitted into angles $\theta_{int} < \theta_c$ escapes, whilst light emitted angles $\theta_{int} > \theta_c$ does not.

The single quantum well active region depicted in figure 5-1 can be modelled as a distribution $G(k_0)$ of Hertzian dipole point sources, each of which emits plane waves propagating with free space wavenumber k_0 and (real) amplitude E_0. A good approximation for the case of emission from a quantum well active region is to consider only dipoles with dipole moments oriented in the plane of the quantum well, i.e. perpendicular to z (Yamanishi and Suemune 1984, cited in Delbeke *et al.* 2002). Each dipole emits TE and TM plane waves of all possible angles θ_{int} between 0 and $\frac{\pi}{2}$. The intensity emitted into TE waves is invariant with θ; the intensity emitted into TM waves varies as $\cos^2\theta_{int}$ (Bjork *et al.* 1995, Delbeke *et al.* 2002). The dipoles are incoherent with one another; although rays emitted at different angles by the same dipole are coherent, this has no impact on the far field as discussed in chapter 4. The function $G(k_0)$ contains both the total number of dipole sources and their frequency distribution; in most practical cases it can be reasonably approximated as a Gaussian function (Schubert 2006 pp. 333-338), hence the choice of notation.

5.2.1 Demonstration: Hertzian dipole in free space

The Poynting vector $\vec{S_0}$ corresponding to a plane wave of electric field amplitude E_0 and unit wavevector $\hat{k}$ propagating in a medium of refractive index n_{int} is given by (4.63):

$$\vec{S_0} = \frac{n_{int}}{2Z_0}|\vec{E_0}|^2\hat{k} = \frac{n_{int}}{2Z_0}E_0^2\hat{k} = S_0\hat{k}. \tag{5.3}$$

The power P_0 is given by (4.33). However, as the power emitted into TE and TM modes varies with θ in different ways, this must be taken into account by multiplying the integrand by a factor of $1 + \cos^2\theta_{int}$:

$$P_0 = \int\int_A \vec{S_0}(1 + \cos^2\theta_{int}) \cdot \mathrm{d}\vec{A}, \tag{5.4}$$

When seeking the power in the far field, $\mathrm{d}\vec{A}$ must be perpendicular to the position vector $\vec{r}$, which means it takes the form of a spherical cap-shaped section of constant radius r as depicted in Figure 5-2 (Delbeke *et al.* 2002, Schubert 2006 pp. 91-93):

$$\mathrm{d}\vec{A} = r^2 \sin\theta \, \mathrm{d}\theta \, \mathrm{d}\phi\hat{r} \tag{5.5}$$

in spherical polar co-ordinates. Substituting (5.5) into (5.4)gives

$$P_0 = r^2 S_0 \int_0^{2\pi} \mathrm{d}\phi \int_0^{\pi} \sin\theta_{int}(1 + \cos^2\theta_{int}) \, \mathrm{d}\theta_{int}, \tag{5.6}$$

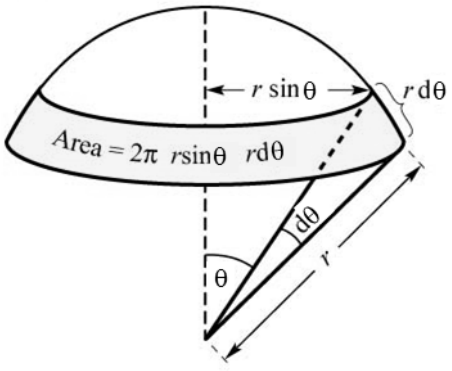

Figure 5-2: Section of a hemisphere defined by angular range dθ.

where the radius r of the sperical cap is arbitrary and can be set such that $2\pi r^2 = 1$ without loss of generality. Setting r to this value and performing the integral in (5.6) yields the final result:

$$P_0 = 2S_0(1 + \tfrac{1}{3}) = \tfrac{8}{3}S_0 = \frac{4n_{int}}{3Z_0}E_0^2. \tag{5.7}$$

The two terms in the brackets correspond to TE and TM waves respectively; the ratio of power in TE and TM waves is 3 to 1. The spectrum-integrated power P_{spec} is given by multiplying P_0 by $G(k_0)$ and integrating over the entire spectrum:

$$P_{spec} = \int_0^\infty P_0 G(k_0)\,\mathrm{d}k_0 = \frac{4E_0^2}{3Z_0}G_{spec}, \tag{5.8}$$

where

$$G_{spec} = \int_0^\infty n_{int}(k_0)G(k_0)\,\mathrm{d}k_0. \tag{5.9}$$

Note that n_{int} remains inside the integral to account for chromatic dispersion. Note also that for P_{spec} to have the correct dimensions, G_{spec} must be dimensionless, which in turn requires $G(k_0)$ to have dimensions of inverse wavenumber (i.e. length).

5.3 Incoherent cavity

If the cavity width d is orders of magnitude larger than the wavelength λ of the emitted light, the phase difference between (coherent) waves emitted at slightly different angles becomes very large (i.e. many multiples of 2π) as the waves travel distances far exceeding λ. Although the exact field is still known, equation (4.81) becomes a very good approximation in practice. Poynting vectors $\vec{S}_N$ associated with each $\vec{E}_N$ can be

defined as follows:

$$\vec{S}_N = \frac{n_{int}}{2Z_0}|\vec{E}_N|^2\hat{k}. \tag{5.10}$$

As all of the $\vec{S}_N$ are parallel for any fixed θ and therefore share the same $\hat{k}$, it is convenient to consider the magnitudes S_N only. If there is no absorption, the S_N are related as follows:

$$\begin{aligned}
S_1 &= (1-R_+)S_0, \\
S_2 &= (1-R_+)R_-S_0 = R_-S_1, \\
S_3 &= (1-R_+)R_-R_+S_0 = (R_+R_-)S_1, \\
S_4 &= (1-R_+)R_-^2R_+S_0 = (R_+R_-)S_2, \\
S_5 &= (1-R_+)R_+^2R_-^2S_0 = (R_+R_-)^2S_1, \\
S_6 &= (1-R_+)R_-^3R_+^2S_0 = (R_+R_-)^2S_2
\end{aligned}$$

and so on, where R_- and R_+ are the reflectances of surfaces + and -, as given by the equation

$$R_\pm = r_\pm r_\pm^* = |r_\pm|^2. \tag{5.11}$$

Define a new index M so that

$$S_M = S_{2M+1} + S_{2M+2} = (1-R_+)(1+R_-)(R_+R_-)^M S_0. \tag{5.12}$$

The total intensity S emitted out of reflector + is therefore given by

$$S = \sum_{N=1}^{\infty} S_N = \sum_{M=0}^{\infty} S_M = S_0(1-R_+)(1+R_-)\sum_{M=0}^{\infty}(R_+R_-)^M. \tag{5.13}$$

As $R_+R_- < 1$, the infinite sum in (5.13) converges in accordance with the identity

$$\sum_{M=0}^{\infty} x = \frac{1}{1-x}, \quad |x| < 1. \tag{5.14}$$

Combining (5.13) and (5.14) yields the final expression for S in terms of S_0:

$$S = \frac{(1-R_+)(1+R_-)}{1-R_+R_-}S_0. \tag{5.15}$$

Equation (5.15) gives the total intensity emitted out of reflector +; the intensity emitted out of reflector - is found by simply exchanging subscripts + and - in (5.15). If this is done and the result added to the original equation (5.15), the total intensity S_T

emitted out of both reflectors is found to be

$$S_T = \frac{(1-R_+)(1+R_-)}{1-R_+R_-} + \frac{(1+R_+)(1-R_-)}{1-R_+R_-} = 2S_0. \tag{5.16}$$

Equation (5.16) makes an important statement about optical cavities and coherence. In the incoherent case, where $d >> \lambda$, the total intensity emitted out of both sides of the cavity is the same as it would be if no cavity were present, regardless of the values of R_+ and R_-. The cavity does not change the total energy output, only how it is divided between the forward and reverse directions. For a dipole source, the extraction efficiency η_{ext} can be found by integrating S_T over the solid angle comprising the light escape cone and dividing by the total power emitted (Schubert 2006 pp. 91-93, Delbeke *et al.* 2002):

$$\eta_{ext} = \frac{2\pi \int_0^{\theta_c} S_T \sin\theta_{int}\, \mathrm{d}\theta_{int}}{2\pi \int_0^{\pi} S_0 \sin\theta_{int}\, \mathrm{d}\theta_{int}}. \tag{5.17}$$

Given that a dipole oriented in the plane of the quantum well emits $\frac{3}{4}$ of its power into TE waves and $\frac{1}{4}$ into TM waves as shown in section 5.2.1, it is helpful to split η_{ext} into TE and TM components:

$$\eta_{ext} = \tfrac{3}{4}\eta_{TE} + \tfrac{1}{4}\eta_{TM}. \tag{5.18}$$

For TE waves E_0 and therefore S_0 are independent of θ, therefore

$$\eta_{TE} = 1 - \cos\theta_c. \tag{5.19}$$

By substituting (5.2) into (5.21) and using the trigonometric identity

$$\cos(\arcsin x) = \sqrt{1-x^2}, \tag{5.20}$$

it can be shown that for the incoherent case of $d >> \lambda$,

$$\eta_{TE} = 1 - \sqrt{1 - \left(\frac{n_{ext}}{n_{int}}\right)^2}. \tag{5.21}$$

For TM waves

$$\eta_{TM} = \frac{2\pi \int_0^{\theta_c} S_T \cos^2\theta_{int} \sin\theta_{int}\, \mathrm{d}\theta_{int}}{2\pi \int_0^{\pi} S_0 \cos^2\theta_{int} \sin\theta_{int}\, \mathrm{d}\theta_{int}}; \tag{5.22}$$

substituting (5.16) ($S_T = 2S_0$) into (5.22) gives

$$\eta_{TM} = 1 - \left[1 - \left(\frac{n_{ext}}{n_{int}}\right)^2\right]^{\frac{3}{2}}. \tag{5.23}$$

Substituting (5.21) and (5.23) into (5.18) yields

$$\eta_{ext} = 1 - \frac{3}{4}\sqrt{1 - \left(\frac{n_{ext}}{n_{int}}\right)^2} - \frac{1}{4}\left[1 - \left(\frac{n_{ext}}{n_{int}}\right)^2\right]^{\frac{3}{2}}. \tag{5.24}$$

This is a more exact formulation of the approximate result derived by Schubert (2006 pp. 93). For the typical case of a GaN ($n \approx 2.45$) LED chip emitting into epoxy ($n \approx 1.5$), $\eta_{ext} \approx 28\%$ (in practice, η_{ext} is lower still due to absorption and mirror losses), placing an upper limit of 28% on both the external quantum efficiency and power conversion efficiency. Making d much smaller, of the order of λ, it is possible to use optical interference effects to boost the extraction efficiency and/or cause the angular emission pattern to be non-Lambertian. This technique is much easier to illustrate by temporarily setting aside the cavity and instead considering the much simpler case of a single mirror.

5.4 Single perfect reflector

The simplest possible case is that of a single quantum well placed a distance d from a perfect metallic reflector as depicted in Figure 5-3, where $d \sim \lambda$. This section extends the theory developed by Benisty *et al.* (1998), who introduce their work in the same manner, for describing the enhancement of light emission by a nearby perfect reflector. The entire space above the mirror is filled with a medium of refractive index n. As

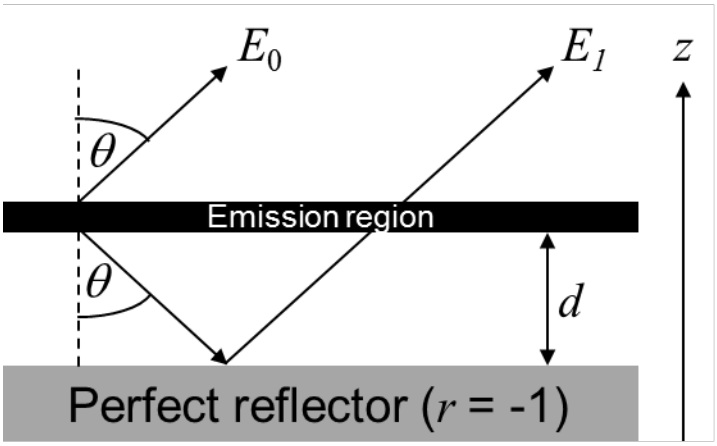

Figure 5-3: A single quantum well active region emitting close to a perfect metallic reflector.

in section 4.5, the electric field $\vec{E}$ of an electromagnetic plane wave can be expressed

without loss of generality in the form

$$\vec{E} = \vec{E}_0 \mathrm{e}^{\mathrm{i}(\kappa x + \beta z - \omega t)}, \tag{5.25}$$

where

$$\kappa = k_0 n \sin\theta \quad \text{and} \quad \beta = k_0 n \cos\theta. \tag{5.26}$$

As discussed in section 4.9, the difference between coherent and incoherent electromagnetic waves is that in the coherent case the relative phases of the different waves are known. On travelling a distance z, the electric field $\vec{E}$ of a plane wave incurs a phase shift of βz. The phase in this work is defined as being zero on emission, therefore E_0 is always real. For any one value of θ, $\vec{E}_0$ and $\vec{E}_1$ are parallel, as depicted in Figure 5-3 so only the complex amplitudes E_0 and E_1 need be considered. Assuming that reflection and absorption by the quantum well to be negligible (Leung *et al.* 1998, Shi and Chi 2007, Miyajima *et al.* 2011), E_1 is related to E_0 by

$$E_1 = -E_0 \mathrm{e}^{2\mathrm{i}\beta d}. \tag{5.27}$$

Equation (4.78) can be used to find the total Poynting vector due to the two waves:

$$\vec{S} = \frac{n}{2Z_0}|E_0 + E_1|^2 \hat{k} = 2S_0[1 - \cos(2\beta d)]\hat{k}, \tag{5.28}$$

where

$$\hat{k} = \hat{z}\cos\theta + \hat{x}\sin\theta. \tag{5.29}$$

As in section 5.3, it is easier to work with the magnitude S:

$$S = |\vec{S}| = 2S_0[1 - \cos(2\beta d)]. \tag{5.30}$$

Inspection of (5.30) reveals that the Poynting vector S emitted into angle θ is equal to $2S_0$ if the upward and downward emitted waves are out of phase, $4S_0$ if they are in phase and zero is they are antiphase. In contrast with the incoherent cavity where d is very large, the emitted power can be changed significantly by the presence of the mirror if it is close enough to the source. The enhancement $U(k_0)$ of the total emitted power is given by integrating S over all θ, including the usual factor of $1 + \cos^2\theta$ and dividing by the power P_0 emitted by the same dipole with no mirror:

$$U(k_0) = \frac{1}{P_0}\int_0^{\frac{\pi}{2}} S(1 + \cos^2\theta)\,\mathrm{d}\theta = 1 - \frac{3}{2}\left(\frac{\sin x}{x} - \frac{\cos x}{x^2} + \frac{\sin x}{x^3}\right), \tag{5.31}$$

where $x = 2k_0nd$. It is again convenient to split U into TE and TM components:

$$U(k_0) = \tfrac{3}{4}U_{TE}(k_0) + \tfrac{1}{4}U_{TM}(k_0), \tag{5.32}$$

where

$$U_{TE}(k_0) = 1 - \frac{\sin x}{x} = 1 - \mathrm{sinc}(x) \tag{5.33}$$

and

$$U_{TM}(k_0) = 1 - 3\mathrm{sinc}(x) - \frac{6\cos x}{x^2} + \frac{6\sin x}{x^3}, \tag{5.34}$$

where

$$\mathrm{sinc}(x) = \frac{\sin x}{x}. \tag{5.35}$$

The spectrum-integrated enhancement U_{spec} is given by

$$U_{spec} = \frac{\int_0^\infty P_0 W(k_0) G(k_0)\,\mathrm{d}k_0}{\int_0^\infty P_0 G(k_0)\,\mathrm{d}k_0}. \tag{5.36}$$

Substituting (5.8) and (5.32) into (5.36) gives

$$U_{spec} = \frac{1}{G_{spec}} \int_0^\infty \left[\tfrac{3}{4}U_{TE}(k_0) + \tfrac{1}{4}U_{TM}(k_0)\right] n(k_0) G(k_0)\,\mathrm{d}k_0. \tag{5.37}$$

The Gaussian nature of $G(k_0)$ means that U_{spec} must be evaluated numerically, even if chromatic dispersion is negligible.

5.4.1 Numerical evaluation of spectrum-integrated enhancement: Gaussian blue spectrum

LED emission spectra are usually given in terms of the photon energy E_{ph} as opposed to k_0. These two quantities are related by

$$E_{ph} = h\nu = \frac{hc_0}{\lambda_0} = \frac{hc}{2\pi}k_0. \tag{5.38}$$

The Gaussian function $G(E_{ph})$ is given in terms of the peak photon energy E_{peak} and full width at half maximum W by

$$G(E_{ph}) = \frac{1}{C_{norm}} \exp\left(-4\ln(2)\left(\frac{E_{ph} - E_{peak}}{W}\right)^2\right), \tag{5.39}$$

where the normalization constant C_{norm} is given by

$$C_{norm} = \int_{E_{peak}-1.5W}^{E_{peak}+1.5W} \exp\left(-4\ln(2)\left(\frac{E_{ph}-E_{peak}}{W}\right)^2\right) \mathrm{d}E_{ph}, \tag{5.40}$$

i.e. the $G(E_{ph})$ is normalized so that its integral over the range $E_{peak} - 1.5W \leq E - ph \leq E_{peak} + 1.5W$ is unity. This normalization also ensures $G(E_{ph})$ has the correct dimensions of inverse energy. These limits were chosen because $1.5W$ is more than three times the standard deviation σ_g of a Gaussian function; for $|E-E_{peak}| > 3\sigma_g$, the value of the Gaussian is negligible. Replacing the infinite integral over k_0 in (5.37) with a finite integral over E_{ph} yields

$$U_{spec} = \frac{1}{G_{spec}} \int_{E_{peak}-1.5W}^{E_{peak}+1.5W} \left[\tfrac{3}{4}U_{TE}(E_{ph}) + \tfrac{1}{4}U_{TM}(E_{ph})\right] G(E_{ph})\, \mathrm{d}E_{ph}, \tag{5.41}$$

where G_{spec} is now given by

$$G_{spec} = \int_{E_{peak}-1.5W}^{E_{peak}+1.5W} n_{int} G(E_{ph})\, \mathrm{d}E_{ph}. \tag{5.42}$$

Figure 5-4 shows how the TE, TM and total components of U_int as given by (5.41) vary with d for a Gaussian distribution given by (5.39), where $E_{peak} = 2.696$ eV (corresponding to $\lambda_0 = 460$ nm) and $W = 0.12$ eV. These values were based on data provided by Plessey Semiconductors for a set of blue LEDs (Plessey Semiconductors 2014). For each value of d the integral was calculated using a composite Boole's rule over a range of 61 photon energy points. Both the TE and TM components of U_{spec} tend to zero as $d \to 0$ as the upward and downward emitted waves E_0 and E_1 become antiphase for all θ, resulting in destructive interference (this is equivalent to the image dipole effect). As d is increased from zero U_{spec} rises rapidly before transitioning to a decaying oscillation around unity, which U_{spec} tends towards as $d \to \infty$. The variation in U_{spec} attributable to TM waves is much greater than that attributable to TE waves; this is because the sinc$x$ term in (5.34) is 3 times that in (5.33). The oscillations of the two components come into phase as d is increased due to the x^{-2} and x^{-3} terms in (5.34) falling off for large d. Focusing on U_{spec} as a whole (solid line), it can be seen that the maximum variation of U_{spec} from unity is around 20% for $d = 100$ nm; this is important as 100 nm is the smallest confinement layer thickness seen in typical commercial LED wafers (Epistar 2012, Plessey Semiconductors 2014). For $d = 200$ nm the maximum variation falls to around 10%.

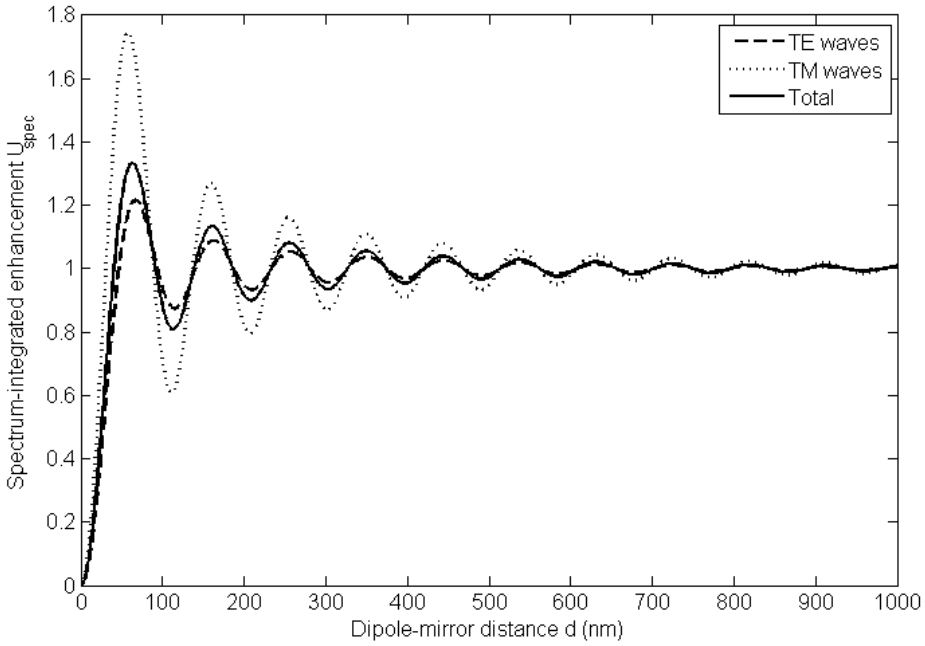

Figure 5-4: Variation of spectrum-integrated enhancement U_{spec} with the distance d between a perfect metallic reflector and a distribution $G(E_{ph})$ of Hertzian dipoles with dipole moment tagential to the metal surface. $G(E_{ph})$ was chosen to be a Gaussian distribution typical of a blue LED (Plessey Semiconductors 2014)

5.4.2 The physics of emission enhencement

It was shown in section 2.2 that the sponteneous emission rate can be varied by altering the photon energy density, also known as the optical density of states, by varying the refractive index of the medium in which the emission takes place. This point is made explicitly by Yariv (1982, pp. 143). Bjork *et al.* (1995), and Schubert (2006, pp. 244-253), among others. The presence of interfaces between media causes the spontaneous emission rate to be position-dependent, with the spatial dependence becoming weaker as the distance between the interface and the emitting dipole decreases. The simple example of a perfect metallic reflector enables this concept to be intitively understood through the electromagnetic method of images, although this is not explicitly done here. Benisty *et al.* (1998) show that the same fundamental physics can be applied to more complex cases such as lossy reflectors, dielectric-dielectric interfaces and even multiple interfaces.

5.5 Coherent cavity

Returning to the case of a full one-dimensional cavity as depicted in Figure 5-1, similar methods to those used for the perfect reflector case can be applied.

5.5.1 Quantifying the resonant cavity effect

For any one value of θ_{int} the $\vec{E}_N$ are all parallel, so only the complex amplitudes E_N are considered. Assuming the quantum well is non-reflecting and has the same power absorbance A_{QW} for all k_0 and θ_{int}, the E_N are related to one another as follows:

$$
\begin{aligned}
E_1 &= t_+ \exp(\mathrm{i}\beta d_+)E_0, \\
E_2 &= t_+ r_- \sqrt{1-A_{QW}} \exp(\mathrm{i}(\beta d_+ + 2\beta d_-))E_0 = r_- \sqrt{1-A_{QW}}\mathrm{e}^{2\mathrm{i}\beta d_-}E_1, \\
E_3 &= t_+ r_+ r_- (1-A_{QW}) \exp(\mathrm{i}(3\beta d_+ + 2\beta d_-))E_0 = r_+ r_- (1-A_{QW})\mathrm{e}^{2\mathrm{i}\beta d}E_1, \\
E_4 &= t_+ r_+ r_-^2 (1-A_{QW})^{\frac{3}{2}} \exp(\mathrm{i}(3\beta d_+ + 4\beta d_-))E_0 = r_+ r_- (1-A_{QW})\mathrm{e}^{-2\mathrm{i}\beta d}E_2, \\
E_5 &= t_+ r_+^2 r_-^2 (1-A_{QW})^2 \exp(\mathrm{i}(5\beta d_+ + 4\beta d_-))E_0 = (r_+ r_- (1-A_{QW})\mathrm{e}^{-2\mathrm{i}\beta d})^2 E_1, \\
E_6 &= t_+ r_+^2 r_-^3 (1-A_{QW})^{\frac{5}{2}} \exp(\mathrm{i}(5\beta d_+ + 6\beta d_-))E_0 = (r_+ r_- (1-A_{QW})\mathrm{e}^{-2\mathrm{i}\beta d})^2 E_2
\end{aligned}
$$

and so on, where $\beta = k_0 n_{int} \cos\theta_{int}$ and $d = d_+ + d_-$ as before. Define a new index M so that

$$
E_M = E_{(2N+1)} + E_{(2N+2)} = E_0 t_+ \mathrm{e}^{\mathrm{i}\beta d_+}(1 + r_- t_{QW}\mathrm{e}^{2\mathrm{i}\beta d_-})(r_+ r_- t_{QW}^2 \mathrm{e}^{-\mathrm{i}\beta d})^M, \quad (5.43)
$$

where

$$
t_{QW} = \sqrt{1-A_{QW}} \quad (5.44)
$$

is the transmission coefficient of the quantum well. The total complex electric field amplitude E emitted out of reflector + is therefore given by

$$
E = \sum_{N=1}^{\infty} = \sum_{M=0}^{\infty} E_M = E_0 t_+ \mathrm{e}^{\mathrm{i}\beta d_+}(1 + r_- t_{QW}\mathrm{e}^{2\mathrm{i}\beta d_-}) \sum_{M=0}^{\infty} (r_+ r_- t_{QW}^2 \mathrm{e}^{2\mathrm{i}\beta d})^M. \quad (5.45)
$$

Assuming $|r_+ r_-| < 1$, the infinite sum in (5.45) converges in accordance with (5.14), yielding

$$
E(k_0, \theta_{int}) = \frac{t_+ \mathrm{e}^{\mathrm{i}\beta d_+}(1 + r_- t_{QW}\mathrm{e}^{2\mathrm{i}\beta d_-})}{1 - r_+ r_- t_{QW}^2 \mathrm{e}^{2\mathrm{i}\beta d}} E_0 = \tau(k_0, \theta_{int}) E_0, \quad (5.46)
$$

where $\tau(k_0, \theta_{int})$ is the transmission coefficient for the cavity system as a whole. The electric field emitted out of reflector - can be found by simply exchanging the + and - subscripts in (5.46), although for the remainder of this chapter it is generally assumed

that $t_- = 0$, which corresponds to the presence of a thick absorbing layer, such as a metallic mirror or absorbing substrate, behind reflector -.

5.5.2 Far field emission pattern

The intensity $I_{ext}(k_0, \theta_{ext})$ emitted out of the cavity into the encapsulant of refractive index n_{ext} for a single wavenumber k_0 and a single propagation angle θ_{ext} in the encapsulant is given by (Yeh 1988 pp. 65, Hecht 2005 pp. 119)

$$I_{ext}(k_0, \theta_{ext}) = \frac{n_{ext} \cos\theta_{ext}}{2Z_0 \cos\theta_{int}} E_0^2 \sum_{TE,TM} |\tau(k_0, \theta_{int})|^2, \tag{5.47}$$

where θ_{int} and θ_{ext} are related by (5.1). The summation can be replaced with a function $F(k_0, \theta_{int})$:

$$I_{ext}(k_0, \theta_{ext}) = \frac{n_{ext} \cos\theta_{ext}}{2Z_0 \cos\theta_{int}} F(k_0, \theta_{int}) E_0^2, \tag{5.48}$$

where

$$F(k_0, \theta_{int}) = |\tau_{TE}(k_0, \theta_{int})|^2 + \cos^2\theta_{int} |\tau_{TM}(k_0, \theta_{int})|^2 \tag{5.49}$$

accounts for the dipole nature of the sources. Assuming the encapsulant is non-absorbing, the single-wavelength output intensity $I(k_0, \theta_{ext})$ that reaches an external observer viewing the LED from angle θ_{ext} is found by subtracting from $I_{ext}(k_0, \theta_{ext}$ any power reflected by the encapsulant/air interface. If the encapsulant forms a large hemisphere around the chip as discussed in section 3.7, the light is normally incident upon this interface so there is no refraction and the reflectance is given by

$$R_{dome} = \left(\frac{n_{ext} - 1}{n_{ext} + 1} \right)^2, \tag{5.50}$$

assuming the refractive index of air is unity. For the case of an unencapsulated LED, $R_{dome} = 0$ and $n_{ext} = 1$. The spectrum-integrated output intensity $I_{spec}(\theta_{ext})$ due to a distribution $G(k_0)$ of incoherent dipole sources is defined as

$$I_{spec}(\theta_{ext}) = (1 - R_{dome}) \int_0^\infty G(k_0) I(k_0, \theta_{ext}) \, \mathrm{d}k_0 \tag{5.51}$$

and given by

$$I_{spec}(\theta_{ext}) = \frac{(1 - R_{dome}) n_{ext} E_0^2}{2Z_0 \cos\theta_{int}} \int_0^\infty G(k_0) \cos\theta_{ext} F(k_0, \theta_{int}) \, \mathrm{d}k_0, \tag{5.52}$$

assuming n_{ext} is non-dispersive. Like (5.37), integral (5.52) cannot be done analytically and must therefore be evaluated numerically.

5.5.3 Multiple quantum wells

Up to now this chapter has considered the case of a single quantum well active region, but real LEDs have many quantum wells. If each quantum well is assigned an index w, where $w = 1, 2...N_{QWs}$ and w increases along the z axis, each well has its own values of $d_{\pm}$ associated with it, denoted here as $d_{w\pm}$. However, the total cavity length d is self-evidently independent of the quantum well's position, as expressed by the equation

$$d_{w+} + d_{w-} = d \; \forall w. \tag{5.53}$$

The transmission coefficients τ for each quantum well are different. If all the quantum wells have the same absorbance A, the τ are given by

$$\tau = \frac{t_+ t_{QW}^{\chi} \mathrm{e}^{-\mathrm{i}\beta d_{w+}} (1 + r_- t_{QW}^{\upsilon} \mathrm{e}^{-2\mathrm{i}\beta d_{w-}})}{1 - r_+ r_- t_{QW}^{2N_{QWs}} \mathrm{e}^{-2\mathrm{i}\beta d}}, \tag{5.54}$$

where

$$\chi = N_{QWs} - w \quad \text{and} \quad \upsilon = N_{QWs} + w - 1. \tag{5.55}$$

As the different quantum wells are incoherent, the single-wavelength output intensity $I(k_0, \theta_{ext})$ of the MQW is given by

$$I(k_0, \theta_{ext}) = (1 - R_{dome}) \frac{n_{ext} \cos\theta_{ext}}{2 Z_0 \cos\theta_{int}} E_0^2 \sum_{w=1}^{N_{QWs}} F_w(k_0, \theta), \tag{5.56}$$

while the spectrum-integrated output intensity $I_{spec}(\theta_{ext})$ is given by

$$I_{spec}(\theta_{ext}) = \frac{(1 - R_{dome}) n_{ext} E_0^2}{2 Z_0 \cos\theta_{int}} \sum_{w=1}^{N_{QWs}} \int_0^{\infty} G(k_0) \cos\theta_{ext} F_w(k_0, \theta_{int}) \, \mathrm{d}k_0. \tag{5.57}$$

Note that F now depends on w. Note also that (5.57) does not distinguish components of different wavelengths, but for many applications this is not a problem, especially if $G(k_0)$ is strongly peaked.

5.5.4 Enhancement of the extracted power

The single-wavelength intensity $I(k_0, \theta_{ext})$ can be used to calculate the power P emitted into in a spherical cap-shaped area of the type depicted in Figure 5-2, where

$$\mathrm{d}A = r^2 \sin\theta_{ext}\,\mathrm{d}\theta_{ext}\,\mathrm{d}\phi. \tag{5.58}$$

The entire output power $P(k_0)$ can be found by integrating $I\,\mathrm{d}A$ over the entire hemisphere:

$$P(k_0) = \int_0^{\frac{\pi}{2}} I\,\mathrm{d}A = (1 - R_{dome})\frac{n_{ext}}{2Z_0}E_0^2 \sum_{w=1}^{N_{QWs}} \int_0^{\frac{\pi}{2}} \frac{\cos\theta_{ext}}{\cos\theta_{int}} F_w(k_0, \theta_{int}) \sin\theta_{ext}\,\mathrm{d}\theta_{ext}, \tag{5.59}$$

where $2\pi r^2 = 1$ as before. Likewise, the spectrum-integrated power $P_{spec}(\Theta)$ can be found by integrating $I_{spec}\,\mathrm{d}A$ over the same range:

$$\begin{aligned} P_{spec} &= \int_0^{\frac{\pi}{2}} I_{spec}\,\mathrm{d}A \\ P_{spec} &= (1 - R_{dome})\frac{n_{ext}}{4Z_0}E_0^2 \sum_{w=1}^{N_{QWs}} \int_0^{\infty} G(k_0) \int_0^{\frac{\pi}{2}} \frac{\sin 2\theta_{ext}}{\cos\theta_{int}} F_w(k_0, \theta_{int})\,\mathrm{d}\theta_{ext}\,\mathrm{d}k_0. \end{aligned} \tag{5.60}$$

As the analysis presented above covers only radiation modes and does not extend to guided modes (see section 4.7), the overall emission enhancement U cannot be evaluated by these methods alone. However, it is possible to define the single-wavelength enhancement $U'(k_0, \Theta)$ of the extracted power, by dividing $P(k_0)$ by the power that would be extracted from an incoherent cavity of the type considered in section 5.3:

$$U'(k_0, \Theta) = P(k_0, \Theta)\left[2S_0 \int_0^{\frac{\pi}{2}} (1 + \cos^2\theta_{int}) \sin\theta_{ext}\,\mathrm{d}\theta_{ext}\right]^{-1}. \tag{5.61}$$

Likewise, the spectrum-integrated enhancement $U'_{spec}(\Theta)$ is given by

$$U'_{spec} = P_{spec}\left[\frac{E_0^2}{Z_0}G_{spec} \int_0^{\frac{\pi}{2}} (1 + \cos^2\theta_{int}) \sin\theta_{ext}\,\mathrm{d}\theta_{ext}\right]^{-1}. \tag{5.62}$$

The above analysis does not explicitly account for any absorption outside of the quantum wells, although the equations remain valid if the values of the r and t coefficients imply that losses are present. Absorption inside the cavity must be neglected, however, as a complex value of n_{int} would require the emission angle θ to be complex as well; similarly, a complex value of n_{ext} would require θ_{ext} to be complex. However, this is

not a major concern as for any useful LED device n_{ext} would have to be transparent with a very small imaginary part. In addition, losses within the cavity (i.e. the GaN epilayer) are often negligible compared to losses due to the quantum wells or losses that can be implied in the value of the Fresnel coefficients; see, for example, Schad *et al.* (2004) and Miyajima *et al.* (2011).

5.6 Summary

This chapter provides a review of the literature around resonant cavities, introducing key concepts that will be crucial in later chapters. Sections 5.1 and 5.2 establish that all LEDs with smooth surfaces form resonant cavities and that emission from quantum wells can be and usually is modelled by considering a Gaussian distribution $G(k_0)$ of Hertzian dipoles with dipole moments oriented in the plane of the quantum well. Section 5.3 calculates the extration efficiency for a set of such dipoles inside a thick GaN slab, a benchmark that will be used in chapter 8. Section 5.4 extends the mathematics of Benisty *et al.* (1998) to provide an analytic formula for the single-wavelength angle-integrated emission enhancement U of a dipole near a perfect metallic reflector, while demonstrating the concept of spectrum-integrated enhancement with a numerical calculation, building on the methods of Schubert (2006, pp. 250). Section 5.5 draws together the analyses of Bjork *et al.* (1995), Benisty *et al.* (1998) and Delbeke *et al.* (2002) to provide a formulation of the resonant cavity problem that is both relevant to lighting applications and considers phase shifts caused by reflections, which is neglected by many authors on the subject (for example, Deppe *et al.* 1994 and Bjork *et al.* 1995).

Chapter 6

Modal methods

6.1 Introduction

This chapter forms the beginning of the core of this thesis: it describes optical modelling of cylindrical nanostructures using modal methods. This chapter provides an introduction to modal methods and presents cylindrical analogues of the plane waves discussed in section 4.4. The nanostructures themselves are discussed and analysed in the following chapters. The modal methods in this chapter and in the rest of the thesis draw heavily from Snyder and Love's textbook *Optical Waveguide Theory* (1983) due to the authors' rigorous treatment of cylindrical waveguides, particularly the radiation modes thereof. Page numbers have been included when citing specific sections of this textbook.

In linear, isotropic and homogeneous media with no charges or currents, the six Maxwell equations (4.1)-(4.6) can be combined to form the wave equations (4.21) and (4.22). Assuming harmonic time dependence of the type $\mathrm{e}^{-\mathrm{i}\omega t}$ (4.23), the wave equations become

$$\nabla^2 \vec{E} = -k_0^2 n^2 \vec{E} \tag{6.1}$$

$$\nabla^2 \vec{H} = -k_0^2 n^2 \vec{H}. \tag{6.2}$$

The general solution to the wave equations gives the electromagnetic fields for all space and time. As with any differential equation, the general solution must be a complete orthonormal set of functions. For unbounded homogeneous media, plane waves are sufficient to form a complete orthonormal set, though other such sets of functions are also suitable. For systems with interfaces between media, plane waves alone do not form a complete orthonormal set of functions and other solutions must therefore be

sought. For systems where all interfaces are parallel to a certain axis, denoted here as z, harmonic dependence in the z direction may still be assumed (Snyder and Love 1983 pp. 208-217, 516-517) and the total fields can be written in the form

$$\vec{E}(\vec{r}) = \sum_j C_j \hat{E}_j(\vec{r}_t) \mathrm{e}^{\mathrm{i}\beta_j z} + \sum \int c(\beta) \hat{e}(\vec{r}_t, \beta) \mathrm{e}^{\mathrm{i}\beta z} \, \mathrm{d}\beta \tag{6.3}$$

$$\vec{H}(\vec{r}) = \sum_j C_j \hat{H}_j(\vec{r}_t) \mathrm{e}^{\mathrm{i}\beta_j z} + \sum \int c(\beta) \hat{h}(\vec{r}_t, \beta) \mathrm{e}^{\mathrm{i}\beta z} \, \mathrm{d}\beta, \tag{6.4}$$

where the β_j, $\hat{E}_j(\vec{r}, t)$, $\hat{H}_j(\vec{r}, t)$ and c_j are the propagation constants of the guided modes, the β, $\hat{E}(\vec{r}, t, \beta)$, $\hat{H}(\vec{r}, t, \beta)$ and $c(\beta)$ are the propagation constants of the radiation modes and $\vec{r}_t = \hat{z} \times \vec{r} \times \hat{z}$ is the transverse position vector. The vector functions $\hat{E}_j$, $\hat{H}_j$, $\hat{e}$ and $\hat{h}$ inside the summation and integral are known as modes and have the defining characteristic of being completely invariant in both z and t, except for phase; the phase variation is governed by the propagation constant β. The total fields $\vec{E}(\vec{r}, t)$ and $\vec{H}(\vec{r}, t)$ are expressed as a superposition of both guided modes that have discrete β_j and radiation modes that occupy a continuum of β; the proportion of each mode is given by the expansion coefficients C_j and $c(\beta)$. The radiation modes have two distinct types: propagating modes have real β and carry real power, while evanescent modes have imaginary β and do not carry power, instead corresponding to stored energy. Note the use of uppercase letters for the guided modes and lowercase for the radiation modes. Note also that the modes are denoted as unit vectors. This does not signify that the field vectors have unit magnitude. Rather, it indicates that the modes have been normalized to carry unit power (Snyder and Love 1983 pp. 214).

6.2 Cylindrical polar coordinates

Both planar and cylindrical nanorod structures have cylindrical symmetry, making the cylindrical polar coordinate system convenient to work with. The three orthogonal coordinates ρ, ϕ and z are related to their rectangular Cartesian counterparts x, y and z as follows:

$$\rho = \sqrt{x^2 + y^2} \tag{6.5}$$

$$\phi = \tan^{-1}\left(\frac{y}{x}\right) \tag{6.6}$$

$$z = z. \tag{6.7}$$

Cylindrical polar coordinates are fundamentally different from Cartesian coordinates in that the direction of the unit vectors are not fixed as the Cartesian unit vectors are; the directions of $\hat{\rho}$ and $\hat{\phi}$ depend on ϕ, although $\hat{z}$ is still fixed. The unit vectors can be expressed in terms of their Cartesian counterparts as follows:

$$\hat{\rho} = \hat{x}\cos\phi + \hat{y}\sin\phi \tag{6.8}$$

$$\hat{\phi} = \hat{y}\cos\phi - \hat{x}\sin\phi \tag{6.9}$$

$$\hat{z} = \hat{z}. \tag{6.10}$$

Inspection of (6.8)-(6.10) shows that $\hat{\rho}\cdot\hat{\phi} = \hat{\rho}\cdot\hat{z} = \hat{\phi}\cdot\hat{z} = 0$, i.e. the three unit vectors opf the cylindrical coordinate system are orthogonal regardless of ϕ.

6.3 Cylindrical symmetry

Cylindrical symmetry can be formally defined in terms of cylindrical polar co-ordinates. An optical system is cylindrically symmetric if n is invariant in the ϕ direction, i.e. all interfaces are parallel to the ϕ axis. It can be shown from (6.1) and (6.2) that the z components of the electromagnetic fields satisfy (Snyder and Love 1983 pp. 249, 592)

$$\frac{\partial^2 E_z}{\partial\rho^2} + \frac{1}{\rho}\frac{\partial E_z}{\partial\rho} + \frac{1}{\rho^2}\frac{\partial^2 E_z}{\partial\phi^2} + \frac{\partial^2 E_z}{\partial z^2} = -k_0^2 n^2(\rho) E_z \tag{6.11}$$

$$\frac{\partial^2 H_z}{\partial\rho^2} + \frac{1}{\rho}\frac{\partial H_z}{\partial\rho} + \frac{1}{\rho^2}\frac{\partial^2 H_z}{\partial\phi^2} + \frac{\partial^2 H_z}{\partial z^2} = -k_0^2 n^2(\rho) H_z. \tag{6.12}$$

Substituting (6.3) and (6.4) gives the wave equations for individual modes:

$$\frac{\partial^2 \hat{E}_z}{\partial\rho^2} + \frac{1}{\rho}\frac{\partial \hat{E}_z}{\partial\rho} + \frac{1}{\rho^2}\frac{\partial^2 \hat{E}_z}{\partial\phi^2} + \kappa^2(\rho)\hat{E}_z = 0 \tag{6.13}$$

$$\frac{\partial^2 \hat{H}_z}{\partial\rho^2} + \frac{1}{\rho}\frac{\partial \hat{H}_z}{\partial\rho} + \frac{1}{\rho^2}\frac{\partial^2 \hat{H}_z}{\partial\phi^2} + \kappa^2(\rho)\hat{H}_z = 0, \tag{6.14}$$

where

$$\kappa(\rho) = \sqrt{k_0^2 n^2(\rho) - \beta^2} \tag{6.15}$$

in keeping with the notation of previous chapters, although κ is now allowed to vary with ρ for cases such as that of the cylindrical nanorod where there are interfaces perpendicular to the ρ axis. Assuming cylindrical symmetry as previously defined, (6.13) and (6.14) can be solved by setting

$$\hat{E}_z \sim f(N\phi) \quad \text{and} \quad \hat{H}_z \sim g(N\phi), \tag{6.16}$$

where N is a non-negative integer,

$$f(N\phi) = \begin{cases} \sin(N\phi) \\ \cos(N\phi) \end{cases} \quad \text{and} \quad g(N\phi) = \frac{\mathrm{d}f(N\phi)}{\mathrm{d}(N\phi)} = \begin{cases} \cos(N\phi) \\ -\sin(N\phi). \end{cases} \tag{6.17}$$

It should be noted that (6.13), (6.14) and (6.16) apply to guided modes, radiation modes and evenescent modes. It can be shown that in cylindrically symmetric systems the wavevector $\vec{k}$ has no ϕ component; there is only the z component β and the ρ component κ.

6.4 Orthonormality of modes

It can be shown (Snyder and Love 1983 pp. 214, 602-605) that the guided modes obey the orthonormality condition

$$\frac{1}{2}\int_0^{2\pi}\int_0^{\infty} \hat{E}_j(\rho,\phi) \times \hat{H}_k^*(\rho,\phi) \cdot \hat{z}\rho \,\mathrm{d}\rho \,\mathrm{d}\phi = \delta_{jk}, \tag{6.18}$$

where k is a dummy index and δjk is the Kronecker Delta:

$$\delta_{jk} = \begin{cases} 1 & j = k \\ 0 & j \neq k. \end{cases} \tag{6.19}$$

Another advantage of using the cylindrical polar coordinate system is that it provides a convenient way of normalizing the radiation modes in terms of κ as $\rho \to \infty$:

$$\kappa_\infty = \lim_{\rho\to\infty}\left(\sqrt{k_0^2 n^2(\rho) - \beta^2}\right). \tag{6.20}$$

This expression is useful because it allows both the propagating (real β) and evanescent (imaginary β) radiation modes to be included as part of a single integral over κ_∞:

$$\vec{E}(\vec{r}) = \sum_j C_j \hat{E}_j(\rho,\phi)\mathrm{e}^{\mathrm{i}\beta_j z} + \sum \int_0^{\infty} c(\kappa_\infty)\hat{e}(\rho,\phi,\kappa_\infty)\mathrm{e}^{\mathrm{i}\beta z}\,\mathrm{d}\kappa_\infty \tag{6.21}$$

$$\vec{H}(\vec{r}) = \sum_j C_j \hat{H}_j(\rho,\phi)\mathrm{e}^{\mathrm{i}\beta_j z} + \sum \int_0^{\infty} c(\kappa_\infty)\hat{h}(\rho,\phi,\kappa_\infty)\mathrm{e}^{\mathrm{i}\beta z}\,\mathrm{d}\kappa_\infty. \tag{6.22}$$

The summation before the integral sign extends over all possible N, the two choices of $f(N\phi)$ and two different polarizations. The orthonormality condition for the radiation modes can now be defined: it is similar to that for the guided modes but is defined in

terms of the Dirac delta function (Snyder and Love 1983 pp. 518, 602-606):

$$\frac{1}{2}\int_0^{2\pi}\int_0^{\infty}\hat{E}(\rho,\phi,\kappa_\infty)\times\hat{H}^*(\rho,\phi,\kappa'_\infty)\cdot\hat{z}\rho\,\mathrm{d}\rho\,\mathrm{d}\phi=\delta(\kappa_\infty-\kappa'_\infty), \tag{6.23}$$

where κ'_∞ is a dummy variable. The presence of the Dirac delta function places emphasis on the fact that radiation modes, unlike guided modes, do not represent anything physical unless they are within an integral.

6.5 Excitation of modes by a Hertzian dipole

In an LED, the various modes j are excited by a current of areal density $\vec{J}$ to varying extents, as quantified by the expansion coefficients C_j (Snyder and Love 1983 pp. 444, 520):

$$C_j=-\tfrac{1}{4}\int\int\int_V\hat{E}_j^*(\rho,\phi)\cdot\vec{J}\mathrm{e}^{-\mathrm{i}\beta_j z}\,\mathrm{d}V, \tag{6.24}$$

where V is the volume occupied by $\vec{J}$. Equation (6.24) is a general formula that applies to both guided and radiation modes and any type of $\vec{J}$. However, it can be simplified considerably by modelling each event of photon emission from the quantum well as a Hertzian dipole (Snyder and Love 1983 pp. 445):

$$\vec{J}=\vec{j}\frac{\delta(\rho-\rho_D)}{\rho}\delta(\phi-\phi_D)\delta(z)\mathrm{e}^{-\mathrm{i}\omega t}, \tag{6.25}$$

where ρ_D and ϕ_D are the respective ρ and ϕ coordinates of the dipole and the quantum well is assumed to be located at $z=0$. For emission from a quantum well it can be assumed that the dipole moment is in the plane of the well (Bjork *et al.* 1995), i.e.

$$\vec{j}=|\vec{j}|(\hat{\rho}\cos\Phi+\hat{\phi}\sin\Phi), \tag{6.26}$$

where Φ is the angle between $\vec{j}$ and $\hat{\rho}$. Substituting (6.25) and (6.26) into (6.24) yields the much simpler expression

$$C_j=-\tfrac{1}{4}\vec{E}_j^*(\rho_D,\phi_D)\cdot\vec{j}\mathrm{e}^{-\mathrm{i}\omega t}=-\tfrac{1}{4}|\vec{j}|\left[\vec{E}_{\rho j}^*(\rho_D,\phi_D)\cos\Phi+\vec{E}_{\phi j}^*(\rho_D,\phi_D)\sin\Phi\right]\mathrm{e}^{-\mathrm{i}\omega t}. \tag{6.27}$$

The physical origin of the previously assumed $\mathrm{e}^{-\mathrm{i}\omega t}$ dependence is now revealed to be the Hertzian dipole emitter. It should be reiterated that (6.27) applies to both guided and radiation modes. For guided modes, the power P_j emitted into mode j is given by the square magnitude of C_j:

$$P_j=|C_j|^2. \tag{6.28}$$

For radiation modes, the power of a single mode is physically meaningless and an integral over a range of the continuum is required:

$$P(\kappa_\infty) = \int |c(\kappa_\infty)|^2 \, \mathrm{d}\kappa_\infty. \tag{6.29}$$

For propagating radiation modes ($0 \leq \kappa_\infty \leq k_0 n_\infty$), where n_∞ is the refractive index as ρ_∞, it can be shown (see section 6.8) that the power in the mode is observed in the far field at an angle θ to the z axis. Using

$$\kappa_\infty = k_0 n_\infty \sin\theta \quad \text{and} \quad \beta = k_0 n_\infty \cos\theta, \tag{6.30}$$

the far field angular emission pattern is given by making a change of variables in (6.29) and summing over all possible N, both choices of $f(N\phi)$ and both polarizations:

$$P(\theta) = \sum \int |c(\theta)|^2 \beta(\theta) \, \mathrm{d}\theta. \tag{6.31}$$

Calculating the intensity $I(\theta)$ is possible but not as straightforward as for plane waves, so it is often simpler in practice to take the integral (6.31) over a finite range $\delta\theta = \theta_2 - \theta_1$ and divide by the area of the spherical cap section defined by $\delta\theta$ as shown in Figure 6-1:

$$I(\theta_1, \theta_2) = \frac{\sum \int_{\theta_1}^{\theta_2} |c(\theta)|^2 \beta(\theta) \, \mathrm{d}\theta}{2\pi r^2 \int_{\theta_1}^{\theta_2} \sin\theta \, \mathrm{d}\theta}, \tag{6.32}$$

where the hemisphere radius r is an arbitrary constant and can be set to unity without loss of generality. It should be noted that each value of κ_∞ within the range $0 \leq \kappa_\infty \leq$

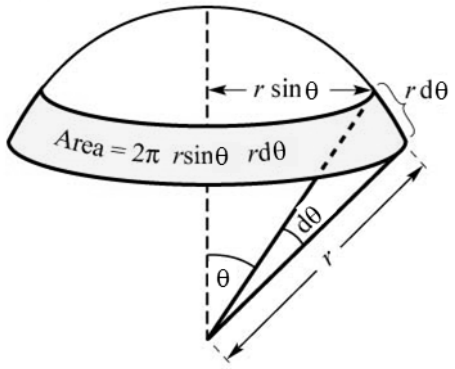

Figure 6-1: Section of a hemisphere defined by angular range dθ. © E. Fred Schubert (2006), published by Cambridge University Press, adapted with permission.

$k_0 n_\infty$ corresponds to two different values of θ:

$$\theta_\pm = \frac{\pi}{2} \mp \arcsin\left(\frac{\kappa_\infty}{k_0 n_\infty}\right). \tag{6.33}$$

Assuming the distribution of dipoles is also cylindrically symmetric, i.e. for every dipole with coordinates (ρ_D,ϕ_D,0) there is another dipole of equal $|\vec{j}|$ and Φ with coordinates (ρ_D,$\phi_D \pm \pi$,0), the far field distribution is also cylindrically symmetric, varying only in θ and not ϕ.

6.6 Radiation modes of a homogeneous medium

An unbounded homogenous medium has no guided modes. Also, n and therefore κ are the same everywhere, so $\kappa_\infty = \kappa$. Equations (6.21) and (6.22) therefore become

$$\vec{E}(\vec{r}) = \sum \int_0^\infty c(\kappa)\hat{e}(\rho,\phi,\kappa)\mathrm{e}^{\mathrm{i}\beta z}\,\mathrm{d}\kappa_\infty \tag{6.34}$$

$$\vec{H}(\vec{r}) = \sum \int_0^\infty c(\kappa)\hat{h}(\rho,\phi,\kappa)\mathrm{e}^{\mathrm{i}\beta z}\,\mathrm{d}\kappa_\infty. \tag{6.35}$$

In Cartesian rectangular coordinates, the radiation modes of an unbounded homogenous medium take the form of plane waves. In cylindrical polar coordinates, they are defined in terms of the Bessel function J_N of the first kind of order N, where N is the same non-negative integer that governs the azimuthal variation $f(N\phi)$ and $g(N\phi)$ (6.16). The exact form of the modes is given by Table 6.1, where

$$\Xi_{0N} = \begin{cases} \frac{1}{\sqrt{2}} & N = 0 \\ 1 & N \neq 0. \end{cases} \tag{6.36}$$

Note that, as with plane waves, the modes are divided into those of TE polarization ($E_z = 0$) and TM polarization ($H_z = 0$). The asymptotic form of J_N for large arguments is

$$\lim_{x\to\infty}[J_N(x)] = \sqrt{\frac{2}{\pi x}}\cos[\mathrm{i}(x - N\tfrac{\pi}{2} - \tfrac{\pi}{4})]. \tag{6.37}$$

Equation (6.37) allows for the derivation of an orthonormality relation for $J_N(\kappa\rho)$ (Arfken and Weber 2005):

$$\int_0^\infty J_N(\kappa\rho)J_M(\kappa'\rho)\rho\,\mathrm{d}\rho = \frac{\delta_{NM}\delta(\kappa-\kappa')}{\kappa}, \tag{6.38}$$

	TE modes	TM modes
$\hat{e}\cdot\hat{z}$	0	$-\mathrm{i}AJ_N(\kappa\rho)f(N\phi)$
$\hat{h}\cdot\hat{z}$	$-\mathrm{i}AJ_N(\kappa\rho)g(N\phi)$	0
$\hat{e}\cdot\hat{\rho}$	$-A\frac{Nk_0Z_0}{\kappa^2}\frac{J_N(\kappa\rho)}{\rho}f(N\phi)$	$A\frac{\beta}{\kappa^2}\frac{\mathrm{d}J_N(\kappa\rho)}{\mathrm{d}\rho}f(N\phi)$
$\hat{h}\cdot\hat{\rho}$	$A\frac{\beta}{\kappa^2}\frac{\mathrm{d}J_N(\kappa\rho)}{\mathrm{d}\rho}g(N\phi)$	$-A\frac{Nk_0n^2}{Z_0\kappa^2}\frac{J_N(\kappa\rho)}{\rho}g(N\phi)$
$\hat{e}\cdot\hat{\phi}$	$-A\frac{k_0Z_0}{\kappa^2}\frac{\mathrm{d}J_N(\kappa\rho)}{\mathrm{d}\rho}g(N\phi)$	$A\frac{N\beta}{\kappa^2}\frac{J_N(\kappa\rho)}{\rho}g(N\phi)$
$\hat{h}\cdot\hat{\phi}$	$-A\frac{N\beta}{\kappa^2}\frac{J_N(\kappa\rho)}{\rho}f(N\phi)$	$A\frac{k_0n^2}{Z_0\kappa^2}\frac{\mathrm{d}J_N(\kappa\rho)}{\mathrm{d}\rho}f(N\phi)$
A	$\Xi_{0N}\kappa\sqrt{\frac{2\kappa}{\pi k_0Z_0\beta}}$	$\Xi_{0N}\frac{\kappa}{n}\sqrt{\frac{2m_{0N}Z_0\kappa}{\pi k_0\beta}}$

Table 6.1: Electromagnetic field components of the radiation modes of a homogeneous medium (Snyder and Love 1983 pp. 522).

where δ_{NM} is the Kronecker delta and $\delta(\kappa-\kappa')$ is the Dirac delta. If a single Hertzian dipole is placed at the coordinate origin ($\rho=0$) and pointing in the ρ direction ($\Phi=0$), the excitation of the TE modes is determined by the value of $\hat{e}_\rho$ at that point:

$$\hat{e}_\rho(\rho=0)=\begin{cases}-\sqrt{\frac{k_0Z_0\kappa}{2\pi\beta}} & N=1\\ 0 & N\neq 1,\end{cases} \tag{6.39}$$

i.e. only $N=1$ modes are excited. Substituting (6.39) into (6.27) gives

$$c_{TE}(\kappa)=\frac{1}{4}\sqrt{\frac{k_0Z_0\kappa}{2\pi\beta}}\mathrm{e}^{-\mathrm{i}\omega t}. \tag{6.40}$$

The TE far-field power distribution $p_{TE}(\theta_1,\theta_2)$ is found by substituting (6.40) into (6.31):

$$p_{TE}(\theta_1,\theta_2)=\int_{\theta_1}^{\theta_2}|c_{TE}(\theta)|^2\beta(\theta)\,\mathrm{d}\theta=\left[-\frac{k_0^2nZ_0}{32\pi}\cos\theta\right]_{\theta_1}^{\theta_2}. \tag{6.41}$$

The TM far-field power distribution $p_{TM}(\theta_1,\theta_2)$ is found by applying the same procedure to TM modes:

$$p_{TM}(\theta_1,\theta_2)=\int_{\theta_1}^{\theta_2}|c_{TM}(\theta)|^2\beta(\theta)\,\mathrm{d}\theta=\left[-\frac{k_0^2nZ_0}{96\pi}\cos^3\theta\right]_{\theta_1}^{\theta_2}. \tag{6.42}$$

Equations (6.41) and (6.42) match the results given in Bjork *et al.* (1995) and Delbeke *et al.* (2002), although their results are given in terms of the Poynting vector intensity $|\vec{S}|$ so (4.33) must be used to find the power. The total radiated power P_{TE} of TE polarization is found by integrating over the range of propagating modes:

$$P_{TE} = 2\int_0^{\frac{\pi}{2}} |c_{TE}(\theta)|^2 \beta(\theta)\,\mathrm{d}\theta = \frac{k_0^2 n Z_0}{16\pi}, \tag{6.43}$$

where the factor of 2 accounts for emission in both the $+z$ and $-z$ directions. The total radiated power P_{TM} of TM polarization is found likewise:

$$P_{TM} = 2\int_0^{\frac{\pi}{2}} |c_{TM}(\theta)|^2 \beta(\theta)\,\mathrm{d}\theta = \frac{k_0^2 n Z_0}{48\pi}. \tag{6.44}$$

The total power P_{total} is given by adding the two polarizations:

$$P_{total} = P_{TE} + P_{TM} = \frac{k_0^2 n Z_0}{12\pi}, \tag{6.45}$$

which is identical to the standard textbook result (Sadiku 2007 pp. 635). The ability of the modal expansion principle to reproduce standard results found in the literature provides a degree of validation. The rest of this thesis focuses on applying the modal expansion principle to more complex problems.

6.7 Cylindrical radiation modes and Fresnel's equations

It is shown here that the radiation modes satisfy Fresnel's equations, as just plane waves do. This allows planar interfaces (i.e. interfaces perpendicular to the z axis) to be treated rigorously in a system with cylindrical symmetry.

Consider a single planar interface between two semi-infinite homogeneous media as depicted in Figure 6-2; the space where $z < 0$ is occupied by a medium of refractive index n_1 while the space where $z > 0$ is occupied by a medium of index n_2. Conservation of the wavevector requires that

$$\kappa_i = \sqrt{k_0^2 n_1^2 - \beta_i^2}, \quad \kappa_r = \sqrt{k_0^2 n_1^2 - \beta_r^2}, \quad \text{and} \quad \kappa_t = \sqrt{k_0^2 n_2^2 - \beta_t^2}. \tag{6.46}$$

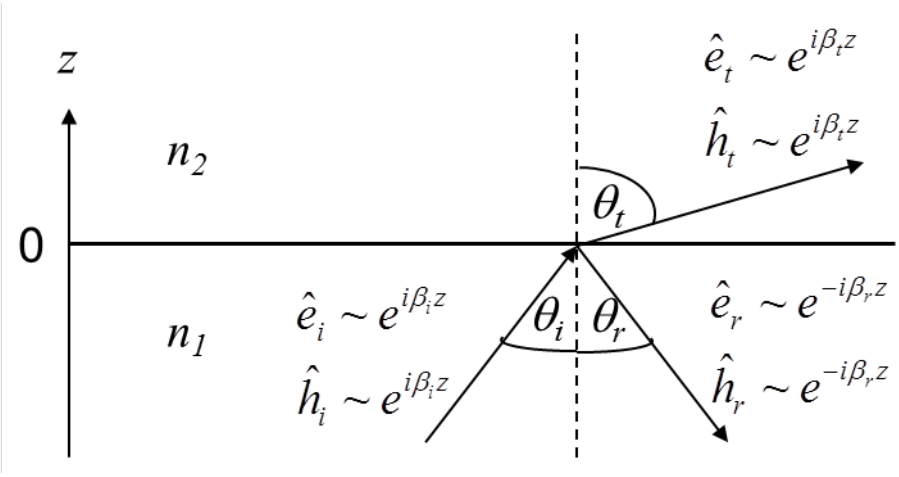

Figure 6-2: Reflection and refraction of a radiation mode at a planar interface. The phase of the backward-propagating reflected mode r varies as $\mathrm{e}^{-\mathrm{i}\beta_r z}$ while those of the forward-propagating incident mode i and transmitted mode t vary as $\mathrm{e}^{+\mathrm{i}\beta_i z}$ and $\mathrm{e}^{+\mathrm{i}\beta_t z}$ respectively.

The κ and β are related to the angle θ between $\vec{k}$ and the surface normal vector $\hat{z}$ as follows:

$$\beta_i = k_0 n_1 \cos\theta_i, \quad \beta_r = k_0 n_1 \cos\theta_r, \quad \beta_t = k_0 n_2 \cos\theta_t, \tag{6.47}$$

$$\kappa_i = k_0 n_1 \sin\theta_i, \quad \kappa_r = k_0 n_1 \sin\theta_r \quad \text{and} \quad \kappa_t = k_0 n_2 \sin\theta_t. \tag{6.48}$$

If a set of radiation modes originates from $z \to \infty$ and is incident upon the interface, the electromagnetic fields in each medium take the following form:

$$\vec{E}_1(\vec{r},t) = \mathrm{e}^{-\mathrm{i}\omega t} \sum \int_0^\infty c_i(\kappa_i)\hat{e}_i(\rho,\phi,\kappa_i)\mathrm{e}^{\mathrm{i}\beta_i z}\,\mathrm{d}\kappa_i + \sum \int_0^\infty c_r(\kappa_r)\hat{e}_r(\rho,\phi,\kappa_r)\mathrm{e}^{-\mathrm{i}\beta_r z}\,\mathrm{d}\kappa_r \tag{6.49}$$

$$\vec{H}_1(\vec{r},t) = \mathrm{e}^{-\mathrm{i}\omega t} \sum \int_0^\infty c_i(\kappa_i)\hat{h}_i(\rho,\phi,\kappa_i)\mathrm{e}^{\mathrm{i}\beta_i z}\,\mathrm{d}\kappa_i + \sum \int_0^\infty c_r(\kappa_r)\hat{h}_r(\rho,\phi,\kappa_r)\mathrm{e}^{-\mathrm{i}\beta_r z}\,\mathrm{d}\kappa_r \tag{6.50}$$

$$\vec{E}_2(\vec{r},t) = \mathrm{e}^{-\mathrm{i}\omega t} \sum c_t(\kappa_t)\hat{e}_t(\rho,\phi,\kappa_t)\mathrm{e}^{\mathrm{i}\beta_t z}\,\mathrm{d}\kappa_t \tag{6.51}$$

$$\vec{H}_2(\vec{r},t) = \mathrm{e}^{-\mathrm{i}\omega t} \sum c_t(\kappa_t)\hat{h}_t(\rho,\phi,\kappa_t)\mathrm{e}^{\mathrm{i}\beta_t z}\,\mathrm{d}\kappa_t, \tag{6.52}$$

where $c_i(\kappa_1)$, $\hat{e}_i(\rho,\phi,\kappa_1)$ and $\hat{h}_i(\rho,\phi,\kappa_1)$ are the respective expansion coefficient, electric fields and magnetic fields of the radiation modes incident upon the interface, $c_r(\kappa_1)$, $\hat{e}_r(\rho,\phi,\kappa_1)$ and $\hat{h}_r(\rho,\phi,\kappa_1)$ are the expansion coefficients, electric fields and magnetic fields of the radiation modes reflected from the interface and $c_t(\kappa_2)$, $\hat{e}_t(\rho,\phi,\kappa_2)$ and

$\hat{h}_t(\rho, \phi, \kappa_2)$ are the expansion coefficients, electric fields and magnetic fields of the radiation modes transmitted through the interface. These radiation modes take the same form as those in Table 6.1. For the incident and transmitted modes, the + branch is taken and n_+ becomes n_1 for incident modes or n_2 for transmitted modes; for the reflected modes the − branch is taken and n_- is replaced with n_1. At $z = 0$ the tangential components of the total electric and magnetic fields must match:

$$\sum \int_0^\infty c_i \hat{e}_i \times \hat{z} \, \mathrm{d}\kappa_i + \sum \int_0^\infty c_r \hat{e}_r \times \hat{z} \, \mathrm{d}\kappa_r = \sum c_t \hat{e}_t \times \hat{z} \, \mathrm{d}\kappa_t \tag{6.53}$$

$$\sum \int_0^\infty c_i \hat{h}_i \times \hat{z} \, \mathrm{d}\kappa_i + \sum \int_0^\infty c_r \hat{h}_r \times \hat{z} \, \mathrm{d}\kappa_r = \sum c_t \hat{h}_t \times \hat{z} \, \mathrm{d}\kappa_t. \tag{6.54}$$

Taking the vector product of (6.53) with $(\hat{h}_i^* \times \hat{z})$ and performing an area integral over the interface at $z = 0$, taking the vector product of (6.54) with $(\hat{e}_i^* \times \hat{z})$ and likewise integrating and utilising (6.38) yields two different sets of equations for TE and TM modes, which can be rearranged to give the Fresnel equations. The process of doing this yields a much more fundamental result, however, namely that the incident, reflected and transmitted modes are orthogonal to one another except when all three share the same value of κ:

$$\kappa = \kappa_i = \kappa_r = \kappa_t \tag{6.55}$$

Substituting (6.48) into (6.55) yields both the law of reflection

$$\theta_i = \theta_r \tag{6.56}$$

and Snells law

$$n_1 \sin \theta_i = n_2 \sin \theta_t. \tag{6.57}$$

What this also means is that for every value of κ, N, the TE and TM polarization states and each choice of azimuthal variation $f(N\phi)$ can and indeed must be considered separately. For TE modes, the result of this orthogonalization process is

$$c_i(\kappa) + c_r(\kappa) = c_t(\kappa) \sqrt{\frac{\beta_i}{\beta_t}} \tag{6.58}$$

$$c_i(\kappa) - c_r(\kappa) = c_t(\kappa) \sqrt{\frac{\beta_t}{\beta_i}}, \tag{6.59}$$

which can be rearranged to give the Fresnel equations for TE modes:

$$\frac{c_t}{c_i} = \frac{2\sqrt{\beta_i\beta_t}}{\beta_i+\beta_t} = t\sqrt{\frac{\beta_t}{\beta_i}} = \sqrt{T} \tag{6.60}$$

$$\frac{c_r}{c_i} = \frac{\beta_i-\beta_t}{\beta_i+\beta_t} = r = \sqrt{R}, \tag{6.61}$$

where r and t are the Fresnel reflection and transmission coefficients of each radiation mode and R and T are the corresponding reflectivity and transmittivity numbers that give the fraction of power in each radiation mode that is reflected and transmitted. The equivalent equations for TM modes are

$$c_i(\kappa) + c_r(\kappa) = c_t(\kappa)\frac{n_1}{n_2}\sqrt{\frac{\beta_t(\kappa)}{\beta_i(\kappa)}} \tag{6.62}$$

$$c_i(\kappa) - c_r(\kappa) = c_t(\kappa)\frac{n_2}{n_1}\sqrt{\frac{\beta_i(\kappa)}{\beta_t(\kappa)}} \tag{6.63}$$

$$\frac{c_t}{c_i} = \frac{2n_1n_2\sqrt{\beta_i\beta_t}}{n_1^2\beta_t+n_2^2\beta_i} = t\sqrt{\frac{\beta_t}{\beta_i}} = \sqrt{T} \tag{6.64}$$

$$\frac{c_r}{c_i} = \frac{n_1^2\beta_t-n_2^2\beta_i}{n_1^2\beta_t+n_2^2\beta_i} = r = \sqrt{R}. \tag{6.65}$$

It is worth noting that the Fresnel coefficients do not depend on N or $f(N\phi)$ in any way. The total power P transmitted across the interface at $z=0$ is given by

$$P = \tfrac{1}{2}\int_0^{2\pi}\int_0^{\infty} \vec{E}(\rho,\phi,z=0,t)\times\vec{H}^*(\rho,\phi,z=0,t)\cdot\hat{z}\rho\,\mathrm{d}\rho\,\mathrm{d}\phi \tag{6.66}$$

$$P = \sum\int_0^{\infty}|c_t(\kappa)|^2\,\mathrm{d}\kappa = \sum\int_0^{\infty}(|c_i(\kappa)|^2-|c_r(\kappa)|^2)\,\mathrm{d}\kappa, \tag{6.67}$$

as expected.

6.8 Far field Poynting vector

There is a difficulty with the Bessel function modes described in the previous section, however: the time-averaged Poynting vector lies in the z direction only, regardless of θ. This can be resolved by replacing the J_N in Table 6.1 with Hankel functions $H_N^{(1)}(\kappa\rho)$ of the first kind of order N:

$$H_N^{(1)}(x) = J_N(x) + \mathrm{i}Y_N(x), \tag{6.68}$$

where Y_N is the Bessel function of the second kind, also referred to as the Neumann function. The asymptotic form of $H_N^{(1)}$ for large arguments is

$$\lim_{x\to\infty}[H_N^{(1)}(x)] = \sqrt{\frac{2}{\pi x}}\exp[\mathrm{i}(x - N\tfrac{\pi}{2} - \tfrac{\pi}{4})], \tag{6.69}$$

i.e. Hankel functions behave like plane waves propagating in the ρ direction in the limit where $\rho \to \infty$. The electromagnetic fields of the orthonormal radiation modes based on Hankel functions are denoted $\tilde{e}$ and $\tilde{h}$ and given in Table 6.2. Using (6.69), it

	TE modes	TM modes
$\tilde{e}\cdot\hat{z}$	0	$-\mathrm{i}AH_N^{(1)}(\kappa\rho)f(N\phi)$
$\tilde{h}\cdot\hat{z}$	$-\mathrm{i}AH_N^{(1)}(\kappa\rho)g(N\phi)$	0
$\tilde{e}\cdot\hat{\rho}$	$-A\frac{Nk_0Z_0}{\kappa^2}\frac{H_N^{(1)}(\kappa\rho)}{\rho}f(N\phi)$	$A\frac{\beta}{\kappa^2}\frac{\mathrm{d}H_N^{(1)}(\kappa\rho)}{\mathrm{d}\rho}f(N\phi)$
$\tilde{h}\cdot\hat{\rho}$	$A\frac{\beta}{\kappa^2}\frac{\mathrm{d}H_N^{(1)}(\kappa\rho)}{\mathrm{d}\rho}g(N\phi)$	$-A\frac{Nk_0n^2}{Z_0\kappa^2}\frac{H_N^{(1)}(\kappa\rho)}{\rho}g(N\phi)$
$\tilde{e}\cdot\hat{\phi}$	$-A\frac{k_0Z_0}{\kappa^2}\frac{\mathrm{d}H_N^{(1)}(\kappa\rho)}{\mathrm{d}\rho}g(N\phi)$	$A\frac{N\beta}{\kappa^2}\frac{H_N^{(1)}(\kappa\rho)}{\rho}g(N\phi)$
$\tilde{h}\cdot\hat{\phi}$	$-A\frac{N\beta}{\kappa^2}\frac{H_N^{(1)}(\kappa\rho)}{\rho}f(N\phi)$	$A\frac{k_0n^2}{Z_0\kappa^2}\frac{\mathrm{d}H_N^{(1)}(\kappa\rho)}{\mathrm{d}\rho}f(N\phi)$
A	$\Xi_{0N}\kappa\sqrt{\frac{2\kappa}{\pi k_0Z_0\beta}}$	$\Xi_{0N}\frac{\kappa}{n}\sqrt{\frac{2Z_0\kappa}{\pi k_0\beta}}$

Table 6.2: Electromagnetic field components of the radiation modes of a homogeneous medium based on Hankel functions instead of Bessel functions (Snyder and Love 1983 pp. 522).

can be shown that radiation modes described in Table 6.2 have time-averaged Poynting vectors parallel to their wavevectors, like plane waves but unlike Bessel function modes. However, there is also a problem with modes based on Hankel functions: $Y_N(x)$ has a singularity as $x = 0$, which makes Hankel functions very difficult to work with. For one thing, the singularity prevents the Hankel function modes from being normalized in the usual way, so another method must be used.

Consider a planar interface similar to that in Figure 6-2, replacing $\hat{e}_t$ and $\hat{h}_t$ with

$\tilde{e}$ and $\tilde{h}$ and setting $n_1 = n_2 = n$. Under these conditions, (6.53) and (6.54) become

$$\sum \int_0^\infty c_i \hat{e}_i \times \hat{z}\, \mathrm{d}\kappa + \sum \int_0^\infty c_r \hat{e}_r \times \hat{z}\, \mathrm{d}\kappa = \sum \tilde{c}\tilde{e} \times \hat{z}\, \mathrm{d}\kappa \tag{6.70}$$

$$\sum \int_0^\infty c_i \hat{h}_i \times \hat{z}\, \mathrm{d}\kappa + \sum \int_0^\infty c_r \hat{h}_r \times \hat{z}\, \mathrm{d}\kappa = \sum \tilde{c}\tilde{h} \times \hat{z}\, \mathrm{d}\kappa. \tag{6.71}$$

Taking the vector product of (6.70) with $(\hat{h}_i^* \times \hat{z})$ and performing an area integral over the interface at $z = 0$, taking the vector product of (6.71) with $(\hat{e}_i^* \times \hat{z})$ and likewise integrating results in the same pair of equations for TE and TM modes:

$$c_i + c_r = \tilde{c} \tag{6.72}$$

$$c_i - c_r = \tilde{c}. \tag{6.73}$$

Rearranging yields

$$c_i = \tilde{c} \quad \text{and} \quad c_r = 0. \tag{6.74}$$

Equation (6.74) shows that power is conserved across the interface and therefore the Hankel function radiation modes are already normalized correctly. The main significance of this result, however, is that it allows the far field due to radiation modes based on Bessel functions to be calculated by using a fictitious interface to convert them to modes based on Hankel functions, as has just been done.

6.9 Summary

In this chapter, the theory of optical modes presented by Snyder and Love (1983) is presented, along with proofs, derived as part of this research, that the radiation modes of homogeneous media obey the Fresnel equations, carry power in the direction of the wavevector and can be used to reproduce the well-documented result for a Hertzian dipole in free space. This is done by using two different formulations of the these modes: one uses the Bessel function J_N and is denotes by $\hat{e}$ and $\hat{h}$, while the other uses the Hankel function $H_N^{(1)}$ and is denoted by $\tilde{e}$ and $\tilde{h}$. Both of these sets of modes are required for a rigorous mathematical understanding of the finite length nanorods discussed in chapters 9 and 10. The more basic modal theory, presented in sections 6.1-6.5, is sufficient to understand the infinitely long nanorod structure discussed in chapter 8. However, a literature review and qualitiative discussion of nanorod LEDs is required prior to detailed quantitative analysis. Such a qualitative discussion is presented in the next chapter.

Chapter 7

Nanorod emitters

7.1 Introduction

A promising path towards low-cost efficient LEDs lies in arrays of GaN nanorod emitters fabricated by self-assembly (Kim *et al.* 2004, Bavencove *et al.* 2011), catalytic growth (Fan *et al.* 2006, Li and Wang 2008), uncontrolled etching (Lee *et al.* 2009, Bai *et al.* 2012) and controlled etching (Li *et al.* 2011, Bae *et al.* 2013, Zhuang *et al.* 2013a). These have been the subject of significant research over the last decade. This chapter provides an explanation of what nanorod LEDs are, a literature review of the various methods for fabricating them and a discussion of the motivations for researching them.

Nanorod emitters are cylinders of GaN with typical lengths ranging between 400 nm and 2 μm and typical diameters ranging between 50 and 600 nm, with InGaN quantum wells located within the nanorod as depicted in figure 7-1.

7.2 Fabrication

The literature contains many different methods of nanorod fabrication, the precise details of which are generally unique to each research group. However, the methods can be grouped into four general types, which are reviewed by Li and Waag (2012).

7.2.1 Self-assembly

Self-assembled GaN nanorod LEDs have been grown on both sapphire (Kim *et al.* 2004) and silicon (Bavencove *et al.* 2011) substrates and were the first type to be reported. These are grown in a different manner to planar semiconductor layers. Instead of

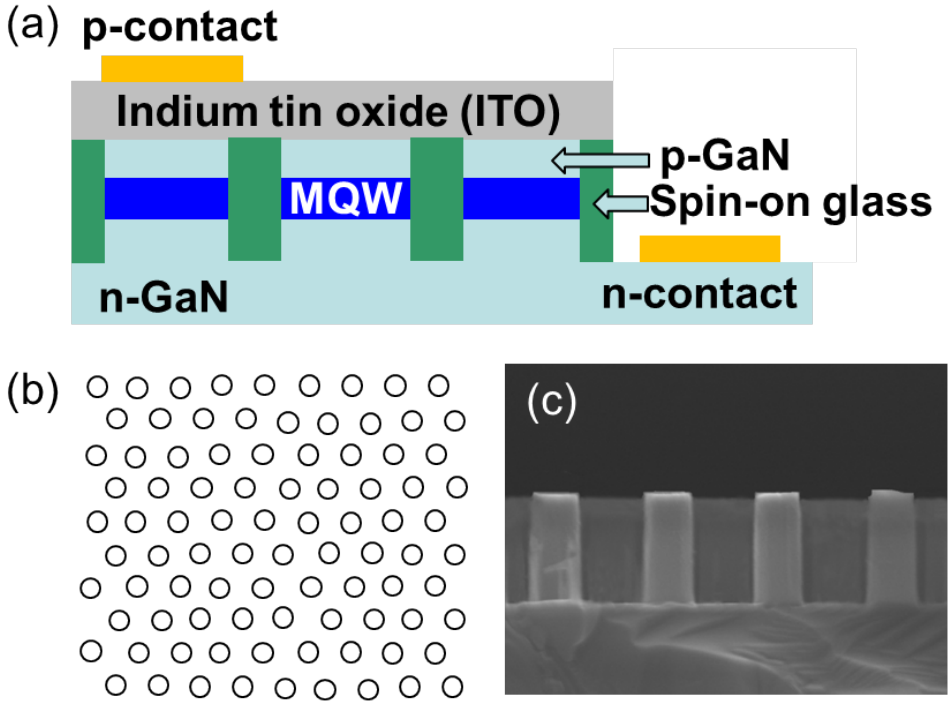

Figure 7-1: (a) Schematic diagram of a laterally-contacted nanorod array LED from the side. (b) Schematic of the array from above. A hexagonal pattern is usually preferred for nanorod arrays created by controlled etching, while those created by self-assembly tend to be randomly positioned. (c) Scanning electron microscope image of a nanorod array before ITO transparent contact deposition. (Zhuang *et al.* 2013b)

growing an entire layer on the substrate using a catalyst, nanometre-sized seeds are grown more slowly on the subtrate without a catalyst; the nanorods are then grown on the seeds. The resulting nanorods are completely free of dislocations but have random positions and sizes.

7.2.2 Catalytic growth

This method works by spreading metal droplets across the substrate; the droplets are used as a catalyst for nanorod growth. GaN forms on the metal surface before diffusing downwards, causing a nanorod to grow beneath the catalyst, lifting up the metal droplet as it grows (Li and Wang 2008). Like self-assembled nanorods, these nanorods are randomly distributed, unless the position and size of the metal droplets is controlled. Fan *et al.* (2006) provide a detailed review.

7.2.3 Uncontrolled etching

Uncontrolled etching techniques take a planar LED wafer and self-assembling an etch mask (usually Ni dots) on top of the wafer (Lee *et al.* 2009, Bai *et al.* 2012). Once the etch mask is in place, an inductively coupled plasma (ICP) is used to each past the MQW region, exposing GaN facets that can be further etched by hot KOH until only the nanorods and a planar n-type GaN layer remain. As the etch mask is self-assembled, the Ni dots have random positions and sizes, resulting in the nanorods being similar to those grown by self-assembly.

7.2.4 Controlled etching

Controlled etching is similar to uncontrolled etching except that the etch mask, usually either Ni or SiO_2, is much more ordered, resulting in highly ordered nanorod arrays (in most cases the arrays have hexagonal symmetry) where each nanorod is the same size. The fabrication of such ordered etch masks is usually accomplished by nano-imprint lithography (Bae *et al.* 2013, Zhuang *et al.* 2013a) although Langmuir-Blodgett techniques have also been reported (Li *et al.* 2011).

7.3 Advantages of nanorod array LEDs

- The use of nanorods greatly diminishes the total internal reflection problem associated with planar structures, increasing the extraction efficiency (see chapter 8).
- Photonic crystal diffraction effects can further increase the extraction efficiency (David *et al.* 2007, Wierer *et al.* 2009), Zhuang *et al.* 2013a).
- Nanorods form three-dimensional optical cavities with which the Purcell effect (Purcell 1946) can be exploited (Xu *et al.* 2007).
- The small size of nanorods means that the vast majority of nanorods in an array are dislocation-free, increasing the internal quantum efficiency (Li *et al.* 2011).
- Strain relaxation at the sidewalls of the nanorods could potentially allow the growth of high-quality InGaN quantum walls with high In content (Bavencove *et al.* 2011, Zhuang *et al.* 2013a). This could not only further increase internal quantum efficiency and help to alleviate the 'green gap' problem, but it even potentially allows InGaN quantum wells to emit in the yellow and red spectral

ranges, paving the way forward for single-chip phosphor-free white LEDs consisting of different nanorods emitting different wavelengths on the same chip (Kishino *et al.* 2013).

- The cylindrical shape of nanorods allows them to act as waveguides. The waveguiding properties can be tailored to give a customizable angular emission pattern, which is especially useful for applications such as displays and projectors where the degree of compactness required rules out the use of secondary optics.

7.4 Other types of nano-LEDs

Although cylindrical nanorods are the most commonly investigated structure, there has also been research on other nanostructures, such as hexagonal prism-shaped nanorods (Hersee *et al.* 2006, Kishino *et al.* 2009) and nanopyramids (Liu *et al.* 2008) grown by selective area growth. Hexagonal prism-shaped core-shell nanorods (Li and Waag 2012, Le Boulbar *et al.* 2013), in which the quantum wells run along the nanorod walls as opposed to a cross-section, are likely to be a major research focus in the coming years due to the non-polar nature of the quantum wells, increased active surface area and potential for a greater colour range.

7.5 Optical modelling of nanorod LEDs

Unlike planar LEDs, nanorod LEDs are three-dimensional and therefore have much more complex optical properties. In order to maximize the extraction efficiency and customize the emission pattern, a comprehensive model of the waveguiding properties of LED nanorods is required. Most of the literature on this subject uses finite-difference time-domain (FDTD) methods (Xu *et al.* 2007, Kölper *et al.* 2011). While it is possible to achieve highly accurate estimates of the power distribution with these methods, doing so is computationally intensive. In addition, it can be difficult to determine the physical mechanisms responsible for behaviour predicted by these methods. These problems leave space for a more mathematical method of optical modelling that is less computationally intensive and is capable of tracking the physics responsible for predictions. The remainder of this thesis outlines the construction and implementation of such a model. Chapter 8 shows how the well-established theory of optical fibres can be applied to a single nanorod of infinite length by taking advantage of the cylindrical symmetry of such structures. Chapter 9 outlines a novel mathematical technique that can be used to combine the waveguiding analysis of chapter 8 with the resonant cavity analysis of chapter 5 to evaluate the angular emission pattern of a single nanorod of

finite length. Sloped or tapered nanorods are beyond the scope of this work, although small slopes can be neglected if the nanorods are sufficiently short, as shown in chapters 9 and 10 (see also Lis *et al.* 2013).

7.6 Summary

This chapter provides an introduction to and a literature review of nanorod LEDs. A motivation for quasi-analytic optical modelling of nanorod LEDs is then presented, followed by a brief roadmap for developing such a model.

Chapter 8

The infinitely long nanorod

8.1 Introduction

In order to gain a mathematical understanding of finite length nanorod LEDs, it is necessary to understand the simpler case of an infinitely long nanorod. Using the methods of Adams (1981) and Snyder and Love (1983), the guided and radiation modes of the infinite nanorod system are derived. Numerical calculations of the dispersion relations and Poynting vectors of the guided modes are presented, followed by numerical calculations of the total power emitted into guided and radiation modes by a Hertzian dipole within the nanorod. Through doing this, the theoretical extraction efficiencies of infinitely long nanorod LEDs are compared with those predicted by (5.24) for planar LEDs for a range of dipole positions, nanorod radii and types of cladding at a constant free space wavelength of $\lambda_0 = 460$ nm.

8.2 The structure under consideration

The infinitely long nanorod is depicted in figure 8-1; a cylinder with an infinite length along the z direction, a finite radius R and refractive index n_{core}, surrounded by an infinite cladding of refractive index n_{clad}. The core is assumed to consist of GaN, a dispersion relation for which is given by Takeuchi *et al.* (2010), while three different types of cladding are considered: air, SiO_2 (glass) and Si_3N_4 (silicon nitride). As the core-cladding interface is parallel to z and no other interfaces are present, it is possible

to expand the electromagnetic fields $\vec{E}$ and $\vec{H}$ in terms of modes as in (6.21) and (6.22):

$$\vec{E}(\vec{r}) = \sum_j C_j \hat{E}_j(\rho,\phi)\mathrm{e}^{\mathrm{i}\beta_j z} + \sum \int_0^\infty c(\kappa_\infty)\hat{e}(\rho,\phi,\kappa_\infty)\mathrm{e}^{\mathrm{i}\beta z}\,\mathrm{d}\kappa_\infty \tag{8.1}$$

$$\vec{H}(\vec{r}) = \sum_j C_j \hat{H}_j(\rho,\phi)\mathrm{e}^{\mathrm{i}\beta_j z} + \sum \int_0^\infty c(\kappa_\infty)\hat{h}(\rho,\phi,\kappa_\infty)\mathrm{e}^{\mathrm{i}\beta z}\,\mathrm{d}\kappa_\infty, \tag{8.2}$$

where $\hat{E}_j$ and $\hat{H}_j$ are the electromagnetic fields of the guided modes, $\hat{e}$ and $\hat{h}$ are those of the radiation modes and

$$\kappa_\infty = \sqrt{k_0^2 n_{clad}^2 - \beta^2} = \sigma. \tag{8.3}$$

As $n_{core} > n_{clad}$ in all of the cases being considered, both guided and radiation modes exist.

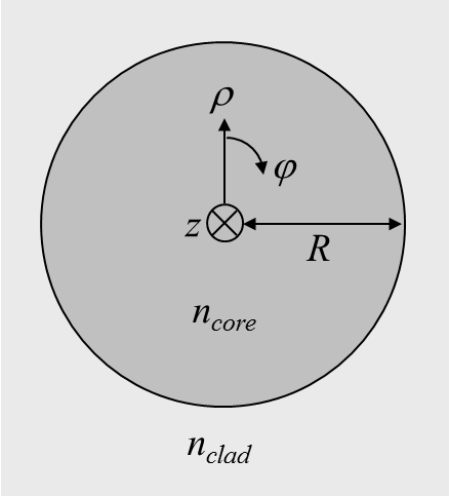

Figure 8-1: The structure to be modelled, in cylindrical polar coordinates.

8.3 Guided modes of the infinite nanorod

The form of the guided modes is well-documented by Adams (1981, p217-225) and Snyder and Love (1983, p248-251) among others; their electromagnetic field components are given in Table 8.1 for $\rho \leq R$ and Table 8.2 for $\rho \geq R$, where N is a non-negative integer, J_N is the Bessel function of the first kind of order N, K_N is the modified Bessel function of the second kind of order N, $f(N\phi)$ and $g(N\phi)$ are given by (6.17),

$$\kappa_j = \sqrt{k_0^2 n_{core}^2 - \beta_j^2}, \quad \gamma_j = \sqrt{\beta_j^2 - k_0^2 n_{clad}^2} \tag{8.4}$$

and A_j and B_j are constants to be found. The fields in Tables 8.1 and 8.2 have been

$\hat{E}_j \cdot \hat{z}$	$-\mathrm{i}A_j \dfrac{J_N(\kappa_j \rho)}{J_N(\kappa_j R)} f(N\phi)$
$\hat{H}_j \cdot \hat{z}$	$-\mathrm{i}B_j \dfrac{J_N(\kappa_j \rho)}{J_N(\kappa_j R)} g(N\phi)$
$\hat{E}_j \cdot \hat{\rho}$	$\left(A_j \beta_j \dfrac{\partial J_N(\kappa_j \rho)}{\partial \rho} - B_j N k_0 Z_0 \dfrac{J_N(\kappa_j \rho)}{\rho} \right) \dfrac{f(N\phi)}{\kappa_j^2 J_N(\kappa_j R)}$
$\hat{H}_j \cdot \hat{\rho}$	$\left(B_j \beta_j \dfrac{\partial J_N(\kappa_j \rho)}{\partial \rho} - A_j \dfrac{N k_0 n_{core}^2}{Z_0} \dfrac{J_N(\kappa_j \rho)}{\rho} \right) \dfrac{g(N\phi)}{\kappa_j^2 J_N(\kappa_j R)}$
$\hat{E}_j \cdot \hat{\phi}$	$\left(A_j N \beta_j \dfrac{J_N(\kappa_j \rho)}{\rho} - B_j k_0 Z_0 \dfrac{\partial J_N(\kappa_j \rho)}{\partial \rho} \right) \dfrac{g(N\phi)}{\kappa_j^2 J_N(\kappa_j R)}$
$\hat{H}_j \cdot \hat{\phi}$	$\left(A_j \dfrac{k_0 n_{core}^2}{Z_0} \dfrac{\partial J_N(\kappa_j \rho)}{\partial \rho} - B_j N \beta_j \dfrac{J_N(\kappa_j \rho)}{\rho} \right) \dfrac{f(N\phi)}{\kappa_j^2 J_N(\kappa_j R)}$

Table 8.1: Electromagnetic field components of the guided modes of an optical fibre in the core ($\rho \leq R$).

$\hat{E}_j \cdot \hat{z}$	$-\mathrm{i}A \dfrac{K_N(\gamma_j \rho)}{K_N(\gamma_j R)} f(N\phi)$
$\hat{H}_j \cdot \hat{z}$	$-\mathrm{i}B \dfrac{K_N(\gamma_j \rho)}{K_N(\gamma_j R)} g(N\phi)$
$\hat{E}_j \cdot \hat{\rho}$	$\left(B_j N k_0 Z_0 \dfrac{K_N(\gamma_j \rho)}{\rho} - A_j \beta_j \dfrac{\partial K_N(\gamma_j \rho)}{\partial \rho} \right) \dfrac{f(N\phi)}{\gamma_j^2 K_N(\gamma_j R)}$
$\hat{H}_j \cdot \hat{\rho}$	$\left(A_j \dfrac{N k_0 n_{clad}^2}{Z_0} \dfrac{K_N(\gamma_j \rho)}{\rho} - B_j \beta_j \dfrac{\partial K_N(\gamma_j \rho)}{\partial \rho} \right) \dfrac{g(N\phi)}{\gamma_j^2 K_N(\gamma_j R)}$
$\hat{E}_j \cdot \hat{\phi}$	$\left(B_j k_0 Z_0 \dfrac{\partial K_N(\gamma_j \rho)}{\partial \rho} - A_j N \beta_j \dfrac{K_N(\gamma_j \rho)}{\rho} \right) \dfrac{g(N\phi)}{\gamma_j^2 K_N(\gamma_j R)}$
$\hat{H}_j \cdot \hat{\phi}$	$\left(B_j N \beta_j \dfrac{K_N(\gamma_j \rho)}{\rho} - A_j \dfrac{k_0 n_{clad}^2}{Z_0} \dfrac{\partial K_N(\gamma_j \rho)}{\partial \rho} \right) \dfrac{f(N\phi)}{\gamma_j^2 K_N(\gamma_j R)}$

Table 8.2: Electromagnetic field components of the guided modes of an optical fibre in the cladding ($\rho \geq R$).

chosen so that both $\hat{E}_j \cdot \hat{z}$ and $\hat{H}_j \cdot \hat{z}$ are continuous at $\rho = R$ as required by Maxwell's equations, which also require $\hat{E}_j \cdot \hat{\phi}$ and $\hat{H}_j \cdot \hat{\phi}$ to be continuous at $\rho = R$, resulting in the relationships

$$\frac{B_j}{A_j} = \frac{N \beta_j V^2}{k_0 Z_0 R^3 \kappa_j^2 \gamma_j^2} \left(\frac{J_N'(\kappa_j R)}{\kappa_j J_N(\kappa_j R)} + \frac{K_N'(\gamma_j R)}{\gamma_j K_N(\gamma_j R)} \right)^{-1} \tag{8.5}$$

and

$$\left(\frac{J'_N(\kappa_j R)}{\kappa_j J_N(\kappa_j R)} + \frac{K'_N(\gamma_j R)}{\gamma_j K_N(\gamma_j R)}\right)\left(\frac{J'_N(\kappa_j R)}{\Delta\kappa_j J_N(\kappa_j R)} + \frac{K'_N(\gamma_j R)}{\gamma_j K_N(\gamma_j R)}\right) = \left(\frac{N\beta_j V^2}{k_0 R^3 \kappa_j^2 \gamma_j^2}\right)^2, \tag{8.6}$$

where

$$J'_N(\kappa_j R) = \left.\frac{\mathrm{d}J_N(x)}{\mathrm{d}x}\right|_{x=\kappa_j R} \qquad K'_N(\gamma_j R) = \left.\frac{\mathrm{d}K_N(x)}{\mathrm{d}x}\right|_{x=\gamma_j R} \tag{8.7}$$

and

$$\Delta = \frac{n_{clad}^2}{n_{core}^2} \quad V = k_0 R\sqrt{n_{core}^2 - n_{clad}^2} = k_0 R n_{core}\sqrt{1-\Delta}. \tag{8.8}$$

Equation (8.6) is the eigenvalue equation: its solutions are the combinations of N and β for the guided modes for a fibre defined by k_0, R, n_{core} and n_{clad}. For the case of $N = 0$, (8.6) can be simplified to

$$\left(\frac{J'_N(\kappa_j R)}{\kappa_j J_N(\kappa_j R)} + \frac{K'_N(\gamma_j R)}{\gamma_j K_N(\gamma_j R)}\right) = 0 \tag{8.9}$$

for transverse electric (TE) modes and

$$\left(\frac{J'_N(\kappa_j R)}{\Delta\kappa_j J_N(\kappa_j R)} + \frac{K'_N(\gamma_j R)}{\gamma_j K_N(\gamma_j R)}\right) = 0 \tag{8.10}$$

for transverse magnetic (TM) modes. TE modes are characterized by having $\hat{E}_j \cdot \hat{z} = 0$ and therefore $A_j = 0$, while TM modes are characterized by $\hat{H}_j \cdot \hat{z} = 0$ and therefore $B_j = 0$. Modes for which $N \neq 0$ are referred to as hybrid modes as all six field components are generally non-zero. Full solution of (8.6) is required to find hybrid modes.

The eigenvalue equations are transcendental and can therefore only be solved numerically, searching within the interval $k_0 n_{clad} < \beta < k_0 n_{core}$. Note that $f(N\phi)$, which gives the azimuthal (ϕ) variation, does not appear in (8.6). This means that each solution to the eigenvalue equation is actually two modes, which have exactly the same N and β but different ϕ variation: one mode has $f(N\phi) = \sin(N\phi)$ while the other has $f(N\phi) = \cos(N\phi)$. The exception to this is the $N = 0$ case, where there is no ϕ variation.

Note that the z components of the modal electromagnetic fields are imaginary while the transverse components are real. This results in the time-averaged Poynting vector having only a z component. This physically corresponds to the power being guided along the waveguide axis, hence the name. The A_j (B_j for TE modes) normalizing

each mode via to carry unit power:

$$\tfrac{1}{2}\int_0^{2\pi}\int_0^{\infty}[\hat{E}_j(\rho,\phi)\times\hat{H}_k^*(\rho,\phi)]\cdot\hat{z}\rho\,\mathrm{d}\rho\,\mathrm{d}\phi=\delta_{jk}, \tag{8.11}$$

where δ_{jk} is the Kronecker delta and $\hat{H}_k^*$ denotes the complex conjugate of $\hat{H}_k$.

8.4 Radiation modes of the infinite nanorod

The mathematical form of the normalized radiation mode fields $\hat{e}_R(\rho,\phi,\sigma)$ and $\hat{h}_R(\rho,\phi,\sigma)$ is given by Snyder and Love (1983 p525). These radiation modes are functions of $\sigma=\sqrt{k_0^2n_{clad}^2-\beta^2}$, so that the total fields $\vec{E}(\vec{r})$ and $\vec{H}(\vec{r})$ are given by the following expansion:

$$\vec{E}(\vec{r})=\sum_j C_j\hat{E}_j(\rho,\phi)\mathrm{e}^{\mathrm{i}\beta_j z}+\sum\int_0^{\infty}c(\sigma)\hat{e}_R(\rho,\phi,\sigma)\mathrm{e}^{\mathrm{i}\beta z}\,\mathrm{d}\sigma \tag{8.12}$$

$$\vec{H}(\vec{r})=\sum_j C_j\hat{H}_j(\rho,\phi)\mathrm{e}^{\mathrm{i}\beta_j z}+\sum\int_0^{\infty}c(\sigma)\hat{h}_R(\rho,\phi,\sigma)\mathrm{e}^{\mathrm{i}\beta z}\,\mathrm{d}\sigma, \tag{8.13}$$

where the summation before the integral extends over the two choices of $f(N\phi)$, all non-negative integers N and the two polarizations of radiation modes: ITE (incident transverse electric) and ITM (incident transverse magnetic), which are similar to the respective TE and TM modes of homogeneous media. The radiation fields in the cladding are decomposed (Snyder and Love 1983 p523-524) into free space and scattered components, represented by Bessel and Hankel functions of the first kind respectively. For ITE modes the free space component of $\hat{e}_R\cdot\hat{z}$ is zero; for ITM modes the free space component of $\hat{h}_R\cdot\hat{z}$ is zero. It is convenient to define the functions $\psi_e(\rho,\sigma)$ and $\psi_h(\rho,\sigma)$, which are defined in Table 8.3. Note that $\kappa=\sqrt{k_0^2n_{core}^2-\beta^2}$ as for the guided modes. The six algebraic constants $a(\sigma)$, $b(\sigma)$, $c_f(\sigma)$, $c_s(\sigma)$, $d_f(\sigma)$ and $d_s(\sigma)$ featured

	$\rho\le R$	$\rho\ge R$
$\psi_e(\rho,\sigma)$	$a(\sigma)J_N(\kappa\rho)$	$c_f(\sigma)J_N(\sigma\rho)+c_s(\sigma)H_N^{(1)}(\sigma\rho)$
$\psi_h(\rho,\sigma)$	$b(\sigma)J_N(\kappa\rho)$	$d_f(\sigma)J_N(\sigma\rho)+d_s(\sigma)H_N^{(1)}(\sigma\rho)$

Table 8.3: Definition of the functions $\psi_e(\rho,\sigma)$ and $\psi_h(\rho,\sigma)$ used in the mathematical formulation of the radiation modes.

in Table 8.3 have two different sets of values, corresponding to ITE and ITM radiation modes, which are given in Table 8.4. The subscripts f and s correspond to the free space and scattered components respectively. The terms Δ, $X(\sigma)$, $Y(\sigma)$, $M(\sigma)$ and

	ITE modes	ITM modes
$a(\sigma)$	$\dfrac{4N(1-\Delta)}{\pi R^4\kappa^2\sigma^2 J_N(\kappa R)M_N(\sigma)}\sqrt{\dfrac{k_0 Z_0\beta}{2\pi\sigma}}$	$\dfrac{-4\Xi_{0N}\Delta X_N(\sigma)}{\pi R^3 n_{clad}\kappa\sigma J_N(\kappa R)M_N(\sigma)}\sqrt{\dfrac{Z_0}{2\pi k_0\sigma\beta}}$
$b(\sigma)$	$\dfrac{-4\Xi_{0N}Y_N(\sigma)}{\pi R^3\kappa\sigma J_N(\kappa R)M_N(\sigma)\sqrt{2\pi k_0 Z_0\sigma\beta}}$	$\dfrac{4Nn_{clad}(1-\Delta)}{\pi R^4\kappa^2\sigma^2 J_N(\kappa R)M_N(\sigma)}\sqrt{\dfrac{k_0\beta}{2\pi Z_0\sigma}}$
$c_f(\sigma)$	0	$2\mathrm{i}\Xi_{0N}\dfrac{\sigma}{n_{clad}}\sqrt{\dfrac{Z_0\sigma}{2\pi k_0\beta}}$
$c_s(\sigma)$	$a(\sigma)\dfrac{J_N(\kappa R)}{H_N^{(1)}(\sigma R)}$	$\dfrac{c_f(\sigma)}{H_N^{(1)}(\sigma R)}\left(\dfrac{2\mathrm{i}\Delta R X_N(\sigma)}{\pi\sigma^2 M_N(\sigma)} - J_N(\sigma R)\right)$
$d_f(\sigma)$	$2\mathrm{i}\Xi_{0N}\sigma\sqrt{\dfrac{\sigma}{2\pi k_0 Z_0\beta}}$	0
$d_s(\sigma)$	$\dfrac{d_f(\sigma)}{H_N^{(1)}(\sigma R)}\left(\dfrac{2\mathrm{i}RY_N(\sigma)}{\pi\sigma^2 M_N(\sigma)} - J_N(\sigma R)\right)$	$b(\sigma)\dfrac{J_N(\kappa R)}{H_N^{(1)}(\sigma R)}$

Table 8.4: Algebraic constants $a(\sigma)$, $b(\sigma)$, $c_f(\sigma)$, $c_s(\sigma)$, $d_f(\sigma)$ and $d_s(\sigma)$ for ITE and ITM radiation modes.

Ξ_{0N} in Table 8.4 are given by

$$\Delta = \frac{n_{clad}^2}{n_{core}^2} \quad X(\sigma) = \frac{J_N'(\kappa R)}{\kappa J_N(\kappa R)} - \frac{H_N^{(1)\prime}(\sigma R)}{\sigma H_N^{(1)}(\sigma R)} \quad Y(\sigma) = \frac{J_N'(\kappa R)}{\kappa J_N(\kappa R)} - \Delta\frac{H_N^{(1)\prime}(\sigma R)}{\sigma H_N^{(1)}(\sigma R)}$$

$$M(\sigma) = H_N^{(1)}(\sigma R)\left(\frac{[Nk_0 n_{core}\beta(1-\Delta)]^2}{[R\kappa\sigma]^4} - \frac{X_N(\sigma)Y_N(\sigma)}{R^2}\right)$$

$$\Xi_{0N} = \begin{cases} \frac{1}{\sqrt{2}} & N = 0 \\ 1 & N \neq 0, \end{cases} \tag{8.14}$$

where

$$J_N'(\kappa R) = \left.\frac{\mathrm{d}J_N(x)}{\mathrm{d}x}\right|_{x=\kappa R} \quad H_N^{(1)\prime}(\sigma R) = \left.\frac{\mathrm{d}H_N^{(1)}(x)}{\mathrm{d}x}\right|_{x=\sigma R} \tag{8.15}$$

as in (8.7). Now that the functions $\psi_e(\rho,\sigma)$ and $\psi_h(\rho,\sigma)$ are fully defined, they can be used to define the electromagnetic fields of the radiation modes, as shown in Table 8.5. Note that, since $f(N\phi)$ does not appear anywhere in ψ_e or ψ_h, modes with different $f(N\phi)$ but identical ψ_e and ψ_h form degenarate pairs, as with the guided modes.

8.5 Dispersion relations of the guided modes

The propagation constants β_j of the guided modes were found by solving (8.6), (8.9) and (8.10) using a bisection method designed to solve to six significant figures. A useful

$\hat{e}_R \cdot \hat{z}$	$\psi_e(\rho,\sigma) f(N\phi)$
$\hat{h}_R \cdot \hat{z}$	$\psi_h(\rho,\sigma) g(N\phi)$
$\hat{e}_R \cdot \hat{\rho}$	$\frac{\mathrm{i}}{k_0^2 n^2(\rho) - \beta^2} \left(\beta \frac{\mathrm{d}\psi_e}{\mathrm{d}\rho} - N k_0 Z_0 \frac{\psi_h}{\rho} \right) f(N\phi)$
$\hat{h}_R \cdot \hat{\rho}$	$\frac{\mathrm{i}}{k_0^2 n^2(\rho) - \beta^2} \left(\beta \frac{\mathrm{d}\psi_h}{\mathrm{d}\rho} - \frac{N k_0 n^2(\rho)}{Z_0} \frac{\psi_e}{\rho} \right) g(N\phi)$
$\hat{e}_R \cdot \hat{\phi}$	$\frac{\mathrm{i}}{k_0^2 n^2(\rho) - \beta^2} \left(N\beta \frac{\psi_e}{\rho} - k_0 Z_0 \frac{\mathrm{d}\psi_h}{\mathrm{d}\rho} \right) g(N\phi)$
$\hat{h}_R \cdot \hat{\phi}$	$\frac{\mathrm{i}}{k_0^2 n^2(\rho) - \beta^2} \left(\frac{k_0 n^2(\rho)}{Z_0} \frac{\mathrm{d}\psi_e}{\mathrm{d}\rho} - N\beta \frac{\psi_h}{\rho} \right) f(N\phi)$

Table 8.5: Electromagnetic fields of the radiation modes of an optical fibre, in terms of $\psi_e(\rho,\sigma)$ and $\psi_h(\rho,\sigma)$.

number to consider when discussing guided modes is the modal index n_m:

$$n_m = \frac{\beta}{k_0}. \tag{8.16}$$

A guided mode propagating in the z direction has the same z variation as a plane wave travelling in the z direction in a medium of refractive index n_m. The variation of modal index with nanorod radius R was plotted for all guided modes over the range R=50-200 nm and for all three cladding types: air (Figure 8-2), SiO_2 (Figure 8-3) and Si_3N_4 (Figure 8-4). The free space wavelength was fixed at 460 nm; the refractive index of GaN is $n_{core} = 2.4575$ at this wavelength (Takeuchi *et al.* 2010), while those of SiO_2 and Si_3N_4 are taken as n_{clad}=1.465 and 2.05 respectively (Palik c. 1998).

This thesis uses the standard notation for optical fibre modes (Snitzer 1961, Adams 1981, Snyder and Love 1983), which is briefly explained as follows. Hybrid modes are denoted by HE and EH, while TE and TM modes are denoted by TE and TM respectively. The first digit in the subscript is N.

Figure 8-3 is very similar to the corresponding plot in Kölper *et al.* (2011), which assumes similar core and cladding indices of 2.4 and 1.5 respectively. However, there are visible differences between Figure 8-3 and Figure 2 of Kölper *et al.* (2011), so another set of dispersion curves was plotted in Figure 8-5 for $n_{core} = 2.4$, $n_{clad} = 1.5$, $\lambda_0 = 550$ nm and varying R, as used by Kölper *et al.*. Figure 8-5 is virtually identical to Figure 2 of Kölper *et al.* (2011), providing strong evidence to support the dispersion relations in Figures 8-2-8-4.

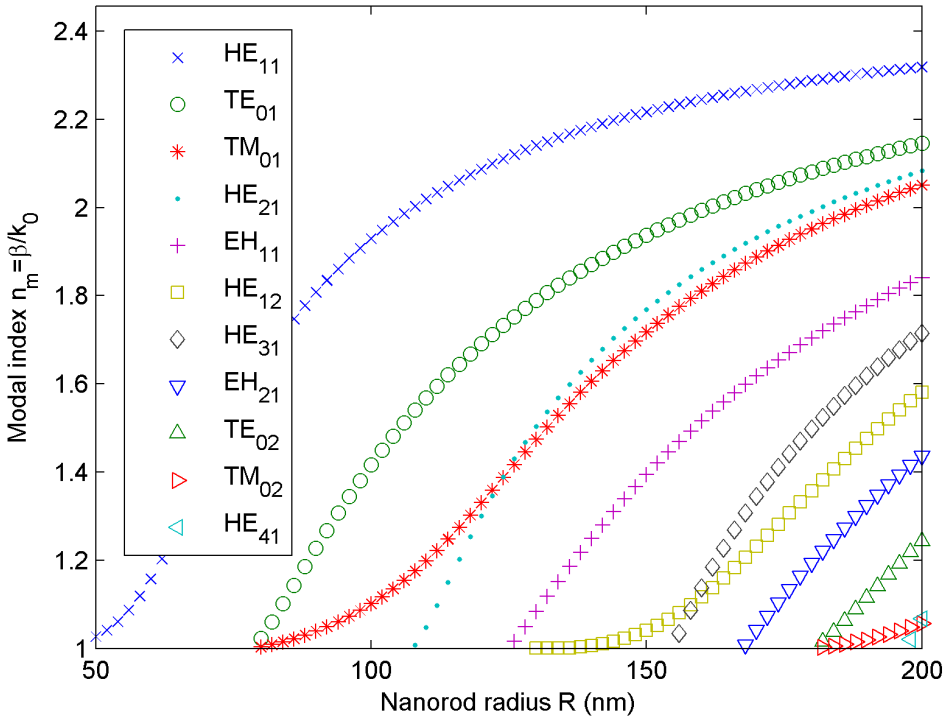

Figure 8-2: Variation of modal indices with R for air cladding at $\lambda_0 = 460$ nm.

More generally, the number of guided modes increases with R. As R is decreased, n_m for each mode falls until $n_m = n_{clad}$, at which point the mode is cut-off and ceases to be guided. The exception is the fundamental mode HE_{11}, which always exists provided that $n_{core} > n_{clad}$. Decreasing the wavelength (and thereby increasing k_0) has a similar effect to increasing R, while increasing n_{clad} (and therefore decreasing the refractive index step) has the effect of moving the curves to the right and therefore decreasing the number of guided modes. The relationship between n_m and the proportion of optical power in the core (as opposed to in the cladding) is not simple, although modes with larger n_m generally have a greater proportion of power in the core. As such, modes with higher n_m are more 'strongly guided', as shown by Snyder and Love (1983, pp. 255) for a situation comparable with that of a GaN nanorod surrounded by SiO_2.

In terms of optical fibre theory, the case of a GaN nanorod is interesting because the often-used linear polarization (LP) approximation is unsuitable for the large index steps being considered. As the index step is decreased, the guided modes form clusters

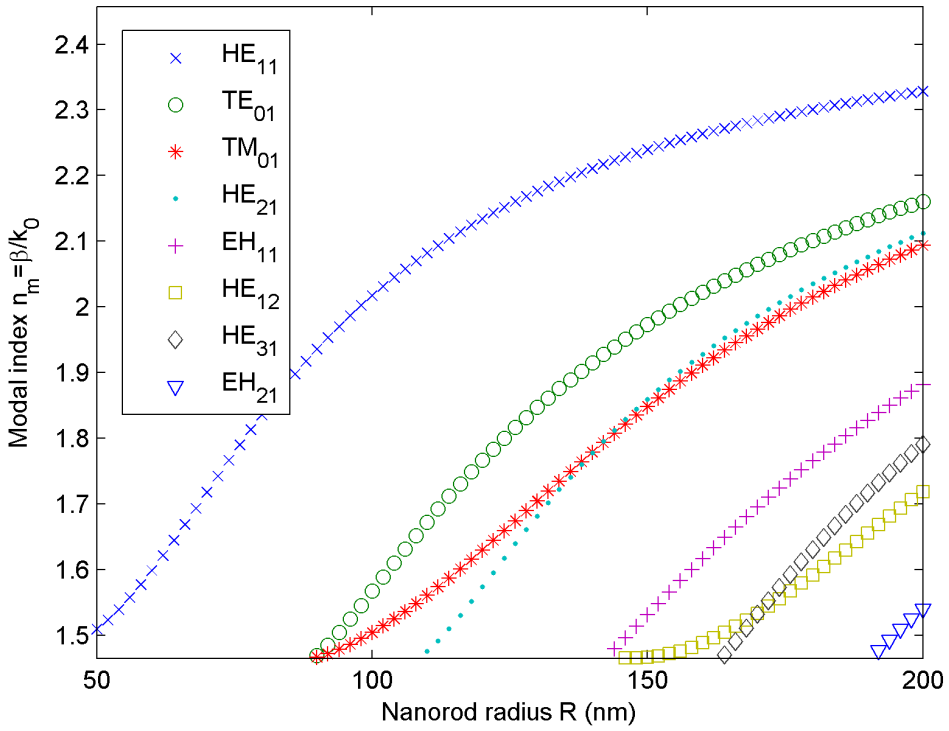

Figure 8-3: Variation of modal indices with R for SiO_2 cladding at $\lambda_0 = 460$ nm.

of several modes with similar n_m; for very small index steps these clusters become degenerate and can be considered as single modes called LP modes (Adams 1981 pp. 232). The n_m of LP modes are functions of V solely (where V is defined in (8.8)); increasing the index step lifts the degeneracy and causes them to become functions of Δ also, where Δ is given by (8.14). Inspection of Figures 8-2-8-4 shows that the modes do indeed appear to form 'bunches' as n_{clad} increases.

Regardless of Δ, the last modes to be cut-off as V is decreased are the TE_{01} and TM_{01} modes (HE_{11} is never cut-off). These modes are cut-off when $V = 2.4048$, i.e. the first zero of $J_0(V)$. Rearranging the expression for V yields the corresponding value of R: 78.4 nm for air cladding, 89.2 nm for SiO_2 cladding and 130 nm for Si_3N_4 cladding. Both TE_{01} and TM_{01} are cut-off at $V = 2.4048$ regardless of Δ, although the properties of the TE and TM modes diverge as Δ is increased.

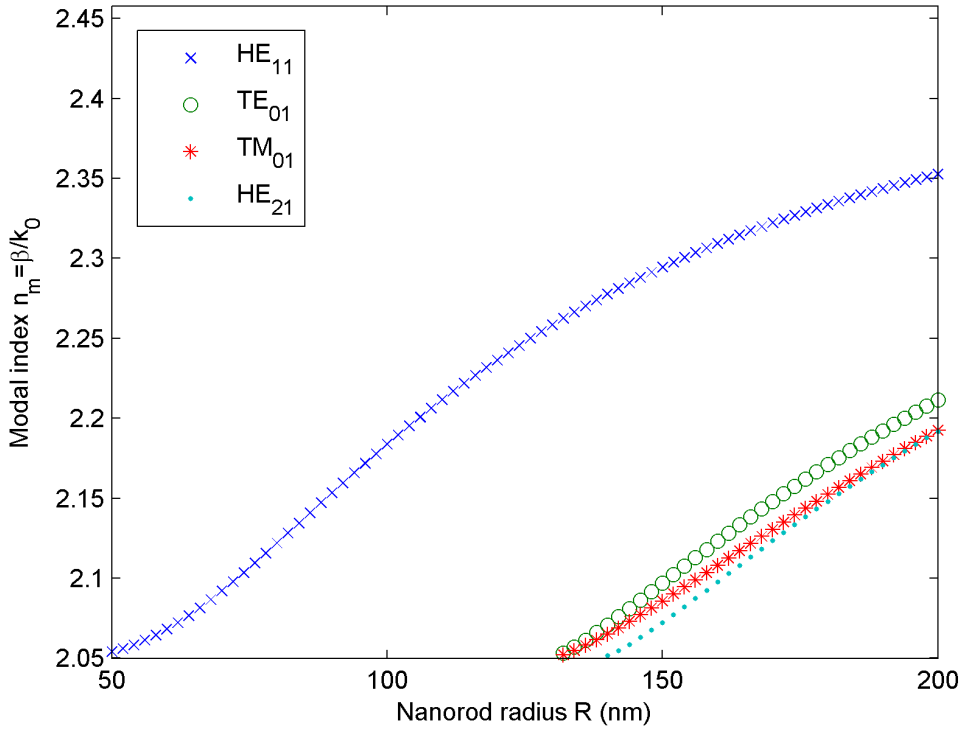

Figure 8-4: Variation of modal indices with R for Si_3N_4 cladding at $\lambda_0 = 460$ nm.

8.6 Poynting vector of the guided modes

As mentioned in section 8.3, the time-averaged Poynting vector $\vec{S}$ lies entirely in the z direction and is given by

$$\vec{S}(\rho, \phi) = \tfrac{1}{2}(E_\rho H_\phi - E_\phi H_\rho)\hat{z}. \tag{8.17}$$

For TE modes, the first term in (8.17) is zero therefore dipoles oriented in the ρ direction will not emit into them; for TM modes, the second term is zero therefore dipoles oriented in the ϕ direction will not excite them. For hybrid modes both terms are generally non-zero. It should be noted that the first term varies as $\sin^2(N\phi)$ and the second term as $\cos^2(N\phi)$, or vice-versa. Assuming the distribution of dipoles is cylindrically symmetric, the pair of modes with different $f(N\phi)$ are equally excited and the total Poynting vector of the pair of modes is ϕ-invariant. Figure 8-6 depicts the variation of the scalar terms of (8.17) inside the brackets with ρ for all six modes of a GaN nanorod with $R = 150$ nm and $n_{clad} = 1$ at a free space wavelength of 460 nm.

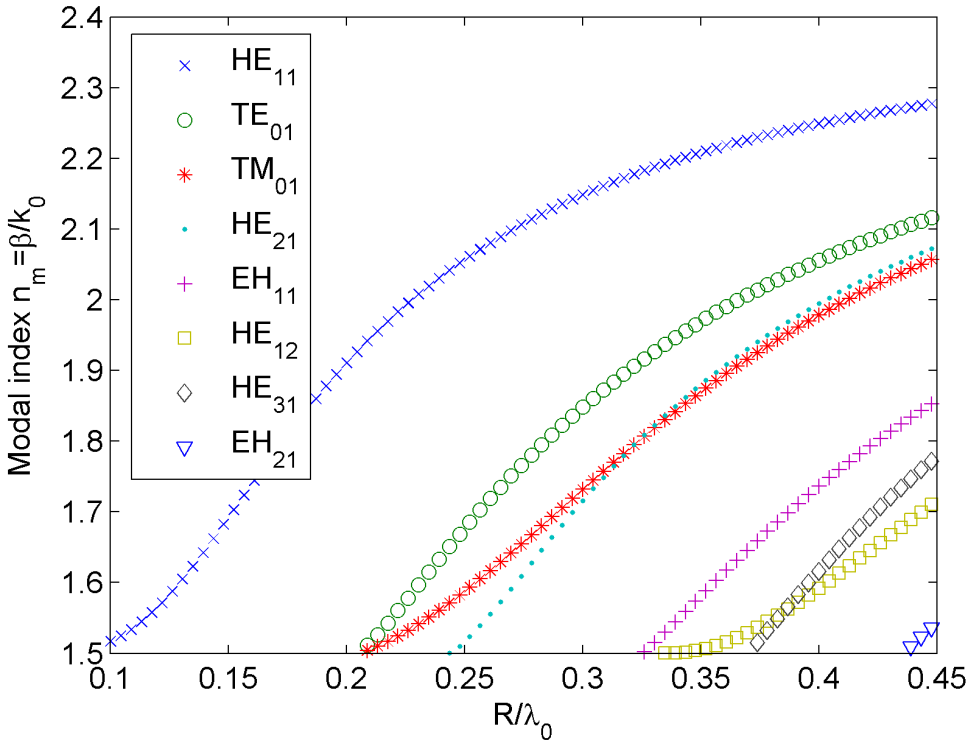

Figure 8-5: Variation of modal indices with $R\lambda_0^{-1}$ for $n_{core} = 2.4$, $n_{clad} = 1.5$ and $\lambda_0 = 550$ nm, intended for comparison with Figure 2 of Kölper *et al.* (2011).

The modes are the same as those in Figure 8-2 and presented in order from highest n_m to lowest. All the $N \neq 1$ modes have zero power in the centre of the nanorod ($\rho = 0$); this can be shown to be true for all modes (guided and radiation) by using the small-argument asymptotic expansions of the Bessel functions. The full Poynting vector (solid line) peaks at $\rho = 0$ for HE_{11} and HE_{12} but elsewhere inside the core for the other modes. For hybrid modes, the two terms are equal at $\rho = 0$ where the ρ and ϕ coordinates are degenerate, but diverge as ρ increases. With the exception of HE_{12}, the second term is greater as $\rho \to R$ within the core region for the modes supported by this structure.

Part of the cladding region is also shown; for modes with higher n_m, the electromagnetic fields and therefore the Poynting vector generally decay more quickly as ρ increases, compared with modes with lower n_m. The first term in (8.17) is discontinuous at $\rho = R$ due to the discontinuity in E_ρ required by Maxwell's equations. The relationship between the (discontinuous) magnitude of the electromagnetic fields at

$\rho = R$ is not simple; notice for example that there is little power in the cladding for the HE_{21} mode despite the relatively slow decay rate, because fields there are small to begin with.

8.7 Excitation of guided and radiation modes by a Hertzian dipole

The methods of section 6.5 can be used to calculate the total power P_g and P_r emitted into guided and radiation modes respectively by a Hertzian dipole inside an infinite nanorod, where

$$P_g = \sum_j |C_j|^2 \tag{8.18}$$

and

$$P_r = \sum \int_0^{k_0 n_{clad}} |c(\kappa)|^2 \, \mathrm{d}\kappa \tag{8.19}$$

are found using (6.27) for the dipole position and orientation in question:

$$C_j = -\tfrac{1}{4}\vec{E}_j^*(\rho_D, \phi_D) \cdot \vec{j} \mathrm{e}^{-\mathrm{i}\omega t} = -\tfrac{1}{4}|\vec{j}| \left[\vec{E}_{\rho j}^*(\rho_D, \phi_D)\cos\Phi + \vec{E}_{\phi j}^*(\rho_D, \phi_D)\sin\Phi\right] \mathrm{e}^{-\mathrm{i}\omega t}. \tag{8.20}$$

As in section 8.4, the summation in (8.19) sums over all possible N (in practice, summing up to $N = 12$ was found to achieve power conservation), the ITE and ITM mode polarizations and both choices of $f(N\phi)$. Given that

$$f(N\phi) = \begin{cases} \sin(N\phi) \\ \cos(N\phi), \end{cases} \tag{8.21}$$

the azimuthal position ϕ_D of the dipole has no effect on P_r and only the radial position ρ_D and orientation (angle between dipole current and ρ axis) Φ need be considered.

The variation of P_g, P_r and $P_T = P_g + P_r$ with the radial position ρ_D of the dipole was investigated for four radii (R=40, 75, 150 and 300 nm), all three cladding types and two orientations of the dipole: ρ-oriented ($\Phi = 0$) and ϕ-oriented ($\Phi = \frac{\pi}{2}$). The free space wavelength was fixed at 460 nm as in section 8.5, resulting in all refractive indices being the same as in that section. The results are presented in Figures 8-7 (R=40 nm), 8-8 (R=75 nm), 8-9 (R=150 nm) and 8-10 (R=300 nm). The power is normalized to the total power that would be emitted by the same dipole in homogenous GaN into the $z > 0$ hemisphere, so that a dipole emitting the same upwards total power as a dipole

in homogenous GaN has $P_T = 1$: this was done by setting

$$|\vec{j}|^2 = \frac{24\pi}{k_0^2 Z_0 n_{core}}. \tag{8.22}$$

As the system is cylindrically and axially symmetric, the power emitted into the $z > 0$ and $z < 0$ hemispheres is identical, making it simpler to consider modes propagating in the $+z$ direction only. The power P_b extracted from an horizontal dipole source of the same strength in a thick GaN slab clad on both sides by a dielectric of refractive index n_{clad} is a useful benchmark and is therefore shown for comparison as a faint horizontal line. As the total power emitted by such a dipole is normalized to unity, the extracted power is equal to the extraction efficiency and is found using (5.24):

$$P_b = 1 - \frac{3}{4}\sqrt{1 - \left(\frac{n_{ext}}{n_{int}}\right)^2} - \frac{1}{4}\left[1 - \left(\frac{n_{ext}}{n_{int}}\right)^2\right]^{\frac{3}{2}}. \tag{8.23}$$

It is possible to define the extraction efficiency η_{ext} of an infinite nanorod structure using the equation

$$\eta_{ext} = \frac{P_r}{P_T}. \tag{8.24}$$

The extraction efficiencies are plotted in Figure 8-11. The extraction efficiencies for $R = 300$ nm have been omitted as they follow similar trends to those for $R = 150$ nm.

8.7.1 Guided power

For $R = 40$ nm and $R = 75$ nm (Figures 8-7 and 8-8 respectively), only the fundamental HE_{11} mode is guided, so the guided power P_g reflects the characteristic fundamental mode shape with its central peak as depicted in Figure 8-6. The slope of P_g appears to increase strongly with both R and $\sqrt{n_{core}^2 - n_{clad}^2}$ in this regime, implying that V is a key factor. The magnitude of P_g is more heavily influenced by other factors; for $R = 40$ nm, the peak of P_g for SiO_2 cladding is around six times that for air cladding, despite V being lower. This is counter-intuitive but not physically impossible; as mentioned previously, some of the assumptions often used in optical fibre theory are not valid for the large index steps under consideration. Wider nanorods (Figures 8-9 and 8-10) support additional modes with maxima at progressively larger ρ_D, as shown in the previous section. This causes P_g to be fairly flat, with small oscillations, at the centre of the nanorod and dropping off sharply towards the edge. The gradient near the edge increases with V as observed for smaller nanorods. Notably, the average value of the oscillations is similar to the peak value of P_g for the equivalent $R = 75$ nm case.

8.7.2 Radiated power

The radiated power P_r generally shows oscillatory behaviour and is generally greater than the power η_{ext} extracted from an equivalent dipole in a thick GaN slab, shown as thin grey lines in Figures 8-7 to 8-10. The average value of these oscillations appears to be proportional to n_{clad}. However, for ρ-oriented dipoles, the behaviour of P_r within around 75 nm of the nanorod edge is not oscillatory and instead decays considerably as $\rho_D \to R$, causing P_r to drop below the grey line. This effect, which is significantly weaker in the case of the Si_3N_4 cladding where the refractive index step is much smaller, is due to the discontinuity in E_ρ caused by said index step. The amplitude of the oscillations appears to be inversely proportional to Δ within around 150 nm of the nanorod centre. For the $R = 40$ nm case, decaying behaviour can be observed for all ρ_D and all n_{clad}.

8.7.3 Total power

For $R = 40$ nm, P_g is small compared to P_r so the total power P_T mirrors the decaying behaviour of P_r. For larger R, P_T is again oscillatory, with an average value that is variable but close to unity, i.e. the total power emitted is little different from that emitted by an equivalent dipole in homogeneous GaN. For ρ-oriented dipoles within around 75 nm of the nanorod edge, P_T drops rapidly as seen with both the guided and radiation modes; the value of P_T at the edge appears to be directly proportional to Δ. Returning to the $R = 40$ nm case, the average value of P_T is around 0.75 for Si_3N_4 cladding and decreases very rapidly as n_{clad} is decreased. This suggests Purcell cavity suppression as a possible physical mechanism for the unusual behaviour observed in this case.

8.7.4 Extraction efficiency

The extraction efficiency η_{ext} exceeds the 20% figure quoted for GaN in epoxy in almost all of the cases studied here, except for dipoles close the nanorod centre for $R = 75$ nm and $n_{ext} = 1$. In all cases, P_g falls off much faster than P_r towards the nanorod edge, causing η_{ext} to rapidly increase as $\rho_D \to R$. For $R = 40$ nm η_{ext} exceeds 85% under all conditions. This suggests that these very small nanorods could be superior to surface-roughened LEDs in terms of extraction efficiency. However, this advantage comes at the cost of a significant fall in P_T and by extension the internal quantum efficiency (see next subsection).

8.7.5 Interpretation

Interpreting the large quantity of data present in Figures 8-7-8-10 requires a robust understanding of the physics. As discussed in subsection 5.4.2, the spontaneous emission rate is directly proportional to P_T. Equation (2.15) can therefore be rewritten as

$$\eta_{IQE} = \frac{P_T A' np}{\delta n \sum \frac{1}{\tau_{nr}} + P_T A' np + C_n n^2 p + C_p p^2 n}, \tag{8.25}$$

where $A = P_T A'$ and all other quantities are defined in section 2.3. Substituting (8.25) and (8.24) into (1.1) yields

$$\eta_{EQE} = \frac{P_r \eta_{inj} A' np}{\delta n \sum \frac{1}{\tau_{nr}} + P_T A' np + C_n n^2 p + C_p p^2 n}, \tag{8.26}$$

where η_{inj} is the carrier injection efficiency. Equation (8.26) is somewhat pathological due to having multiple terms in the denominator, but there are two regimes where the behaviour is easier to understand. At one extreme where the internal quantum efficiency is very low, due to one or more of the non-radiative recombination rates τ_{nr}^{-1} being very high or the carrier densities being far from optimum, the external quantum efficiency is approximately proportional to P_r. At the other extreme where the internal quantum efficiency is close to unity, the external quantum efficincy becomes approximately proportional to the extraction efficiency η_{ext} given by (8.24). Inputting the values of P_T from air-clad nanorods into (8.26) shows that both extremes can be represented by different dipoles in the same system.

For most of the hypothetical infinite nanorod structures studied in this chapter, P_r and η_{ext} are both shown to compare favourably with those of thick GaN slabs with the same cladding, suggesting that η_{EQE} will also be superior to that of slabs. Whether or not nanorod LEDs can pass the 80% extraction efficiency benchmark (Shcheckin *et al* 2006, cited in Mottier 2009) required to directly compete with surface-roughened LEDs is less clear. η_{ext} exceeds 80% for all dipoles in the $R = 40$ nm case and for ϕ-oriented dipoles close to the edge in the $R = 75$ nm case, but this is only the critical factor for cases of very high internal quantum efficiency. The absolute radiated power, which is the key quantity for devices with low IQE, is less favourable; $P_r < 0.8$ in all cases. The only way to finding out for certain if nanorod LEDs can compete with surface-roughened ones is to consider any additional radiated power due to diffraction of guided modes at the nanorod ends. Such a model is considered in the chapters that follow.

8.8 Summary

This chapter provides mathematical expressions for the electromagnetic fields of the guided and radiation modes of an infinitely long nanorod, based on the analysis of Adams (1981) and Snyder and Love (1983). The dispersion relations (modal index vs. radius) of the guided modes of GaN nanorods with three different cladding types at $\lambda_0 = 460$ nm are calculated and discussed in section 8.5. In section 8.6 the variation of Poynting vector with position is plotted and discussed for the six guided modes supported by a GaN nanorod of radius $R = 150$ nm surrounded by air. In section 8.7, the variation of the total guided power P_g, total radiated power P_r and total power $P_T = P_g + P_r$ emitted by a Hertzian dipole with the radial position ρ_D of said dipole is plotted and analysed for three types of cladding, four different nanorod radii and two different orientations of the dipole. The dipole current density $|\vec{j}|$ and free space wavelength were kept constant throughough this exercise. The main findings of these simulations were that these hypothetical infinite nanorod structures have superior extraction efficiencies to planar LEDs and that P_T and therefore the internal quantum efficiency can vary significantly from those of planar devices. The diffraction of guided modes at the nanorod ends is essential to determine the precise extraction efficiency and the directionality of the emitted light, so the remaining chapters will focus on this.

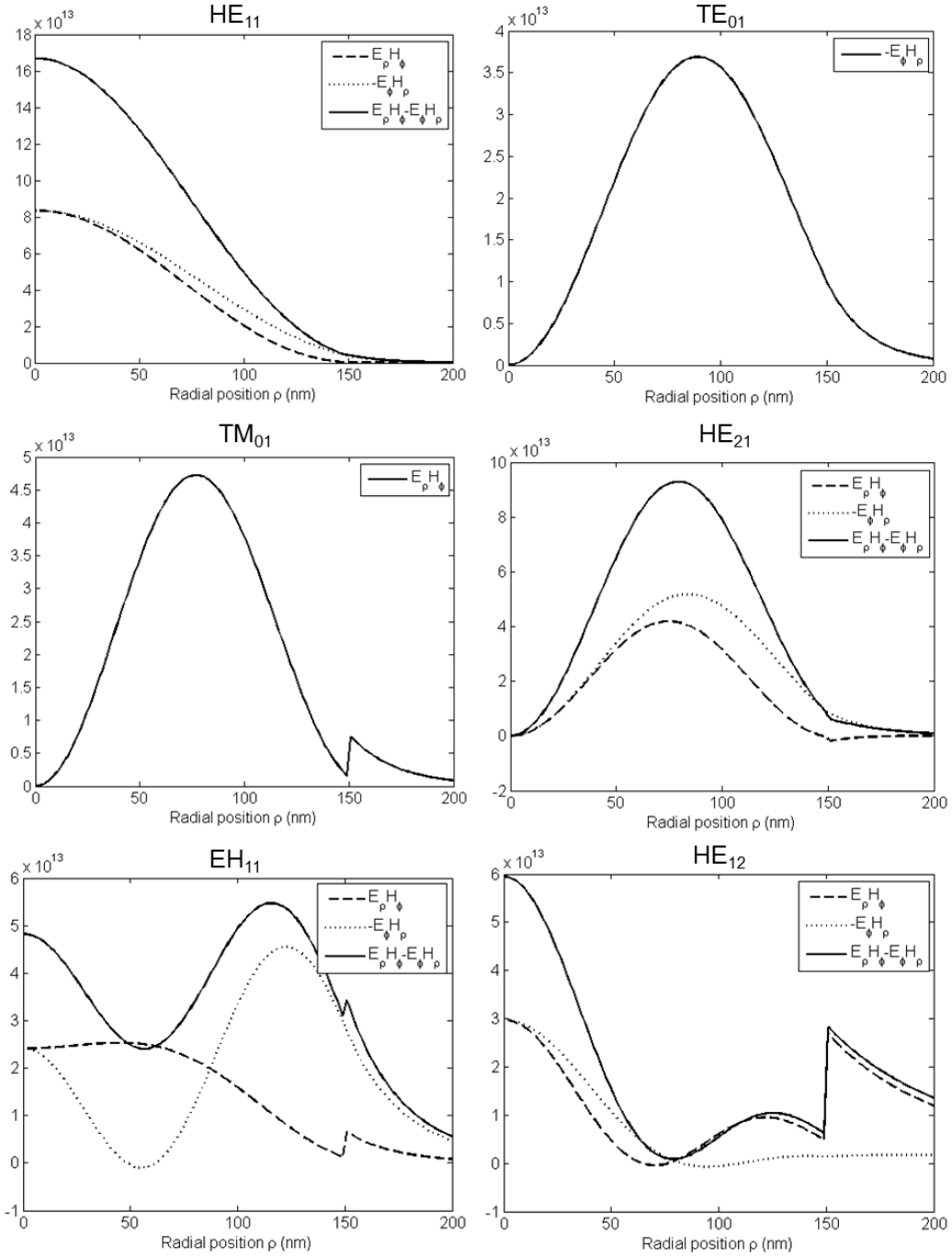

Figure 8-6: Variation of the Poynting vector for all six guided modes of a GaN nanorod with radius $R = 150$ nm surrounded by air at free space wavelength 460 nm. The full Poynting vector is given by the solid line; for hybrid modes, the two terms of (8.17) are also shown as dashed and dotted lines respectively. The modes are normalized to carry unit power.

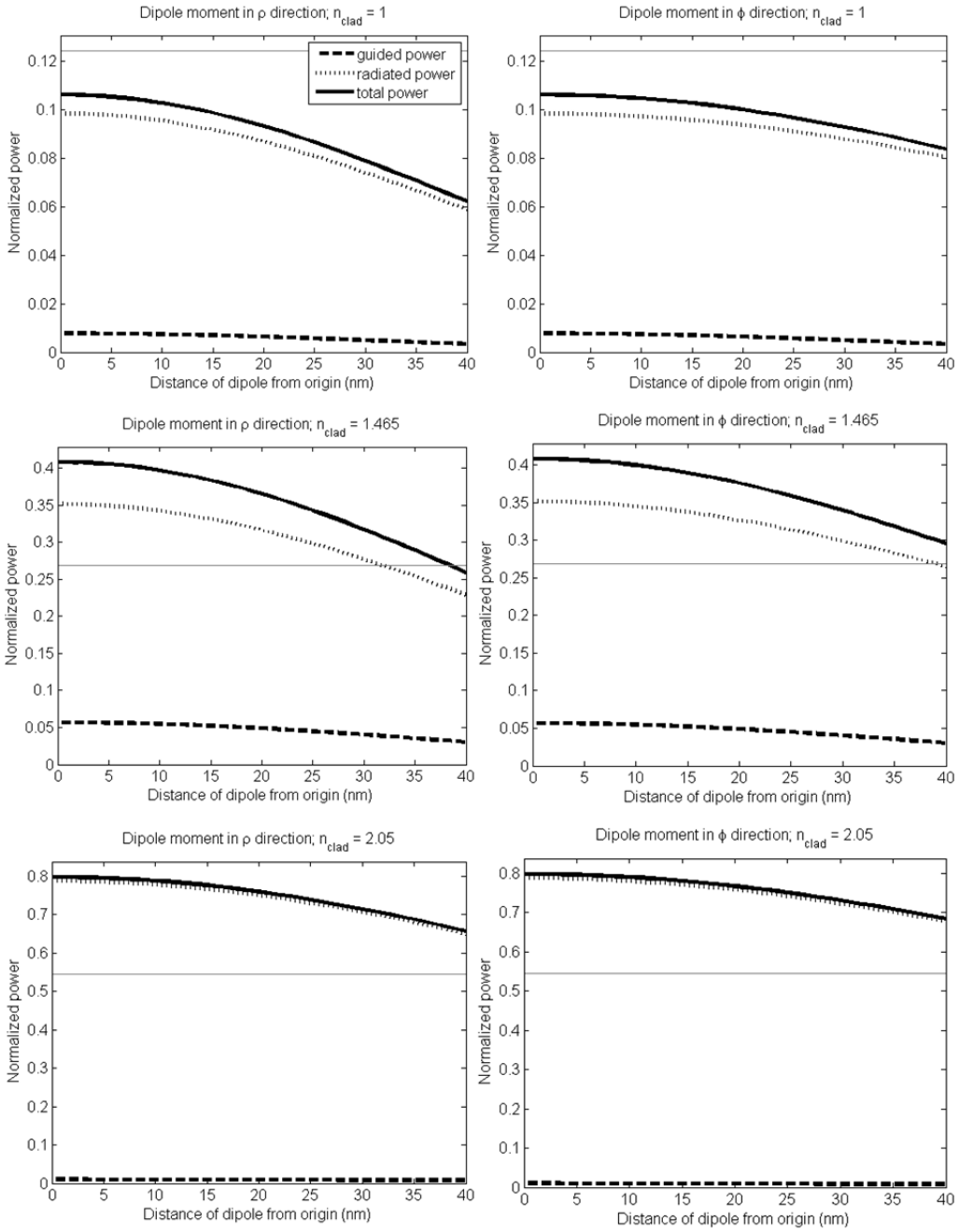

Figure 8-7: Variation of the guided power P_g, radiated power P_r and total power $P_T = P_g + P_r$ with dipole position ρ_D for nanorods of radius $R = 40$ nm. The plots are normalized to the power emitted by an identical dipole in homogeneous GaN. The grey horizontal line represents the power extracted (i.e. not trapped by total internal reflection) from an identical horizontal dipole emitting inside a thick GaN slab clad on both sides by a dielectric of refractive index n_{clad} and is given for reference.

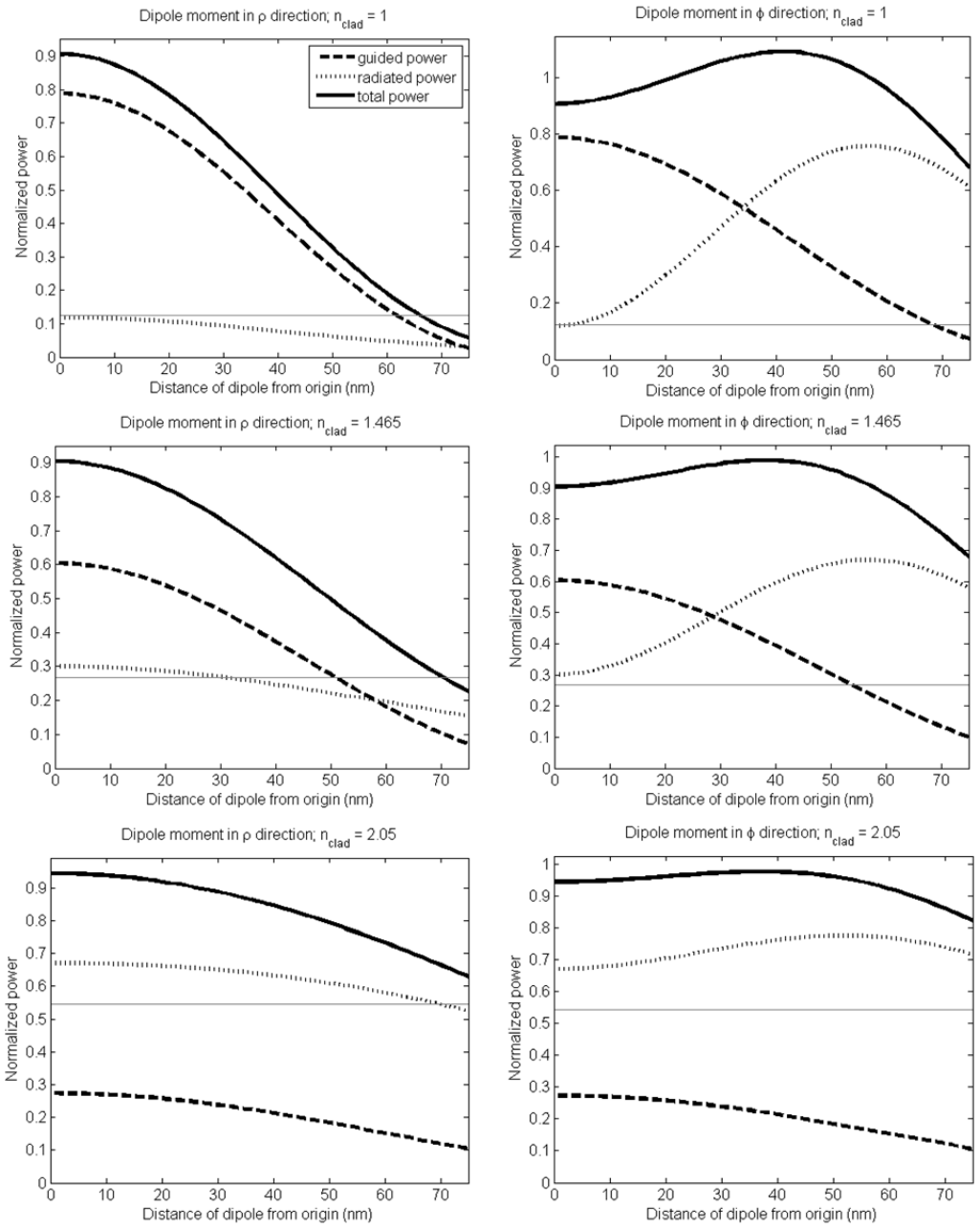

Figure 8-8: Variation of the guided power P_g, radiated power P_r and total power $P_T = P_g + P_r$ with dipole position ρ_D for nanorods of radius $R = 75$ nm. The plots are normalized to the power emitted by an identical dipole in homogeneous GaN. The grey horizontal line represents the power extracted (i.e. not trapped by total internal reflection) from an identical horizontal dipole emitting inside a thick GaN slab clad on both sides by a dielectric of refractive index n_{clad} and is given for reference.

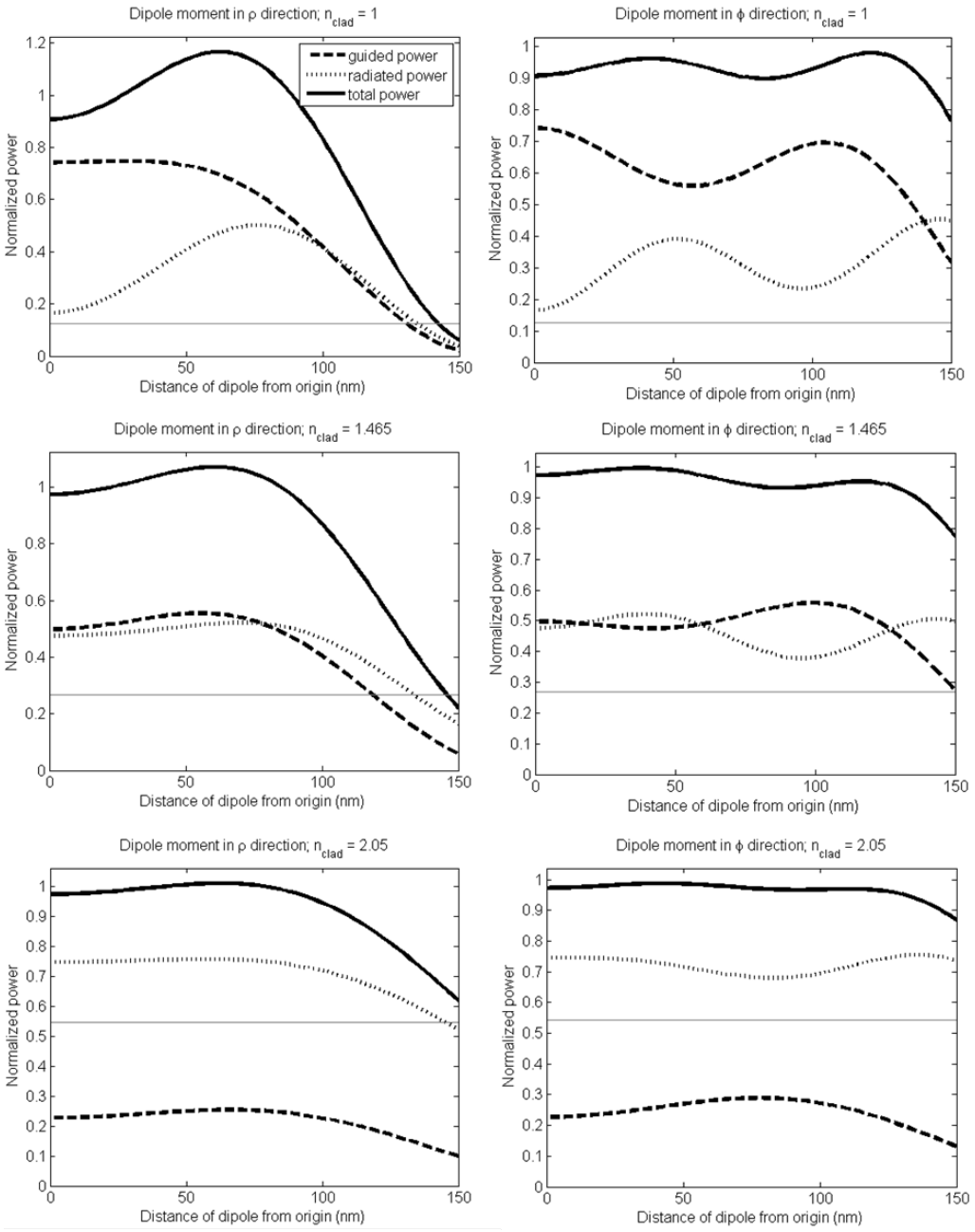

Figure 8-9: Variation of the guided power P_g, radiated power P_r and total power $P_T = P_g + P_r$ with dipole position ρ_D for nanorods of radius $R = 150$ nm. The plots are normalized to the power emitted by an identical dipole in homogeneous GaN. The grey horizontal line represents the power extracted (i.e. not trapped by total internal reflection) from an identical horizontal dipole emitting inside a thick GaN slab clad on both sides by a dielectric of refractive index n_{clad} and is given for reference.

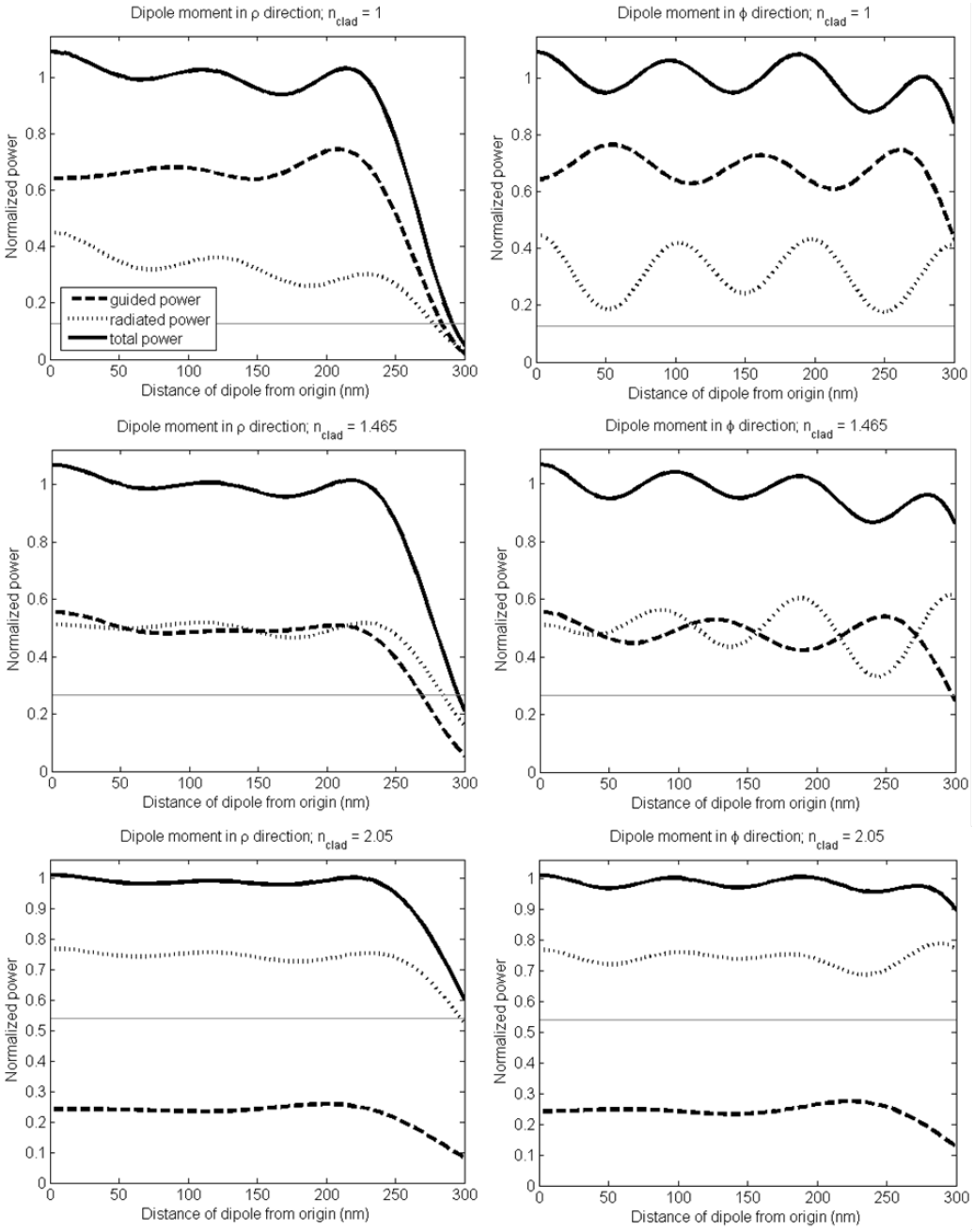

Figure 8-10: Variation of the guided power P_g, radiated power P_r and total power $P_T = P_g + P_r$ with dipole position ρ_D for nanorods of radius $R = 300$ nm. The plots are normalized to the power emitted by an identical dipole in homogeneous GaN. The grey horizontal line represents the power extracted (i.e. not trapped by total internal reflection) from an identical horizontal dipole emitting inside a thick GaN slab clad on both sides by a dielectric of refractive index n_{clad} and is given for reference.

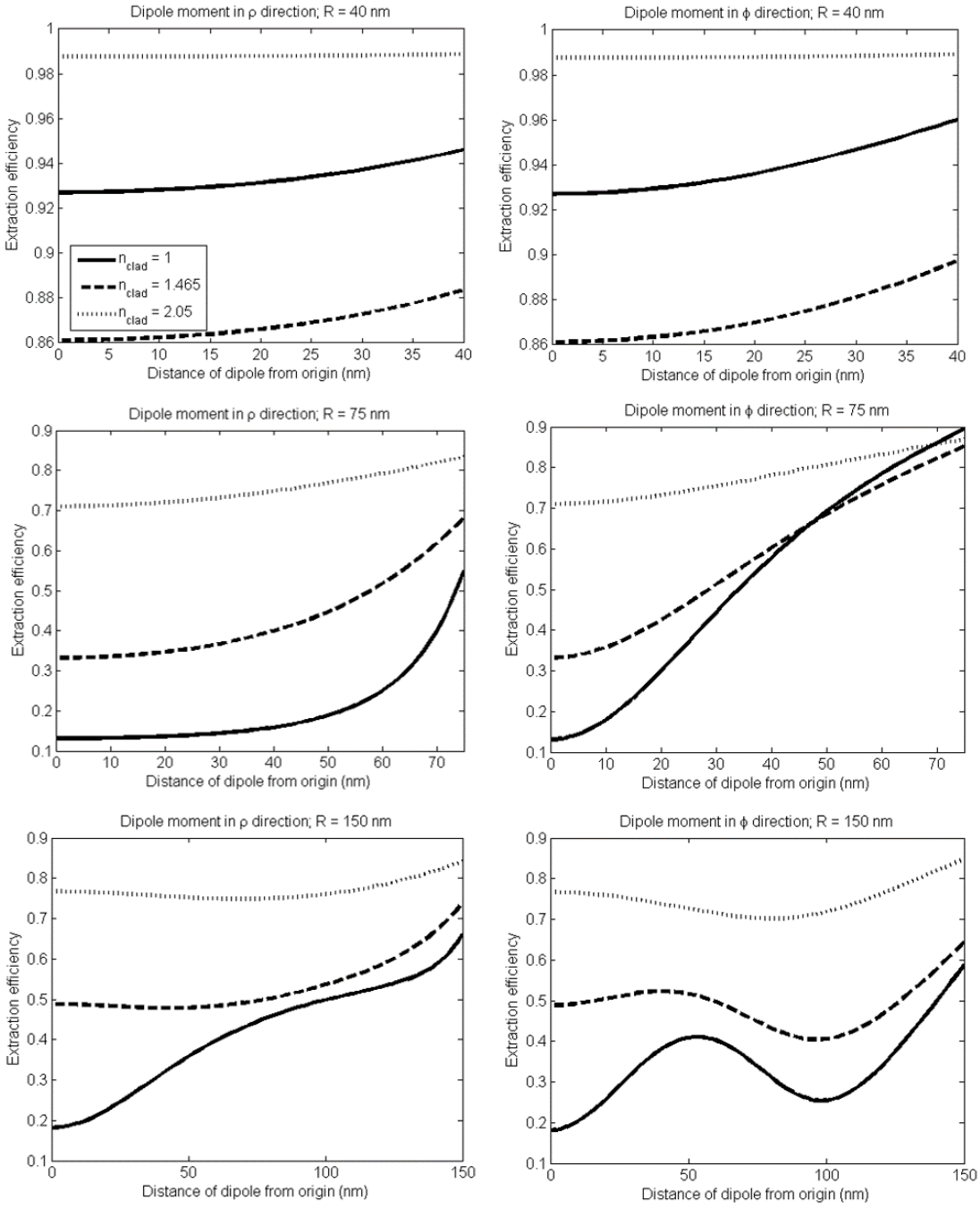

Figure 8-11: Variation of the extraction effiency η_{ext} with dipole position ρ_D.

Chapter 9

Finite length nanorod

9.1 Introduction

Real nanorod LEDs are not infinitely long but usually have lengths between 400 nm and 2 μm, as reported in the literature reviewed in chapter 7. In order to develop an optical model suitable for nanorods of finite length, reflection and diffraction of guided and radiation modes at both ends of the nanorod must be considered. O'Kane *et al.* (2014) report a mathematical technique capable of doing this for guided modes and compare the numerical results with measured data. In this chapter, O'Kane *et al.*'s work on guided modes is reproduced and embellished with additional numerical results and measured data, particularly an investigation of the effect of wavelength. A section on radiation modes, which are not covered in the aforementioned work, is also included.

9.2 The structure under consideration

A nanorod can be modelled by treating it as an optical fibre of finite length bound above and below by two semi-infinite homogenous media. The space where $z_- < z < z_+$ is occupied by the optical fibre, which consists of a cylindrical core of radius R and refractive index n_{core} surrounded by an infinite cladding of refractive index n_{clad}. This simplification neglects the refractive index steps that occur at any heterojunctions between the basic nanorod substructure and an embedded disc-shaped multiple quantum well (MQW) emission region perpendicular to the z axis (see Figure 7-1). This is justified because these refractive index changes are typically quite small (Leung *et al.* 1998, Shi and Chi 2007, Miyajima *et al.* 2011) compared with the step changes at $z = z_+$ and $z = z_-$ (Takeuchi *et al.* 2010, Palik c. 1998) and therefore will marginally perturb the waveguiding properties. The space where $z > z_+$ is occupied by a semi-infinite

homogenous medium of refractive index n_+, while the space where $z < z_-$ is occupied by a semi-infinite homogenous medium of refractive index n_-. The entire structure remains cylindrically symmetric, therefore the cylindrical polar coordinate system can again be used, with the z axis ($\rho = 0$) being at the centre of the fibre as in chapter 8. For convenience, $z = 0$ is set to correspond with the location of the emitting dipole.

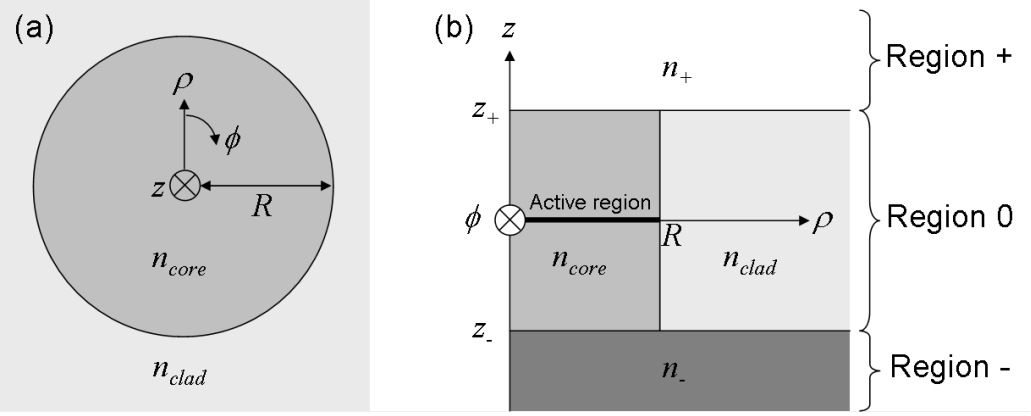

Figure 9-1: The structure to be modelled, in cylindrical polar coordinates. (a) A cross-section through the nanorod. (b) The full structure including vertical confinement.

9.3 Electromagnetic modes of each region

It can be shown (Snyder and Love 1983 pp. 210) that the electromagnetic fields in any z-invariant structure or substructure can be expressed as a superposition of a complete orthonormal set of functions (i.e. the modes) that do not vary in the z direction except for phase. The structure of interest, as depicted in Figure 9-1, consists of three z-invariant regions. In this case, the electromagnetic fields in each region can be expressed as a superposition of modes of that region, provided that the components of the total $\vec{E}$ and $\vec{H}$ fields perpendicular to $\hat{z}$ are continuous at the interface between each region (Chew 1995).

9.3.1 Optical fibre/nanorod region 0

The total electric field $\vec{E}_0(\vec{r}, t)$ and the total magnetic field $\vec{H}_0(\vec{r}, t)$ in the optical fibre region 0 can be expressed as a superposition of the same guided and radiation modes

that the fibre would support if it was infinitely long:

$$\vec{E}_0(\vec{r}) = \sum_j C_j \hat{E}_j(\rho,\phi) \mathrm{e}^{\mathrm{i}\beta_j z} + \sum \int_0^\infty \tilde{c}_0(\sigma_0) \hat{e}_R(\rho,\phi,\sigma_0) \mathrm{e}^{\mathrm{i}\beta_0 z}\, \mathrm{d}\sigma_0 \tag{9.1}$$

$$\vec{H}_0(\vec{r}) = \sum_j C_j \hat{H}_j(\rho,\phi) \mathrm{e}^{\mathrm{i}\beta_j z} + \sum \int_0^\infty \tilde{c}_0(\sigma_0) \hat{h}_R(\rho,\phi,\sigma_0) \mathrm{e}^{\mathrm{i}\beta_0 z}\, \mathrm{d}\sigma_0. \tag{9.2}$$

Equations (9.1) and (9.2) are identical to (8.1) and (8.2) respectively; the only difference is the addition of the subscript 0 to avoid confusion with the radiation modes of regions + and -. The tilde on $\tilde{c}_0$, which is generally complex, is meant to distinguish it from the phase velocity c_0 of light in a vacuum.

9.3.2 Semi-infinite regions + and -

The electric field $\vec{E}_\pm(\vec{r},t)$ and magnetic field $\vec{H}_\pm(\vec{r},t)$ of regions $\pm$ of refractive index $n_\pm$ are expanded in terms of radiation modes only, as there are no guided modes:

$$\vec{E}_\pm(\vec{r},t) = \sum \int_0^\infty c_\pm(\sigma_\pm) \tilde{e}_\pm(\rho,\phi,\sigma_\pm) \mathrm{e}^{\mathrm{i}(\pm\beta_\pm z - \omega t)}\, \mathrm{d}\sigma_\pm \tag{9.3}$$

$$\vec{H}_\pm(\vec{r},t) = \sum \int_0^\infty c_\pm(\sigma_\pm) \tilde{h}_\pm(\rho,\phi,\sigma_\pm) \mathrm{e}^{\mathrm{i}(\pm\beta_\pm z - \omega t)}\, \mathrm{d}\sigma_\pm, \tag{9.4}$$

where

$$\sigma_\pm = \sqrt{k_0^2 n_\pm^2 - \beta_\pm^2} \tag{9.5}$$

and the $c_\pm(\sigma_\pm)$ are the expansion coefficients. The electric fields $\tilde{e}_\pm(\rho,\phi,\sigma_\pm)$ and the magnetic fields $\tilde{h}_\pm(\rho,\phi,\sigma_\pm)$ of the radiation modes are given in Table 9.1, which was created by applying the convention (Snyder and Love 1983 pp. 212) where the electric fields of forward and backward-propagating modes have the same sign but their magnetic fields have opposite signs, to Table 6.2.

As discussed in section 6.8, $\beta_\pm$ and $\sigma_\pm$ are related to the angle $\theta_\pm$ between the time-averaged Poynting vector and the z axis:

$$\beta_\pm = k_0 n_\pm \cos(\theta_\pm) \quad \sigma_\pm = k_0 n_\pm \sin(\theta_\pm). \tag{9.6}$$

	TE modes	TM modes
$\tilde{e}_\pm \cdot \hat{z}$	0	$\mp \mathrm{i} A H_N^{(1)}(\kappa\rho) f(N\phi)$
$\tilde{h}_\pm \cdot \hat{z}$	$-\mathrm{i} A H_N^{(1)}(\kappa\rho) g(N\phi)$	0
$\tilde{e}_\pm \cdot \hat{\rho}$	$-A\frac{Nk_0Z_0}{\kappa^2}\frac{H_N^{(1)}(\kappa\rho)}{\rho} f(N\phi)$	$A\frac{\beta}{\kappa^2}\frac{\mathrm{d}H_N^{(1)}(\kappa\rho)}{\mathrm{d}\rho} f(N\phi)$
$\tilde{h}_\pm \cdot \hat{\rho}$	$\pm A\frac{\beta}{\kappa^2}\frac{\mathrm{d}H_N^{(1)}(\kappa\rho)}{\mathrm{d}\rho} g(N\phi)$	$\mp A\frac{Nk_0n^2}{Z_0\kappa^2}\frac{H_N^{(1)}(\kappa\rho)}{\rho} g(N\phi)$
$\tilde{e}_\pm \cdot \hat{\phi}$	$-A\frac{k_0Z_0}{\kappa^2}\frac{\mathrm{d}H_N^{(1)}(\kappa\rho)}{\mathrm{d}\rho} g(N\phi)$	$A\frac{N\beta}{\kappa^2}\frac{H_N^{(1)}(\kappa\rho)}{\rho} g(N\phi)$
$\tilde{h}_\pm \cdot \hat{\phi}$	$\mp A\frac{N\beta}{\kappa^2}\frac{H_N^{(1)}(\kappa\rho)}{\rho} f(N\phi)$	$\pm A\frac{k_0n^2}{Z_0\kappa^2}\frac{\mathrm{d}H_N^{(1)}(\kappa\rho)}{\mathrm{d}\rho} f(N\phi)$
A	$\Xi_{0N}\kappa\sqrt{\frac{2\kappa}{\pi k_0 Z_0 \beta}}$	$\Xi_{0N}\frac{\kappa}{n}\sqrt{\frac{2Z_0\kappa}{\pi k_0\beta}}$

Table 9.1: Electromagnetic field components of the radiation modes of regions + and - (Snyder and Love 1983 pp. 522).

9.4 Decomposition of the guided modes into radiation modes of effective homogeneous media

The radiation modes of a homogeneous medium are a complete orthonormal set of functions. It therefore follows that any arbitrary electromagnetic field may be decomposed into a spectrum of these functions, even if the medium is not homogeneous. It is convenient to model the guided modes of region 0 in this way as all the radiation modes that make up the guided mode must have the same β as the guided mode:

$$\hat{E}_j(\rho,\phi) = \sum_{TE,TM} \int_0^\infty c_j(\kappa)\hat{e}_j(\rho,\phi,\kappa)\,\mathrm{d}\kappa \tag{9.7}$$

$$\hat{H}_j(\rho,\phi) = \sum_{TE,TM} \int_0^\infty d_j(\kappa)\hat{h}_j(\rho,\phi,\kappa)\,\mathrm{d}\kappa, \tag{9.8}$$

where $\hat{e}_j$ and $\hat{h}_j$ are referred to as 'cylindrical waves' from now on to avoid confusion with the true radiation modes $\hat{e}_R$ and $\hat{h}_R$ of region 0.

As the spectrum of cylindrical waves that makes up each guided mode all share the same z-directed wavevector β (otherwise the composite field ceases to be a mode) but have different ρ-directed wavevectors κ, conservation of wavevector requires that each wave in the spectrum propagates in a homogeneous medium of a different effective

refractive index $n_j(\kappa)$, given by (Kressel and Butler 1977)

$$k_0^2 n_j^2(\kappa) = \kappa^2 + \beta_j^2$$
$$n_j(\kappa) = \frac{\sqrt{\kappa^2 + \beta_j^2}}{k_0}. \tag{9.9}$$

As with the radiation modes of homogeneous media, β and κ are related to the angle $\theta_j(\kappa)$ between the wavevector and the z axis:

$$\beta_j = k_0 n_j(\kappa)\cos[\theta_j(\kappa)] \quad \kappa = k_0 n_j(\kappa)\sin[\theta_j(\kappa)]. \tag{9.10}$$

It is important to note the effective indices do not correspond to any physical media and are merely mathematical abstractions.

The form of $\hat{e}_j$ and $\hat{h}_j$ is now known and displayed in Table 9.2; it is given by substituting $\beta = \beta_j$ and $n = n_j(\kappa)$ into Table 6.1. As the time-averaged Poynting vector

	TE modes	TM modes
$\hat{e}_j \cdot \hat{z}$	0	$-\mathrm{i}AJ_N(\kappa\rho)f(N\phi)$
$\hat{h}_j \cdot \hat{z}$	$-\mathrm{i}AJ_N(\kappa\rho)g(N\phi)$	0
$\hat{e}_j \cdot \hat{\rho}$	$-A\frac{Nk_0Z_0}{\kappa^2}\frac{J_N(\kappa\rho)}{\rho}f(N\phi)$	$A\frac{\beta_j}{\kappa^2}\frac{\mathrm{d}J_N(\kappa\rho)}{\mathrm{d}\rho}f(N\phi)$
$\hat{h}_j \cdot \hat{\rho}$	$A\frac{\beta_j}{\kappa^2}\frac{\mathrm{d}J_N(\kappa\rho)}{\mathrm{d}\rho}g(N\phi)$	$-A\frac{Nk_0n_j^2(\kappa)}{Z_0\kappa^2}\frac{J_N(\kappa\rho)}{\rho}g(N\phi)$
$\hat{e}_j \cdot \hat{\phi}$	$-A\frac{k_0Z_0}{\kappa^2}\frac{\mathrm{d}J_N(\kappa\rho)}{\mathrm{d}\rho}g(N\phi)$	$A\frac{N\beta_j}{\kappa^2}\frac{J_N(\kappa\rho)}{\rho}g(N\phi)$
$\hat{h}_j \cdot \hat{\phi}$	$-A\frac{N\beta_j}{\kappa^2}\frac{J_N(\kappa\rho)}{\rho}f(N\phi)$	$A\frac{k_0n_j^2(\kappa)}{Z_0\kappa^2}\frac{\mathrm{d}J_N(\kappa\rho)}{\mathrm{d}\rho}f(N\phi)$
A	$\Xi_{0N}\kappa\sqrt{\frac{2\kappa}{\pi k_0 Z_0 \beta_j}}$	$\Xi_{0N}\frac{\kappa}{n_j(\kappa)}\sqrt{\frac{2Z_0\kappa}{\pi k_0\beta_j}}$

Table 9.2: Electromagnetic field components of the cylindrical waves used to decompose the guided modes (Snyder and Love 1983 pp. 522).

for guided modes lies entirely in the z direction, the use of Bessel functions as opposed to the Hankel functions used for the modes of regions + and - is appropriate. Note that because the entire structure depicted in Figure 9-1 is azimuthally symmetric, the cylindrical waves must have the same N value and ϕ variation $f(\phi)$ as the guided mode j being decomposed. The $c_j(\kappa)$ and $d_j(\kappa)$ in (9.7) and (9.8) are found by subjecting

the modal fields $\hat{E}_j$ and $\hat{H}_j$ to integral transforms:

$$c_j(\kappa) = \tfrac{1}{2}\int_0^{2\pi}\int_0^{\infty} \hat{E}_j(\rho,\phi) \times \hat{h}_j(\rho,\phi,\kappa) \cdot \hat{z}\rho \,\mathrm{d}\rho \,\mathrm{d}\phi \tag{9.11}$$

$$d_j(\kappa) = \tfrac{1}{2}\int_0^{2\pi}\int_0^{\infty} \hat{e}_j(\rho,\phi,\kappa) \times \hat{H}_j(\rho,\phi) \cdot \hat{z}\rho \,\mathrm{d}\rho \,\mathrm{d}\phi. \tag{9.12}$$

For the TE waves, for which $n_j(\kappa)$ does not enter (9.11) or (9.12), $c_j(\kappa) = d_j(\kappa)$. For TM waves this is not the case and the impedance Z of the cylindrical waves is distorted by a factor of $\zeta_j(\kappa)$:

$$Z = \zeta_j(\kappa)\frac{Z_0}{n_j(\kappa)}, \tag{9.13}$$

where

$$\zeta_j(\kappa) = \frac{c_j(\kappa)}{d_j(\kappa)}. \tag{9.14}$$

This can be simulated by treating the effective media as being magnetic with effective permeabilities $\mu_j(\kappa) = \zeta_j(\kappa)\mu_0$ (Jackson 199 pp. 303-306, Sadiku 2006 pp. 473). As $n_j(\kappa)$ must be unchanged so that the wavevector is still conserved, the effective permittivities $\epsilon_j(\kappa)$ must be adjusted to compensate:

$$n_j(\kappa) = k_0^{-1}\sqrt{\beta_j^2 + \kappa^2} = \sqrt{\mu_j(\kappa)\epsilon_j(\kappa)}. \tag{9.15}$$

It should again be emphasized that the effective permeability and permittivity are not physical. What the effective permeability corresponds to physically is the discontinuity in $\hat{E}_j \cdot \hat{\rho}$ at $\rho = R$ that arises in TM and hybrid modes. Such a discontinuity cannot be reproduced through a superposition of cylindrical waves in non-magnetic media. As this problem does not arise for TE modes, the effective media for TE waves are non-magnetic.

It is even possible for $\zeta_j(\kappa)$ to be negative. In this case the effective medium becomes a negative-index or left-handed medium (Veselago 1968), for which the phase velocity and group velocity become antiparallel. Cylindrical waves in negative-index media therefore carry negative power, although the total power in the mode being decomposed remains positive. Indeed, the concept of negative $\zeta_j(\kappa)$ is required to satisfy power conservation at the $z = z_{\pm}$ interfaces. For most cases of practical interest, cylindrical waves with negative $\zeta_j(\kappa)$ lie outside the light extraction cone and undergo total internal reflection.

Through this method, each guided mode of the nanorod can be modelled as a spectrum of cylindrical waves in effective homogeneous media. This allows a far-field diffraction

pattern resulting from a given guided mode to be computed. As both the cylindrical waves and radiation modes of regions + and - have already been shown to satisfy the Fresnel equations in sections 6.7 and 6.8, the effects of the Fabry-Pérot cavity formed by the two ends of the nanorod can also be accounted for, as follows. The reflection coefficients $r_{j\pm}(\kappa)$ and transmission coefficients $t_{j\pm}(\kappa)$ at $z = z_\pm$ are given by substituting (9.15) into the Fresnel equations (4.45), (4.46), (4.47) and (4.48):

$$r_{j\pm}(\kappa) = \frac{\beta_j - \beta_\pm(\kappa)}{\beta_j + \beta_\pm(\kappa)} \tag{9.16}$$

$$t_{j\pm}(\kappa) = \frac{2\beta_j}{\beta_j + \beta_\pm(\kappa)} \tag{9.17}$$

for TE waves and

$$r_{j\pm}(\kappa) = \frac{n_j^2(\kappa)\beta_\pm(\kappa) - |\zeta_j(\kappa)|n_\pm^2\beta_j}{n_j^2(\kappa)\beta_\pm(\kappa) + |\zeta_j(\kappa)|n_\pm^2\beta_j} \tag{9.18}$$

$$t_{j\pm}(\kappa) = \frac{2n_\pm n_j(\kappa)\beta_j(\kappa)}{n_j^2(\kappa)\beta_\pm(\kappa) + |\zeta_j(\kappa)|n_\pm^2\beta_j} \tag{9.19}$$

for TM waves. However, the $t_{j\pm}(\kappa)$ are the transmission coefficients for the individual interfaces only. The two parallel interfaces form a Fabry-Pérot cavity, causing interference effects to occur so that the 'total' transmission coefficient $\tau_{j\pm}(\kappa)$ out of the $z = z_\pm$ end of the cavity is given by (5.46) (for simplicity, the absorbance of the quantum wells is neglected):

$$\tau_{j\pm}(\kappa) = \frac{t_{j\pm}(\kappa)\mathrm{e}^{\mathrm{i}\beta_j|z_\pm|}\left(1 + r_{j\mp}\mathrm{e}^{\mathrm{i}\beta_j|z_\mp|}\right)}{1 - r_{j+}r_{j-}\mathrm{e}^{\mathrm{i}\beta_j(|z_+|+|z_-|)}}. \tag{9.20}$$

The transmittance $T_{j\pm}(\kappa)$ (enhancement/suppression by the cavity in terms of optical power) is then given by

$$T_{j\pm}(\kappa) = |\zeta_j(\kappa)|\frac{\mathrm{Re}[\beta_\pm(\kappa)]}{\beta_j}|\tau_{j\pm}(\kappa)|^2. \tag{9.21}$$

The transmitted power $p_{j\pm}$ of a cylindrical wave is given by

$$\begin{aligned} p_{j\pm}(\kappa) &= \tfrac{1}{2}c_j(\kappa)d_j^*(\kappa)T_{j\pm}(\kappa)\int_0^{2\pi}\int_0^\infty \hat{e}_j \times \hat{h}_j^* \cdot \hat{z}\rho\,\mathrm{d}\rho\,\mathrm{d}\phi \\ &= c_j(\kappa)d_j^*(\kappa)T_{j\pm}(\kappa) \\ &= \mathrm{sign}[\zeta_j(\kappa)]\frac{\beta_\pm(\kappa)}{\beta_j}|c_j(\kappa)\tau_{j\pm}(\kappa)|^2. \end{aligned} \tag{9.22}$$

However, as the cylindrical waves are a continuum of radiation modes, any physical power $P_{j\pm}$ and corresponding intensity $I_{j\pm}$ must be found using (6.31) and (6.32):

$$P_{j\pm} = \int_{\theta_1}^{\theta_2} p_{j\pm}\beta_{\pm}\,\mathrm{d}\theta_{\pm}. \tag{9.23}$$

and

$$I_{j\pm} = \frac{\int_{\theta_1}^{\theta_2} p_{j\pm}\beta_{\pm}\,\mathrm{d}\theta_{\pm}}{2\pi r^2 \int_{\theta_1}^{\theta_2} \sin(\theta_{\pm})\,\mathrm{d}\theta_{\pm}}, \tag{9.24}$$

where the hemisphere radius r is an arbitrary constant and can be set to unity without loss of generality.

As in chapter 5, it is possible to generalize the model outlined in this chapter to situations where there are multilayered optical materials at either end of the fibre, provided that these materials vary in the z direction only, using the transfer matrix method (Hecht 2005 pp. 426-428), provided the semi-infinite layers at both ends of the stack are not absorbing (Yeh 1988 pp. 65).

9.5 Treatment of radiation modes

The radiation modes of the nanorod can also be decomposed into cylindrical waves in a homogeneous medium. The electromagnetic fields $\hat{e}_R$ and $\hat{h}_R$ of the radiation modes are given by the methods of section 8.4, setting $\sigma = \sigma_0$:

$$\sigma_0 = \sqrt{k_0^2 n_{clad}^2 - \beta_0^2}. \tag{9.25}$$

Unlike the guided modes, the radiation modes have a real part to the radial components of their Poynting vectors, so they should be decomposed in terms of propagating (Hankel function) cylindrical waves of homgeneous media:

$$\hat{e}_R(\rho,\phi,\sigma_0) = \sum_{TE,TM} \int_0^{\infty} c(\sigma_0,\kappa)\tilde{e}(\rho,\phi,\kappa)\,\mathrm{d}\kappa \tag{9.26}$$

$$\hat{h}_R(\rho,\phi,\sigma_0) = \sum_{TE,TM} \int_0^{\infty} d(\sigma_0,\kappa)\tilde{h}(\rho,\phi,\kappa)\,\mathrm{d}\kappa, \tag{9.27}$$

where

$$c(\sigma_0,\kappa) = \tfrac{1}{2}\int_0^{2\pi}\int_0^{\infty} \hat{e}_R(\rho,\phi,\sigma_0)\times\tilde{h}(\rho,\phi,\sigma_0,\kappa)\cdot\hat{z}\rho\,\mathrm{d}\rho\,\mathrm{d}\phi \tag{9.28}$$

$$d(\sigma_0,\kappa) = \tfrac{1}{2}\int_0^{2\pi}\int_0^{\infty} \tilde{e}(\rho,\phi,\sigma_0,\kappa)\times\hat{h}_R(\rho,\phi,\sigma_0)\cdot\hat{z}\rho\,\mathrm{d}\rho\,\mathrm{d}\phi, \tag{9.29}$$

the functions $\tilde{e}$ and $\tilde{h}$ are given by Table 9.3 and

$$n(\sigma_0,\kappa) = k_0^{-1}\sqrt{\beta_0^2+\kappa^2}. \tag{9.30}$$

As with the guided modes, $\beta = \beta_0\,\forall\kappa$, otherwise the radiation mode ceases to be a

	TE modes	TM modes
$\tilde{e}\cdot\hat{z}$	0	$-\mathrm{i}AH_N^{(1)}(\kappa\rho)f(N\phi)$
$\tilde{h}\cdot\hat{z}$	$-\mathrm{i}AH_N^{(1)}(\kappa\rho)g(N\phi)$	0
$\tilde{e}\cdot\hat{\rho}$	$-A\frac{Nk_0Z_0}{\kappa^2}\frac{H_N^{(1)}(\kappa\rho)}{\rho}f(N\phi)$	$A\frac{\beta}{\kappa^2}\frac{\mathrm{d}H_N^{(1)}(\kappa\rho)}{\mathrm{d}\rho}f(N\phi)$
$\tilde{h}\cdot\hat{\rho}$	$A\frac{\beta}{\kappa^2}\frac{\mathrm{d}H_N^{(1)}(\kappa\rho)}{\mathrm{d}\rho}g(N\phi)$	$-A\frac{Nk_0n^2(\sigma_0,\kappa)}{Z_0\kappa^2}\frac{H_N^{(1)}(\kappa\rho)}{\rho}g(N\phi)$
$\tilde{e}\cdot\hat{\phi}$	$-A\frac{k_0Z_0}{\kappa^2}\frac{\mathrm{d}H_N^{(1)}(\kappa\rho)}{\mathrm{d}\rho}g(N\phi)$	$A\frac{N\beta}{\kappa^2}\frac{H_N^{(1)}(\kappa\rho)}{\rho}g(N\phi)$
$\tilde{h}\cdot\hat{\phi}$	$-A\frac{N\beta}{\kappa^2}\frac{H_N^{(1)}(\kappa\rho)}{\rho}f(N\phi)$	$A\frac{k_0n^2(\sigma_0,\kappa)}{Z_0\kappa^2}\frac{\mathrm{d}H_N^{(1)}(\kappa\rho)}{\mathrm{d}\rho}f(N\phi)$
A	$\Xi_{0N}\kappa\sqrt{\frac{2\kappa}{\pi k_0Z_0\beta}}$	$\Xi_{0N}\frac{\kappa}{n}\sqrt{\frac{2Z_0\kappa}{\pi k_0\beta}}$

Table 9.3: Electromagnetic field components of the cylindrical waves used to decompose the radiation modes (Snyder and Love 1983 pp. 522).

mode. It is convenient to denote the electric field $\hat{e}_R$ of the radiation modes in a piecewise manner:

$$\hat{e}_R(\rho,\phi,\sigma_0) = \begin{cases}\hat{e}_{core} & \rho\le R\\ \hat{e}_{clad} & \rho\ge R\end{cases} \tag{9.31}$$

and likewise for $\hat{h}_R$. Substituting (9.31) into (9.28) gives

$$c(\sigma_0,\kappa) = \tfrac{1}{2}\int_0^{2\pi}\left[\int_0^{R}\hat{e}_{core}\times\tilde{h}\cdot\hat{z}\rho\,\mathrm{d}\rho + \int_R^{\infty}\hat{e}_{clad}\times\tilde{h}\cdot\hat{e}\rho\,\mathrm{d}\rho\right]\mathrm{d}\phi. \tag{9.32}$$

Equation (9.32) contains two integrals over ρ inside the square brackets. The first integral is taken over a finite range and is therefore negligibly small compared to the

second integral, which takes the form of a delta function with complex amplitude $\tilde{a}$:

$$c(\sigma_0,\kappa) \approx \tfrac{1}{2}\int_0^{2\pi}\int_0^{\infty} \hat{e}_{clad}\times\tilde{h}\cdot\hat{z}\rho \mathrm{d}\rho\,\mathrm{d}\phi = \tilde{a}(\sigma_0)\delta(\kappa-\sigma_0). \tag{9.33}$$

Substituting $\kappa=\sigma_0$ into (9.30) gives $n(\sigma_0=\kappa)=n_{clad}\,\forall\sigma_0$. This means the effective medium is non-magnetic and therefore

$$d(\sigma_0,\kappa) \approx c(\sigma_0,\kappa) \approx \tilde{a}(\sigma_0)\delta(\kappa-\sigma_0). \tag{9.34}$$

Substituting (9.33) and (9.34) into (9.26) and (9.27) yields

$$\hat{e}_R(\rho,\phi,\sigma_0) \approx \tilde{a}_{TE}\tilde{e}_{TE}(\rho,\phi,\sigma_0=\kappa)+\tilde{a}_{TM}\tilde{e}_{TM}(\rho,\phi,\sigma_0=\kappa) \tag{9.35}$$

$$\hat{h}_R(\rho,\phi,\sigma_0) \approx \tilde{a}_{TE}\tilde{h}_{TE}(\rho,\phi,\sigma_0=\kappa)+\tilde{a}_{TM}\tilde{h}_{TM}(\rho,\phi,\sigma_0=\kappa). \tag{9.36}$$

It is important to note that the above are approximations and that the fields in and around the nanorod core will be slightly different. When evaluating the fields at any particular point (e.g. for calculating the mode excitation) it is strongly advised that the more rigorous treatment in section 8.4 is used. The expressions for $\tilde{a}_{TE}$ and $\tilde{a}_{TM}$ for ITE (initially transverse electric) and ITM (initially transverse magnetic) radiation modes are given in Table 9.4 in terms of the algebraic constants c_f, c_s, d_f and d_s defined in Table 8.4. Inspection of these Tables shows that while power is conserved ($|\tilde{a}_{TE}+\tilde{a}_{TM}|^2=1$), the presence of the nanorod induces a phase shift relative to what would be the case if there was no nanorod. This phase shift is not predicted for the guided modes. Equations (9.20) to (9.24) can be applied to radiation modes by setting

Mode polarization	$\tilde{a}_{TE}$	$\tilde{a}_{TM}$
TE ($N=0$)	$-\mathrm{i}(d_f+2d_s)\sqrt{\dfrac{\pi k_0 Z_0\beta_0}{\sigma_0^3}}$	0
TM ($N=0$)	0	$-\mathrm{i}n_{clad}(c_f+2c_s)\sqrt{\dfrac{\pi k_0\beta_0}{Z_0\sigma_0^3}}$
ITE ($N\neq 0$)	$-\mathrm{i}(d_f+2d_s)\sqrt{\dfrac{\pi k_0 Z_0\beta_0}{2\sigma_0^3}}$	$-\mathrm{i}n_{clad}c_s\sqrt{\dfrac{2\pi k_0\beta_0}{Z_0\sigma_0^3}}$
ITM ($N\neq 0$)	$-\mathrm{i}d_s\sqrt{\dfrac{2\pi k_0 Z_0\beta_0}{\sigma_0^3}}$	$-\mathrm{i}n_{clad}(c_f+2c_s)\sqrt{\dfrac{\pi k_0\beta_0}{2Z_0\sigma_0^3}}$

Table 9.4: Expressions for $\tilde{a}_{TE}$ and $\tilde{a}_{TM}$ for different radiation mode polarizations.

$\zeta = 1$, $\beta_j = \beta = 0$ and $c_j = d_j = \tilde{a}$, so that

$$p_{\pm}(\sigma_0) = \frac{\beta_{\pm}(\sigma_0)}{\beta_0(\sigma_0)} |\tilde{a}(\sigma_0)\tau(\sigma_0)|^2 \tag{9.37}$$

and

$$I_{\pm} = \frac{\int_{\theta_1}^{\theta_2} p_{\pm}\beta_{\pm}\,\mathrm{d}\theta_{\pm}}{2\pi r^2 \int_{\theta_1}^{\theta_2} \sin(\theta_{\pm})\,\mathrm{d}\theta_{\pm}}. \tag{9.38}$$

9.6 Implementation

A nanorod with a gallium nitride (GaN) core of radius $R = 140$ nm and an air ($n_{clad} = 1$) cladding was considered. The refractive index n_{core} of the GaN as a function of wavelength was calculated using a Sellmeier function (Takeuchi *et al.* 2010). As blue and green LEDs are a matter of considerable research interest (Harbers *et al.* 2007), the free space wavelength range $\lambda_0 = 460 - 580$ nm was chosen for investigation. Such a fibre supports four guided modes at the long wavelength end of this range and six modes at the short wavelength end as depicted in Figure 9-2, which shows how the modal index $n_m = \beta_j k_0^{-1}$ varies with wavelength. All modes tend towards cut-off (when $n_m = n_{clad}$) with increasing wavelength apart from the fundamental mode HE_{11} that exists for all wavelengths. Note that $n_m = n_j(\kappa = 0)$.

The effect of vertical confinement on the modes depicted in Figure 9-2 was evaluated using the methods in section 9.4. The simulated device structure, depicted in Figure 9-3, is based on an experimental nanorod array fabricated by Zhuang (2012) from a commercial wafer (Epistar 2012) and similar to that realized by Zhuang *et al.* (2013a). A GaN nanorod of radius $R = 140$ nm and height $z_+ + z_- = 400$ nm is surrounded by air in the ρ and $+z$ directions; in the $-z$ direction is a planar GaN layer 3100 nm thick followed by what is effectively a semi-infinite layer of sapphire (Al_2O_3). The fabricated nanorods formed a hexagonal array with pitch (distance between nanorod centres) $\Lambda = 600$ nm, although only one isolated nanorod was considered in the simulation. Different positions of a single quantum well (SQW) active region are considered. The refractive index of sapphire was calculated using a Sellmeier fit to data from Palik *et al.* (1998).

The far field diffraction pattern is calculated by taking the + branch of (9.24) and integrating over ranges of $\delta\theta_+ = \theta_2 - \theta_1 = 1^\circ$ for each data point. Each of the waveguide modes was considered on an individual basis and normalized so that it would carry unit power in a waveguide of infinite length. The position of the quantum well is

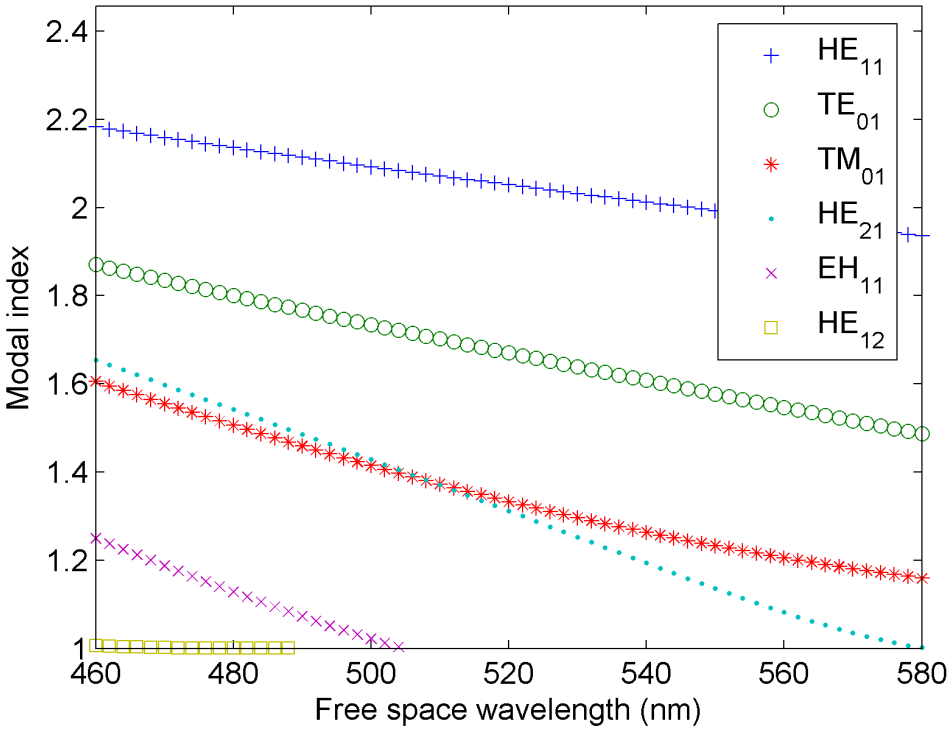

Figure 9-2: Variation of modal index with wavelength of all six guided modes supported by a GaN cylinder of radius $R = 140$ nm surrounded by air.

only taken into account when calculating the transmission coefficients τ_+. As a result, the far-field intensity pattern $I_+(\theta_+)$ takes into account any enhancement/suppression resulting from Fabry-Pérot interference effects.

9.7 Effect of quantum well position and excitation on the diffraction pattern of the fundamental mode

9.7.1 Single quantum well

The effect of changing the position of the quantum well relative to the nanorod, i.e. varying z_- while maintaining $z_+ + z_- = 400$ nm, was investigated for the fundamental HE_{11} mode at $\lambda_0 = 460$ nm. The results are shown in Figure 9-4, which takes the form of polar plots of the far-field intensity $I_+(\theta_+)$, as do all subsequent Figures. Inspection of Figure 9-4 shows that the diffraction patterns corresponding to the six positions of the active region vary significantly in a systematic fashion. As the distance z_- between the quantum well and the planar GaN layer (see Figure 9-3) is increased, the

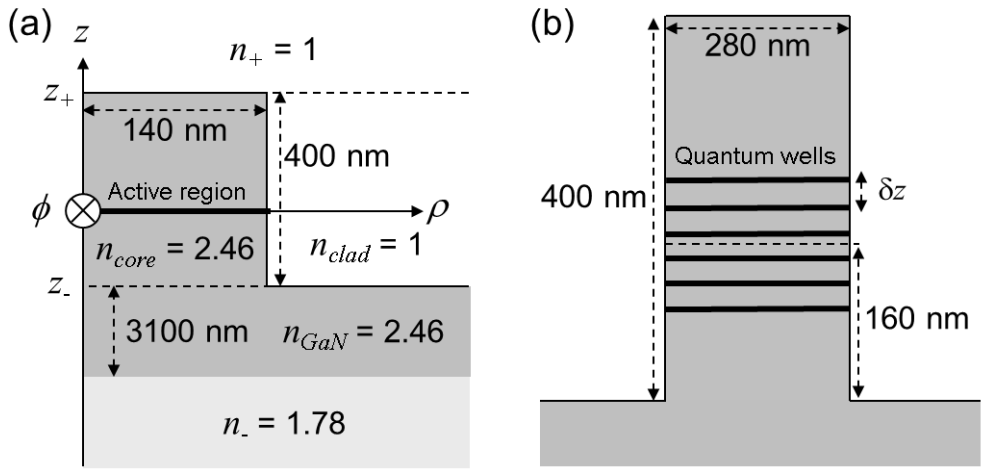

Figure 9-3: (a) The GaN-on-sapphire nanorod structure being investigated, in cylindrical coordinates; refractive index values for $\lambda_0 = 502$ nm. (b) Nanorod without coordinate system, with relative positions of the six quantum wells. Diagrams not to scale.

central lobe oscillates in strength through what is almost a complete cycle, as expected from (9.20), while the side lobes move outwards and decrease in intensity, gradually separating from the central lobe before evolving back into the original shape.

9.7.2 Multiple quantum well: effect of well separation

Most practical devices use multiple quantum well (MQW) active regions, so any practical HE_{11} diffraction pattern will not conform to one of the shapes presented in Figure 9-4 but a composite of all of them. This can be simulated by performing the calculation for each quantum well and adding the results incoherently (i.e. adding the intensities together). For the case of photoluminescence, it is safe to assume that all six of the quantum wells depicted in Figure 9-3 (b) are equally excited, as the quantum wells have absorption coefficients of around 5000 cm^{-1} (Miyajima *et al.* 2011) and widths of around 2.5 nm (Zhuang 2012), resulting in a total absorption through the MQW of $\sim 1\%$. This was done for six different values of the quantum well separation ($\delta z = 20$, 18, 16, 14, 12, 10 nm) for the fundamental HE_{11} mode at $\lambda_0 = 460$ nm. The centre of the MQW was fixed to be 160 nm from the nanorod base, as shown in Figure 9-3 (b), while the quantum well separation was varied. The results are shown in Figure 9-5. As δz is decreased, all of the quantum wells move towards the central 160 nm point, resulting in the side lobes becoming slightly more prominent at the expense of the central lobe. These results are consistent with Figure 9-4, which shows that the side

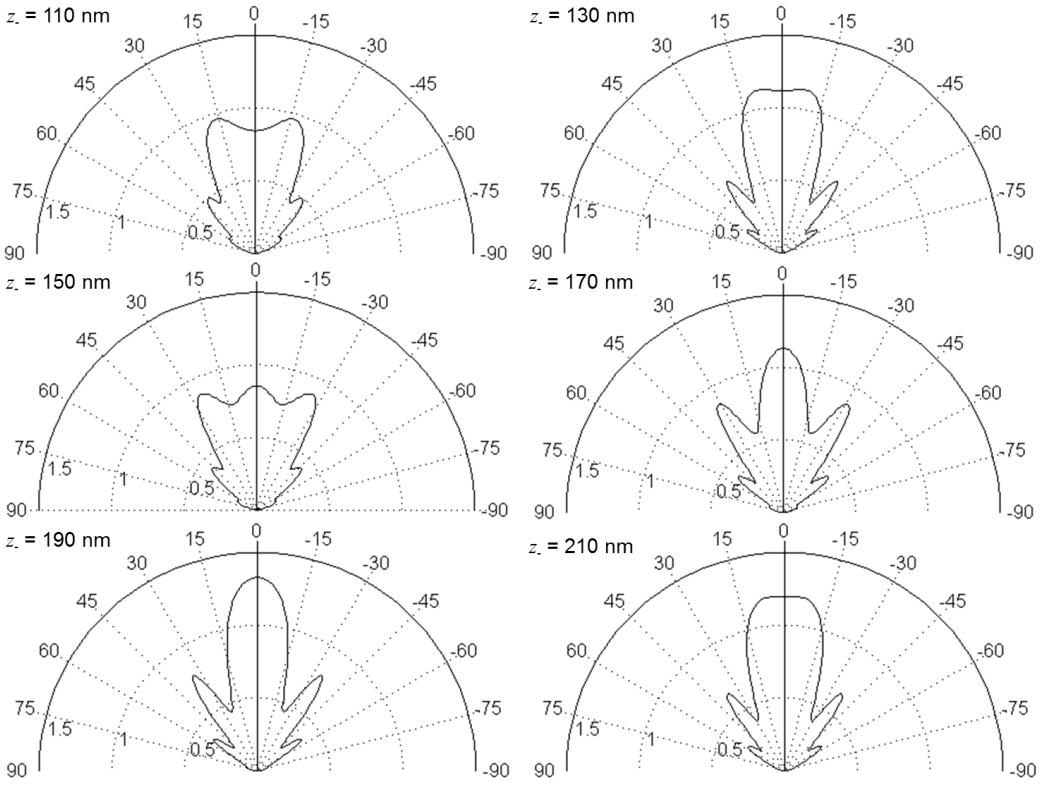

Figure 9-4: Diffraction pattern $I_+(\theta_+)$ of the fundamental HE_{11} mode at $\lambda_0 = 460$ nm for six positions of the active region, with spacing $\delta z = 20$ nm, within the nanorod structure of Figure 9-3. The mode is normalized so that it would carry unit power in an infinitely long nanorod.

lobes at around 30° and 50° are especially strong for emission close to the central 160 nm point, while the central and 37.5° lobes are strongest for emission from quantum wells located far from 160 nm.

Based on the results presented in Figures 9-4 and 9-5, it can be seen that the position of the MQW, the number of quantum wells and their separation can all have a significant effect on the direction of light emission from a nanorod LED. These are identified here as critical parameters in the design of highly directional nanorod LEDs.

9.7.3 Multiple quantum well: effect of unequal excitation

The assumption that all quantum wells are equally excited works well for photoluminescence but not for electroluminescence. The mobility of electrons in GaN is greater than that of holes; as a result, the quantum wells on the p-side of the device (in this

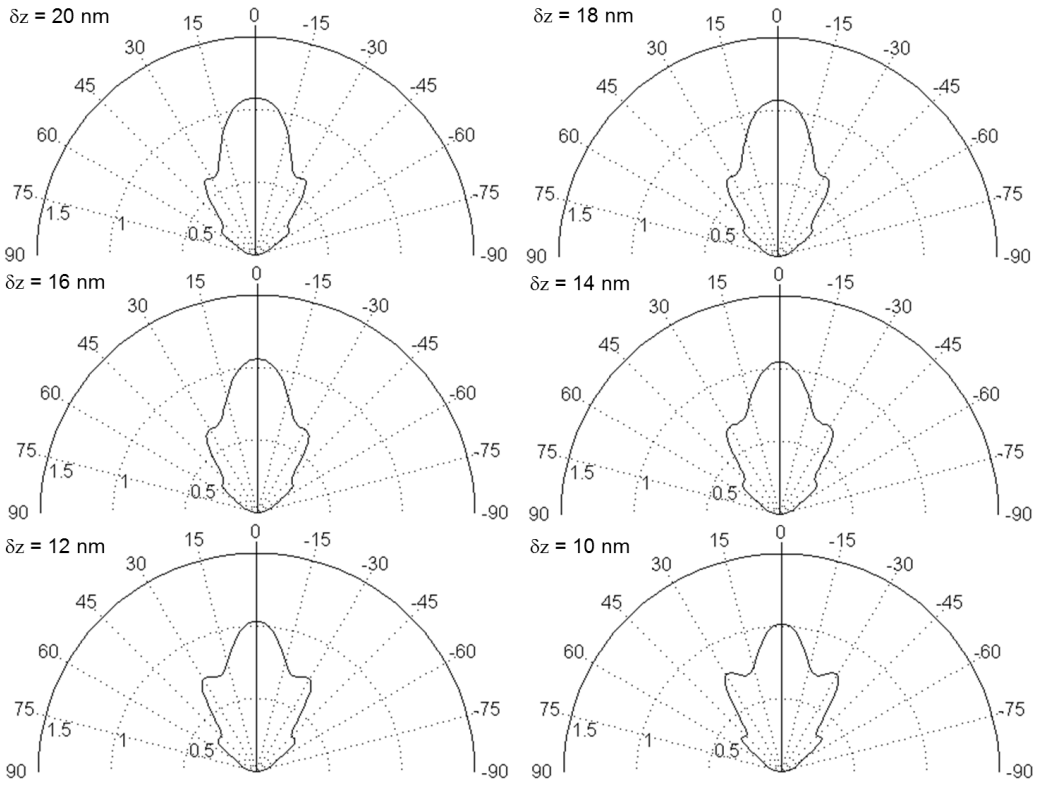

Figure 9-5: Diffraction pattern $I_+(\theta_+)$ of the fundamental HE_{11} mode at $\lambda_0 = 460$ nm, adding the intensity contributions from six quantum wells with equal emission strength and separation Δz.

case, towards the top of the nanorod) emit more light than those on the n-side (Li *et al.* 2013). This can be simulated with reasonable accuracy by having the relative optical power P_w emitted by each well decay exponentially from the top quantum well ($w = 0$) to the bottom one ($w = 5$):

$$P_w = \mathrm{e}^{-\alpha w}, \tag{9.39}$$

where w is a label applied to each quantum well and has a value equal to the number of quantum wells above well w. The decay constant α depends on the electrical properties of the nanorod structure. Figure 9-6 shows the effect of varying α upon the diffraction pattern of HE_{11} at $\lambda_0 = 460$ nm, where $\delta z = 20$ nm. As α is increased, the overall intensity is reduced and the angular emission pattern increasingly resembles that of the top quantum well as it dominates the emission. Both of these results are expected.

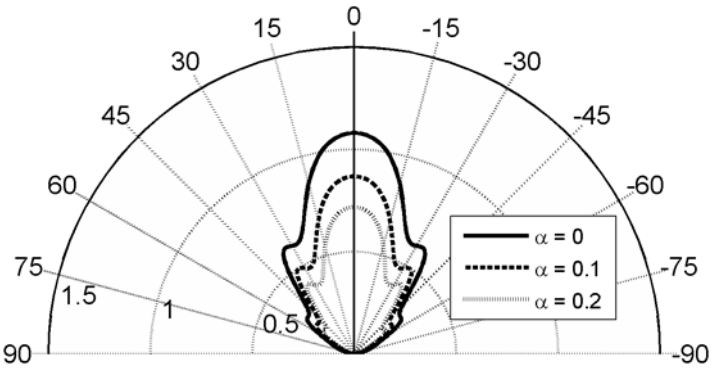

Figure 9-6: Diffraction pattern $I_+(\theta_+)$ of the fundamental HE_{11} mode at $\lambda_0 = 460$ nm for the case of unequal emission from the six quantum wells, governed by (9.39); $\delta z = 20$ nm.

9.8 Higher-order guided modes

Returning to the case of all six quantum wells being equally excited and $\delta z = 20$ nm, the far-field diffraction patterns for all six guided modes that exist for the structure depicted in Figure 9-3 at $\lambda_0 = 460$ nm were calculated. The results are shown in Figure 9-7. Note the use of different scales for each mode; this is justified by the fact that in a practical device the modes will be excited to different extents, so unlike in previous Figures the plots are not directly comparable in the same way. It can be shown that for $N \neq 1$ there is no emission at $\theta_+ = 0$; the far field patterns in Figure 9-7 confirm this (N is the first digit of the subscript on each mode label). Inspection of Figure 9-2 shows that the HE_{12} mode is very close to cut-off and therefore has a very small γ_j, meaning the electromagnetic fields are virtually flat in the cladding, decaying very slowly. This in turn means that only cylindrical waves with small κ, which correspond to small θ_+, have non-negligible overlap with the modal field profile, resulting in the extremely narrow diffraction pattern seen in Figure 9-7.

The far-field diffraction patterns of the various guided modes were also calculated for $\lambda_0 = 520$ nm and $\lambda_0 = 580$ nm, again assuming equal excitation of quantum wells with separation $\delta z = 20$ nm. Inspection of Figure 9-2 reveals that the structure only supports four modes at these two wavelengths, with the HE_{12} and EH_{11} modes being cut-off. Figure 9-8 shows the diffraction patterns of the four guided modes at $\lambda_0 = 520$ nm. The ranges of angles each mode emits power into are similar to those for $\lambda_0 = 460$ nm, although the fine structure of the peaks differs. For the TM_{01} and HE_{21} modes, however, even the fine structure is almost identical, which is not entirely surprising given that the dispersion curves for those two modes cross at around $\lambda_0 = 510$ nm.

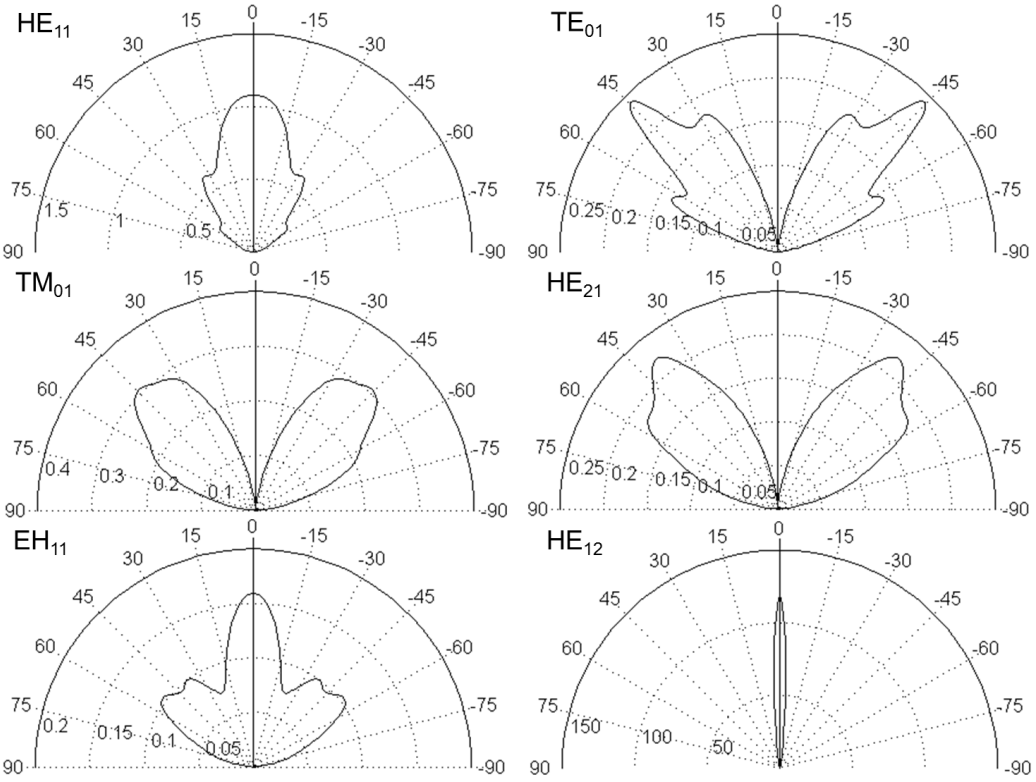

Figure 9-7: Diffraction patterns $I_+(\theta_+)$ of all six guided modes of the nanorod structure of Figure 9-3 at $\lambda_0 = 460$ nm, with equal emission from the six quantum wells with separation $\delta z = 20$ nm.

Figure 9-9 shows the diffraction patterns of the same four modes at $\lambda_0 = 580$ nm. Inspecting Figure 9-2 reveals that the HE_{21} mode is very close to cut-off, just as the HE_{12} mode was for $\lambda_0 = 460$ nm. A similar extremely narrow diffraction pattern is observed in Figure 9-9, except that this pattern has a zero at $\theta_+ = 0$, as required for all $N \neq 1$ modes. The HE_{11} and TE_{01} modal diffraction patterns remain relatively unchanged save for fine structure, while the TM_{01} modal diffraction pattern appears to have shifted inwards compared with this same pattern corresponding pattern for shorter wavelengths.

9.9 Comparison with measurement

Photoluminescence (PL) measurements have been performed by Lewins and Fox (2013) on the experimental nanorod array on which the structure in Figure 9-3 was based, which was fabricated by Zhuang (2012) from a commercial wafer (Epistar 2012) and

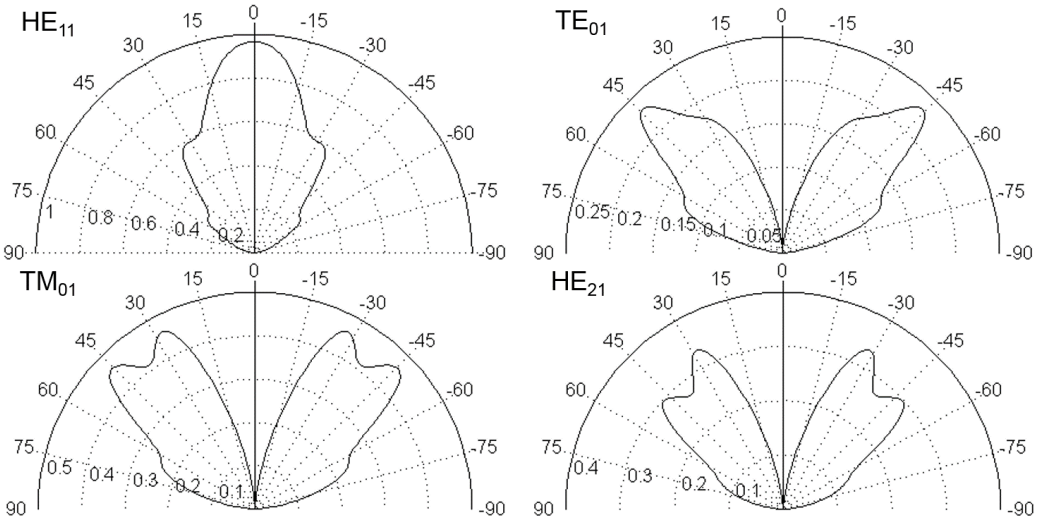

Figure 9-8: Diffraction patterns $I_+(\theta_+)$ of all four guided modes of the nanorod structure of Figure 9-3 at $\lambda_0 = 520$ nm, with equal emission from the six quantum wells with separation $\delta z = 20$ nm.

is similar to that realized by Zhuang *et al.* (2013a), using the hyperspectral imaging system designed and built by Lewins *et al.* (2013) and depicted in Figure 9-10. An optical fibre, connected to a spectrometer, is pointed towards the LED sample. The fibre is scanned along an arc of constant distance r from the sample but varying inclinal angles θ, always pointing towards the sample. As the nanorods point towards $\theta = 0$, θ is equivalent to the quantity θ_+ used in this chapter. This allows the intensity I emitted by the sample to be measured at all wavelengths and all θ_+. For this experiment the azimuthal angle ϕ was kept constant.

Figure 9-11 (a) shows the results of the hyperspectral measurements. The quantity plotted is the normalized intensity $I_{norm}(\lambda_0, \theta_+)$, which is given by normalizing the measured intensity using the method of Lewins (2015): "Firstly, each spectrum taken is divided by its mean intensity value to produce a normalised spectrum with a mean of 1 for each point in the dataset. The mean spectrum of all these normalised spectra is taken to give one 'characteristic' spectrum for the whole dataset. The normalised dataset is then obtained by dividing each of the normalised spectra by the 'characteristic' spectrum. The effect this has is to remove the intensity variations with wavelength and observation angle from normal incidence so that just the features remain." In other words, this is a two-step normalization processes, where the data are first normalized

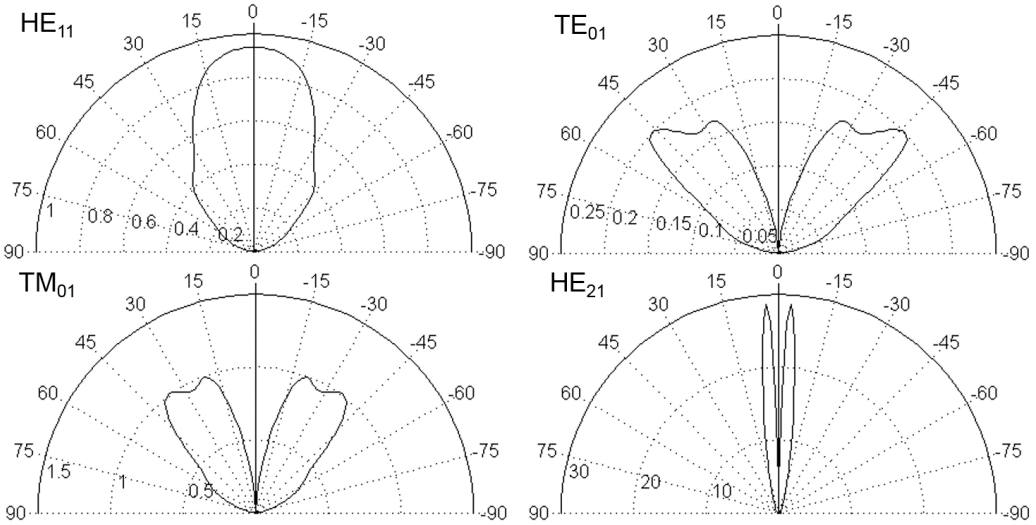

Figure 9-9: Diffraction patterns $I_+(\theta_+)$ of all four guided modes of the nanorod structure of Figure 9-3 at $\lambda_0 = 580$ nm, with equal emission from the six quantum wells with separation $\delta z = 20$ nm.

with respect to wavelength, then with respect to angle:

$$I'(\lambda_0, \theta_+) = \frac{I_+(\lambda_0, \theta_+) N_\lambda}{\sum_\lambda I_+(\lambda_0, \theta_+)} \forall \theta_+, \tag{9.40}$$

$$I_{norm}(\lambda_0, \theta_+) = \frac{I'(\lambda_0, \theta_+) N_\theta}{\sum_\theta I'(\lambda_0, \theta_+)} \forall \lambda_0, \tag{9.41}$$

where N_λ is the number of wavelength values for which data were recorded and N_θ is the number of angle values. For the data considered in this thesis, $N_\lambda = 1024$ and $N_\theta = 361$.

Three different types of features are observed in Figure 9-11. The sharp lines are identified by Lewins *et al.* (2013) as photonic crystal diffraction features caused by the symmetry of the nanorod array. The angular resolution was 0.5° while the wavelength resolution was 0.1343 nm. The broader periodic features are identified in the same work as Fabry-Pérot oscillations. The broadest features, the clearest example of which is the pair of low intensity areas centred around ±37.5° at the short wavelength end of the spectrum, are shown in this section to originate from the diffraction patterns of the guided modes of a single nanorod.

The photonic crystal diffraction features cannot be predicted by the model outlined in this thesis, which only considers a single nanorod. These features can be removed by

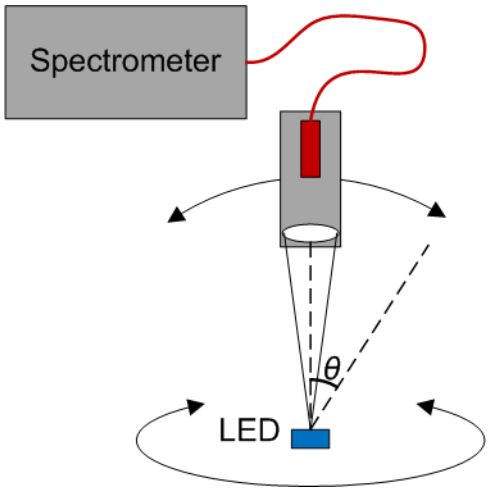

Figure 9-10: The hyperspectral imaging system used for angular photoluminescence measurements (Lewins *et al.* 2013). A resolution of 0.5° was used for these measurements.

averaging the data over a range that is large enough to include at least one peak and trough of a photonic crystal diffraction line but small enough to preserve the broader Fabry-Pérot and modal features. In order to do this, the normalized intensity data were averaged over 2 nm or wavelength and 2° of inclinal angle. Figure 9-11 (b) shows the data after being subjected to this averaging process. The photonic crystal diffraction lines have been almost completely smeared out, making the Fabry-Pérot fringes much easier to see.

Broad dark features in the range $30° < \theta_+ < 50°$ for $\lambda_0 < 505$ nm are clearly visible in both the averaged and non-averaged data. The wavelength at which this feature appears/disappears is significant as it corresponds to the cut-off wavelength of the EH_{11} mode. Inspection of Figure 9-7 shows that the angular diffraction patterns of the TE_{01}, TM_{01} and HE_{21} modes are strongest in this angle range. It is therefore likely that the onset of the EH_{11} mode causes there to be a smaller proportion of power coupled into those modes for $\lambda_0 < 505$ nm, resulting in the dark features in the $30° < \theta_+ < 50°$ region. For $\lambda_0 > 505$ nm, bright features occur at a similar angle range. Returning to $\lambda_0 < 505$ nm, bright features occur around $\theta_+ \approx 0°$ and for large θ_+, corresponding to the two peaks of the EH_{11} diffraction pattern.

Similar variations in the directionality of the emission can be achieved at a given wavelength by fabricating nanorods of a different diameter. For example, slightly wider nanorods would support EH_{11} at $\lambda_0 = 520$ nm, resulting in reduced emission in the

range $30° < \theta_+ < 50°$ relative to the rest of the angular emission pattern at such an emission wavelength. The effect of nanorods on the absolute emitted power is discussed in chapter 10.

Figure 9-12 shows the unnormalized angular intensity distribution $I_+(\theta_+)$ for $\lambda_0 = 460$ nm before and after the averaging process. The raw data has many sharp peaks corresponding to the photonic crystal diffraction lines, while the averaged data has smaller, smoother intensity variations on the gross modal features. Most of these intensity variations appear to correspond with the Fabry-Pérot fringes visible in Figure 9-11, except for the small variations in the range of θ_+ between 10° and 25°, which could be artefacts of the averaging process. Inspection of Figure 9-12 (a) reveals that the photonic crystal diffraction appears to be particularly strong in this angle range.

Some of the key features in Figure 9-12 (b) can be shown to correspond to the modal diffracion patterns in Figure 9-7, which also correspond to $\lambda_0 = 460$ nm. Note that these are PL measurements, meaning that the relative contribution from each quantum well can be assumed to be equal (see section 9.7), making such a direct comparison possible. Figure 9-13 shows the TE_{01} and EH_{11} diffraction patterns from Figure 9-7 superimposed on the averaged measured data from Figure 9-12 (b). These modes were chosen as their diffraction patterns are more sharply peaked than the others, making it easier to attribute specific features to those modes.

It can be seen that in the range of θ_+ between 25° and 65° each maximum in one mode corresponds to a minimum in the other, which could explain why the measured data are fairly flat in this angle range. For $\theta_+ < 25°$, the intensity of the EH_{11} diffraction pattern rises rapidly as $\theta_+ \to 0$, which is also reflected in the measurement. The measured intensity drops off fairly rapidly for $\theta_+ > 65°$, although not as rapidly as the simulated diffraction patterns, suggesting a significant contribution from radiation modes and/or scattering by the other nanorods in the array. This possibility is further explored in section 10.3.

Strong contributions from HE_{11}, TM_{01} and HE_{21} are also expected. Referring back to Figure 9-7, the HE_{11} diffraction pattern is strong for $\theta_+ < 25°$, while the TM_{01} and HE_{21} diffraction patterns are strong in the range $25° < \theta_+ < 60°$. As these patterns are less sharply peaked than those of TE_{01} and EH_{11}, it is quite possible that the former three modal diffraction patterns act to make the measured output smoother than it would be if only the latter two modes were present.

9.10 Discussion

Comparing the simulated data in section 9.8 with the measured data in section 9.9, it is possible to directly relate the two types of features predicted in the simulations to the three types of features observed in the measurements. The broadest features in the measurements correspond to entire modes. The gross structure of each mode is given by the overlap integrals $c_j(\kappa)$ and $d_j(\kappa)$, which define the broad range of angles the modal power diffracts into. For modes far from cut-off, this angle range varies very slowly with wavelength. For the HE_{11} mode diffracted power is observed between 0° and 60° with a peak at 0° for the entire range of wavelengths considered, while the equivalent range for the TE_{01} mode is between 15° and 75° with a peak around 45°, again for the whole wavelength range. Close to cut-off, however, this range of angles moves closer to 0°, as seen for the TM_{01} and HE_{21} modes.

Imposed on this gross structure are the Fabry-Pérot interference fringes, which are govered by (9.20) and constitute the fine structure of the simulated data. These effects can move the peak away from the location predicted using the overlap integrals alone, or even split the peak into multiple smaller peaks. However, these effects are strongly dependent on wavelength and quantum well position and can be smeared out by averaging over large ranges of wavelength, leaving only the gross modal features. The Fabry-Pérot effects can also be significantly weakened, although not eliminated altogether, by considering many quantum wells. The third feature of the measured data, the ultra-fine diffraction lines, are not predicted in the simulations, which consider only one nanorod as opposed to an array.

The apparent agreement between simulation and measurement makes it possible for simulation results to inform nanorod LED design. The results of section 9.7 illustrate the ability of the quantum well position, separation and relative excitation to affect the directionality of the emission significantly. The most significant effect, however, is the gross variation due to the entire modes. For GaN nanorods with radii below 150 nm, the fundamental HE_{11} mode appears to be the key to obtaining highly focused emission along the nanorod axis. The measured data appears to suggest that contribution of HE_{12} to the far field is smaller than might be expected, presumably because this mode is very close to cut-off and therefore strongly couples with the HE_{12} modes of the other nanorods in the array (see, for example, chapter 29 of Snyder and Love 1983). This oddity is further studied in section 10.3. Therefore, efforts should be taken to maximize the excitation of HE_{11} if highly focused emission is desired.

The ability of these modal methods to identify the modes responsible for key features in measured angular emission patterns is something the fully numerical methods that are more frequently applied to these problems cannot offer, as discussed in section 7.5. Another key advantage of quasi-analytic methods such as modal methods is computational speed: for example, the results in Figure 9-7 were obtained in 8.5 minutes using an Intel® Core™ Duo processor, compared to FDTD simulations that can take days. The main disadvantage of modal expansion is that it relies on the cylindrical symmetry of the structure in order to function and fails if the cylindrical symmetry is broken, for example by neighbouring nanorods. Possible ways of dealing with this problem are discussed in chapter 11.

9.11 Summary

This chapter introduces a novel mathematical technique to calculate the diffraction patterns from guided modes of a finite length nanorod and presents detailed numerical results obtained using this method, as in O'Kane *et al.* (2014). Sections 9.2 and 9.3 introduce the mathematics of the problem in terms of the more familiar modes of chapter 8. Section 9.4 explains the core mathematics of the diffraction calculation, accounting for cavity resonances of the type discussed in chapter 5. Section 9.5 uses similar methods to give approximate analytic formulae the phase shift incurred by ratiation modes exiting the nanorod into free space. The effect of the finite nanorod on the different types of modes emitted by a dipole is summarized in Figure 9-14. Section 9.6 gives the dimensions of a system for which photoluminescence measurements have been taken and therefore gives the opportunity to experimentally test the methods of section 9.4. Simulations of this system are presented, focusing in detail on the fundamental mode at $\lambda_0 = 460$ nm in section 9.7 before considering other modes and wavelengths in section 9.8. The measured data is presented in section 9.9, where gross features of the data are explained in terms of the modal diffraction patterns in section 9.8. More general insights from comparing the simulated and measured data are discussed in section 9.10. Despite these insights and the apparent agreement between theory and experiment, the model is by no means complete and further insights can be made through further improvements. This is the focus of chapters 10 and 11.

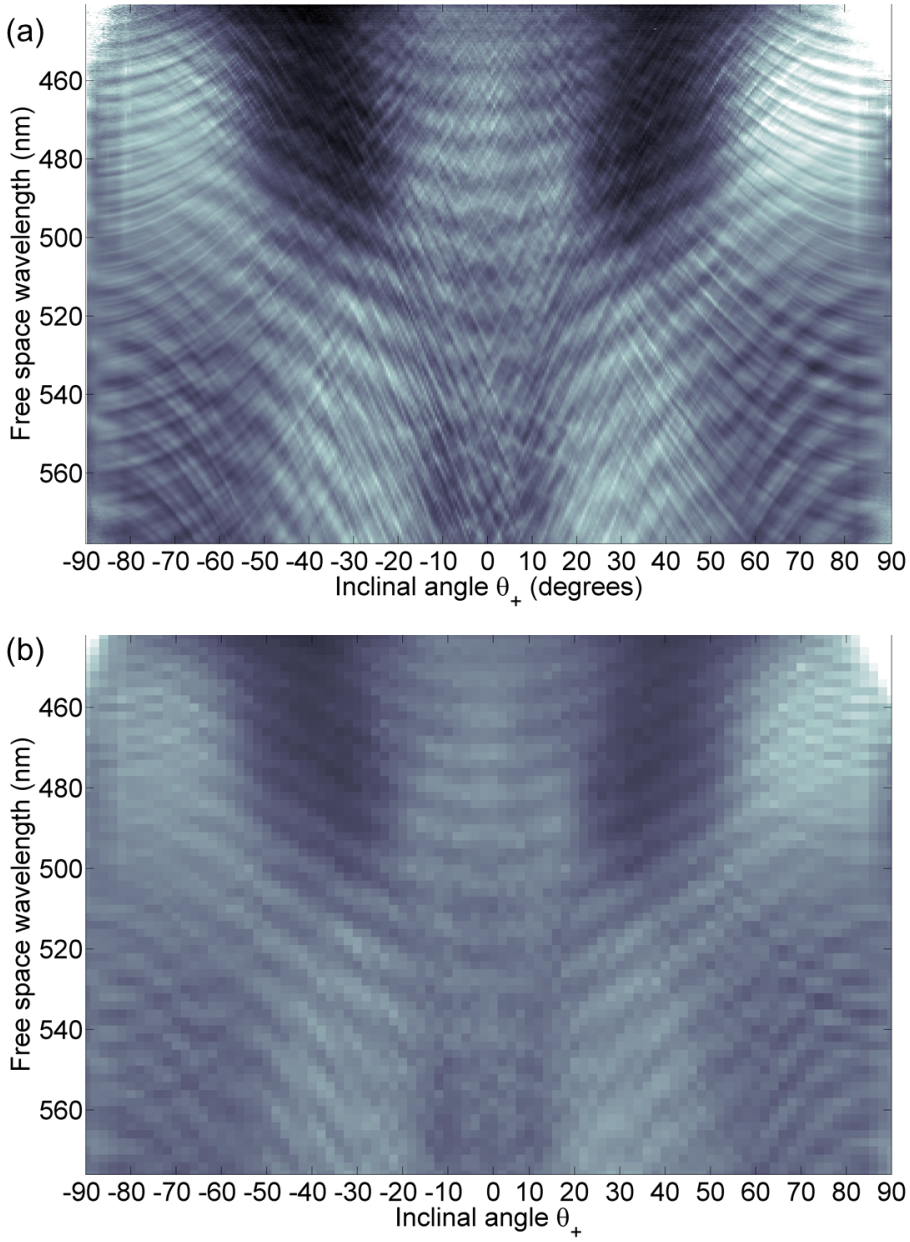

Figure 9-11: Hyperspectral measurements (Zhuang 2012, Lewins and Fox 2013) of normalized intensity I_{norm} as a function of free space wavelength λ_0 and inclinal angle θ_+ for constant azimuthal angle ϕ. The measured data is presented in part (a), while part (b) shows the same data averaged over 2 nm of free space wavelength and 2° of inclinal angle to eliminate the sharp lines caused by photonic crystal diffraction. White corresponds to the highest normalized intensity while black corresponds to the lowest.

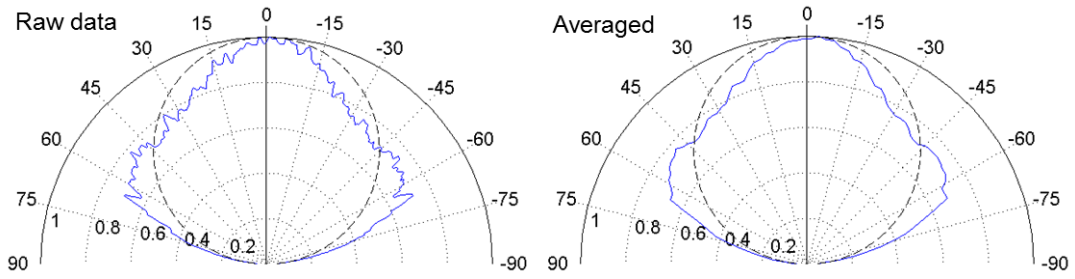

Figure 9-12: Unnormalized angular intensity distribution $I_+(\theta_+)$ (Zhuang 2012, Lewins and Fox 2013) for $\lambda_0 = 460$ nm before and after averaging over 2 nm of free space wavelength and 2° of inclinal angle θ_+. The pre-averaging results are normalized so that the maximum value of $I_+(\theta_+)$ is 1.

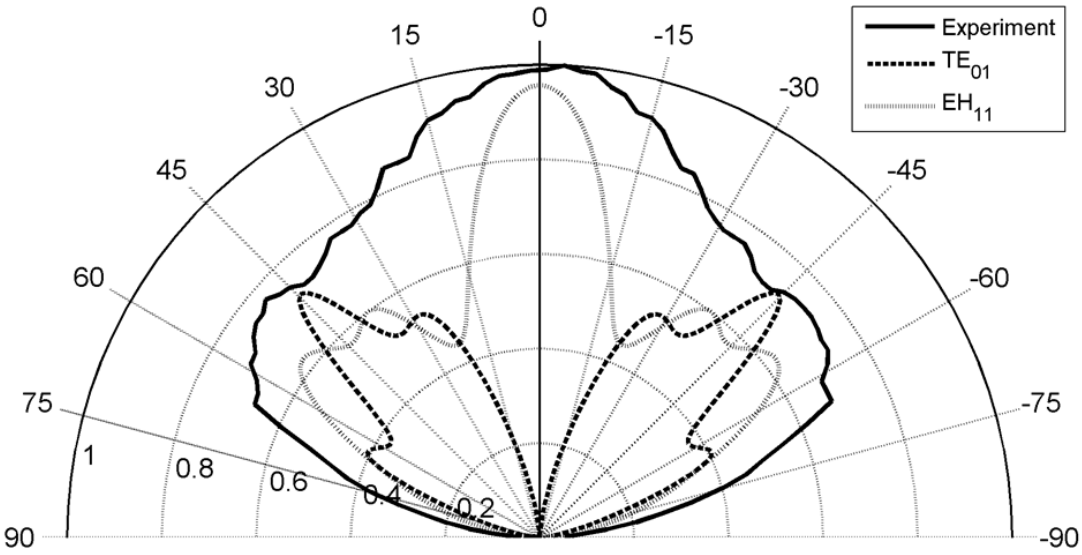

Figure 9-13: Averaged measured far-field photoluminescence data (Zhuang 20120, Lewins and Fox 2013) from Figure 9-12 (b) (solid line); calculated diffraction patterns for the TE_{01} and EH_{11} modes from Figure 9-7 (dashed and dotted lines respectively). The calculated modes have been multiplied by arbitrary factors for the sake of clarity.

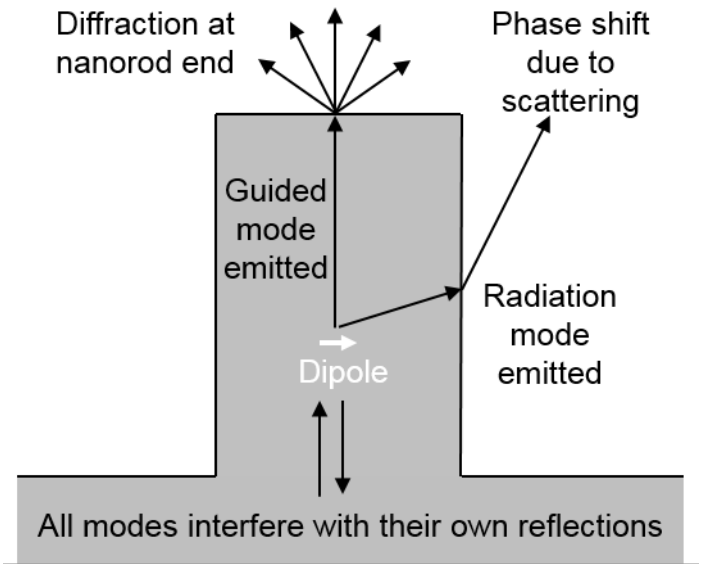

Figure 9-14: A graphical summary of the effect of a finite length nanorod on the guided and radiation modes excited by a Hertzian dipole.

Chapter 10

Multimodal interference effects

10.1 Introduction

Chapter 9 establishes how the far field angular diffraction pattern corresponding to an individual guided mode or a set of radiation modes can be calculated. In practical devices, however, the modes cannot be considered in isolation. All of the guided and radiation modes will be excited by a Hertzian dipole emission event to different extents, determined by the location and orientation of the dipole through (6.27):

$$C_j = -\tfrac{1}{4}\vec{E}_j^*(\rho_D,\phi_D)\cdot\vec{j}\mathrm{e}^{-\mathrm{i}\omega t} = -\tfrac{1}{4}|\vec{j}|\left[\vec{E}_{\rho j}^*(\rho_D,\phi_D)\cos\Phi + \vec{E}_{\phi j}^*(\rho_D,\phi_D)\sin\Phi\right]\mathrm{e}^{-\mathrm{i}\omega t}, \tag{10.1}$$

All of the modes emitted by the same dipole emission event, including radiation modes, are coherent and therefore interfere with one another. This chapter shows how the effect of interference between modes of the same N on the far field can be calculated. It is also shown that interference between modes of different N has no effect on the far field. The theory of multimodal interference is then used to estimate the fractions of power originating from dipoles at the centre of the nanorod, dipoles at the nanorod edge and Lambertian scattering, by finding a best fit to the measured data. Key physical insights obtained from this process are discussed in the context of ongoing work by other authors on the subject of LED nanorods.

10.2 Theory

The geometry of the system is given in Figure 9-1, which is reproduced here for clarity. Substituting (9.7), (9.8), (9.35) and (9.36) into (9.1) and (9.2) gives

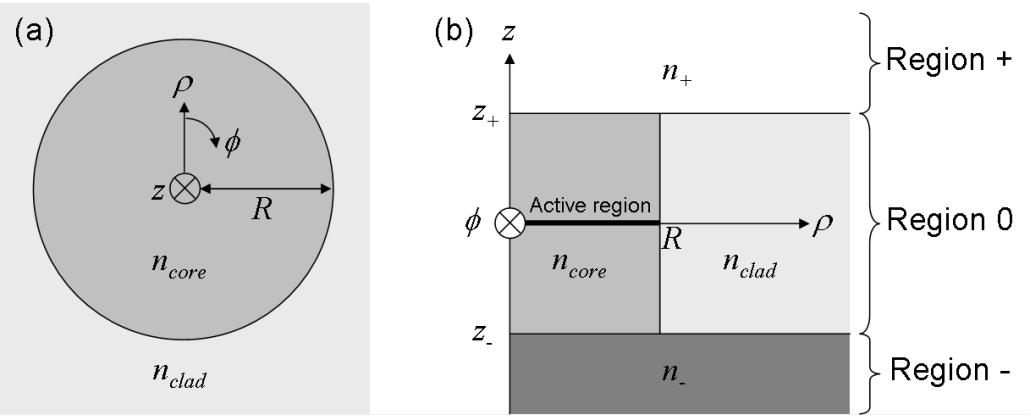

Figure 10-1: The structure to be modelled, in cylindrical polar coordinates. (a) A cross-section through the nanorod. (b) The full structure including vertical confinement.

$$\vec{E}_0(\vec{r}) \approx \sum_j C_j \sum_{TE,TM} \int_0^\infty c_j \hat{e}_j \, \mathrm{d}\kappa + \sum \int_0^\infty \tilde{c}_0 \left[\tilde{a}_{TE}\tilde{e}_{TE} + \tilde{a}_{TM}\tilde{e}_{TM}\right] \mathrm{d}\sigma_0 \qquad (10.2)$$

$$\vec{H}_0(\vec{r}) \approx \sum_j C_j \sum_{TE,TM} \int_0^\infty d_j \hat{h}_j \, \mathrm{d}\kappa + \sum \int_0^\infty \tilde{c}_0 \left[\tilde{a}_{TE}\tilde{h}_{TE} + \tilde{a}_{TM}\tilde{h}_{TM}\right] \mathrm{d}\sigma_0, \qquad (10.3)$$

where c_j is given by (9.11) and should not be confused with C_j or $\tilde{c}_0$, which are given by (10.1). Equations (10.2), (10.3) and those that follow are only approximate due to the first term of (9.32) being neglected. The overlaps $\tilde{a}_{TE}$ and $\tilde{a}_{TM}$ between the radiation modes of the nanorod and free space are given in Table 9.4. The summations in the second terms of (10.2) and (10.3) are over all N, the two choices of $f(N\phi)$ and the ITE (incident transverse electric) and ITM (incident transverse magnetic) radiation mode polarizations. The Fabry-Pérot interference effects caused by the nanorod's finite length can be accounted for by splitting the fields into TE and TM components and considering continuity of the field components parallel to the interfaces at $z = z_\pm$. The entirety of the electric field of the TE component and the magnetic field of the TM components are parallel to said interfaces and therefore continuous. The effect of the cavity on the TE component is to multiply the c_j and a_{TE} by their respective values of the cavity transmission coefficient $\tau_\pm$:

$$\vec{E}_{TE}(\rho, \phi, z = z_\pm) \approx \sum_j C_j \int_0^\infty \tau_{j\pm} c_j \hat{e}_j \, \mathrm{d}\kappa + \sum \int_0^\infty \tilde{c}_0 \tau_\pm \tilde{a}_{TE} \tilde{e}_{TE} \, \mathrm{d}\sigma_0. \qquad (10.4)$$

The effect of the cavity on the TM component is to multiply the d_j by $\zeta_j n_\pm n_j^{-1}\tau_\pm$ and the a_{TM} by $n_\pm n_{clad}^{-1}\tau_\pm$:

$$\begin{aligned}\vec{H}_{TM}(\rho,\phi,z=z_\pm) &\approx \sum_j C_j \int_0^\infty \frac{n_\pm}{n_j}\tau_{j\pm}\zeta_j d_j \hat{h}_j \,\mathrm{d}\kappa + \sum \int_0^\infty \tilde{c}_0 \frac{n_\pm}{n_{clad}}\tau_\pm \tilde{a}_{TM}\tilde{h}_{TM}\,\mathrm{d}\sigma_0 \\ &\approx \sum_j C_j \int_0^\infty \frac{n_\pm}{n_j}\tau_{j\pm} c_j \hat{h}_j \,\mathrm{d}\kappa + \sum \int_0^\infty \tilde{c}_0 \frac{n_\pm}{n_{clad}}\tau_\pm \tilde{a}_{TM}\tilde{h}_{TM}\,\mathrm{d}\sigma_0.\end{aligned} \tag{10.5}$$

All of the $\tau_\pm$ in (10.4) and (10.5) are given by (9.20). As in section 6.7, continuity of $\vec{E}_{TE}$ and $\vec{H}_{TM}$ allows (10.4) and(10.5) to be cast in terms of the radiation modes of region $\pm$:

$$\sum_j C_j \int_0^\infty \tau_{j\pm} c_j \hat{e}_j \,\mathrm{d}\kappa + \sum \int_0^\infty \tilde{c}_0 \tau_\pm \tilde{a}_{TE}\tilde{e}_0 \,\mathrm{d}\sigma_0 \approx \sum \int_0^\infty \Omega_\pm \tilde{e}_\pm \,\mathrm{d}\sigma_\pm \tag{10.6}$$

$$\sum_j C_j \int_0^\infty \frac{n_\pm}{n_j}\tau_{j\pm} c_j \hat{h}_j \,\mathrm{d}\kappa + \sum \int_0^\infty \tilde{c}_0 \frac{n_\pm}{n_{clad}}\tau_\pm \tilde{a}_{TM}\tilde{h}_0 \,\mathrm{d}\sigma_0 \approx \sum \int_0^\infty \Omega_\pm \tilde{h}_\pm \,\mathrm{d}\sigma_\pm, \tag{10.7}$$

where the summations on the right hand sides sum over all N and both choices of $f(N\phi)$. The magnitude squared of $\Omega_\pm(\sigma_\pm)$ yields the total angular far field pattern emitted by the dipole and is therefore the quantity of greatest interest. As shown in section 6.8, the Bessel and Hankel function representations of the radiation modes of homogeneous media can be readily interchanged by using a fictitious boundary. In order to avoid the problems caused by the singularity of $H_N^{(1)}(x)$ at $x=0$, it is necessary to replace $\tilde{e}_\pm$ with its Bessel function equivalent $\hat{e}_\pm$:

$$\sum_j C_j \int_0^\infty \tau_{j\pm} c_j \hat{e}_j \,\mathrm{d}\kappa + \sum \int_0^\infty \tilde{c}_0 \tau_\pm \tilde{a}_{TE}\tilde{e}_0 \,\mathrm{d}\sigma_0 \approx \sum \int_0^\infty \Omega_\pm \hat{e}_\pm \,\mathrm{d}\sigma_\pm \tag{10.8}$$

$$\sum_j C_j \int_0^\infty \frac{n_\pm}{n_j}\tau_{j\pm} c_j \hat{h}_j \,\mathrm{d}\kappa + \sum \int_0^\infty \tilde{c}_0 \frac{n_\pm}{n_{clad}}\tau_\pm \tilde{a}_{TM}\tilde{h}_0 \,\mathrm{d}\sigma_0 \approx \sum \int_0^\infty \Omega_\pm \hat{h}_\pm \,\mathrm{d}\sigma_\pm. \tag{10.9}$$

Taking the vector product of (10.8) and $(\hat{h}_\pm^* \times \hat{z})$ and integrating over the interface at $z = z_\pm$ yields an approximation for $\Omega_\pm$ for TE modes:

$$\Omega_\pm(\sigma_\pm) \approx \sum_j C_j \tau_{j\pm}(\sigma_\pm) c_j(\sigma_\pm)\sqrt{\frac{\beta_\pm}{\beta_j}} + \sum_{ITE,ITM} \tilde{c}_0(\sigma_\pm)\tau_\pm(\sigma_\pm)\tilde{a}_{TE}(\sigma_\pm)\sqrt{\frac{\beta_\pm}{\beta_0}}. \tag{10.10}$$

The summations over N and the two variants of $f(N\phi)$ disappear due to the orthogonality of f, while the integrals over κ, σ_0 and $\sigma_\pm$ disappear due to the orthogonality of the Bessel functions ($\kappa = \sigma_0 = \sigma_\pm$). However, the summation over j does not disappear as the only difference between the cylindrical wave functions corresponding to different guided modes is the z variation (i.e. β) and no integral over z was performed. The summation over ITE and ITM modes also remains as the cylindrical wave functions corresponding to these modes are wholly identical. The presence of these summations means that the relative phases (i.e. multimodal interference effects) of $\tilde{c}_0$, $\tilde{a}_{TE}$, $\tau_\pm$ and the $\tau_{j\pm}$ affect the magnitude of $\Omega_\pm$ and are therefore not trivial.

However, the modes of region $\pm$ with different N and/or $f(N\phi)$ are orthogonal to one another and each have their own $\Omega_\pm$, the magnitudes squared of which must therefore be added incoherently in order to obtain the total angular emission pattern. This means that interference between modes of different N and/or f does not affect the far field pattern; the incoherence between the modes of different N and/or f removes the phase information.

Taking the vector product of (10.9) and $(\hat{e}_\pm^* \times \hat{z})$ and integrating over the interface for TM modes yields an identical expression for TM modes:

$$\Omega_\pm(\sigma_\pm) \approx \sum_j C_j \tau_{j\pm}(\sigma_\pm) c_j(\sigma_\pm) \sqrt{\frac{\beta_\pm}{\beta_j}} + \sum_{ITE,ITM} \tilde{c}_0(\sigma_\pm)\tau_\pm(\sigma_\pm)\tilde{a}_{TM}(\sigma_\pm)\sqrt{\frac{\beta_\pm}{\beta_0}}. \quad (10.11)$$

Equation (10.11) is only valid when ζ_j is positive. For $\sigma_\pm < k_0$ (i.e. within the light escape cone for air), it can be safely assumed that $\zeta > 0$. The power P in the far field can be found by integrating $|\Omega_\pm|^2$ with respect to $\sigma_\pm$:

$$P_\pm = \sum \int_{\sigma_1}^{\sigma_2} |\Omega_\pm|^2 \, \mathrm{d}\sigma_\pm = \sum \int_{\theta_1}^{\theta_2} |\Omega_\pm|^2 \beta_\pm \, \mathrm{d}\theta_\pm, \quad (10.12)$$

where the summation is over all N and both $f(N\phi)$. The intensity I is found by dividing (10.12) by area as before:

$$I_\pm = \frac{\sum \int_{\theta_1}^{\theta_2} |\Omega_\pm|^2 \beta_\pm \, \mathrm{d}\theta_\pm}{2\pi r^2 \int_{\theta_1}^{\theta_2} \sin(\theta_\pm) \mathrm{d}\theta_\pm}. \quad (10.13)$$

A useful quantity to define is the total power emitted into the top (+) or bottom (-) hemispheres. This is denoted $P_{r\pm}$ as it is analogous to the quantity P_r defined by

(8.19):

$$P_{r\pm} = \sum \int_0^{\frac{\pi}{2}} |\Omega_\pm|^2 \beta_\pm, \mathrm{d}\theta_\pm. \tag{10.14}$$

10.3 Comparison with measurement

The model described in section 10.2 was implemented for the same structure as that investigated in section 9.6. Using cathodoluminescence studies, Zhuang *et al.* (2013c) found that emission from quantum wells in nanorods tends to originate predominantly from either the centre of the nanorod ($\rho_D \ll R$) or the edge ($\rho_D \approx R$), with little emission in between. Therefore, the angular intensity distributions due to three different dipoles were considered, as depicted in Figure 10-2. The intensity $I_0(\theta_+)$ due to a dipole situated at $\rho_D = 0$ (where the ρ and ϕ directions are degenerate) was considered, along with two such distributions, $I_\rho(\theta_+)$ and $I_\phi(\theta_+)$, for dipoles near the nanorod edge ($\rho_D = 130$ nm). The angular intensity due to a dipole with $\rho_D = 130$ nm with dipole moment in the ρ direction ($\Phi = 0$) is denoted $I_\rho(\theta_+)$ while that due to a dipole with $\rho_D = 130$ nm with dipole moment in the ϕ direction ($\Phi = \frac{\pi}{2}$) is denoted $I_\phi(\theta_+)$. For reasons discussed in section 6.5, the angular emission patterns can be assumed to be cylindrically symmetric.

As in section 8.7, the dipole current densities were normalized using (8.22):

$$|\vec{j}|^2 = \frac{24\pi}{k_0^2 Z_0 n_{core}}. \tag{10.15}$$

Two wavelengths were considered: $\lambda_0 = 460$ nm and $\lambda_0 = 520$ nm. These wavelengths were considered because they are sufficiently far from both the 'green-yellow band' defect-related emission peak centred around $\lambda_0 \approx 550$ nm (Grieshaber *et al.* 1996, cited in Schubert 2006) and the cut-off of the EH_{11} mode at $\lambda_0 \approx 505$ nm, both of which make fitting the measured data problematic around those wavelengths. Conveniently, the guided mode diffraction patterns for both of these wavelengths is given in section 9.8, specifically Figure 9-7 and 9-8. The total power P_{r+} emitted into the top hemisphere, as defined by (10.14), for the three dipoles depicted in Figure 10-2 at both wavelengths is given in Table 10.1.

Inspection of Table 10.1 shows that the dipoles with current density vectors in the ρ direction emit much less power than those with current density in the ϕ direction; this is true for both the raw and modified data sets. Due to the large discontinuity in $\vec{E} \cdot \hat{\rho}$ that occurs at the nanorod edge, this is not surprising and is consistent with the

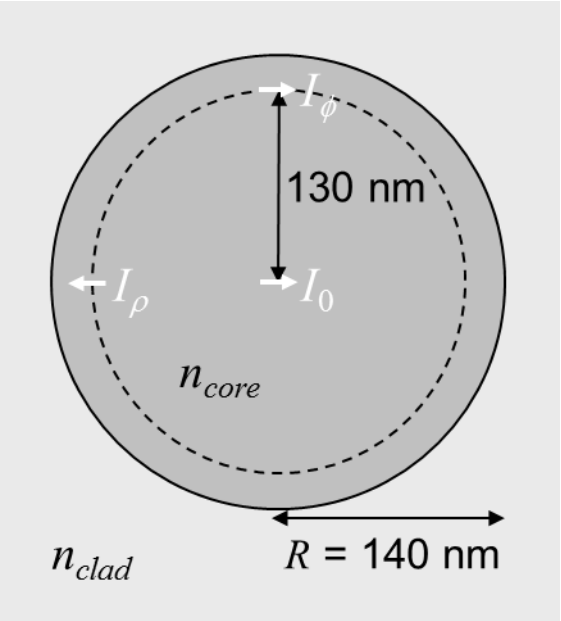

Figure 10-2: Position and orientation of three different dipoles, which result in the angular emission intensity patterns $I_0(\theta_+)$, $I_\rho(\theta_+)$ and $I_\phi(\theta_+)$.

data presented in section 8.7. As a consequence of this, it was found that the effect of I_ρ on the fits to the measured data is small, although the best fits were obtained in the case where I_ρ was omitted altogether (see Figure 10-5). Emphasis is therefore placed on I_0 and I_ϕ. A possible reason for this is explored in section 10.4.

There are two important things to note regarding the angular intensity data presented in this chapter. Firstly, the range $\delta\theta_+$ over which the integral (10.13) is taken is 2°, as opposed to 1° as used throughout chapter 9. This is done to give a more accurate comparison with the averaged measured data, which is averaged over the same angle range in order to average out the effect of photonic crystal diffraction features. Secondly, the total power emitted by a dipole can be altered drastically by various factors discussed in this section, making use of the same scale for all intensity plots impractical. Care must therefore be taken to read the scales when analysing these data. The measurements and fits to measurements use the same scale, which has a maximum of 1, for ease of comparison.

The angular photoluminescence measurement (Zhuang 2012, Lewins and Fox 2013) for $\lambda_0 = 460$ nm averaged over 2° of inclinal angle and 2 nm of free space wavelength, as depicted on the right hand side of Figure 9-12, is repeated in Figure 10-3

λ_0	Dipole	P_{r+} (raw data)	P_{r+} (modified)
460 nm	I_0	0.393	0.360
	I_ρ	0.111	0.106
	I_ϕ	0.457	0.452
520 nm	I_0	1.69	0.253
	I_ρ	0.0926	0.0485
	I_ϕ	1.12	0.106

Table 10.1: Normalized power emitted from the three dipoles depicted in Figure 10-2 at free space wavelengths $\lambda_0 = 460$ nm and $\lambda_0 = 520$ nm. 'Raw data' refers to the the results with all modes included, while the 'modified' results include the modifications described and justified later in this section. For $\lambda_0 = 460$ nm the power in the HE_{12} mode is reduced in the modified data, while for $\lambda_0 = 520$ nm the radiation modes for which $N = 1$ are ignored. These results are depicted in Figures 10-3, 10-4, 10-5 and 10-6.

(a). The angular intensities $I_0(\theta_+)$ due to the central dipole and $I_\phi(\theta_+)$ due to the ϕ-oriented edge dipole for $\lambda_0 = 460$ nm are depicted in Figure 10-3 (b) and (c) respectively. Both of these emission patterns contain a sharp feature centred around $\theta_+ = 0°$, which corresponds to the HE_{12} mode of this structure. This feature does not appear in the measurements due to strong interaction between this mode and its counterparts of neighbouring nanorods, as discussed in section 9.10. Figure 10-3 (e) and (f) show $I_0(\theta_+)$ and $I_\phi(\theta_+)$ with this mode artificially removed, i.e. the expansion coefficient C_{HE12} for this mode was made to be zero. This results in the sharp peaks in the emission patterns being replaced by sharp dips, which do not appear in the measurement either.

Evidently, the contribution of the HE_{12} mode to the measured data, which is determined by the expansion coefficient C_{HE12}, is not zero but is less than the value predicted by (10.1). It was found that, by reducing C_{HE12} to $\frac{1}{\sqrt{3}}$ of the value predicted by (10.1), resulting in the power emitted into this mode being reduced by a third, a compromise was obtained where there was no sharp feature at $\theta_+ = 0$. These results are depicted in Figure 10-3 (f) and (g). This modification was therefore applied to I_0, I_ϕ and I_ρ before beginning the fitting process.

Figure 10-4 (a) shows the emission pattern resulting from assuming equal contributions from the three dipoles depicted in Figure 10-2. There is no a priori reason to

believe this would constitute an accurate fit and indeed it does not remotely resemble the measurement, which is repeated in Figure 10-4 (d). A best fit $I_{bf}(\theta_+)$ to the angular photoluminescence data is depicted in Figure 10-4 (c). The fit $I_{bf}(\theta_+)$ was obtained using a linear combination of $I_0(\theta_+)$, $I_\phi(\theta_+)$ and a Lambertian term $I_L = \cos\theta_+$ designed to give a first approximation for simulating light scattered by the neighbouring nanorods and the unpolished rear surface of the sapphire. The former of these scattering mechanisms is more accurately described by Bragg scattering (Fox *et al.* 2015), while the latter is Lambertian due to the surface roughness being random (see Figure 1-4). A visual fitting method was used. The least squares regression (LSR) method was considered but would be difficult to implement given the mathematical complexity of the angular emission patterns. Visual fitting is useful for reproducing the key features of the emission pattern, whereas LSR is better at ensuring the total emitted power matches that in the measurement. However, the main disadvantage of visual fitting is its susceptiblity to confirmation bias; in an attempt to circumvent this, a next best fit $I_{nbf}(\theta_+)$ is shown in addition to the best fit $I_{bf}(\theta_+)$, which is given by

$$I_{bf}(\theta_+) = 0.3I_0(\theta_+) + 0.675I_\phi(\theta_+) + 0.7\cos\theta_+ \quad \text{for} \quad \lambda_0 = 460 \text{ nm}. \tag{10.16}$$

The agreement between Figure 10-4 (c) and (d) is strong but not perfect, as the intensity in the fit in the regions around $\theta_+ = 15°$ and $\theta_+ = 40°$ is markedly lower compared to the measurement. A previous fit attempt $I_{nbf}(\theta_+)$ involving all three dipoles and the Lambertian term is also included in Figure 10-4 (b); it is similar to I_{bf} but has visibly smaller intensity in the range $15° < \theta_+ < 30°$. The formula for $I_{nbf}(\theta_+)$ is given in Table 10.2.

A similar treatment was applied to the case of $\lambda_0 = 520$ nm. The HE_{12} guided mode that caused difficulties at $\lambda_0 = 460$ nm is cut off at this longer wavelength, although a similar problem is presented by the radiation modes corresponding to $N = 1$ (see sections 8.4 and 9.5 for context). The angular intensity patterns emitted by the central dipole and the ϕ-oriented edge dipole, with all guided modes and all $N \neq 1$ radiation modes excluded, are depicted in Figure 10-5 (a) and (b) respectively. These extremely sharp features are not observed in the angular photoluminescence measurement for this wavelength, averaged over 2 nm and 2° as before, which is depicted in Figure 10-5 (h). The angular intensity patterns $I_0(\theta_+)$ and $I_\phi(\theta_+)$ with the $N = 1$ radiation modes excluded are depicted in Figure 10-5 (c) and (d) respectively. The best fit for this wavelength is depicted in Figure 10-5 (g) and is given by

$$I_{bf}(\theta_+) = 0.0625I_0(\theta_+) + 4.5I_\phi(\theta_+) + 0.65\cos\theta_+ \quad \text{for} \quad \lambda_0 = 520 \text{ nm}. \tag{10.17}$$

The best fit has the same overall shape as the measured data, with a broad peak between $\theta_+ = 25°$ and $\theta_+ = 45°$. However, the slight drop in intensity observed in the measurement around $\theta_+ = 15°$ is not reproduced in the fit. This may be due to the failure to integrate the $N = 1$ radiation modes into the fit. The fit also has noticeably lower intensity in the region around $\theta_+ = 60°$. Two next best fits $I_{nbf1}(\theta_+)$ and $I_{nbf2}(\theta_+)$ are included in the form of Figure 10-5 (e) and (f), while the fomulae are given in Table 10.2. Figure 10-5 (e) is interesting in that it has very a slight intensity drop at a similar angle to that in the measurement, although the measurement shows a much more visible intentisy drop and much more power in the region $40° < \theta_+ < 60°$. The fit in Figure 10-5 (f) also has too little power in this region, hence the fit in Figure 10-5 (g) being chosen.

The formulae for the best fits and next best fits are given in Table 10.2. Notably, all

λ_0	Function
460 nm	$I_{nbf}(\theta_+) = 0.3I_0(\theta_+) + 0.6I_\rho(\theta_+) + 0.6I_\phi(\theta_+) + 0.65\cos\theta_+$
	$I_{bf}(\theta_+) = 0.3I_0(\theta_+) + 0.675I_\phi(\theta_+) + 0.7\cos\theta_+$
520 nm	$I_{nbf1}(\theta_+) = 1.25I_0(\theta_+) + 5I_\rho(\theta_+) + 5I_\phi(\theta_+)$
	$I_{nbf2}(\theta_+ = 0.125I_0(\theta_+) + 3I_\rho(\theta_+) + 3I_\phi(\theta_+) + 0.65\cos\theta_+$
	$I_{bf}(\theta_+) = 0.0625I_0(\theta_+) + 4.5I_\phi(\theta_+) + 0.65\cos\theta_+$

Table 10.2: Formulae for the best fits and next best fits depicted in Figures 10-4 and 10-5

the next best fits assume equal contributions from the ρ and ϕ-oriented edge dipoles, while both the best fits assume zero contribution from the ρ-oriented edge dipole. The formula for $I_{nbf1}(\theta_+)$ does not include a Lambertian term, which explains the lack of power in the region $40° < \theta_+ < 60°$. For completeness, the original and modified $I_\rho(\theta_+)$ data is depicted in Figure 10-6.

10.4 Discussion

For both of the wavelengths studied, the fits take the general form

$$I_{bf} = A_0 I_0(\theta_+) + A_\phi I_\phi(\theta_+) + A_L \cos\theta_+. \tag{10.18}$$

The radiated power P_{bf} present in the fit is therefore given by

$$P_{bf} = A_0 P_{r+}(I_0) + A_\phi P_{r+}(I_\phi) + \tfrac{1}{2} A_L, \tag{10.19}$$

given that the radiated power present in the Lambertian distribution $I_L = \cos\theta_+$ is equal to $\frac{1}{2}$. Two quantities are of particular physical interest when analysing these results: the fraction Γ_s of total radiated power due to the Lambertian scattering term and the fraction Γ_0 of non-Lambertian radiated power emitted by the central dipole. These quantities are given by

$$\Gamma_s = \frac{A_L}{2P_{bf}} \quad \text{and} \quad \Gamma_0 = \frac{A_0 P_{r+}(I_0)}{P_{bf} - \frac{1}{2} A_L}. \tag{10.20}$$

The quantities Γ_s and Γ_0 are defined in such a way that the definitions remain valid if further dipoles are added. The values of Γ_s and Γ_0 for the two wavelengths under investigation are tabulated in Table 10.3. The fraction Γ_s of scattered power, as simu-

λ_0	Γ_s	Γ_0
460 nm	0.459	0.261
520 nm	0.397	0.0321

Table 10.3: Values of power fractions Γ_s and Γ_0, as defined by (10.20), for the wavelengths under investigation.

lated by the Lambertian term, is well over a third for both wavelengths, suggesting that scattering is very significant. This scattering could be due to either the neighbouring nanorods or the unpolished rear surface of the sapphire substrate. Lewins *et al.* (2013, 2014) and Fox *et al.* (2014) discuss the importance of photonic crystal and Bragg scattering in nanostructured LEDs respectively. However, neither of these papers contain any attempts to calculate the fraction of power that is scattered. Calculating the fraction of scattered power using the more sophistacted models used in these papers is a possible avenue for future work.

The fraction Γ_0 of non-scattered power emitted by the central dipole is 26.1% for $\lambda_0 = 460$ nm but only 3.21% for $\lambda_0 = 520$ nm. This is consistent with the conclusion of Zhuang *et al.* (2013c) that the central area of the nanorod contributes more power for shorter wavelengths.

As noted in the previous section, the angular intensity patterns $I_\rho(\theta_+)$ due to ρ-oriented

dipoles near the nanorod edge were calculated for both wavelengths. These dipoles emit little power and therefore their influence on the fitting process is small, unless $A_\rho \gg A_\phi$. The best fits were obtained using $A_\rho = 0$. There is a possible physical reason for this. The assumption, introduced in section 5.2, that there are no dipoles with moments perpendicular to the plane of the quantum well, due to the strong quantum confinement in that direction, has been used throughout this work. It is quite possible that the presence of the nanorod introduces confinement in the ρ direction also, causing the strain-relaxed region of the quantum well at the nanorod edge to behave somewhat like a quantum wire. A possible intepretation of the observations of Zhuang *et al.* (2013c), which is consistent with the lack of any strong indicators of emission from ρ-oriented dipoles, is that the strong emission from the central and edge regions of the nanorod are due to valleys in the bandstructure created by strain-based effects. The converse hypothesis, in which there is confinement in the ϕ direction, is less likely, due to the apparent lack of any physical mechanism for this in the cylindrical nanorods considered in this thesis. Therefore, the case of $A_\rho \gg A_\phi$ was not considered. However, bandstrucure simulations for quantum wells in nano-LEDs with hexagonal cross-sections predict confinement in both radial and azimuthal directions (Böcklin *et al.* 2010).

10.5 Comparison with the literature

Although the literature contains many reports of optical simulations of nanorod LEDs, most of which use finite-difference time-domain (FDTD) methods, there have been few attempts to calculate angular intensity distributions, with most emphasis instead being placed on extraction efficiency. Kölper *et al.* (2011) have been among those to attempt this. However, that work did not state how many incoherent dipoles were used to produce the final results, noting only that the dipoles were equally spaced. The more abstract work of Paniagua-Domínguez *et al.* (2013), who considered indium phosphide (InP) nanorods suurrounded by an infinite vacuum in all directions, was selected for comparison, as in that work only one dipole was used to produce each angular emission pattern.

Paniagua-Domínguez *et al.* (2013) used two different methods. Firstly, a finite element method was used to solve the wave equations numerically, in contrast to FDTD methods that solve Maxwell's equations directly. The second method was a semi-empirical modal expansion method derived by the authors. The standard eigenvalue equation (8.6) was used to find the modal propagation constants β_j, which were then substituted into the cavity interference equation (5.46) in order to convert the Hertzian

dipole within the nanorod into a series of finite length dipoles (one dipole for each mode) in free space, from which the far field could be calculated. Unlike the modal expansion method of this thesis, which is derived from first principles, the modal method of Paniagua-Domínguez *et al.* (2013) relies on fitting the modal reflection coefficients $r_{j\pm}$ to other simulations and/or measurements.

For the purposes of this comparison, the key result of Paniagua-Domínguez *et al.* (2013) is contained in Fig. 7 of that work, which is reproduced here as Figure 10-7. Far-field intensity patterns are calculated used both methods for dipoles located at the centre ($\rho_D = 0$, $d_+ = d_- = \frac{1}{2}d$) of InP ($n_{core} = 3.42$) nanorods of constant radius $R = 126$ nm, surrounded by all sides by an infinite vacuum ($n_{clad} = 1$). The free space wavelength was also kept constant at $\lambda_0 = 880$ nm. Unfortunately, the notation used by Paniagua-Domínguez *et al.* for the nanorod lengths appears to be inconsistent with that used in the rest of the paper, in which L' is not defined at all. Both L and L' are defined in terms of the modal wavelength $\lambda_z^{(j)} = 2\pi\beta_j^{-1}$. The HE_{11} mode has $\lambda_z^{\mathrm{HE11}} = 355$ nm and is excited by dipoles at $\rho_D = 0$ for which $\vec{j}$ has components in non-z directions; the TM_{01} mode has $\lambda_z^{\mathrm{TM01}} = 825$ nm and is excited by dipoles at $\rho_D = 0$ for which $\vec{j}$ has a z component. The TE_{01} mode is also supported by this structure but has zero electric field at $\rho = 0$ and therefore cannot be excited by dipoles at $\rho_D = 0$.

Figure 10-8 shows TE and TM angular intensity patterns obtained using the methods of this thesis for $d_+ = d_- = 7\lambda_z^{\mathrm{HE11}} = 2485$ nm ($d = 4970$ nm). The TE angular inensity pattern is very similar to the pattern in Figure 10-7 (a) in the y-z plane, where y is the direction in which the dipole points, whereas the TM intensity pattern is similar to that in the x-z plane of Figure 10-7 (a). Through trial and error, it was determined that the methods of this thesis were able to reproduce the results of Figure 10-7 if L is interpreted to be the nanorod half-length (i.e. $L = d_+ = d_-$) and L' is interpreted to be the full length ($L' = d_+ + d_- = d$). Figure 10-9 shows the results of this comparison; panels (a)-(h) correspond to those in Figure 10-7 and the agreement is strong. Paniagua-Domínguez and Sánchez-Gil, the main authors of the article in question, have been contacted for their opinion on whether or not this interpretation of their work is correct and therefore whether or not Figure 10-9 is a fair comparison. If the comparison is indeed fair, the similarity of the results would be a strong vindication of the model presented in this thesis. Note particularly the central peak in Figure 10-9 (d), which is present in Paniagua-Domínguez *et al.*'s numerical result in Figure 10-7 but not in their modal result. The same can be said of the secondary peak around 60° of the TM emission pattern, which appears to correspond to the x-z plane in Figure

10-7 (a), in Figure 10-8.

Fig. 9 of Paniagua-Domínguez *et al.* (2013) presents far-field angular emission patterns for z-oriented dipoles in a much narrower nanorod ($R = 50$ nm) with other parameters kept the same: $\lambda_0 = 880$ nm, $n_{core} = 3.42$ and $n_{clad} = 1$. All guided modes save for the fundamental HE_{11} mode are cut-off. As the dipoles are aligned in the z direction and positioned at $\rho_D = 0$ where $\hat{E}_{\mathrm{HE}11} \cdot \hat{z} = 0$, HE_{11} is not excited at all and therefore only radiation modes are excited. As a result of this, the emission pattern is completely invariant with $d_{\pm}$, provided no other parameters are changed. Figure 10-10 (a) and (b) are reproductions of those in Paniagua-Domínguez *et al.* (2013), while (c) is the $d_{\pm}$-invariant far-field pattern computed for the same geometry using the methods of this thesis. Figure 10-10 (c) is similar to the top part of (b) for which $d_+ = d_- = 1500$ nm, except that the region of low intensity around $\theta_+ = 75°$ predicted by Paniagua-Domínguez *et al.* is absent from the intensity pattern in (c). The bottom part of (b), on the other hand, is completely different from (c).

Figure 10-10 (a) shows that the total emitted power varies very little with $d_{\pm}$ except in the areas close to the nanorod ends. Leaky modes, which were explicitly considered by Paniagua-Domínguez *et al.* (2013) but not in this work, have electromagnetic fields that vary with z in exactly the manner (oscillations within the exponentially decaying envelope) depicted in Figure 10-10 (a). It is therefore highly probable that these modes, which are solutions to the eigenvalue equation (8.6) with complex β_j, account for the discrepancy. Paniagiua-Domínguez *et al.*, however, did not explicitly consider radiation modes. The precise nature of the relationship between leaky modes and radiation modes must be properly researched in order to avoid double counting.

10.6 Summary

By considering multimodal interference effects, it is possible to simulate the entire angular emission pattern emitted by a given dipole within a nanorod. The theory of how to do this is presented in section 10.2. In section 10.3, the relative power emitted by dipoles at the centre and edge of the nanorod, along with a Lambertian term intended to provide a first approximation for scattering by neighbouring nanorods and/or the unpolished rear surface of the sapphire substrate, is adjusted to provide best fits to measurement. This process achieves good agreement for two wavelengths that are sufficiently far from guided mode cut-offs and the yellow band emission from defects in GaN. Key physical insights resulting from this fitting process are discussed in section

10.4, in the context of ongoing work by other authors on the subject of nanorod LEDs. It is shown in section 10.5 that strong agreement with an article in the literature (Paniagua-Domínguez *et al.* 2013), in which the angular intensity distributions are calculated using both a numerical method and a semi-empirical modal method, has been achieved but significant discrepancies arise when the nanorod radius is very small.

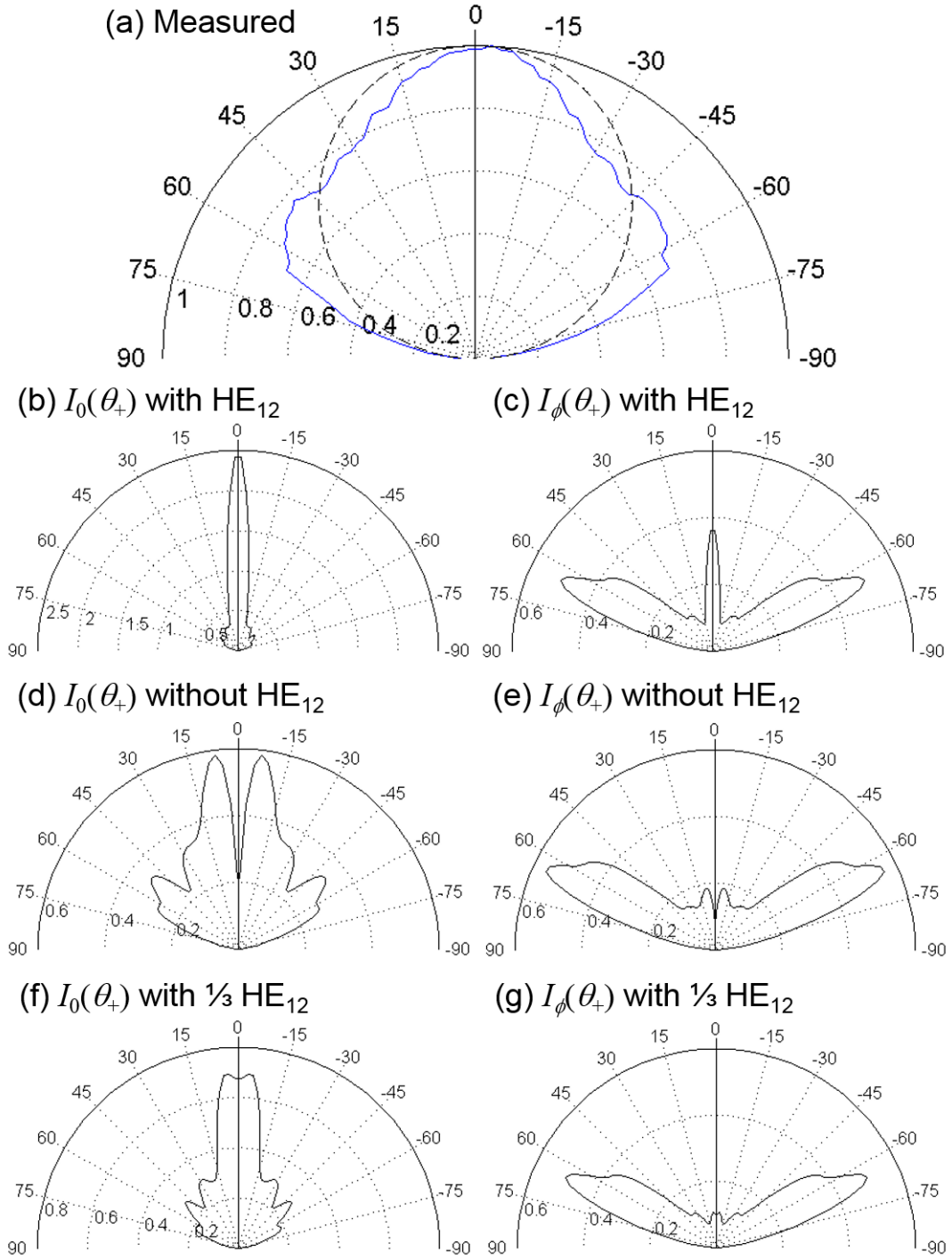

Figure 10-3: (a) Measured angular intensity pattern (Zhuang 2012, Lewins and Fox 2013) at $\lambda_0 = 460$ nm for the structure considered in section 9.6 and depicted in Figure 7; (b)-(g) a series of angular intensity patterns at the same wavelength calculated using the method of section 10.2 in order to illustrate the necessity of reducing the power in the HE_{12} mode in order to predict realistic results.

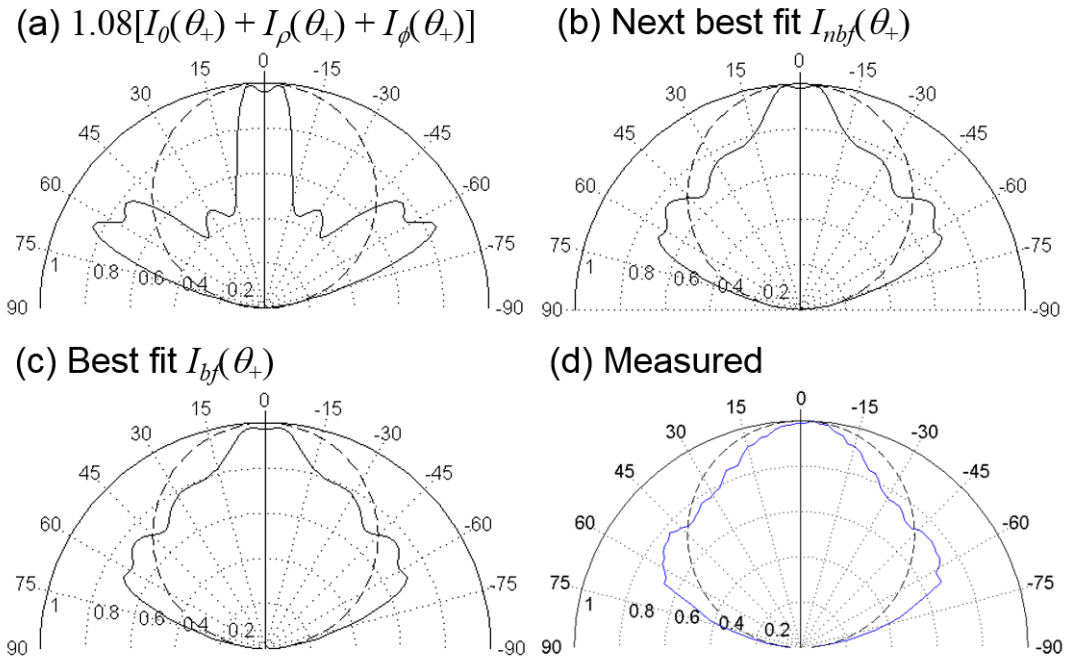

Figure 10-4: Three different attempts to fit the angular photoluminescence measurement for $\lambda_0 = 460$ nm. (a) An emission pattern assuming equal contributions from the three dipoles; (b) the next best fit; (c) the best fit; (d) the measured data, same as that in Figure 10-3 (a). All four plots use the same scale and show a Lambertian emission pattern $I_L = \cos\theta_+$ as a dotted line for ease of comparison.

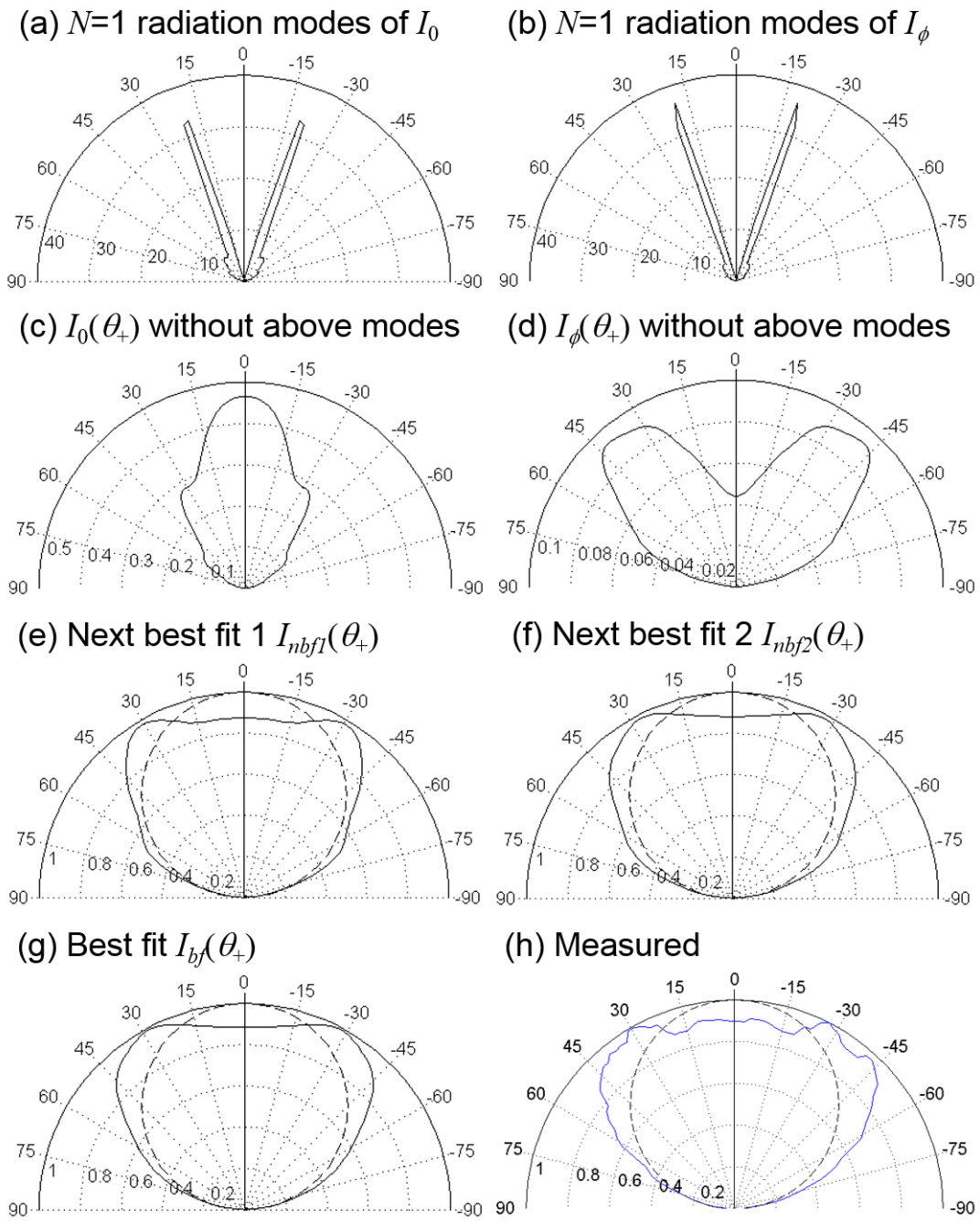

Figure 10-5: Radiation modes for which $N = 1$ due the central (a) and ϕ-oriented edge (b) dipoles depicted in Figure 10-2 for $\lambda_0 = 520$ nm. As these sharp features are not observed in the experiment, $I_0(\theta_+)$ and $I_\phi(\theta_+$ for $\lambda_0 = 520$ nm with the $N = 1$ modes completely removed are depicted in (c) and (d) respecitvely. Three different fits to the measured data (h) (Zhuang 2012, Lewins and Fox 2013) at this wavelength are shown in (e)-(g). Parts (e)-(h) use the same scale and a include a Lambertian pattern $I_L = \cos\theta_+$ shown as a dotted line for each of comparison.

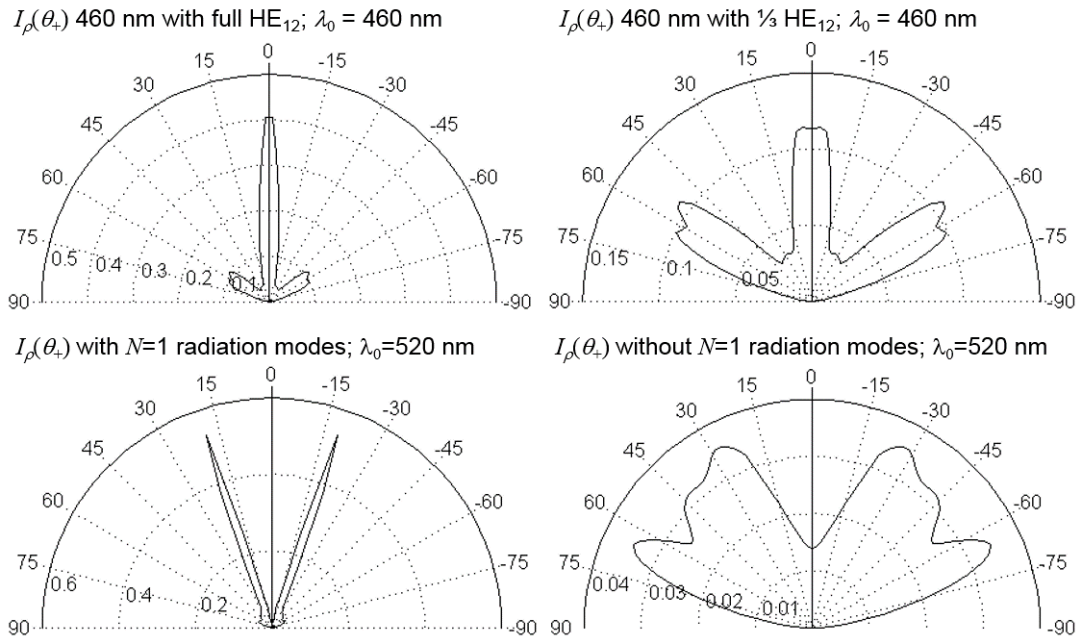

Figure 10-6: Angular intensity patterns for ρ-oriented edge dipoles, correpsonding to the 'Raw data' and 'Modified' entries for $I_\rho(\theta_+)$ in Table 10.1.

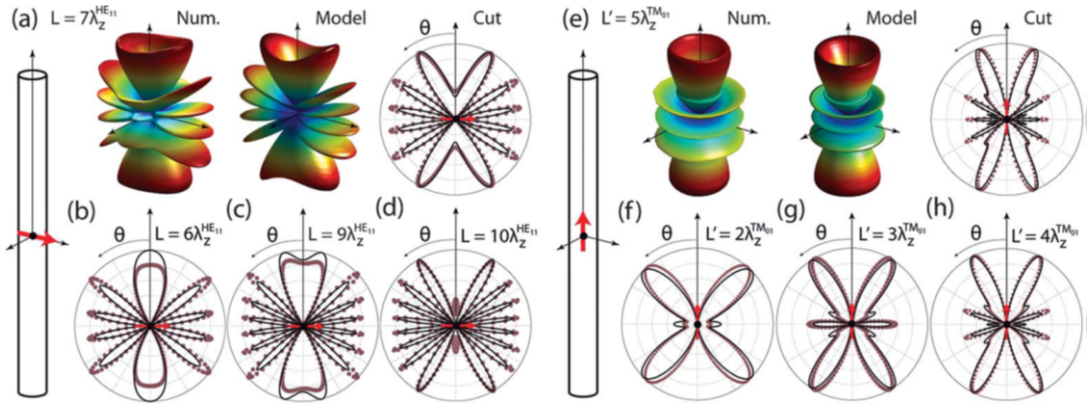

Figure 10-7: Fig. 7 from Paniagua-Domínguez *et al.* (2013). For the two-dimensional polar plots, red circles denote the results of the numerical finite element calculation while black lines denote the results of the modal method. L in this Figure appears to denote the half-length (i.e. $L = d_+ = d_-$), whereas L' appears to denote the full length ($L' = d_+ + d_- = d$). $\lambda_z^{\mathrm{HE11}} = 355$ nm, $\lambda_z^{\mathrm{TM01}} = 825$ nm, $\lambda_0 = 880$ nm and $R = 126$ nm. The dipole points in the y direction; the two-dimensionsal polar plots show the angular intensity distribution in the y-z plane.

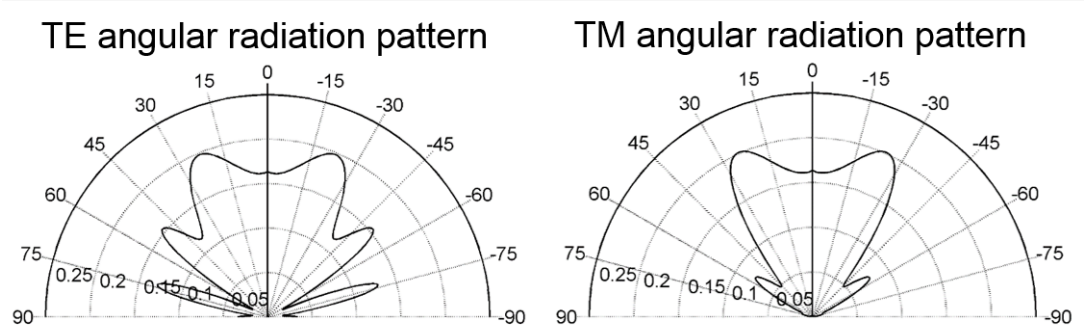

Figure 10-8: TE and TM angular intensity patterns obtained using the methods of this thesis for $d_+ = d_- = 7\lambda_z^{\mathrm{HE11}} = 2485$ nm ($d = 4970$ nm), $\lambda_0 = 880$ nm, $R = 126$ nm, $\rho_D = 0$, $n_{core} = 3.42$ and $n_{clad} = 1$.

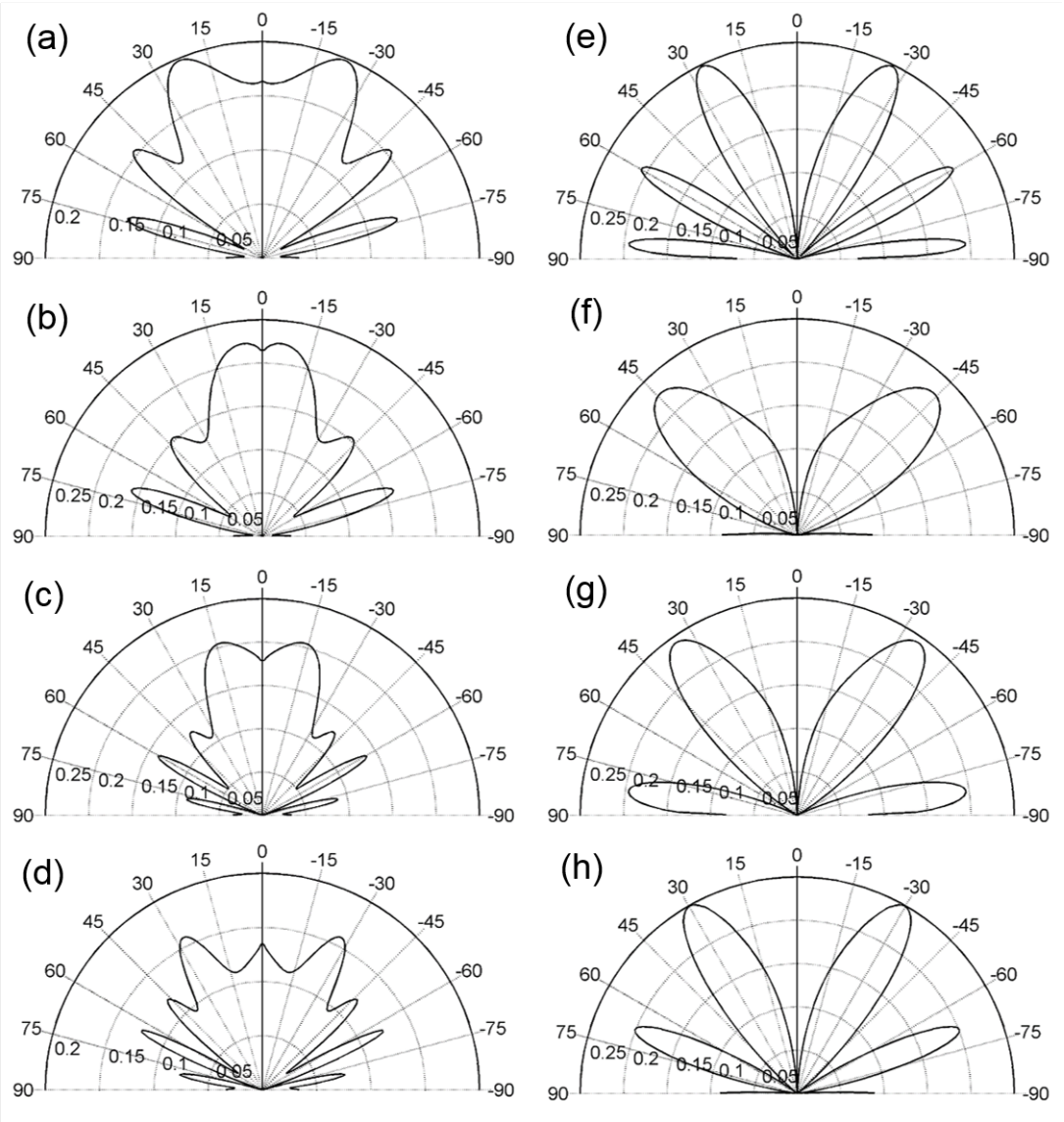

Figure 10-9: Angular intensity patterns obtained using the methods of this thesis; panels (a)-(h) correspond to those in Figure 10-7. Panels (a)-(d) consider TE-polarized radiation due to dipole moments in the y direction perpendicular to the nanorod axis for varying half-lengths $L = d_+ = d_-$: (a) $L = 7\lambda_z^{\mathrm{HE11}} = 2485$ nm, (b) $L = 6\lambda_z^{\mathrm{HE11}} = 2130$ nm, (c) $L = 9\lambda_z^{\mathrm{HE11}} = 3195$ nm and (d) $L = 10\lambda_z^{\mathrm{HE11}} = 3550$ nm. Panels (e)-(h) consider dipoles oriented the nanorod axis z (for which the radiation is entirely TM-polarized) for varying full lengths $L' = d_+ + d_- = d$: (e) $L' = 5\lambda_z^{\mathrm{TM01}} = 4125$ nm, (f) $L' = 2\lambda_z^{\mathrm{TM01}} = 1650$ nm, (g) $L' = 3\lambda_z^{\mathrm{TM01}} = 2475$ nm and (h) $L' = 4\lambda_z^{\mathrm{TM01}} = 3300$ nm. For all cases $\lambda_0 = 880$ nm, $R = 126$ nm, $n_{core} = 3.42$, $n_{clad} = 1$ and the dipole is in the centre of the naonorod ($\rho_D = 0$, $d_+ = d_-$).

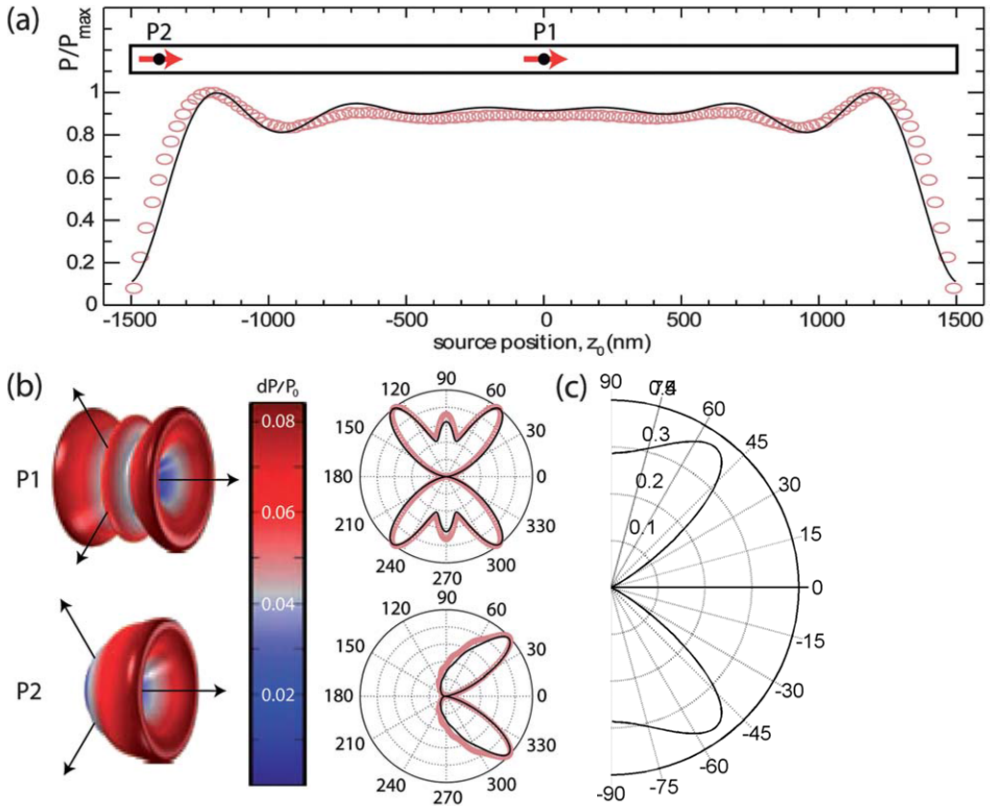

Figure 10-10: Panels (a) and (b) of Fig. 9 from Paniagua-Domínguez *et al.* (2013), displayed alongside the $d_{\pm}$-invariant angular intensity pattern for the same geometry using the methods of this thesis (c). As in Figure 10-7 red circles correspond to finite element calculations while black lines correspond to modal calculations. The quantity P/P_{max} plotted in (a) denotes the total emitted power, where 1 is the maximum. For all panels $R = 50$ nm, $\lambda_0 = 880$ nm, $n_{core} = 3.42$, $n_{clad} = 1$ and $\rho_D = 0$.

Chapter 11

Future work

11.1 Introduction

In this thesis, the first fully quasi-analytic model of light emission from cylindrical nanostructures is presented. However, there are several limitations to the model as it stands. Although it is capable of evaluating the power emitted by a dipole into the semi-infinite regions above and below a nanorod, the amount of power emitted into the horizontally guided modes of the nanorod layer and the planar GaN layer and by extension the extraction efficiency remain elusive. Coupling between nanorods has been completely neglected, in spite of its likely importance. Finally, many applications require consideration of the inverse problem, where cylindrical nanorods are illuminated from above or below. This chapter proposes mathematical methods for resolving these three issues.

11.2 Guided modes of nanorod and planar GaN layers

The amount of power emitted into the semi-infinite regions above and below a single nanorod can be calculated using the methods of chapters 9 and 10. However, these methods do not consider the power emitted into horizontally guided modes of the nanorod layer and the planar GaN layer below them. Considering that the methods of section 9.4 break up the vertically guided modes of the individual nanorods into cylindrical waves in fictitious planar media as shown in Figure 11-1, three types of guided modes are possible in the resulting slab structures, depending on the refractive index $n_j(\kappa)$ of the fictitious medium corresponding to radial wavevector κ.

The range $k_0 n_{max} < \kappa < k_0 n_{GaN}$, where n_{max} is the greater of n_+ and n_-, corresponds

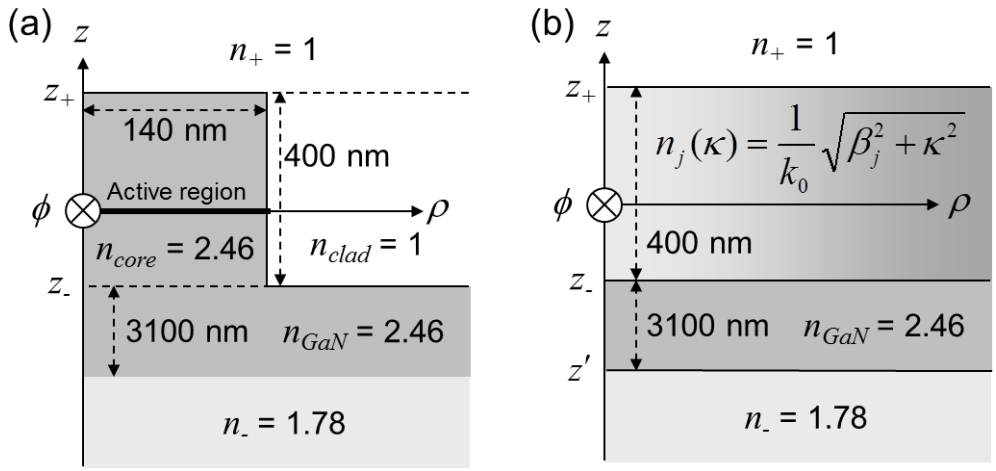

Figure 11-1: The range of indices $n_j(\kappa)$ the effective media can have gives rise to three different types of guided modes in the resulting slab structures.

to modes horizontally guided in both the nanorod and planar GaN layers, henceforth referred to as type I slab modes. For $\kappa > k_0 n_{GaN}$ modes horizontally guided solely in the nanorod layer are possible (type II slab modes). These two mode types account for the power emitted into vertically guided modes of the individual nanorods that is not diffracted into radiation modes. The power emitted into both type I and type II slab modes can be found using the methods of Yeh (1988).

There is also a third type of mode, which is horizontally guided in the planar GaN layer only and evanescent in the nanorod layer (type III slab modes). However, type III slab modes do not correspond to guided modes of the individual nanorods but evanescent modes, which have imaginary values of the axial wavevector β and have not been considered prior to now. However, a much easier method of dealing with the power emitted into type III slab modes is by assigning the nanorod layer a volume-averaged refractive index using the methods of Aspnes (1982) and solving for the guided modes of the resulting structure, again using the methods of Yeh (1988). Lewins *et al.* (2013) have done this for a similar structure and achieved strong agreement with measurement. The power emitted into the type III slab modes can then be calculated by considering the exponential tails of these modes in the volume-averaged region.

Another advantage of the volume-averaging method, in addition to its simplicity, is that it considers the effect of the other nanorods in the array. Given that volume-averaging can also be used to solve for type I slab modes, it may be useful to compare

the results obtained by using volume-averaging and by using $n_j(\kappa)$. Volume-averaging cannot be used for the type II slab modes, although it is anticipated that there will be much less power emitted into these modes than into the type I slab modes.

Once the amount of power emitted into all three types of slab modes is known, the extraction efficiency of the finite nanorod structure can be evaluated. It will also be possible to look for trends in the internal and external quantum efficiencies using the methods of section 8.7.5.

11.3 Inter-nanorod coupling

As previously discussed in chapters 9 and 10, the guided and radiation modes of a nanorod couple to their counterparts in neighbouring nanorods. Calculating the extent of this coupling and the effect on the far field is difficult as the presence of multiple nanorods breaks the cylindrical symmetry on which the methods of this thesis depend. However, two possible approaches are decribed in this section.

11.3.1 Weak coupling via coordinate shifts

An approximate solution for the coupled modes of "...weakly guiding fibers which are sufficiently well separated," (Snyder and Love 1983 pp. 568) in terms of the modes of the individual nanorods can be found using the method described in chapter 29 of Snyder and Love (1983). Although these criteria do not apply to GaN nanorods, it may still be possible to use this method as a first approximation. The key equation of this method is an overlap intergral that can be used to obtain the coupling coefficients (Snyder and Love 1983 pp. 570). As the modes of each nanorod are given in terms of a co-ordinate system with the origin at the centre of that particular nanorod, a series of coordinate shifts is required to calculate this integral. This can be done by transforming all modes into Cartesian coordinates, selecting an arbitrary origin (at the centre of one of the nanorods is convenient) and expressing all modes in terms of this 'master' coordinate system. The modes can then either remain in Cartesian coordinates or be transferred back into cylindrical coordinates; the latter approach is described here with the aid of Figure 11-2.

The coordinate system centred at point 1 is denoted (ρ,ϕ); the system centred at point 2 is denoted (ρ',ϕ'). For simplicity, it is assumed that there is no shift in z, i.e. $z = z'$ and $\hat{z} = \hat{z}'$. Assuming the Cartesian unit vectors of the two systems to be

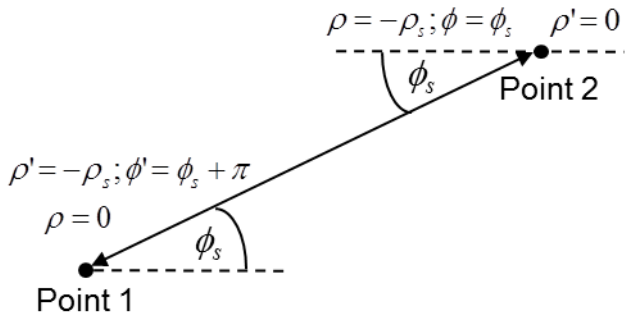

Figure 11-2: A shift between two sets of cylindrical polar coodinates with origins at points 1 and 2.

identical, i.e.

$$\hat{x} = \hat{x}' \quad \text{and} \quad \hat{y} = \hat{y}', \tag{11.1}$$

the shift between the corresponding Cartesian systems (x,y) and (x',y') is simple:

$$x' = x - \rho_s \cos\phi_s \quad \text{and} \quad y' = y - \rho_s \sin\phi_s. \tag{11.2}$$

This shift can then be transferred to cylindrical polars using the identities given in section 6.2:

$$(\rho')^2 = \rho^2 + \rho_s^2 - 2\rho\rho_s(\cos\phi\cos\phi_s + \sin\phi\sin\phi_s) \tag{11.3}$$

and

$$\tan\phi' = \frac{\rho\sin\phi - \rho_s\sin\phi_s}{\rho\cos\phi - \rho_s\cos\phi_s}. \tag{11.4}$$

The advantage of retaining the cylindrical polar coordinate system is that, for the case of $\rho \gg \rho_s$ that is relevant when performing the overlap integral for radiation modes, the two co-ordinate systems become virtually the same, i.e. $\rho = \rho'$ and $\phi = \phi'$. The disadvantage of this notation over Cartesian notation is that, unlike for Cartesian coordinates, the unit vectors of the two systems are not the same but depend on ϕ and ϕ'. Starting from the assumption (11.1) that the corresponding Cartesian unit vectors are the same, the shift in cylindrical unit vectors can also be derived:

$$\hat{\rho}' = \hat{\rho}(\cos\phi\cos\phi' + \sin\phi\sin\phi') + \hat{\phi}(\cos\phi\sin\phi' - \sin\phi\cos\phi') \tag{11.5}$$

and

$$\hat{\phi}' = \hat{\phi}(\cos\phi\cos\phi' + \sin\phi\sin\phi') + \hat{\rho}(\sin\phi\cos\phi' - \cos\phi\sin\phi'). \tag{11.6}$$

The cylindrical unit vectors also become equal in the case of $\rho \gg \rho_s$.

11.3.2 Approximation of the system as volume averaged shells

Another way of estimating the coupling between waveguide modes is, instead of considering the modes of the individual nanorods, to approximate the system in terms of a simpler system that is cylindrically symmetric, then solve for the modes of this composite system. Figure 11-3 depicts how this might be accomplished for a hexagonal lattice with pitch Λ, where the pitch is defined as the distance between the centres of nearest-neighbour nanorods.

If the coordinate origin is placed at the centre of a nanorod, the hexagonal symmetry

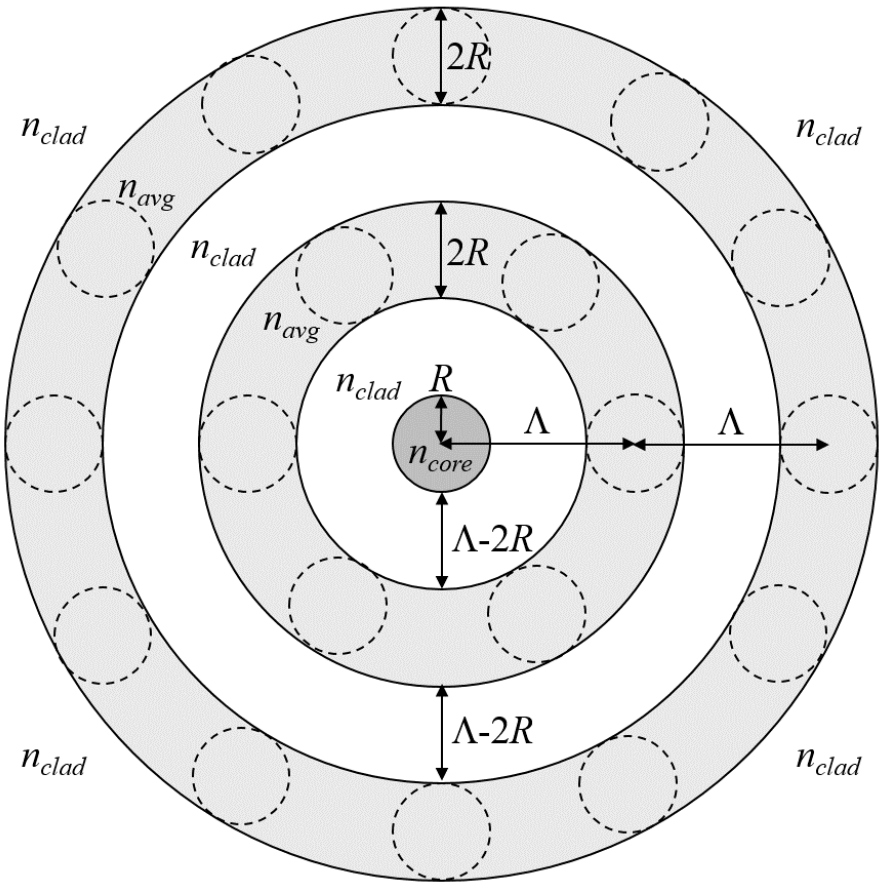

Figure 11-3: A hexagonal array with pitch Λ of nanorods of refractive index n_{core} and radius R, surrounded by a cladding of refractive index n_{clad}, approximated as a series of alternating cylindrical shells with refractive indices n_{clad} and n_{avg}.

of the nanorod array causes the centres of the other nanorods to form rings around this origin; the nearest neighbours lie on one ring, the second nearest neighbours lie

on another and so on. This allows for the possibility of approximating each ring of nanorods as a shell of volume averaged refractive index n_{avg}, using the methods of Aspnes (1982). These shells alternate with shells where there are no nanorods and therefore have refractive index n_{clad}. In the first instance a simple volume averaging process with no consideration of local field effects could be used. It can be readily shown that n_{avg} is the same for each shell and is given by

$$n_{avg} = \frac{6\pi R^2 n_{core} + (4\pi\Lambda R - 6\pi R^2) n_{clad}}{4\pi\Lambda R} = n_{clad} + \frac{3R}{2\Lambda}(n_{core} - n_{clad}). \tag{11.7}$$

The central nanorod is already cylindrically symmetric so no volume averaging is required, resulting in this part of the system uniquely retaining n_{core}. The modes of this simplifies system can be calculated exactly, by applying the methods of Yeh (1988) to a cylindrical layered structure.

11.4 Time-reversal and wider applications

The analysis presented in chapters 9 and 10 applies to emission from within a cylindrical nanorod. Although this thesis considers LED applications, this problem can also arise in laser diodes and single-photon sources for quantum information (Henderson *et al.* 2012). A much wider range of applications for cylindrical nanostructues involves the reverse problem, where the nanorod is illuminated from above or below. Such applications include photonic crystals, solar cells (Kupec *et al.* 2010), photodetectors (Wang *et al.* 2011) and an alternative design for highly directional LEDs (Fox *et al.* 2014). The reverse problem can be solved in a similar way, owing to the time-reversal invariance of Maxwell's equations. Figure 11-4 provides a graphical summary of a scenario where a single nanorod is illuminated from above by a set of radiation modes.

Using the same reasoning as that employed in section 9.5, it can be assumed that the incoming radiation modes, which have infinite spacial extent, couple almost entirely with the corresponding radiation mode of the nanorod, i.e. they miss the nanorod completely. However, a small proportion of the incident power is coupled into guided modes; if the incident power is large enough, this small fraction can be significant. It is simplest to consider a single radiation mode incident from $z = +\infty$ carrying power P_i with a single value of radial wavevector κ_i, a single N, a single choice of azimuthal variation $f(N\phi)$ and a single polarization (TE or TM). It is known from section 9.4 that any given guided mode j can be synthesized in terms of radiation modes of fictitious planar media that share the same axial wavevector β_j as the guided mode. It is

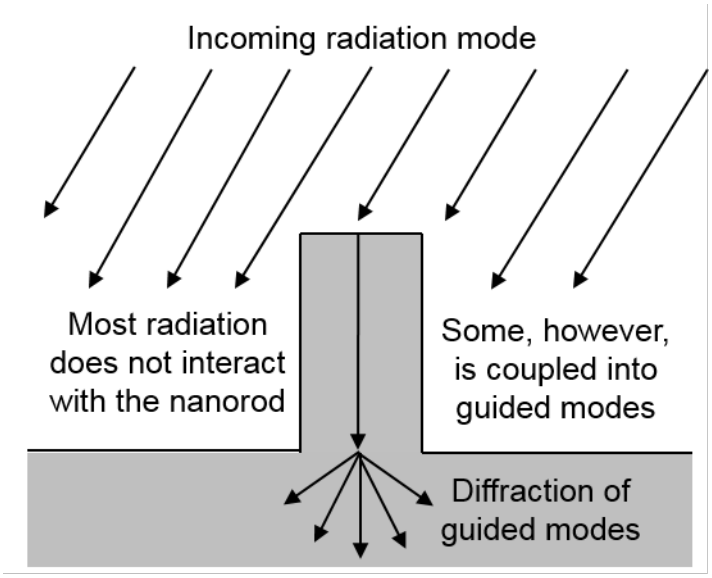

Figure 11-4: A graphical summary of the processes that occur when a single nanorod is illuminated by a set of radiation modes.

also known from section 6.7 that a radiation mode incident on a planar interface will only couple power into other modes of the same κ, N and choice of $f(N\phi)$. Therefore, the incident radiation mode will only excite those components of the guided modes with the same $\kappa = \kappa_i$, N, f and polarization. Performing the inverse process to that in (9.22) yields an expression for the power P_j emitted into a given guided mode j:

$$P_j = P_i \frac{\beta_j}{\beta_i(\kappa_i)} |d_j(\kappa_i) t_{j+}(\kappa_i)|^2 \tag{11.8}$$

Note that d_j, not c_j, appears in (11.8) due to the problem being inverted. Extension to illumination by a distribution of radiation modes results in the more general expression

$$P_j = P_i \sum \int \frac{\beta_j}{\beta_i(\kappa_i)} |d_j(\kappa_i) t_{j+}(\kappa_i)|^2 \, \mathrm{d}\kappa_i, \tag{11.9}$$

where the summation is over all N, both choices of $f(N\phi)$ and both TE and TM polarizations. Once excited by the illumination, the guided modes are subject to the same diffraction and cavity resonance processes that they would be if excited by a dipole. Using the methods of section 9.4 on a single guided mode j, with power P_j as given by (11.9) instead of unit power, results in the angular power integrand $p_{j\pm}(\kappa)$

being given by multiplying (9.22) by P_j:

$$p_{j\pm}(\kappa) = P_j \text{sign}[\zeta_j(\kappa)] \frac{\beta_\pm(\kappa)}{\beta_j} |c_j(\kappa)\tau_{j\pm}(\kappa)|^2. \tag{11.10}$$

As the cavity is illuminated by a single ray from without, as opposed to two coherent rays from within, the numerator of $\tau_{j\pm}$ now has only one term, equal to $t_{j\pm}$:

$$\tau_{j\pm}(\kappa) = \frac{t_{j\pm}(\kappa)}{1 - r_{j+}(\kappa) r_{j-}(\kappa) \mathrm{e}^{2\mathrm{i}\beta_j d}}, \tag{11.11}$$

where d is the nanorod length. The angular intensity distrubution is given by multiplying (9.24) by P_j:

$$I_{j\pm} = P_j \frac{\int_{\theta_1}^{\theta_2} p_{j\pm} \beta_\pm \, \mathrm{d}\theta_\pm}{2\pi r^2 \int_{\theta_1}^{\theta_2} \sin(\theta_\pm) \, \mathrm{d}\theta_\pm}, \tag{11.12}$$

It is also possible to use the methods of chapter 10 in order to account for multimodal interference effects, using the same principles of multiplying by P_j and removing the second term from the numerator of $\tau_{j\pm}$.

11.4.1 Extension to absorbing nanorods

For some applications, such as solar cells, it is essential to consider the case of absorbing nanorods. The guided modes of such systems have complex β_j, which must be found by searching over a section of the complex plane as opposed to an interval of real numbers. In addition, key concepts such as transmittance and power orthogonality of modes are defined in different ways for lossy systems. It is anticipated, however, that these problems are not insurmountable, as Kupec and Witzigmann (2009) have demonstrated using a numerical method to calculate the waveguide modes.

11.5 Summary

This chapter proposes three major avenues for extending the work presented in this thesis. Section 11.2 proposes methods of determining the amount of power emitted by a Hertzian dipole into the guided modes of the nanorod layer and the planar GaN layer below the nanorods. Section 11.3 proposes two methods of dealing with the difficult problem of coupling between nanorods, which has been completely neglected in this thesis. Section 11.4 explores the inverse problem of illumination of nanorods from the outside, which is potentially useful for various applications including solar cells, photodetectors and nanorod LED designs where the quantum well is located

in the planar GaN layer (Fox *et al.* 2014). Note that the methods of section 11.4 could potentially be used to provide an approximate model of sloped nanorods by decomposing the sloped nanorod into a set of multiple non-sloped nanorods, stacked on top of one another, with different widths. Considering that sloped nanorods are frequently reported in the literature and are of considerable research interest (see for example Lewins *et al.* 2014), this is most fortunate.

Chapter 12

Conclusions

Since their invention in the early 1990s, high-efficiency blue and green GaN LEDs, combined with the older red and yellow phosphide LEDs, have quickly come to dominate several lighting applications such as backlighting, displays and signage, due to compactness and rapid response of LEDs compared to older lighting technologies such as incandescent filaments and fluorescent tubes. The high efficiencies and long lifetimes of LEDs have allowed LEDs to make serious inroads into other lighting markets, while the high spectral purity of these devices has oppened up entirely new applications in scientific, architectural, horticultural (Morrow 2009) and medical (Crawford *et al.* 2011) fields.

Nanostructured LEDs have attracted significant research interest over the last decade (for a review see Wiesmann *et al.* 2009) due to their potential to increase light extraction efficiency using photonic crystal diffraction (Lewins *et al.* 2013) and deliver highly directional light emission. Nano-LEDs, where the light-emitting region is close to the nanostructure surface, have the additional potential to emit efficiently in the yellow and red (Bavencove *et al.* 2011, Le Boulbar *et al.* 2013), currently unavailable outside the laboratory with GaN LEDs.

High directionality is useful in backlighting, display, signalling and vehicle headlight applications (among others) and could lead the the realization of new applications such as visible light communication (Zeng *et al.* 2009) and compact projection devices. Originally, photonic band gaps were proposed as a way of achieving high directionality; this has been very difficult to realize, although Lewins *et al.* (2014) have shown a degree of progress. The slow progress in this area has stimulated research into a different approach based on optical waveguiding in the nanostructures.

The waveguiding behaviour of nanostructures is usually modelled using finite-difference time-domain (FDTD) methods (Xu *et al.* 2007, Kölper *et al.* 2011). FDTD methods are computationally expensive and the physics responsible for simulation results is not always apparent, limiting the usefulness of these methods from a design perspective. This thesis explores an alternative approach in which the existing mathematical theory of optical waveguides is extended to provide a quasi-analytic optical model of such nanostructures. The resulting model is shown to achieve good agreement with angular photoluminescence measurements.

As discussed in chapter 7, a large fraction of the literature on LED nanostructures focuses on cylindrically symmetric structures, although hexagonally prismatic, pyramidal and conical structures have also been widely reported. As the most symmetric of these structure types, cylindrical nanorods are the easiest to model. The guided or bound modes of infinitely long cylindrical wavguides have been extensively studied due to their applications in optical fibres; the continuum of radiation modes is of less interest to most authors, with Snyder and Love (1983) among the few to have provided a comprehensive treatment.

In chapter 6, the basics of modal methods in cylindrical polar co-ordinates are introduced, along with the continuum of cylindrical modes of free space. It is shown that the law of reflection, Snell's Law and the Fresnel equations, which are normally applied to plane waves in Cartesian co-ordinates, also apply to these modes. It is also shown that when (6.27) is applied to these modes, the familiar expressions for both the angular intensity distribution and total power emitted by a Hertzian dipole in free space, usually derived in spherical polar co-ordinates (Bjork *et al.* 1995, Delbeke *et al.* 2002, Sadiku 2007 pp. 635) are re-derived. Finally, it is shown that the cylindrical modes of free space can be given in terms of either Bessel or Hankel functions and that one formulation can be converted into the other with a simple procedure.

In chapter 8, fictitious infinitely long optical fibres with a range of cross-sections designed to emulate those of cylindrical nanorods reported in the literature are studied. It is shown that even in this simple system, the total power emitted into guided and radiation modes varies hugely with the position and orientation of the Hertzian dipole emitter with respect to the nanorod geometry. It is also shown that the extraction efficiency of these fictitious structures is vastly superior to that of planar LEDs in almost all cases, while falling short of the best surface-roughened structures (Shcheckin *et al*

2006, cited in Mottier 2009).

In chapter 9, the main results of chapters 6 and 8 are combined to create a model for the angular diffraction patterns that result when a guided mode propagates to the end of the nanorod (O'Kane *et al.* 2014). Using the established theory of emission within planar Fabry-Pérot cavities, which is reviewed in chapter 5, the effects of inter-reflections at the nanorod ends are fully accounted for. By simulating a device structure (Zhuang 2012) for which angular photoluminescence measurements (Lewins and Fox 2013) are available, it is shown that gross features in the measurements can be explained solely in terms of the guided modes. Using a similar method, it is shown that the radiation modes experience a phase shift on reaching the nanorod ends, although the angular direction is unchanged.

The main advantages of this model are high computational efficiency and the aforementioned ability to identify the physics responsible for measured results. The main disadvantage is the reliance on the cylindrical symmetry of the nanorods, which limits the range of structures that can be studied and prevents the effects of coupling between the modes of neighbouring nanorods from being accounted for without further extensions of the model, which are proposed in chapter 11. The method has many similarities with that reported by Paniagua-Domínguez *et al.* (2013). However, the latter model is semi-empirical as the modal reflection coefficients are obtained by fitting to simulations/measurements, whereas the model proposed in this thesis is entirely from first principles.

Other first principles models of finite length cylindrical structures have been reported in the literature, but these are mostly based on matrices (see for example Chew 1985), which is a problem when considering the continuum of radiation modes. Kressel and Butler (1977) provide a formula for the exact radiation patterns resulting from illumination of apertures where the aperture field is known, but their treatment of the aperture field itself is matrix based and therefore suffers from similar limitations. It is therefore not surprising that literature reports on the application of these models to nanorod LEDs are few.

In chapter 10, the effect of interference between different modes that are excited by the same dipole (and are therefore coherent) is discussed. This makes it possible to predict the angular emission pattern arising from a Hertzian dipole emitter of any given position and orientation with respect to the nanorod geometry. It is therefore possible

to estimate the positions and orientations of dipoles by empirically fitting these predictions to measured data. This is difficult as the model does not consider the effects of coupling between nanorods, although good fits to measurement were achieved for two wavelengths. The results of this fitting process are consistent with those of cathodoluminescence studies (Zhuang *et al.* 2013c). It was also found that a large fraction of the power in the fits was due to the Lambertian term added as an attempt to simulate scattering due to neighbouring nanorods. The method was also able to reproduce the results of Paniagua-Domínguez *et al.* (2013), although significant discrepancies arise when the nanorod radius is very small.

By solving the more difficult problem of emission from within a nanorod, it is also possible to solve the simpler and much more common inverse problem where nanorods are illuminated from outside, as explained in section 11.4. This method will be useful for refining the alternative highly directional LED design proposed by Fox *et al.* (2014). The inverse problem also arises in many other applications including photonic crystals, solar cells (Kupec *et al.* 2010) and photodetectors (Wang *et al.* 2011).

In this thesis, classical electromagnetic theory is extended to provide the first quasi-analytic optical model of cylindrical nanostructures from first principles. Detailed numerical results show short computation times, an ability to explain key features in angular photoluminescence data and a limited ability to reproduce said data from first principles. Possible extensions to the method are proposed that could allow much more accurate fits to measurements. The insights gained from this model could make compact, highly directional LEDs a reality, opening up new applications in solid state lighting. Furthermore, the ubiquity of cylindrical nanostructures and the universality of the mathematics could result in this model gaining applications in other industries and research avenues.

References

All URLs last accessed April 2015.

Adams MJ 1981 *An Introduction to Optical Waveguides* Chichester: Wiley

Akasaki I, Amano H, Itoh K, Koide N and Manabe K 1992 "GaN based UV/blue light-emitting devices GaAs and Related Compounds conference *Institute of Physics Conference Series* **129** 851

Arfken GB and Weber HJ 2005 *Mathematical Methods of Physicists (6th Edition)* Boston: Elsevier

Bae SY, Kong DJ, Lee JY, Seo DJ and Lee DS 2013 "Size-controll InGaN.GaN nanorod array fabrication and optical characterization" *Optics Express* **21** *14* 16854-16862

Aspnes DE 1982 "Local-field effects and effective-medium theory: A microscopic perspective" *American Journal of Physics* **50** *8* 704-709

Bai J, Wang Q and Wang T 2012 "Greatly enhanced performance of InGaN/GaN nanorod light emitting diodes" *Physica Status Solidi (a)* **209** *3* 477-480

Bavencove AL, Tourbot G, Garcia J, Desieres Y, Gilet P, Levy F, Andre B, Gayral B, Daudin B and Dang LS 2011 "Submicrometre resolved optical characterization of green nanowire-based light emitting diodes *Nanotechnology* **22** 345705

Benisty H, De Neve H and Weisbuch C 1998 "Impact of planar microcavity effects on light extraction Part I: Basic concepts and analytical trends *IEEE Journal of Quantum Electronics* **34** *9* 1612-1631

Bjork G, Yamamoto Y and Heitmann H 1995 *Confined Electrons and Photons* London: Plenum in cooperation with NATO Scientific Affairs Division 467-501

Böcklin C, Veprek RG, Steiger S and Witzigmann B 2010 "Computational study of an InGaN/GaN nanocolumn light-emitting diode" *Physical Review B* **81** 155306

Bockstaele R, Sys C, Blondelle J, Dhoedt B, Moerman I, Van Daele P, Demesster P and Baets R 1999 "Resonant Cavity LED's Optimized for Coupling to Polymer Optical Fibers" *IEEE Photonics Technology Letters* **11** *2* 158-160

Breitenstein O, Bauer J, Altermatt PP and Ramspack K 2010 "Influence of Defects on Solar Cell Characteristics" *Solid State Phenomena* **156-158** 1-10

Calle F, Naranjo FB, Fernández S, Sánchez-Garcia MA, Calleja E and Muñoz E 2002 "Nitride RCLEDs grown by MBE or POF applications *Physica Status Solidi (a)* **192** *2* 277-285

Chew WC 1990 '*Waves and Fields in Inhomogenous Media* New York: IEEE Press 351-360

Cho HK, Jang J, Choi JH, Choi J, Kim J, Lee JS 2005 "Light extraction enhancement from nano-imprinted photonic crystal GaN-based light emitting diodes *Optics Express* **14** *19* 8654-8660

Cho HK, Kim SK, Bae DK, Kang BC, Lee JS and Lee YH 2008 "Laser liftoff GaN thin-film photonic crystal GaN-based light-emitting diodes *IEEE Photonics Technology Letters* **20** *24* 2096-2098

Clarke RH and Brown J 1980 *Diffraction Theory and Antennas* Chichester: Horwood

Cosendey G, Carlin JF, Kaufmann NAK, Butte R and Grandjean N 2011 "Strain compensation in AlInN/GaN multilayers on GaN substrates: Application to the realization of defect-free Bragg reflectors" *Applied Physics Letters* **98** 181111

Cree 2011 "Cree smashes white LED record again *Optics.org* `http://optics.org/news/2/5/8`

Craford MG, Shaw RW, Herzog AH and Groves WO 1972 "Radiative recombination mechanisms in GaAsP diodes with and without nitrogen doping *Journal of Applied Physics* **43** 4075

Crawford MH, Banas MA, Ross MP, Ruby DS, Nelson JS, Boucher R and Allerman AA 2005 "Final LDRD Report: Ultraviolet Water Purification Systems for Rural Environments and Mobile Applications" *Report from Sandia National Laboratories* `http://prod.sandia.gov/techlib/access-control.cgi/2005/057245.pdf`

David A, Benisty H and Weisbuch C 2007 "Optimization of light-diffracting photonic-crystals for high extraction efficiency LEDs" *Journal of Display Technology* **3** *2* 133-148

Delbeke D, Bockstaele R, Bienstman P, Baets R and Benisty H 2002 "High-efficiency resonant-cavity semiconductor light-emitting diodes: a review *IEEE Journal on Selected Topics in Quantum Electronics* **8** *2* 189-206

Deppe DG, Lei C, Lin CC and Huffaker DL 1994 "Spontaneous Emission from Planar Microstructures" *Journal of Modern Optics* **41** *2* 325-344

Dorsaz J, Carlin JF, Gradecak S and Ilegems M 2005 "Progress in AlInN-GaN Bragg reflectors: Application to a microcavity light emitting diode *Journal of Applied Physics* **97** 084505

Duke CB and Holonyak N 1973 "Advances in light-emitting diodes *Physics Today* **December issue** 23

Epistar 2012 Manufacturer's data sheet for commercial LED wafer

Fan HJ, Werner P and Zacharias M 2006 "Semiconductor Nanowires: From Self-Organization to Patterned Growth" *Small* **2** *6* 700-717
Fink Y, Winn JN, Fan S, Chen C, Michel J, Joannopoulos JD and Thomas EL 1998 "A dielectric omnidirectional reflector *Science* **282** 1679-1682
Fox SA, O'Kane SEJ, Lis SM and Allsopp DWE 2015 "Designing InGaN/GaN nano-LED arrays for étendue-limited applications"
Phys. Stat. Sol. (c) DOI 10.1002/pssc.201400240
Groves WO, Herzog AH and Craford MG 1971 "The effect of nitrogen doping on GaAs1-xPx electroluminescent diodes *Applied Physics Letters* **19** 184
Grieshaber W, Schubert EF, Goepfert ID, Karlicek RF Jr., Schurman MJ and Tran C 1996 "Competition between band gap and yellow luminescence in Gan and its relevance for optoelectronic devices" *Journal of Applied Physics* **80** *8* 4615-4620
Harbers G, Bierhuizen SJ and Krames MR 2007 "Performance of High Power Light Emitting Diodes in Display Illumination Applications" *Journal of Display Technology* **3** *2* 98-109
Hecht E 2005 *Optics (Fourth Edition)* London: Addison-Wesley
Henderson MR, Shahraam AV, Greentree AD and Monro TM 2011 "Dipole emitters in fiber: interface effects, collection efficiency and optimization" *Optics Express* **19** *17* 16182-16194
Hersee SD, Sun XY and Wang X 2006 "The Controlled Growth of GaN Nanowires" *Nano Letters* **6** *8* 1808-1811
Herzog AH, Groves WO and Craford MG 1969 "Electroluminescence of diffused GaAs1-xPx diodes with low donor concentrations *Journal of Applied Physics* **40** 1830
Holonyak N and Bevacqua SF 1962 "Coherent (visible) light emission from Ga(As1-xPx) junctions *Applied Physics Letters* **1** 82
Jackson JD 1999 *Classical Electrodynamics (Third Edition)* Chichester: Wiley
Jiang HX and Lin JY 2013 "Nitride micro-LEDs and beyond - a decade progress review" *Optics Express* **21** *S3* A475-A484
Kasap SO 2013 *Optoelectronics and Photonics: Principles and Practices (Second Edition)* Harlow: Pearson Education 281-289
Kim HM, Cho YH, Lee H, Kim SI, Ryu SR, Kim DY, Kang TW and Chung KS 2004 "High-brightness light emitting diodes using dislocation-free indium gallium nitiride/gallium nitride multiquantum-well nanorod arrays *Nano Letters* **4** *6* 1059-1062
Kishino K, Sekiguchi H, Kikuchi A 2009 "Improved Ti-mask selective-area growth (SAG) by rf-plasma-assisted molecular beam epitaxy demonstrating extremely uniform GaN nanocolumn arrays" *Journal of Crystal Growth* **311** 2063-2068
Kishino K, Nagashima K and Yamano K 2013 "Monolighic Integration of InGaN-Based

Nanocolumn Light-Emitting Diodes with Different Emission Colors" *Applied Physics Express* **6** 012101

Kölper C, Bergbauer W, Drechsel P, Sabathil M, Straßburg M, Lugauer HJ, Witzigmann B, Fündling S, Li S, Wehmann HH and Waag A 2011 "Towards nanorod LEDs: Numerical predictions and controlled growth" *Physica Status Solidi (c)* **8** *7-8* 2305-2307

Kong BH, Cho HK, Kim MY, Choi RJ and Kim BK 2011 "InGaN/GaN blue light emitting diodes using Al-doped ZnO grown by atomic layer deposition as a current spreading layer *Journal of Crystal Growth* **326** *1* 147-151

Kressel H and Butler JK 1977 *Semiconductor Lasers and Heterojuction LEDs* London: Academic Press 187 Kupec J and Witzigmann B 2009 "Dispersion, Wave Propagation and Efficiency Analysis of Nanowire Solar Cells" *Optics Express* **17** *12* 10399-10410

Kupec J, Stoop RL and Witzigmann B 2010 "Light Absorption and emission in nanowire array solar cells" *Optics Express* **18** *26* 27589-27605

LEDs Magazine 2004 "Terminology: LED efficiency Available online at `www.ledsmagazine.com/features/1/1/10`

Le Boulbar ED, Gîrgel I, Lewins CJ, Edwards PR, Martin RW, Šatka A, Allsopp DWE and Shielda PA 2013 "Facet recovery and light emission from GaN/InGaN/GaN core-shell structures grown by metal organic vapour phase epitaxy on etched GaN nanorod arrays" *Journal of Applied Physics* **114** 094302

Lee TX, Gao KF, Chien WT and Sun SS 2007 "Light extraction analysis of GaN-based light-emitting diodes with surface texture and/or patterned substrate *Optics Express* **15** *11* 6670-6676

Lee YJ, Lin SY, Chiu CH, Lu TC, Kuo HC, Wang SC, Chhajed S, Kim JK and Schubert EF 2009 "High output power density from GaN-based two-dimensionsal nanorod light-emitting diode arrays *Applied Physics Letters* **94** 141111

Leung MMY, Djurîšic AB and Li EH 1998 "Refractive index of InGaN/GaN quantum well" *Journal of Applied Physics* **84** *11* 6312-6317

Lewins CJ and Fox SA 2013 Personal communication: Photoluminescence measurements on nanorod LED array fabricated by Zhuang (2012)

Lewins CJ, Allsopp DWE, Shields PA, Gao X, Humphreys B and Wang WN 2013 "Light Extracting Properties of Buried Photonic Quasi-Crystal Slabs in InGaN/GaN LEDs" *Journal of Display Technology* **9** *5* 333-338

Lewins CJ 2015 Doctoral thesis, University of Bath (currently under review)

Lewins CJ, Le Boulbar ED, Lis SM, Edwards PR, Martin RW, Shields PA and Allsopp DWE 2014 "Strong photonic crystal behavior in regular arrays of core-shell and quantum disc InGaN/GaN nanorod light-emitting diodes" *Journal of Applied Physics* **116**

044305
Li CK, Yang HC, Hsu TC, Shen YJ, Liu AS and Wu YR "Three dimensionsal numerical study on the efficiency of a core-shell InGaN/GaN nultiple quantum well nanowire light-emitting diodes" *Journal of Applied Physics* **113** 183104
Li QM and Wang GT 2008 "Improvement in aligned GaN nanowire growth using submonolayer Ni catalyst films" *Applied Physics Letters* **93** 043119
Li QM, Westlake KR, Crawford MH, Lee SR, Koleske DD, Figiel JJ, Cross KC, Fathololoumi S, Mi Z and Wang GT 2013 "Optical performance of top-down fabricated InGaN/GaN nanorod light emitting diode arrays" *Optics Express* **19** *25* 25528-25534
Li SF and Waag A 2012 "GaN based nanorods for solid state lighting" *Journal of Applied Physics* **111** 071101
Lin YH, You JP, Lin YC, Tran NT and Shi FG 2010 "Development of high-performance optical silicone for the packaging of high-power LEDs *IEEE Transactions on Components and Packaging Technologies* **33** *4* 761-766
Lis SM, O'Kane SEJ, Lewins CJ, Fox SA, Zhuang YD, Sarma J and Allsopp DWE 2013 "Factors affecting the directionality of InGaN/GaN nanorod LED arrays" *10th International Conference on Nitrids Semiconductors, Washington, D.C.*
Liu CW, Šatka A, Jagadamma LK, Edwards PR, Allsopp DWE, Martin RW, Shields PA, Kovac J, Uherek F and Wang WN 2009 "Light emission from InGaN quantum wells grown on the facets of closely spaced GaN nano-pyramids formed by nano-imprinting *Applied Physics Express* **2** 121002
Logan RA, White HG and Wiegmann W 1968 "Efficient green electroluminescence in nitrogen-doped GaP p-n junctions *Applied Physics Letters* **13** 139
Logan RA, White HG and Wiegmann W 1971 "Efficient green electroluminescent junctions in GaP *Solid State Electronics* **14** 55
Marcuse D 1982 *Light Transmission Optics (Second Edition)* London: Van Nostrand Reinhold 232-235
Meneghini M, Tazzoli A, Mura G, Meneghesso and Zanoni E 2010 "A Review on the Physical Mechanisms That Limit the Reliability of GaN-Based LEDs" *IEEE Transactions on Electron Devices* **57** *1* 108-118
Miyajima T, Kono S, Watanabe H, Oki T, Koda R, Kuramoto M, Ikeda M and Yokoyama H 2011 "Saturable absorbing dynamics of GaInN multiquantum wall structures *Applied Physics Letters* **98** 171904
Morrow 2008 "LED Lighting in Horticulture" *HortScience* **43** *7* 1947-1950
Mottier P 2009 *LEDs for Lighting Applications* London: ISTE
Nakamura S, Senoh M and Mukai T 1993a "p-GaN/n-InGaN/n-GaN double-heterostructure blue-light-emitting diodes" *Japanese Journal of Applied Physics* **32** L8

Nakamura S, Senoh M and Mukai T 1993b "High-power InGan/GaN double-heterostructure violet light-emitting diodes" *Applied Physics Letters* **62** 2390
Nakamura S, Mukai T and Senoh M 1994 "Candela-class high-brightness InGaN/GaN double-heterostructure blue-light-emitting diodes *Applied Physics Letters* **64** 1687
O'Kane SEJ, Sarma J and Allsopp DWE 2014 "A Quasi-Analytic Modal Expansion Technique for Modeling Light Emission from Nanorod LEDs" *IEEE Journal of Quantum Electronics* **50** *9* 774-781
Osram 2011, consumer catalogue
Palik ED c. 1998 *Handbook of Optical Constants of Solids* San Diego: Academic Press Available online through Knovel
Paniagua-Domínguez R, Grzela G, Gómez Rivas J and Sánchez-gil JA 2013 "Enhanced and directional emission of semiconductor nanowires tailored through leaky/guided modes" *Nanoscale* **5** *21* 10582-10590
Plessey Semiconductors 2014 Manufacturer's data sheet for research-grade LED wafer
Purcell EM 1946 "Spontaneous Emission Probabilities at Radio Frequencies" *Physical Review* **69** 681
Round HJ 1907 "A note on carborundum *Electrical World* **19** 309
Sadiku MNO *Elements of Electromagnetics (Fourth Edition)* Oxford: OUP
Schad SS, Neubert B, Eichler C, Scherer M, Habel F, Seyboth M, Scholz F, Hofstetter D, Unger P, Schmid W, Karnutsch C and Streubel K 2004 "Absorption and scattering in InGaN-on-sapphire- and AlGaInP-based light-emitting diodes *Journal of Lightwave Technology* **22** *10* 2323-2332
Schubert EF and Kim JK 2005 "Solid-state light sources getting smart *Science* **308** 1274-1278
Schubert EF 2006 *Light Emitting Diodes (Second Edition)* Cambridge: CUP First edition diagrams available online at
`www.lightemittingdiodes.org`
Shchekin OB, Epler JE, Trottier TA, Margalith T, Steigerwald DA, Holcomb MO, Martin PS and Krames MR 2006 "High performance thin-film flip-chip InGaN-GaN light emitting diodes *Applied Physics Letters* **89** 071109
Shenai K and Shah K 2011 "Smart DC micro-grid for efficient utilization of distributed renewable energy" *Processings of IEEE Energytech conference*
Snyder AW and Love JD 1983 "Optical Waveguide Theory" London: Chapman and Hall
Shi YM and Chi JJ 2007 "Linear and Nonlinear Intersubband Optical Absorptions and Refractive Index Changes in InGaN Strained Single Quantum Wells: Strong Built-in Electric Field Effects" *Chinese Physics Letters* **24** *8* 2376-2379

Shockley W and Read WT 1952 "Statistics of the Recombinations of Holes and Electrons" *Physical Review* **87** *5* 835-842

Takeuchi K, Adachi S and Ohtsuka K 2010 "Optical properties of AlxGa1-xN alloy *Journal of Applied Physics* **107** 023306

US Department of Energy 2006 *Lifetime of white LEDs* `http://cool.conservation-us.org/byorg/us-doe/lifetime_white_leds_aug16_r1.pdf`

Veselago VG 1968 "The electrodynamics of substances with simultaneously negative value sof ϵ and μ" *Soviet Physics Uspekhi* **10** *4* 509-514

Vredenberg AM, Hunt NEJ, Schubert EF, Jacobson DC, Poate JM and Zydzik GJ 1993 "Controlled Atomic Spontaneous Emission from Er^{3+} in a Transparent Si-SiO2 Microcavity" *Physical Review Letters* **71** 517

Wang SB, Hsiao CH, Chang SJ, Lam KT, Wen KH, Hung SC, Young SJ and Huang BR 2011 "A CuO nanowire infrered photodetector" *Sensors and Actuators A: Physical* **171** 207-211

Wierer JJ, David A and Megens MM 2009 "III-nitride photonic-crystal light-emitting diodes with high extraction efficiency *Nature Photonics* **3** 163-169

Wiesmann C, Bergenek K, Linder N and Schwarz UT 2009 "Photonic crystal LEDs - designing light extraction" *Laser and Photonics Reviews* **3** *3* 262-286

Wysocki A 2007 `en.wikipedia.org/wiki/File:2007-07-24_High-power_light_emiting_diodes_(Luxeon,_Lumiled).jpg`

Xu T, Yang S, Nair SV and Ruda HE 2007 "Nanowire-array-based photonic crystal cavity by finite-difference time-domain calculations *Physical Review B* **75** 125104

Yamada M, Mitani T, Narukawa Y, Shioji S, Niki I, Sonobe S, Deguchi K, Sano M and Mukai T 2002 "InGaN-based near-ultraviolet and blue-light-emitting diodes with high external quantum efficiency using a patterned sapphire substrate and a mesh electrode *Japanese Journal of Applied Physics* **41** L1431-L1433

Yamanishi M and Suemene I 1984 "Comment on polarization dependent momentum matrix elements in quantum well lasers" *Japanese Journal of Applied Physics* **23** L35-L36

Yariv A 1982 *Theory and Applications of Quantum Mechanics* Chichester: Wiley 143

Yeh P 1988 *Optical Waves in Layered Media (First Edition)* Chichester: Wiley

Zeng L, OBrien DC, Minh HL, Faulkner GE, Lee K, Jung D, Oh YJ and Won ET 2009 "High data rate multiple input multiple output (MIMO) optical wireless communication using white LED lighting *IEEE Journal on Selected Areas in Communications* **27** *9* 1654-1662

Zhou Y, Tran N, Lin YC, He Y and Shi FG 2008 "One-component, low-temperature and fast-cure epoxy encapsulant with high refractive index for LED applications *IEEE*

Transactions on Advanced Packaging **31** *3* 484-489
Zhu D, Wallis DJ and Humphreys CJ 2013 "Prospects of III-nitride optoelectronics grown on Si" Reports on Progress in Physics **76** 106501
Zhuang YD 2012 Personal communication: Fabrication of nanorod LED sample from a commercial wafer (Epistar 2012)
Zhuang YD, Lewins CJ, Lis SM, Shields PA and Allsopp DWE 2013a "Fabrication and Characterization of Light-Emitting Diodes Comprising Highly Ordered Arrays of Emissive InGaN/GaN Nanorods" *IEEE Photonics Technology Letters* **25** *11* 1047-1049
Zhuang YD, Lewins CJ, Lis SM, O'Kane SEJ, Fox SA, Shields PA and Allsopp DWE 2013b "Fabrication and Characterization of Ordered Arrays of InGaN/GaN Nanorod LEDs" *UK Nitrides Consortium 2013 Winter Meeting, Cardiff, UK*
Zhuang YD, Lis SM, Bruckbauer J, O'Kane SEJ, Shields PA, Edwards P, Sarma J, Martin RW and Allsopp DWE 2013c "Optical Properties of GaN nanorods Containing a Single or Multiple InGaN Quantum Wells" *Japanese Journal of Applied Physics* **52** 08JE11